CRANFIELD UNIVERSITY

Luis Daniel Cozzolino

Finite element analysis of localised rolling to reduce residual stress and distortion

School of Applied Sciences
Welding Engineering and Laser Processing Centre

PhD
Academic Year: 2009 - 2013

Supervisor: Dr. Paul A. Colegrove
August 2013

CRANFIELD UNIVERSITY

School of Applied Science
Welding Engineering and Laser Processing Centre

PhD Thesis

Academic Year 2009 - 2013

Luis Daniel Cozzolino

Finite element analysis of localised rolling to reduce residual stress and distortion

Supervisor: Dr. Paul A. Colegrove
August 2013

This thesis is submitted in partial fulfilment of the requirements for the degree of Doctor in Philosophy

ABSTRACT

Fusion welding processes cause residual stress due to the uneven heat distribution produced by the moving welding torch. These residual stresses are characterised by a large tensile component in the welding direction. Due to the self-equilibrated nature of the residual stress, compressive ones are present in the far field next to the weld seam, which can cause different kind of distortion such as bending or buckling. Welding residual stress can be responsible of premature failure of the components, such as stress crack corrosion, buckling, and reduction of fatigue life. Localised rolling is a stress engineering technique that can be used to reduce the residual stress and distortion caused by welding. It induces plastic strain in the rolling direction, counteracting the plastic strain produced during welding.

In this thesis three techniques were investigated, pre-weld rolling, post-weld rolling, and *in situ* rolling. These techniques have been seldom studied in the past, particularly pre-weld rolling; consequently the mechanisms are poorly understood. Finite element models allow stress and strain development during both welding and rolling processes to be better understood, providing an improved understanding of the mechanisms involved and aiding process development.

A literature survey was done to find the state of the art of the computational welding mechanics simulations, stress management, and the residual stress measurement techniques, as well as the knowledge gaps such as, the thermal losses through the backing-bar in the thermal simulation, the frictional interaction in the rolling process, and the material properties of the steel used in the models. In the literature not many models that investigate the management of welding residual stress were found.

After this, the general considerations and assumptions for the welding thermal mechanical models presented in this thesis were discussed. The effect of different backing-bar conditions, as well as different material properties where investigated. Both influenced the residual stress profile to varying degrees. In

particular, temperature dependent heat loss to the backing-bar was necessary to capture the improved heat loss near the weld. The distortion predicted by the model was investigated to determine whether it was due to bending or buckling phenomena. Lastly, the temperature distribution and residual stress predictions were validated against thermocouple and neutron diffraction measurements conducted by Coules *et al.* [1–3].

Pre-weld rolling was the first of the three rolling methods considered, in which rolling is applied to the plates before performing GMA butt-welds. The principle behind this technique consisted in inducing tensile residual stress in the weld region before welding; therefore, it is similar to mechanically tensioning the weld, which can significantly reduce the residual stress and distortion. However, there was no significant change in the tensile residual stresses. On the other hand, it was possible to achieve a small reduction in the distortion, when the plates were rolled on the opposite surface to the weld; rolling in this way induced distortion in the opposite direction to the distortion induced by welding, reducing the magnitude of the latter. These results were compared with experiments conducted by Coules *et al.* [1,4]. A subsequent investigation combined pre-weld rolling with post-weld heating. With this additional process the residual stress and distortion were significantly reduced, and flatter residual stress profile was achieved.

The post-weld rolling and *in situ* rolling techniques were discussed afterwards. In the post-weld rolling models, rolling was applied after the weldment was cooled to room temperature. In *in situ* rolling the roller was applied on top of the weld bead at some distance behind the torch, while it was still hot. The principle behind these techniques consisted in applying positive plastic strain to the weld bead region by a roller, counteracting the negative plastic strains produced in the welding process. Two roller profiles were investigated, namely, grooved, and double flat rollers. The post-weld rolling on top of the weld bead models, which used the grooved roller, showed good agreement against experimental results, producing a large reduction of the residual stress and distortion. Some discrepancies were present when the weld toes were rolled with the dual flat

roller. The former roller was more efficient for reducing residual stress and distortion. The influence of different friction coefficients (between the roller and weldment, and between the backing-bar and the weldment), were investigated. It showed significant dependency on the residual stress distribution when high rolling loads were used. The frictional interaction constrained the contact area inducing more compressive stress in the core of the weld bead; therefore it produced more tensile residual stress in the surface of the weldment. Additionally, the influence of rolling parameters on the through-thickness residual stress variation was investigated. Low loads only influence the residual stress near the surface, while high loads affected the material through the entire thickness.

When the dual flat roller was used to roll next to the weld bead, significant compressive residual stress was induce in the weld bead; however, the residual stress reduction was very sensitive to the contact of the roller to the weld toes; therefore, when rolling a weld bead that varies in shape along the weld, the residual stress reduction is not uniform and varies along the length. On the other hand, the *in situ* rolling did not produced significant residual stress or distortion reduction in all the cases analysed. The rolling occurred when the material was still hot and the residual stress was subsequently formed as the material cooled to room temperature. Numerical modelling was a very useful tool for understanding the development of stress and plastic strain during the welding and rolling processes.

Keywords:

Finite element analysis, residual stress, localised rolling, pre-weld rolling, post-weld rolling, *in situ* rolling.

ACKNOWLEDGEMENTS

I would like to acknowledge all the members and fellow PhD. students of the Welding Engineering and Laser Processing Centre at Cranfield University, which by the time I finished this thesis were almost family to me. In particular, I'd like to thank my supervisor Dr. Paul Colegrove, and Prof. Stewart Williams, for all the help, support, patience, and understanding that they provided along the whole period; my industrial supervisor Dr. Shuwen Wen, and my colleague Dr. Harry Coules, who did the experimental part of this project. Without their help and inputs this thesis would not be possible.

I would also like to acknowledge Dr. Jialuo Ding, Dr. Supriyo Ganguly, and the IT department of Cranfield University for all the technical support. This project was sponsored by the UK Engineering and Physical Sciences Research Council (grant no. EP/G014132/1), and Tata Steel UK Ltd. In addition, the neutron diffraction facilities required to the measurements of the residual stresses were provided by the Institut Laue-Langevin, France (ILL, proposal no.s 1- 02-68 and 1-02-80) and the Science and Technology Facilities Council (ISIS facility, proposal no.s 1120159 and 1210128).

I would like to thanks my colleagues and friends Sonia Meco, Gonçalo Pardal, Anthony McAndrew, Usani Ofem, Filomeno Matina, Wojciech Suder and Stephan Herbst which made my time in the PhD office very pleasant.

I would like to dedicate this work to my parents and to Giusy Valvano, who gave me plenty of support in the most critical moments of my research and my life, being in some cases more effective to reduce residual stress than localised rolling.

LIST OF ABBREVIATIONS

Symbol	Description	Units
σ_n	Stress in the n-direction	[MPa]
T	Temperature	[°C] or [K]
ε	Strain	none
ν	Poisson ratio	none
A	Area	[m^2]
E	Young modulus	[GPa]
Q_n	Heat flow per unit time in n-direction	[$J \cdot s^{-1}$]
q_n	Heat flux per units of time and area	[$J \cdot m^{-2} \cdot s$]
k	Thermal conductivity	[$W \cdot m^{-1} \cdot K^{-1}$]
h	Convection coefficient	[$J \cdot m^{-2} \cdot s \cdot K$]
σ	Stefan-Boltzmann constant 5.67×10^{-8}	[$J \cdot m^{-2} \cdot s^{-1} \cdot K^{-4}$]
ρ	Density	[$kg \cdot m^{-3}$]
μ	Dynamic viscosity	[Pa·s]
E_g	Heat generated by the element	[J]
E_s	Heat stored in the element	[J]
t	Time	[s]
K_o	Bessel function of second kind and zero order	none
g	Thickness	[m]
α	Thermal diffusivity $\left(\frac{k}{\rho c_p}\right)$	[$m^2 \cdot s^{-1}$]
c_p	Specific heat capacity at constant pressure	[$J \cdot kg^{-1} \cdot K$]
r	Radial distance, $\sqrt{x^2 + y^2}$	[m]
q	Power density in double ellipsoid distribution or thermal losses	[$W \cdot m^{-3}$] or [W]
v	Travel speed	[$m \cdot s^{-1}$]
p	Point of observation	[mm]
Q	Heat input rate	[J/s]
λ	Wavelength	[m]
d_{hkm}	Interplanar distance	[m]
d_0	Interplanar distance without strain	[m]
V_{pp}	Isotropic principal velocity	[m/s]
V_L^0 V_T^0	Isotropic longitudinal and transversal velocity respectively	[m/s]

LIST OF NOMENCLATURES

PWR	Pre-weld rolling
PoWR	Post-weld rolling
GMA(W)	Gas metal arc either welding or welded
FSW	Friction stir welding
RS	Residual stress
AWL	Applied welding load
CBL	Critical buckling load
CWM	Computational welding mechanics
HAZ	Heat affected zone

TABLE OF CONTENTS

Chapter 1 Literature Review

1.1 Introduction

Residual stress due to welding is widely known to have a detrimental effect on the component lifetime. Uneven heating during welding causes thermal expansion and plastic deformation of the material, generating consequently residual stresses when the material cools down. Distortion, on the other hand, is the response of the material in order to reduce the residual stress.

Computer simulation has been in used on welding since the early 70's [5–7]. However, due to the computer capacity at that time, it was limited to rather simple models. With the advance in computer's speed, capacity, and reliability, computer simulation has consolidated its position on welding, being nowadays fairly commonly used to determine thermal cycles and residual stresses.

This review is focused on fusion welding of steel and the techniques to reduce residual stress and resulting distortion. However, in some cases other welding processes and materials are present in order to show trends and general concepts.

1.2 Residual stress

Manufacturing processes that modify the shape of the workpiece or induce high temperature gradients, as well as chemical reactions, can potentially induce residual stress. It can be beneficial, as for the tempered glasses, or very harmful, as in welding where it can induce buckling distortion and stress corrosion cracking. Figure 1-1 shows the possible effect of the residual stress on the workpiece performance. Withers and Bhadeshia [8] sub-divide the residual stress, according to its length scale perspective, into three types: *type I* or macrostress, which vary in large distances; *type II* or intergranular stress, which vary within grains scale; and *type III* or atomic stress, which vary at atomic scale. Stress of type II and III are inherent to the material. For the objective of this literature review only the stresses of type I will to be discussed.

Figure 1-1 Effect of the residual stress on the workpiece performance [9].

1.2.1 Residual stress formation during welding

In welding, due to the high temperatures involved, localised metallurgical and mechanical changes occur [10]. Normally during welding, the weld metal and the close surrounding material are at a considerably higher temperature than the parent metal. Hence, the material in front and beside the weld pool is in compression due to the thermal expansion of that region and the mechanical constraint of the cooler regions next to it. When the compressive stresses exceed the yielding point of the material, it deforms plastically in compression. As soon as the weld pool starts to solidify and shrink it generates a tensile region on the weld seam and in the surrounding areas [11].

A good example to understand this phenomenon is proposed by Wilson and Hao [12], by the analogy of three bars. Consider three equal steel bars connected at their top and bottom, by undeformable connectors, as shown in figure 1-2 *a*, and the whole assembly is at room temperature. If the middle bar is heated, while the rest of the frame remains isolated, this bar will expand due to the high temperature, generating compressive stresses within it (see figure 1-2 *b*). The yielding strength of steel reduces with the increase of temperature,

therefore, when it is exceeded by the middle bar, plastic flow occurs. The side bars, on the other hand, are under tensile stress to counterbalance the action of the middle bar dilation. The magnitude of the stress in the side bars will be half of that in the middle bar.

As the temperature decreases in the middle bar, compressive stresses in the middle bar diminish, and become tensile, and eventually reach the yielding point, causing further plastic deformation of it. When the middle bar reaches room temperature the residual stresses on it will be equal to the yielding strength plus a contribution from work hardening, while the side bars will have compressive stresses equal to half of the middle bar tensile stress. This example can be easily related to butt or bead-on-plate welding joints, where the weld seam plays the role of the middle bar and the parent material of the side ones.

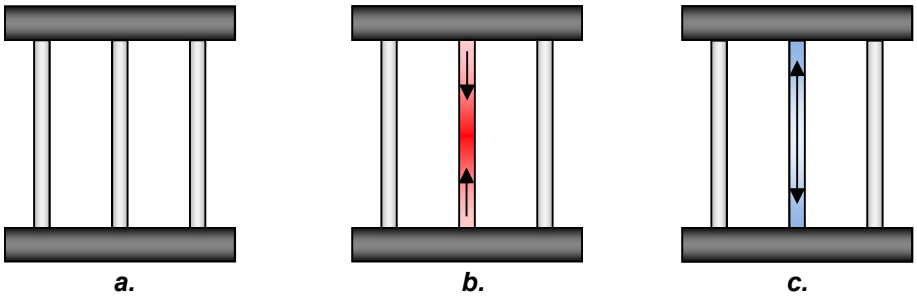

Figure 1-2 Residual stresses generated when connected bars are under different heating condition. *a.* As assembled; *b.* During heating; *c.* After cooling.

Since the temperature distribution, generated by a moving heat source, is non-uniform, strain and consequently stresses change during welding. The transient stresses and eventually residual ones are represented schematically in figure 1-3. Tensile residual stress in the weld seam is compensated with compressive stresses in the parent material, as shown in eq. 1-1, where the sum of the forces across a section must equal zero. The compressive residual stress is responsible for the bucking distortion when a critical stress is exceeded. This critical stress depends on the weldment dimensions and stiffness of the material [13].

$$\int \sigma \, dA = 0 \qquad \text{Eq. 1-1}$$

Buckling is reported to be increased in the last years because of the use of high strength materials that allows implementation of thinner plates [14]. Experiments carried out by Colegrove *et al.* [15] have shown that there is a quasi linear relationship between heat input and distortion, and even stronger correlation between fusion zone dimensions and distortion, having the biggest distortion with the submerged arc welding process (SAW).

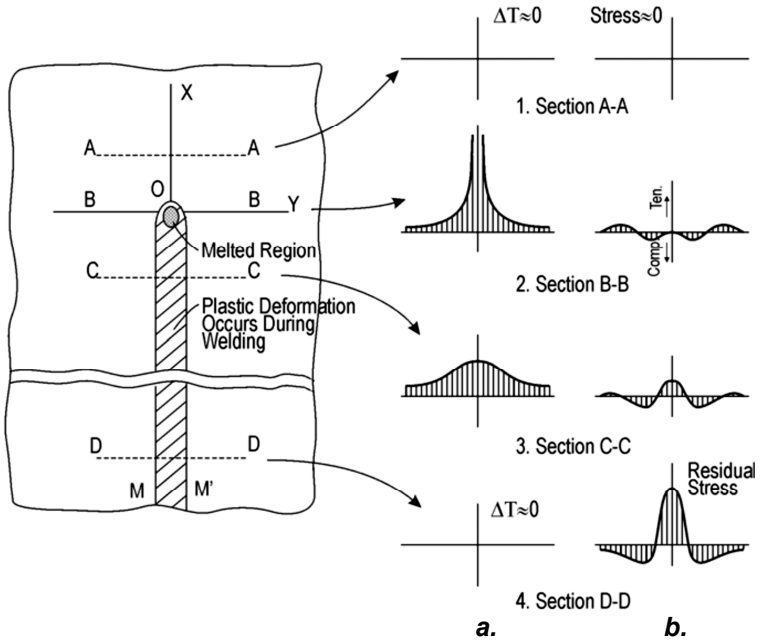

Figure 1-3 Schematic representation of: *a.* temperature changes; and *b.* longitudinal stress during welding [13].

1.2.2 Residual stress measurement

Residual stress measurement can be subdivided in three different groups: destructive, semi destructive, and non-destructive techniques. In the first group, there are techniques such as mechanical relaxation and cracking techniques, where the material should be somehow sectioned (damaged). In the semi destructive group, the workpiece can be partially sectioned, however, in some cases it can be still used. In this group there are techniques such as hole drilling. In the non-destructive ones, there are diffraction techniques, and the

use of the stress-sensitive properties. Figure 1-4 *a* shows the most common residual stress measuring techniques based on the damage induced in the workpiece [16].

It is important to underline that to define the stress field in most cases it is necessary to carry out tens of hundreds of measurements. In that case the accuracy of each measurement is less relevant [9].

Recently Withers *et al.* [17] have made a schematic comparison between the most common methods available, in terms of spatial resolution against penetration, which is shown in figure 1-4 *b*. Most of those methods are briefly explained in the next sections.

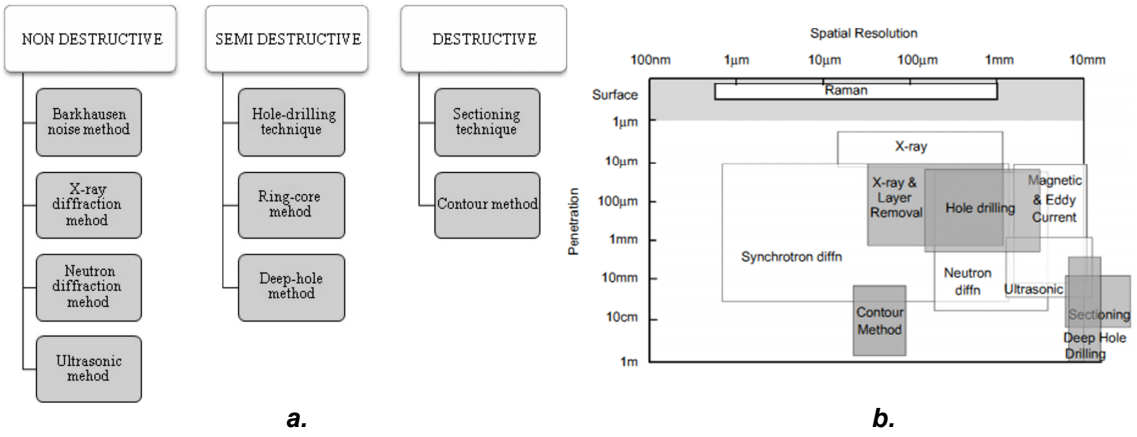

a. ***b.***

Figure 1-4 Most common measuring residual stress techniques divided by: *a.* damage induced in the workpiece [16]; and *b.* the spatial resolution against penetration [17].

Mechanical relaxation techniques

Mechanical relaxation techniques consist in removing a section of material, with a suitable method to avoid inducing further strains, and measuring the elastic strain released. Strains release during sectioning can be measured by electrical or mechanical strain gauges, optical grid system, brittle coatings or photo-elastic coatings. There are plenty of techniques that use mechanical relaxation, the most common mechanical relaxation techniques applied in biaxial field are: hole drilling, trepanning, sectioning and layer removal method.

Hole drilling or Mathar-Soete drilling technique consists in drilling a hole in a material which has residual stress and measure the stress released after it. The hole is made between at least three strain gauges in a rosette distribution [10,18].

Kelsey [19] proposed to drill the hole by steps and measure the strain at each step giving a profile of the residual stresses through the thickness. The problem with this method lies in determining the correlation coefficients needed to establish the stress.

The main advantage of this method is its low cost and flexibility. Moreover, in some cases the workpiece can be still used by filling the hole (for this reason this method is frequently called semi destructive).

Trepanning consists in removing a cylindrical section of the material by an annular cut. Unlike the hole drilling, trepanning measures the strain released by the removed part, and not by the workpiece, giving thus higher accuracy. Its main disadvantage is that it gives only the average residual stress and does not measure local concentrated stress [10].

Layer removal method was proposed by Treuting and Read [20]. It consists in removing uniformly thin layers on one side and measuring the curvature changes in the opposite side, after the layers were removed. It is presumed that stresses change only through the thickness and are constant on the plane [9].

The *contour method* can be classified as one of the mechanical relaxation techniques because the workpiece has to be sectioned to produce contour of the residual stress in the new surface. However, since this technique is relatively new, and to determine the residual stress a finite element software have to be used, this technique is explained in other techniques section, below in this chapter.

Diffraction techniques

Identical atomic planes have in average the same inter-planar distance, d_{hkm}, where h, k, and m are the miller index. If a mechanical force is applied in a piece of metal, that component distorts and strains the inter-planar distance.

The Δd_{hkm} can be determined using the Bragg's law (eq. 1-2), and subsequently the total stress.

$$n\lambda = 2d \sin\theta \qquad \text{Eq. 1-2}$$

Where n is an integer which represent the order of the diffraction (distance between two consecutive planes of the same family), λ is the wavelength of the source; d is the inter-planar space, and θ is the angle between the incident ray and the scattering plane [21].

Residual stress measured by x-ray diffraction, measures the spacing between stressed atomic planes, and from comparison against the unstressed planes, the strain can be obtained, as shown in eq. 1-3 [18,22]. The strain is measured in the scattering direction, which is perpendicular to the diffracting planes.

$$\varepsilon = \frac{\Delta d}{d_0} = -\cot\theta\, \Delta\theta \qquad \text{Eq. 1-3}$$

To determine the stress tensor in an isotropic continuum material, the stress can be obtained in terms of two independent elastic coefficients, the Young's modulus, E, and the Poisson's ratio, ν, by the generalised Hooke's law, as shown in eq. 1-4 [23].

$$\sigma_{ij} = \frac{E}{(1+\nu)}\left[\varepsilon_{ij} + \frac{\nu}{(1-2\nu)}(\varepsilon_{11} + \varepsilon_{22} + \varepsilon_{33})\right] \qquad \text{Eq. 1-4}$$

Laboratory x-ray diffraction. There are three basic techniques based on it, to measure stress; the single exposure or one-angle, the double-exposure or two-angle technique, and the sin-square-psi ($Sin^2\psi$) [9]. Due to the shallow penetration of conventional x-ray in most engineering materials, about 10 μm, these techniques are suitable for measurement of surface in-plane stresses [24,25]. The $Sin^2\psi$ method is a common technique used in the roller bearing sector, due to the relative low measuring time required (~5 min) [26]. However, this technique is not a particularly useful to measure the residual stress in

weldments, where the region of interest are below the workpiece surface. For this kind of measurement synchrotron x-ray or neutron diffraction are preferable.

Synchrotron or hard x-ray diffraction is a technique based on high intensity x-ray (a million times more than laboratory x-ray) [25], which is achieved by the acceleration of charged particles, such as electrons by variation in time of the strength of the magnetic field. When the electrons achieve a certain speed (close to the speed of light), they are forced to suddenly change direction, producing polychromatic x-ray. The x-ray is filtered by monochromators, to select a particular wavelength, and then collimated to generate a narrow low divergence high intensity beam [27].

There are three different methods used with synchrotron x-ray, these are: traditional θ/2θ, high energy two-dimension diffraction, and white beam high energy photons. These techniques are well explained by Withers and Webster elsewhere [25].

Since x-rays interact with the electrons in the material, this technique is suitable for materials with low atomic number. Its main disadvantage lies on its low scattering angle, between 10 to 4°, with moderate (25 keV) and high (80 keV) energies, respectively. High intensity beams have an elongated diamond shaped gauge volume cross-sections, with poor resolution perpendicular to the scattering vector [8]. In addition, the data acquisition times are very fast and can be even less than a second when small lateral gauge dimensions are implemented.

Neutron diffraction in a similar manner to hard x-rays, has very high penetration compared with laboratory x-rays [28], with a high resolution, greater than 1 mm^3 (depending on gauge volume selected). Differing from the hard x-ray, uncharged neutrons do not interact with electronic charge density but with the strong fields established around the atomic nucleus [23]. Its weak interaction with the material allows making measurement in transmission or diffraction at several millimetres from the surface through the thickness, in about 25 mm in steel and 250 mm in aluminium [24].

There are two forms of neutron beams available: continuous beam from reactor sources, and pulsed beam from spallation source. Based on these two sources two different methods have been developed: from the former source a conventional θ/2θ scanning is suitable, while the latter source is appropriate for the time-of-flight method [8].

Withers and Bhadeshia [8] suggest that generally, continuous sources provide the best results, when single peaks of the diffractogram is studied (as for mild steel residual stress measurements), while time-of-flight based instruments are particularly good when the complete diffractogram or a certain number of peaks are necessary, as for a multiphase material. In addition, Webster *et al.* [24] recommend neutron diffraction as the best technique available currently to map two and three-dimensions internal strain.

Other techniques

Ultrasonic velocity is a technique based on the nearly linear change of the ultrasound speed when stress is present in the material [9]. The maximum sensitivity is achieved when the ultrasonic wave is spread in the same direction of the stress. Stress can be determined by eq. 1-5.

$$\frac{V_{pp}-V_L^0}{V_L^0} = \overline{k}_1\sigma_p + \overline{k}_2(\sigma_q + \sigma_s)$$

$$\frac{V_{pq}-V_T^0}{V_L^0} = \overline{k}_3\sigma_p + \overline{k}_4\sigma_q + \overline{k}_5\sigma_s \qquad \text{Eq. 1-5}$$

Where V_L^0 is the isotropic longitudinal velocity; V_{ij} the velocity in direction i, polarised in direction j, p the principal stress direction, q; and s the orthogonal directions; and $\overline{k}_n$ are constants [8].

This method provides a value of macrostresses in a large volume of material, and its magnitude can depend on micro discontinuities present in the microstructure. In addition, it is difficult to separate the effects of multiaxial stresses [8]. However, due to its portability, this technique is suitable for industrial studies and routine inspections [29].

Magnetic Barkhausen Noise (MBN) is a technique that measures unexpected magnetic reorientations made by dilation and reduction of magnetic domains in ferromagnetic metals [9]. Ilker *et al.* [30] claim that MBN is a fast and accurate method to measure residual stresses in welded steel plates. Nevertheless, calibration of the instrument seems to be delicate, and different microstructures need different calibration coefficients, which can be a complication when measuring weldments, since the weld zone, heat affected zone, and parent material have all different microstructures.

Contour method is one of the newest methods available to measure residual stress in mechanical components [17]. It consists in cutting a workpiece into pieces, with a suitable technique, such as electro discharge machine, to avoid inducing further stress, and to make an accurate cut. The workpiece deforms because of the internal residual stress present on it. The contour of the cut piece is measured and modelled with an appropriate design software to be further analysed by finite element modelling. The contour surface is forced back to its original uncut shape. The stress required to do this provide a complete map of the stresses in the cut plane [17,31–33].

The Contour method has been shown to be a good option to measure residual stress in weldments, having results comparable with neutron diffraction, as shown by Prime *et al.* [32].

1.2.3 Mitigation and management of residual stress and distortion

Residual stress and distortion are two phenomena closely related [10] and largely opposed [34]. The uneven heating cycle during welding causes localised plastic stains in the weld metal and surrounding material. This misfit of the plastic strain causes the residual stress. To minimise the strain energy of the weldment, it distorts.

The residual stresses cause different kinds of macroscopic distortion. Figure 1-5 shows the fundamental types of distortion caused by welding [10,35,36]. In the case of straight butt and fillet welds, distortion can arise both in-plane and out of it. In-plane distortions include shrinkage in the transverse and longitudinal directions, and rotational distortion of the workpiece with respect the weld line

due to material shrinkage as the weld progresses. Out-of-plane distortion types include longitudinal bending, buckling, and angular distortion. Dong *et al.* [37,38] distinguishes the distortions which are linearly dependent on the residual stress as stable, while the nonlinear modes are described as unstable (buckling). On the other hand, residual stress after welding has a wider influence than only causing distortion. It could reduce the fatigue life and corrosion resistance, and increase the speed of crack propagation [10,34,39]. Distortion can be effectively reduced by developing welding procedures, or developing proper techniques to remove distortion after it has occurred.

The basic principles behind these techniques can be summarised as follow [40,41]:

- Reduction of the plastic strained region during and after welding.
- Elongation of the shrunk region, produced during cooling.
- Compensation of the welding deformation by pre-welding deformation in the opposite direction.

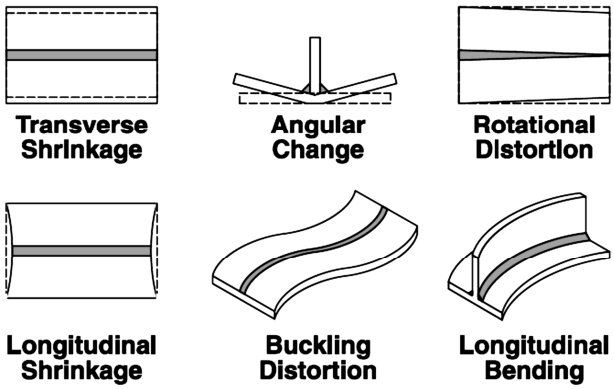

Figure 1-5 Various types of welding distortion [42].

Management of residual stress in welding

These kinds of methods aim to reduce the effect of residual stresses rather than changing the residual stresses generated by welding. Masubuchi [10] and other authors [34,43–51] have shown different welding approaches to reduce distortion.

Masubuchi [10] and Radaj [34] have reported that the length and the number of welds should be minimised. For instance, welding by segments, instead of one continuous weld seam, effectively reduce the longitudinal stresses in fillet welding. The position of the weld seam is another important factor to reduce distortion. Symmetric welding respect to the neutral axis is less prone to angular and bending distortion, as shown in figure 1-6 *a* [52]. The angle on the chamfer should be minimised to reduce the volume of the weld metal, as shown in figure 1-6 *b*. Using double-V chamfer instead of single-V preparation helps the symmetry of the weld seam, and can potentially reduce distortion. In addition, welding alternately, on each part of the bevel, helps to counteract the angular distortion generated by each welding pass (see figure 1-6 *c*).

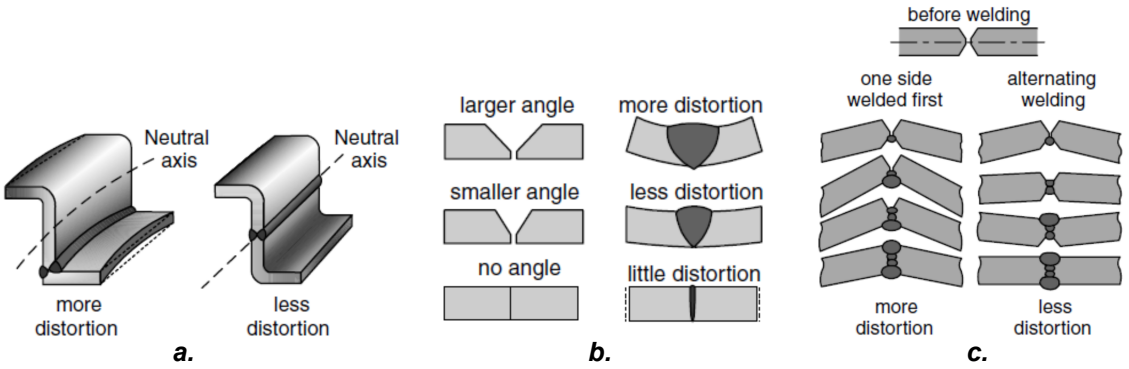

Figure 1-6 **Techniques to reduce distortion by: *a* placing the weld in the neutral axis; *b* reducing volume of weld metal and using high penetration welding; *c* using double V joint and welding alternatively on each part of the chamfer [52] (adapted by Kou [53]).**

Colegrove *et al.* [15] studied the effect of different welding processes on the residual stress and distortion. They found that minimising the width of the weld bead by using high concentrated energy welding, such as electron or laser beam, distortion and residual stresses were reduced. However, concentrated energy welding causes faster cooling rates that alter the microstructures of the weld metal. Nitschke-Pagel and Wohlfahrt [54], and others [55–57], have shown the influence of cooling rates in the microstructure development and its impact in the residual stress. They found that the characteristic longitudinal tensile hill of the residual stress can be reduced or even eliminated with the appropriate thermal cycle. Leblond *et al.* [58] explains that in the case of martensitic

transformation the effect of strain due to phase transformation is typically 25 times larger than the strain due to cooling; consequently the tensile residual stress due to thermal expansion can be reverted by the strain due to phase transformation. Figure 1-7 *a* and *b* show the CCT diagram of a S690QL TIG bead-on-plate welded plate (with no filler metal), with different heat inputs and consequently cooling rates, and their resulting longitudinal residual stress, respectively. The plate with lower heat input (0.6 kJ·mm^{-1}) and higher cooling rate had compressive residual stress in the fusion region, while the weldment with larger heat input (2 kJ·mm^{-1}) and slower cooling rates produced tensile residual stress in the fusion region, as shown in figure 1-7 *b.* Nevertheless, Deng [59] has shown that the effect of phase transformation in mild steel (as the S355) is not significant and consequently it can be ignored in welding simulations with that material.

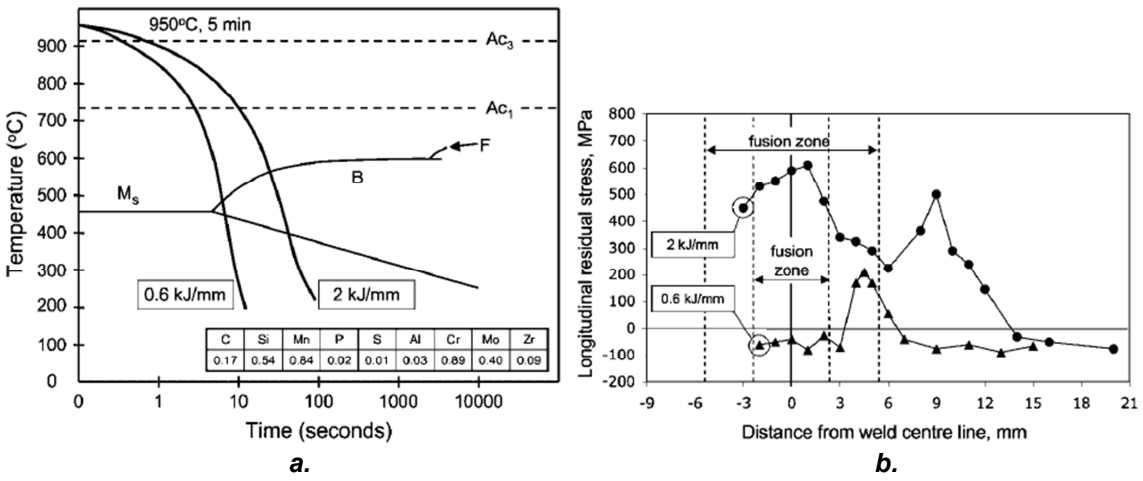

Figure 1-7 Effects of the heat input and cooling rates on *a.* microstructure, and *b.* longitudinal residual stress [54] (adapted by Francis et al. [56]).

Other techniques aim to reduce distortion by pre-applying distortion in the opposite direction of that caused by welding. Elastic or plastic pre-strains can be applied. Experiments carried out by Kumose *et al.* [60], on low-carbon steel, and by Henry [61], on aluminium 5456 fillet weld, have shown that pre bending the substrate in the opposite direction can effectively reduce angular distortion on fillet welds.

The effect of welding sequencing has been studied by different authors [46,48,50,51,62]. They showed that there is an optimum sequence of welding in which the residual stresses interact in a way that distortion is minimised.

Clamping is a technique commonly used to restrain the displacement of the workpieces during welding. It has been found that there is a strong relationship between clamping pressure and distortion [10]. Schenk *et al.* [47,49]. have shown that in overlap joints, high pressure in the clamp devices (1.5 MPa), and long clamping time (unclamping the weldment until it reaches room temperature) can potentially reduce the buckling magnitude and change the buckling direction, as shown in figure 1-8.

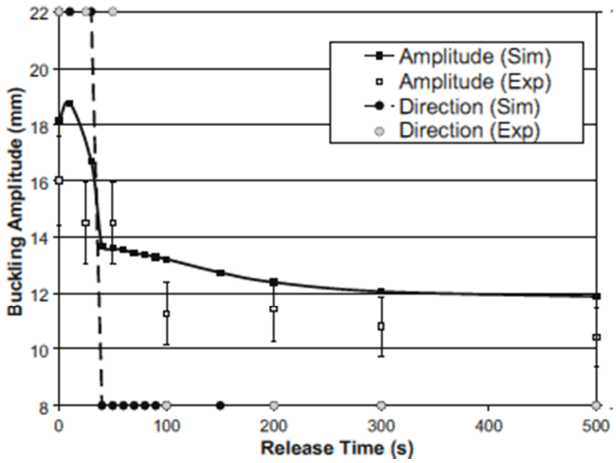

Figure 1-8 Influence of the clamping time on the buckling distortion in simulations (Sim) and experiments (Exp) [47].

Even though clamping can be a good technique to reduce buckling because it is usually used to constrain the workpiece during welding, and it does not need further energy consumption, it cannot remove completely residual distortion, and does not remove the residual stress.

Mitigation of residual stress and distortion during or after welding.

This group of techniques aims to reduce residual stresses and distortion by applying mechanical stresses, which interact with the internal residual stresses generated after welding. These techniques are collectively called stress

engineering (SE) [11], and can be subdivided by thermal and mechanical techniques. These techniques can be applied during or after welding.

Thermal methods use heating / cooling source to induce thermal dilation / contraction on the plate, and hence induce stresses and distortion on the weldment which counteract the residual ones. In addition, the heating techniques have the advantage that at high temperature the yielding point of a large variety of metals, including mild steel, is relatively lower, allowing large strains.

Global heating techniques can be used before or after welding. If applied after welding, it is called annealing for stress relieving. It consists in rising the temperature of the weldment above the recrystallization temperature and holding for a certain time period. The stress relaxation occurs because of the lowering of the yielding point, creep of the weldment with minor deformation, recrystallization, and stress redistribution [10,34].

If heating is applied during welding, it is called global thermal tensioning or just preheating. The objective of this technique is to reduce the temperature gradient across the weldment, and hence reduce the residual stresses. With this practice can be obtained more uniform and suitable microstructures when an appropriate heat cycle is applied [34]; however, this technique can have a harmful effect in some metals such as aged aluminium alloys, in which the high temperature may cause overaging. On the other hand, this method is difficult to apply in large structures and particularly with in the field practice. In addition, it cannot be used on metals in which the microstructure is dependent on complicated previous heat treatments, such as dual phase steels.

Local Heating/Cooling uses localised thermal source (heating or cooling) to interact with precise areas of the weldment during welding. It has been studied first by Guan *et al.* [63] and later by other authors [40,64–66]. The theory behind the local thermal tensioning process is well described by Williams [11] and van der Aa [40].

To simplify comprehension of these techniques some simplifications have to be applied, such as defining the thermal source as a well-defined circular area, and

the material does not undergo any solid state transformation. If the thermal source is a hot source, it causes dilation on the plate, and generates a homogeneous compressive stress in the radial direction. This stress can be decomposed in the longitudinal and transverse directions (parallel and perpendicular to the welding direction, respectively). Hence, the stress is compressive in the longitudinal direction on the right and left of the circular area, and tensile in the upper and lower sides of the circular area, as shown in figure 1-9 *a* [11]. The same principle occurs with the cold source but results in opposite stresses.

There are different sources that can be used to produce the hot spots such as burners, induction systems, lasers, and TIG torches. CO_2 is widely used to produce the heat sink areas because of its high cooling power and it is easy to apply [40,67].

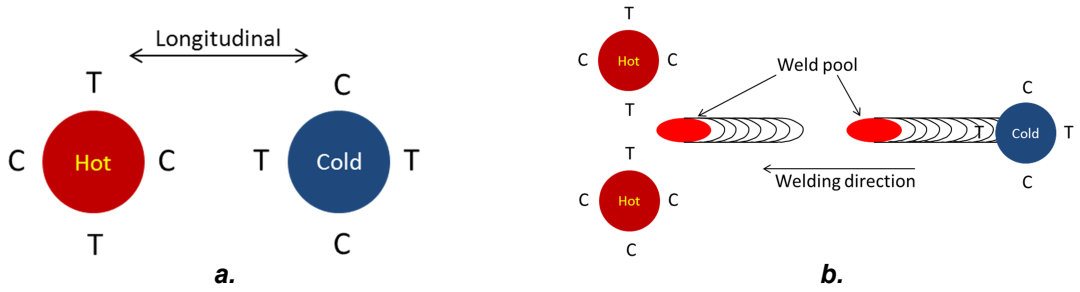

Figure 1-9 Thermal tensioning diagram. *a.* Stress in the longitudinal direction around hot and cold spots. *b.* Appropriated configuration for hot and cold areas.

The exact position and the size of the thermal areas depend on the welding process and the material properties of the plates. However, distortion reduction has been obtained on butt welding by using leading [68], and trailing [69] burners (hot heat source), on the same surface as the welding torch, as shown in figure 1-10. It has been reported that angular distortion reduction on MIG fillet welding using a leading TIG torch [70,71]. In addition, it has been claimed distortion reduction using a trailing heat sink as shown in figure 1-9 *b* [40,64].

Mechanical methods use an external mechanical force to induce strain parallel to the welding direction. This strain can be applied by two methods. In the first method the weldment is stretched in the direction of required stress relief to

cause yielding, and then it is unloaded. The second method imposes a plastic strain in a direction other than that of required stress relief, producing a plastic strain in the required direction by the Poisson effect [72]. In addition, the strain can be induced during or after welding. These techniques offer good controllability but in some cases can cause dimensional changes.

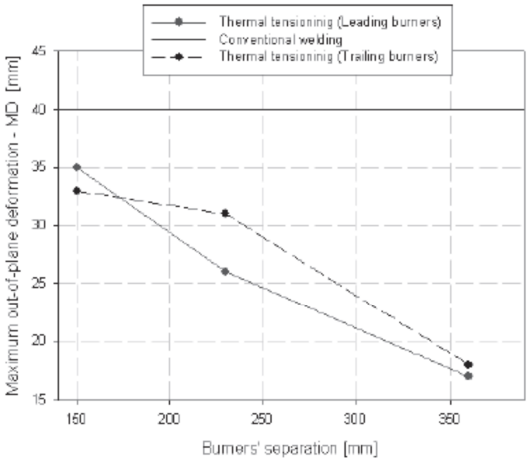

Figure 1-10 Effect of burners distance from the weld [68].

Global mechanical tensioning consists in applying a uniform load on the whole section of the plate to induce plastic strain in the tensile region of the residual stress. To plastically strain the weldment, heavy loads are required. A good explanation of the theory behind this process is provided by Pilipenko [41], and Radaj [34].

The principle behind this method can be explained with an extension of the three bars model already explained in section 1.2.1 above in this chapter. For simplification, it is considered a material that does not undergo through any solid phase transformation, and with perfect elastic-plastic behaviour. The σ_t and σ_c represent the tensile residual stress on the middle bar, and the compressive stress in the side bars, respectively (σ_c = -½ σ_t), as shown in figure 1-11 *b.* Consider a tensile force applied uniformly to the top and bottom constraint, as shown in figure 1-11 *b*. Points 1^T, 1^C, on figure 1-11 *a*, represents the residual stress after welding, in middle and sides bars, respectively. While 1, represents the starting point of the external load. The load increases from 1 to 2

causing uniformly stresses increase in an elastic behaviour, in which the middle bar in 2^T reaches the yielding point.

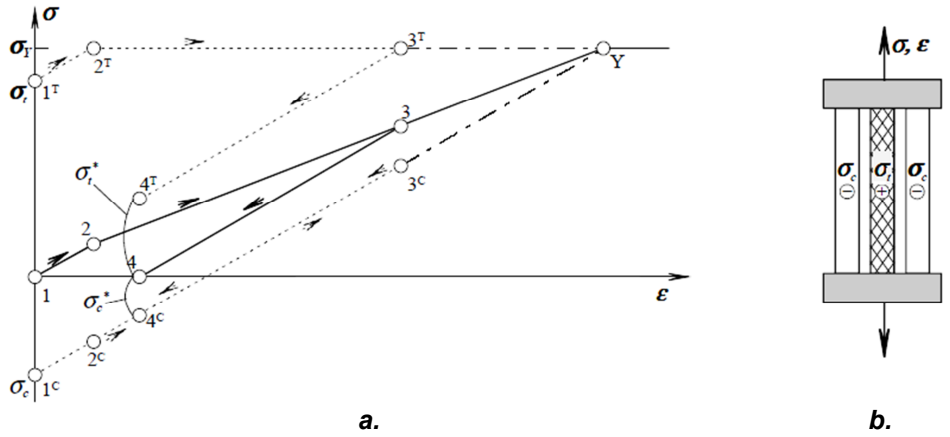

Figure 1-11 Three bars theory to explain principle of mechanical tensioning [41]; *a.* stress diagram for the bars; and *b.* three bars model sketch.

Further increment on the external load, from point 2 to 3, causes plastic deformation on the middle bar (point 3^T). The side bars, on the other hand, undergo only elastic strain (point 3^C), since they have not yet reached the yielding point. The change in slope between segments 1-2 and 2-3 is due to the lack of work hardening assumed for this model. If the external load is removed at point 3, the middle bar relaxes with an elastic trajectory until point 4^T, as well as the side bars until point 4^C. The σ_t* and σ_c* represent tensile and compressive residual stresses after global tensioning in the middle and side bars, respectively. Consequently, the magnitude of the residual stresses after global tensioning is considerably lower than the original residual stresses. In addition, if the external load reaches point Y, all the residual stresses should be theoretically removed.

Wilson *et al.* [12] were the first researchers to study this technique in butt welding steel plates. Their study showed that if a load is applied beyond yielding point, great reduction of the residual stress is produced; however, their work did not considered the effect on distortion. Price *et al.* [73] investigated the influence of mechanical tensioning on friction stir and arc welded aluminium plates. They found that there is an optimum external load to reduce distortion,

which depends on the thermal stress induced by the welding process. Furthermore, when the mechanical tensioning is applied during welding, the load required to reduce distortion is lower than the one needed after welding. If the optimum load is exceeded, distortion reappears. Figure 1-12 show the predicted effect of global mechanical tensioning on the longitudinal residual stress [41].,

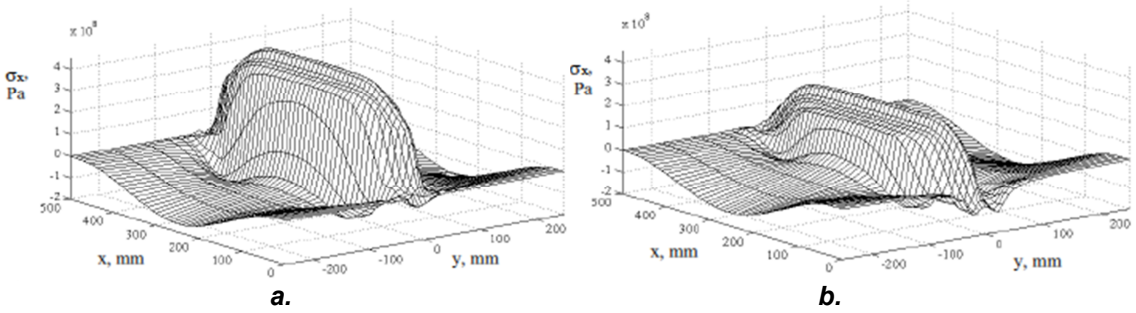

Figure 1-12 Effect of global mechanical tensioning on the longitudinal residual stress *a.* after welding, and *b.* after tensioning [41].

Localised mechanical tensioning techniques are focused on applying mechanical stress on a precise zone of the plate. The principal behind these practices is similar to the hot spot explained above. In this case, an external force exerts pressure on a precise area, normal to the plate surface. Consequently, compressive stresses are applied in the radial direction (from the loaded area) on the surrounding metal, and plastic strain is produced in the in-plane direction by the Poisson's effect. In industry there are several commonly use techniques to induce residual stress such as shot and laser peening, hammering, spot compression, burnishing, and rolling. The advantage of these techniques over the global mechanical tensioning lies in the typical smaller loads required in the former, since the region to applied plastic strain is significantly smaller than the entire workpiece.

Peening consists in battering the surface of the weldment in order to induce compressive residual stresses in the surface. A high-speed stream of metal particles, a pneumatic hammer, or lasers is the most common tools for peening. It has been shown by several authors that peening techniques not only induce a

compressive state on the welding area, but also increase the fatigue life of the workpiece [74–76].

Spot compression is similar to peening. Compressive stresses are induced by locally pressing the plate between dies causing plastic strain. Figure 1-13 *a* shows the residual stress in the radial and tangential direction after a perfect elastic-plastic thin plate was compressed between two dies of radius R. The residual stress distribution is the same as the one obtained by local heating described above. It has been claimed by Trufiakov *et al.* [77] that an increase in fatigue limit between 70 and 100% in joints with longitudinal fillet welds can be obtained. Figure 1-13 *b* shows the recommended position of the compression spot to reduce tensile residual stress in the notch of a fillet weld. The main disadvantages of this technique are the need of having access to both sides of the plate, and the high load required to induce plastic strain.

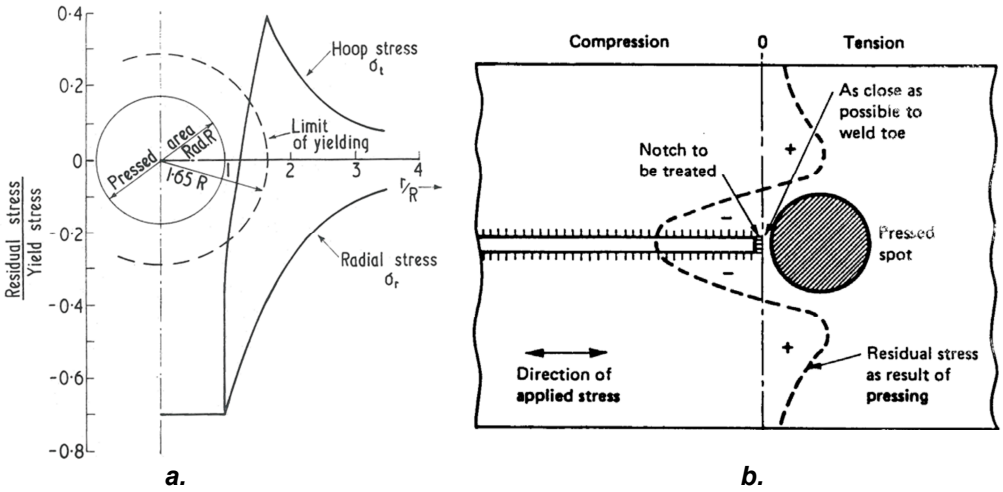

Figure 1-13 ***a.*** **Theoretical residual stress distribution due to spot compression with a round section dies [78];** ***b.*** **Recommended position of pressed spot when treating the end of a longitudinal fillet weld [79] (adapted by Kirkhope *et al.* [80]).**

Vibratory stress relief method consists in applying an oscillating load to the weldment by means of a vibrator, clamped to the workpiece, or by an oscillating table. It uses the energy of elastic waves applied by physically shaking the piece, or by impacting it to cause stress reduction [10,34,39]. Although it has been reported that there is lack of scientific information on how it works

[10,34,39], Munsi *et al.* [81] have reported an increase in the fatigue life between 17 and 30% in MIG welded mild steel plates.

Walker [82] proposed a theory to explain how the residual stress is relieved on large welded fabrications subjected to vibratory stress relief. He claimed that retained austenite in a range from 1 to 25 μm was transform into martensite, induced by dislocation migration due to vibration. The shear deformation caused by retained austenite when transformed into martensite caused relaxation of residual stresses.

Non-contact electromagnetic impact. When discharging a capacitor through a coil, a transient magnetic field is generated. It can induce eddy current on the metal next to the coil. The interaction between eddy current and the magnetic field generates repulsive electromagnetic forces in the metal, which can deform

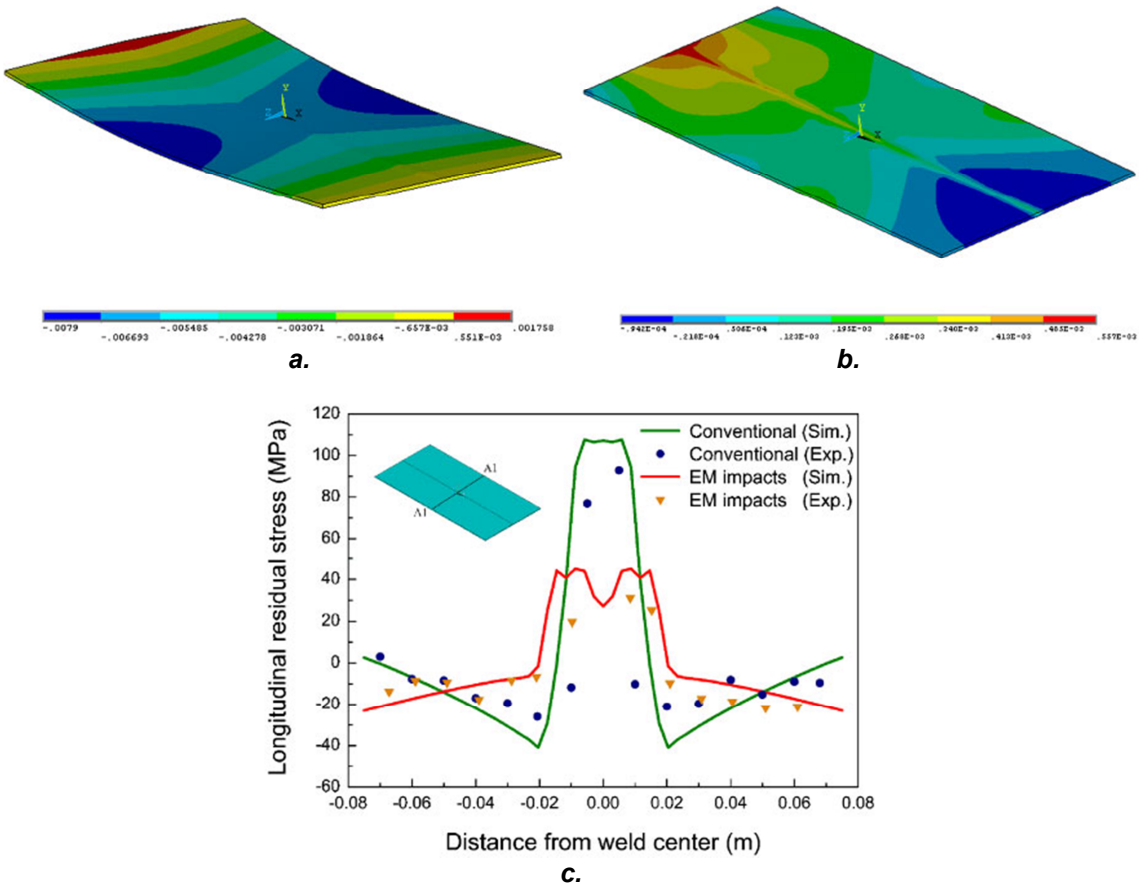

Figure 1-14 Out-of-plane distortion *a.* as welded, and *b.* after electromagnetic (EM) impact. *c.* Comparison of the longitudinal residual stress distribution before and after EM impact in the simulations (Sim.) and experiments (Exp.) [84].

it plastically [83,84]. This technique was originally developed for electromagnetic forming and patented by Harvey *et al.* [85]. Recently Xu *et al.* [84] proposed this method as a technique to reduce residual stresses and distortion. Their experiments were carried out on 1060-H24 aluminium alloy TIG welded plates. The results show that there is a reduction of the distortion around 90%, as shown in figure 1-14 *a* and *b*. However, this technique does not eliminate thoroughly the tensile residual stress on the welding zone, as shown in figure 1-14 *c*. In addition, the longitudinal residual stress reduction was not constant through the workpiece length. Consequently, an overall distortion reduction can be achieved with this method but the risk of fatigue failure, stress corrosion and crack propagation could still be a problem. One advantage of this technique is that the device does not need to be in contact with the workpiece to induce plastic strain; therefore, it does not cause tool prints on the weldment surface.

Localised rolling – Its effect on welding residual stress and distortion

Localised rolling, to reduce residual stress and distortion, is a stress engineering technique that exploits the action of a normal loaded roller to induce strain in the in-plane directions. This technique is proposed in some books [10,34] as a method to reduce distortion. However, there are just few publications about localized rolling [43,86–107], and some of them are only available in Russian, or Chinese. In addition, some of the literature is focused on preventing hot cracking, and improving of mechanical properties rather than reducing residual stresses or distortion.

In the literature different rolling approaches have been found. They can be divided according to the location where the rolling process is applied: rolling both sides of the weld seam simultaneously (upper and lower surfaces) [43,94,99,101,105]; rolling over the weld seam with either one [87,88,90,91,102,104] or two consecutive rollers [86,87]; or rolling beside the weld seam [92,102,104,106], as shown in figure 1-15 *a* to *d*. Additionally, the roller can be applied after welding, or *in situ* at certain distance from the welding torch (or welding tool in FSW). Rolling the upper surface of the weldment has

operational advantage. It can be easily adapted to different weldment geometries, and can be applied *in situ* during welding.

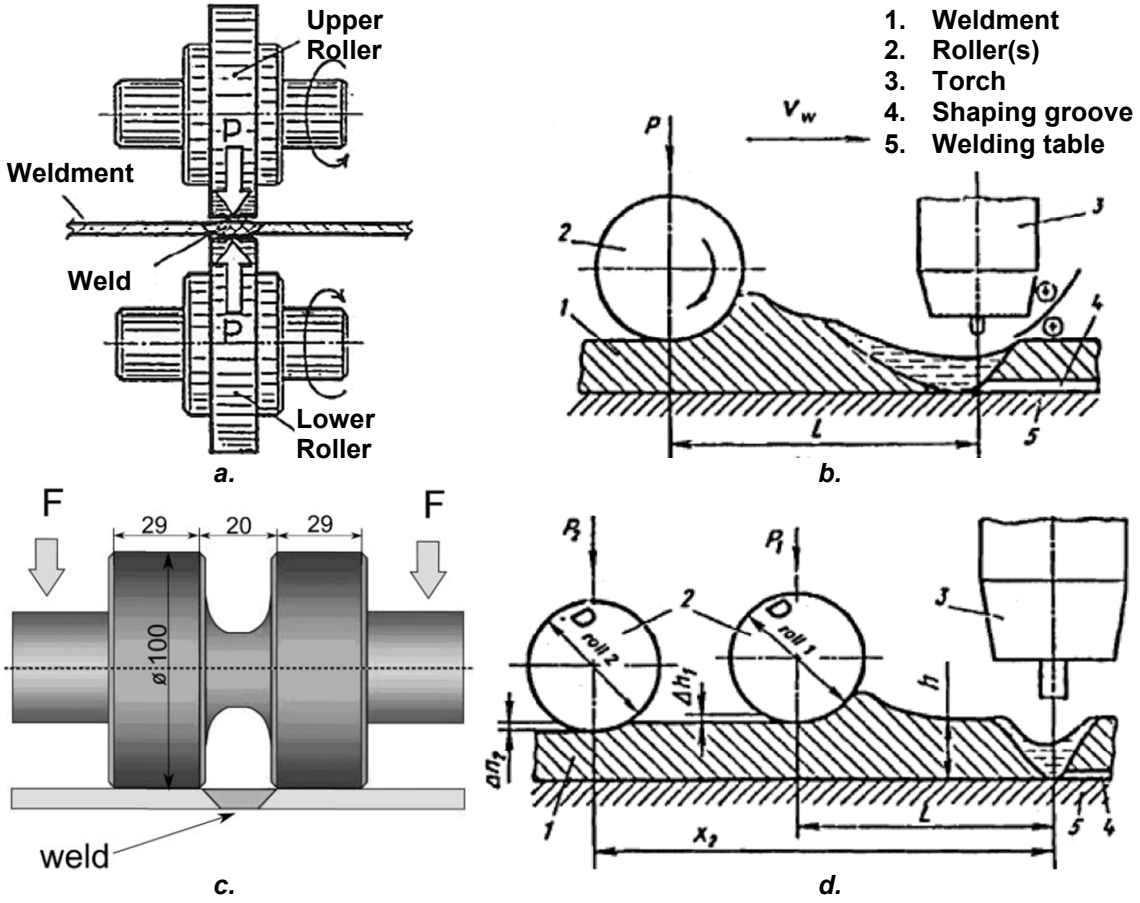

Figure 1-15 Possible rolling configurations *a.* Rolling both sides of the weld bead [94], *b.* rolling the top of the weld bead [87], *c.* rolling beside the weld bead [104], and *d.* rolling the weld bead with two tandem rollers [87].

Kurkin and Tsyao studied the influence of rolling beside of the weld bead of titanium welded alloys, finding that the longitudinal residual stress can be effectively reduced to around zero, in the weld bead region, with 20 kN load [105]. The numerical simulation conducted by Sun *et al.* [101], in post-weld rolling FSW aluminium plates between two rollers, showed a large reduction of the longitudinal tensile residual stress caused by welding, as shown in figure 1-16. In addition, they rolled the workpiece using displacement control, instead of using load control. The rolling force fluctuated along the length. Guan [94] has reported that rolling at both sides of the weld bead, as shown in figure 1-15 *a*, was successfully applied in the Chinese aerospace industry.

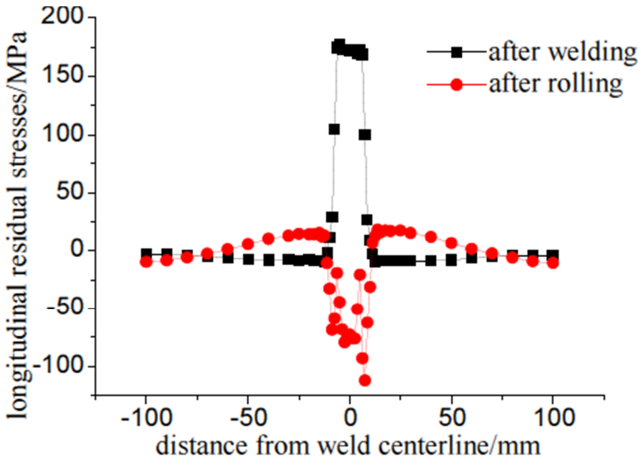

Figure 1-16 Longitudinal predicted residual stress distribution before and after rolling between two rollers [101].

Altenkirch *et al.* [104] studied the effect of localised rolling in aluminium FSW plates, after post-weld, and during welding (*in situ*). They showed that the *in situ* rolling experiments, rolling beside the weld bead (figure 1-15 *c*), did not cause measurable reduction of the residual stress, while post-weld rolling techniques, rolling on top of the weld seam, caused significant residual stress reduction, and with loads larger than 20 kN the tensile residual stress in the weld bead region was reversed. Additionally, Wescott [107] showed that post-weld rolling beside the weld bead, in aluminium FSW plates and mild steel GMAW plates, did not remove the tensile residual stress peak, even after rolling with 50 kN for aluminium or 70 kN for the mild steel. However, Kurkin *et al.* [106] have shown the opposite results in aluminium TIG welded plates, having compressive residual stress after post-weld rolling aluminium plates beside the weld bead with 7 kN load, which are in disagreement with Altenkirch *et al.* results. The results presented are not conclusive and contradict each other.

In situ rolling on top of the weld seam has been successfully used in the past for different applications, such as porosity reduction in titanium PT-3V alloy TIG welded thin plates [91], and mechanical property improvements in aluminium AMg6M alloy TIG welded [87]. However, it has been shown that it is not an effective technique to reduce either residual stress in VT1-1 titanium alloy, and 12Kh18N10T austenitic steel [88], or distortion in AMg6 aluminium alloy TIG welded plates [106]. However, numerical results presented by Wen *et al.* [102],

on aluminium FS welded plates, contradict the previous findings, having residual stress close to zero in the weld region, after *in situ* rolling on the top of the weld seams, at 25 mm behind the welding tool, as shown in figure 1-17.

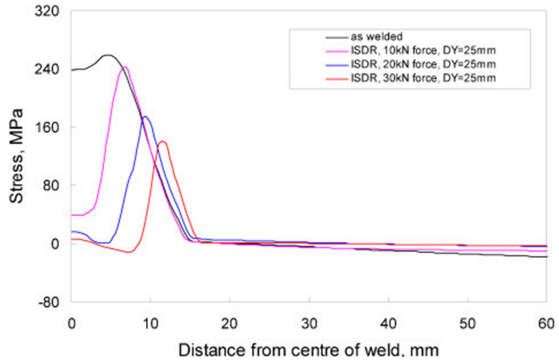

Figure 1-17 Predicted longitudinal residual stress after *in situ* direct rolling (ISDR), rolling at 25 mm behind the welding tool, with different rolling loads .

The tandem rolling system used by Kondakov and Martynov [87] showed good results, in terms of residual stress reduction, and improvement of mechanical properties, in aluminium V92 alloy TIG welded plates. They used this system as a combination of *in situ* and post-weld rolling techniques. The first rolling was used close behind the molten pool where the temperature was between 640 to 760 K, to shape the weld bead and induce improvement in the mechanical properties by recrystallization of the deformed material. The second roller was applied farther away from the molten pool where the temperature was around 500 K, to induce compressive residual stress and therefore counteract the residual stress produced by welding. This technique has the advantage of the *in situ* and post-weld rolling methods in one single process, however, it involved more complicated settings and equipment.

1.3 Heat transfer equations

Heat is the transfer of thermal energy from a system to another with lower temperature. This thermal energy can be generated in many ways such as nuclear reactions, chemical reactions, electromagnetic dissipation or mechanical dissipation. In welding the main heat sources are: flame, electric arc, laser, electron beam, friction, and ultrasound. Heat is transferred to the

weldment (or dissipated from it) by three modes: conduction, convection and radiation.

Conduction

In welding, conduction is the most important mechanism for heat transfer [108]. It is the principal responsible to determine the temperature distribution in a weldment. The law of heat conduction was developed by Joseph Fourier in 1822 [109]. The spatial equation of transient heat transfer conduction in Cartesian coordinates can be written in partial differentials, as shown in eq. 1-6. This is well explained by Simonson [110].

$$\frac{\partial T}{\partial t} = \alpha\left(\frac{\partial^2 T}{\partial x^2} + \frac{\partial^2 T}{\partial y^2} + \frac{\partial^2 T}{\partial z^2}\right) + \frac{q'}{\rho c_p} \qquad \text{Eq. 1-6}$$

Where T is the temperature, t the time, α the thermal diffusivity $(k/(\rho \cdot c_p))$, q' the generated heat rate per unit volume in the control volume, ρ the density, and c_p the specific heat capacity at constant pressure, and k the thermal conductivity coefficient.

Convection

Convective heat transfer is also important in welding process. There are convective phenomena in the molten pool during welding, such as buoyancy force, Lorentz force, Marangoni effect, and arc pressure [53]. In addition, there is convective heat transfer from the top surface of the plate to the surroundings. The latter may be considered as a natural convection, which can be calculated with standard approach as described by Holman [111], and showed in eq. 1-7. It represents the energy equation of the laminar boundary layer on a flat surface.

$$u\frac{\partial T}{\partial x} + v\frac{\partial T}{\partial y} = \alpha\frac{\partial^2 T}{\partial y^2} + \frac{\mu}{\rho c_p}\left(\frac{\partial u}{\partial y}\right)^2 \qquad \text{Eq. 1-7}$$

Where u and v are velocity components and μ is the dynamic velocity of the fluid.

The phenomenon of convection has many factors to take into account such as: the shape and size of the solid-fluid boundary, characteristics of the fluid flow such as regime, speed, and conductivity of the fluid itself, etcetera. Consequently, often a simple approach is preferred.

The equation proposed by Newton, and shown in eq. 1-8, represents the overall effect of convection. It indicates that the heat transfer rate, is function of the area A, and the difference in temperature between the surface of the solid T_1, and the fluid T_2. The convection coefficient, h, takes into account all the factors of each particular case of convection.

$$Q = hA(T_1 - T_2) \qquad \text{Eq. 1-8}$$

Radiation

Radiation is the energy transfer between bodies by electromagnetic waves and occurs most freely through vacuum. Another theory says that radiation is the propagation of particles (photons or quanta). All bodies emit electromagnetic waves if their temperature is above the absolute zero. These emissions are consequence of thermal excitation of the electrons in the surface of the material, and the amount of emission is proportional to the absolute temperature of the body.

The radiation energy per unit time from a blackbody is proportional to the fourth power of the absolute temperature and can be expressed with Stefan-Boltzmann Law in eq. 1-9. Where Q is the heat, and σ the Stefan-Boltzmann constant.

$$Q = \sigma A T^4 \qquad \text{Eq. 1-9}$$

1.4 Solution Method

1.4.1 Analytical solutions

Generally speaking the analytical solution of heat flow in welding is preferable because they are relatively simple equations easy to implement. Despite the

important simplifications of the analytical method, in many cases satisfactory results are obtained. However, it is always necessary to verify with in situ thermocouple measurements or numerical methods [108].

The analytical approach developed by Fourier in heat transfer flow and later applied by Rosenthal [112,113], Adams [114] and others [108,115,116], in moving heat sources is a very popular technique to calculate the heat distribution in welding. The assumptions and simplifications made by Rosenthal in his model make it easy to solve. Such assumptions were: steady state heat flow; constant physical coefficients of the material; heat source is considered as a point; heat exchange with the surrounding atmosphere is neglected; and no convection in the weld pool was considered. Rosenthal also proposed a *"quasi-stationary"* model *i.e.* if the temperature distribution around the heat source is represented as a hill (see figure 1-18), where the different heights are the isotherms, the quasi-stationary behaviour is achieved when the temperature hill moves with the heat source without changing either shape or size. The result of Rosenthal in the two-dimensional case is shown in the in eq. 1-10.

$$T - T_o = \frac{Q}{2\pi k g} e^{\left(\frac{vr}{2a}\right)} K_0\left(\frac{vr}{2\alpha}\right) \qquad \text{Eq. 1-10}$$

Where T is the instantaneous temperature, T_o the initial temperature, k thermal conductivity, g thickness, Q heat, v travel speed, α thermal diffusivity, K_0 modified Bessel function of second kind and zero order (see figure 1-18 *b*), and r the radial distance from the heat source $\left(\sqrt{x^2 + y^2}\right)$.

Grong [108] has reported that Rosenthal equation is not applicable in the initial part of the welding process, because the pseudo steady state is not present at that moment. Additionally, the time needed to achieve the quasi-stationary state is a function of welding speed and diffusivity of the material; therefore, not all the welding conditions achieve a steady state. A thorough explanation about transient and steady state or quasi-stationary state will be done later in this chapter

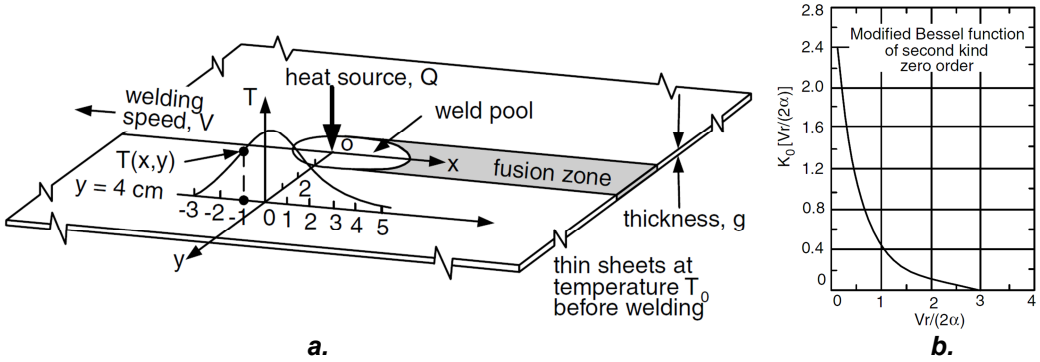

Figure 1-18 ***a.*** **Rosenthal two dimensional heat flow during welding of a thin plates.** ***b.*** **Modified Bessel function for Rosenthal 2D thin welded plates equation (eq. 1-10) [53].**

1.4.2 Numerical solutions.

The application of complex boundary conditions and heat source distributions is difficult with the analytical method. This leads to inaccurate temperature distribution to the fusion zone (FZ) and the heat affected zone (HAZ) [117–119]. Therefore, several authors have used numerical solutions to overcome this limitation. Numerical solutions can be applied not only for quasi-stationary state as analytical method, but also at any stage of the process. In addition, with numerical methods the heat source does not need to be restricted in a point, line, or plane and may be taken into account the geometry of the weldment.

There are different numeric methods and they may be divided into two main categories: the elementary methods, which are suitable to find root of equations, solving linear system of equations or integrating functions, and the intensive ones, which are suitable for modelling practical problems. There are several kinds of numerical methods, such as: smooth particle hydrodynamics (SPH), spectral method, boundary element method (BEM), finite volume method, finite differences method (FDM) and finite element method (FEM). A discussion of the three most relevant methods is provided in 0.

1.5 Material characteristics

The S355 steel grade, which is used for the work presented in this thesis, is commonly used in structural applications and in the offshore sector. According

to the European structural steel standard EN 10025-2 : 2004 [120], its composition is as shown in table 1-1.

Table 1-1 Chemical composition of the ladle analysis for flat and long products of steel grades and qualities with values for the impact strength.

Designation	C in % max. for nominal products thickness in mm			Si % max.	Mn % max.	P % max.	S % max.	N % max.	Cu % max.	Other % max.
	≤16	>16 ≤40	>40							
S355JR	0.24	0.24	0.24	0.55	1.60	0.035	0.035	0.012	0.55	-
S355J0	0.20	0.20	0.22	0.55	1.60	0.030	0.030	0.012	0.55	-
S355J2	0.20	0.20	0.22	0.55	1.60	0.025	0.025	-	0.55	-
S355K2	0.20	0.20	0.22	0.55	1.60	0.025	0.025	-	0.55	-

The steel name consists of the letter “S” for structural steel plus the minimum specified yield strength, for thickness less than 16 mm, expressed in MPa at ambient temperature. In addition, the steel name has a group of letters at the end to indicate the delivery condition, as shown in table 1-2.

Table 1-2 Symbols use in EN 10025-2 : 2004

Nomenclature	Description
...JR..	Longitudinal Charpy V-notch impacts 27 J @ +20°C
...J0..	Longitudinal Charpy V-notch impacts 27 J @ 0°C
...J2..	Longitudinal Charpy V-notch impacts 27 J @ -20°
...K2..	Longitudinal Charpy V-notch impacts 40 J @ -20°C
...+AR	Supply condition as rolled
...+N	Supply condition normalised or normalised rolled

The letter *J* denotes impact resistance, *Q* Indicates quenching and tempering, while *M* and *N* specify thermo-mechanical and normalisation respectively.

1.5.1 Thermal properties

Welding processes are characterised by large gradients of temperature between the weld-line and the parent material. Material properties are

dependent on temperature and their relationship can be nonlinear or even non-smooth. Analytical models conducted by Komanduri and Hou [121], have found good agreement in the weld pool size and heat affected zone, in the range of 2 to 15 %. They studied conduction weld modes (modes with deep penetration such as laser keyhole, and electron beams were excluded from the analysis), using constant thermal properties between 400 to 1300°C. They claimed that the requirement of temperature dependent material properties in analytical model is not necessary to determine accurate temperature profile.

In numerical solution, the scenario is slightly different since thermal dependencies can be easily considered, but drastic change in a property can increase considerably the computational time or even cause divergence from the solution. For this reason, thermal properties are of paramount importance in numerical welding models.

McDill *et al.* [122] analysed the effect of different material properties in numerical predicted distortion calculation. They have reported that thermal properties play a more important role in distortion predictions, in thermal-mechanical analysis, than the mechanical properties. On the other hand, Thistlethwaite [123] conducted a sensitivity modelling analysis to determine the influence of the material properties in the residual stress prediction, in GMAW 4 mm thick AH36 plates, finding that both thermal, and mechanical properties play an important role in the residual stress prediction. He found that variation in the specific heat capacity can modify largely the residual stress prediction than the thermal conductivity. In addition, he showed that variation of the yield stress has the most important influence in the residual stress, and distortion prediction, which contradicts what found by McDill *et al.*. Zhu and Chao [124] studied the influence of the material propertiy variation on the prediction of residual stress and distortion, in GMAW 12.5 mm thick aluminium plates. They found that the mechanical properties, in particular the yield stress, dictated the magnitude of the predicted residual stress, and distortion, which agrees with Thistlethwaite, but they also claimed that the thermal properties had no significant effect in the prediction of residual stress and distortion.

Specific heat capacity.

Specific heat capacity, c_p, is the amount of energy (heat) needed to modify the material temperature of a unit. Different temperature dependent specific heat for steel are shown in figure 1-19 *a* [125] and *b* [119,126]. The specific heat in figure 1-19 *b* is calculated by multiplying the c_p value at room temperature (434 $J \cdot kg^{-1} \cdot °C^{-1}$) for the appropriate factor at the temperature of interest showed in the graph. Both graphs show a maximum value corresponding to the Curie temperature at about 740 °C. However, after that point some researchers use a constant value equal to the maximum value (see figure 1-19 *a*), instead of using the actual values. It is thought that the reason for that is to simplify calculations and improve computational time.

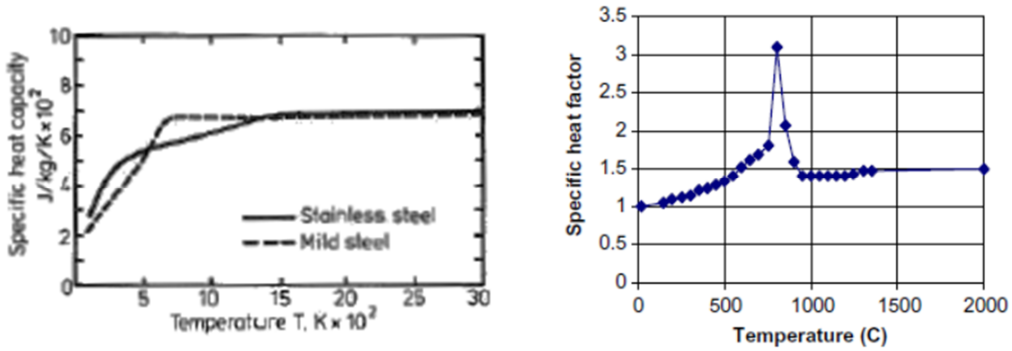

a. *b.*

Figure 1-19 Specific heat for: *a.* mild and stainless steel, using constant value of C_P after a maximum [125]. *b.* mild steel with peak value followed by lower values [119,126].

Zhu and Chao [124] claimed that specific heat dependency on temperature has a negligible effect on the predicted temperature profile for GMAW aluminium thick plates. However, lower values after the peak, as figure 1-19 *b*, are more realistic and correspond to the actual thermal property. Some thermo-physical recommended values for commercial alloys are shown by Mills [127].

Thermal conductivity

Thermal conductivity, k, is the capacity of a material to transport heat from one part to another within the body. It plays an important effect on heat transfer welding simulations [124], since it is the main mechanism to transfer heat in the

work piece during welding. A plot of k for mild steel is shown in figure 1-20. It is important to emphasise that in this graph the real value of thermal conductivity was artificially increased up to 120 $W \cdot m^{-1} \cdot K^{-1}$ after the melting point, but it does not have a physical meaning. The reason for this is to take somehow into account the convective stirring forces generated by the welding process in the weld pool [119,126,128,129].

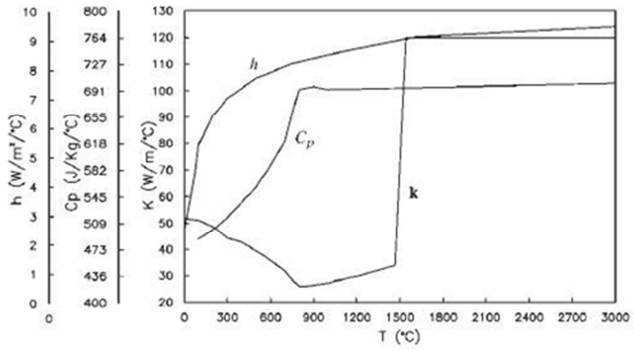

Figure 1-20 Some thermo-physical properties for mild steel [128].

Latent heat

Latent heat is the amount of energy necessary for a phase transformation occurred without temperature changes. In mild steel there are three main transformations: the solid transformation of allotropic faces, $\alpha \leftrightarrow \gamma$, with 7 $kJ \cdot kg^{-1}$ [119], fusion with 272 $kJ \cdot kg^{-1}$ [130], and vaporisation with 6.258 $MJ \cdot kg^{-1}$ [130]. The effect of fusion latent heat variation, in GMAW mild steel plates, was studied by Colegrove *et al.* [15] and Thistlethwaite [123]. They show that the magnitude of fusion latent heat has no significant effect on the residual stresses and peak temperatures in mild steel.

1.5.2 Mechanical properties.

The thermal analysis is a more straightforward task in comparison with mechanical analysis [131]. The thermal load applied by welding process causes dilation and contraction throughout the metal. The strain generated by the uneven temperature distribution causes residual stress. The magnitude of the residual stress is directly related to the mechanical material properties of the

piece, in particular the yield strength [124]. In this section, the main material properties needed in welding analysis are presented.

Linear thermal expansion coefficient

The coefficient of linear thermal expansion, α, measures the dimensional changes of the material in one direction. It determines the thermal strain of the weldment, and takes into account the changes due to solid phase transformations. Hence, it is the driving force for the thermal stresses [131]. Peil and Wichers [132] published a large set of mechanical property data for S355 J2G3 steel, in which appropriate linear thermal expansion coefficient temperature dependent values can be found. Figure 1-21 *a* shows the coefficient of linear thermal expansion with two different instruments. In addition, Peil and Wichers advise the use of the results from the instrument called “Bähr DIL804”, since it provides more precise data. Zhu and Chao [124] showed that the residual stress distribution and distortion are virtually the same when the linear thermal expansion coefficient is considered constant, either using the average value of a welding cycle, or the room temperature value, instead of using the temperature dependent real values.

Elastic properties

All models calculate stress from elastic strains according to Hooke’s law. The stress is usually divided in the hydrostatic and deviatoric parts. The former is completely elastic. The properties required by the model for anisotropic material are the Young modulus and the Poisson’s ratio. Tekriwal and Mazumder [133] have reported that the Poisson’s ratio has an insignificant effect on the residual stresses and deformation. In addition, they suggest to avoid the uncompressible condition (Poisson’s ratio = 0.5) since it causes numerical complications. Figure 1-21 *b* shows the temperature dependent Poisson’s ratio for mild steel, and other mechanical properties. Zhu and Chao [124] concluded that the Young modulus has a small effect on both residual stress and distortion. However, the results presented in their paper suggest that Young modulus has a non-negligible effect on residual stress. Figure 1-21 *c* shows the Young modulus for

S355 J2G3 steel with three different strain rates (v1 = v2 = 0.005; v3 = 0.05 min^{-1}).

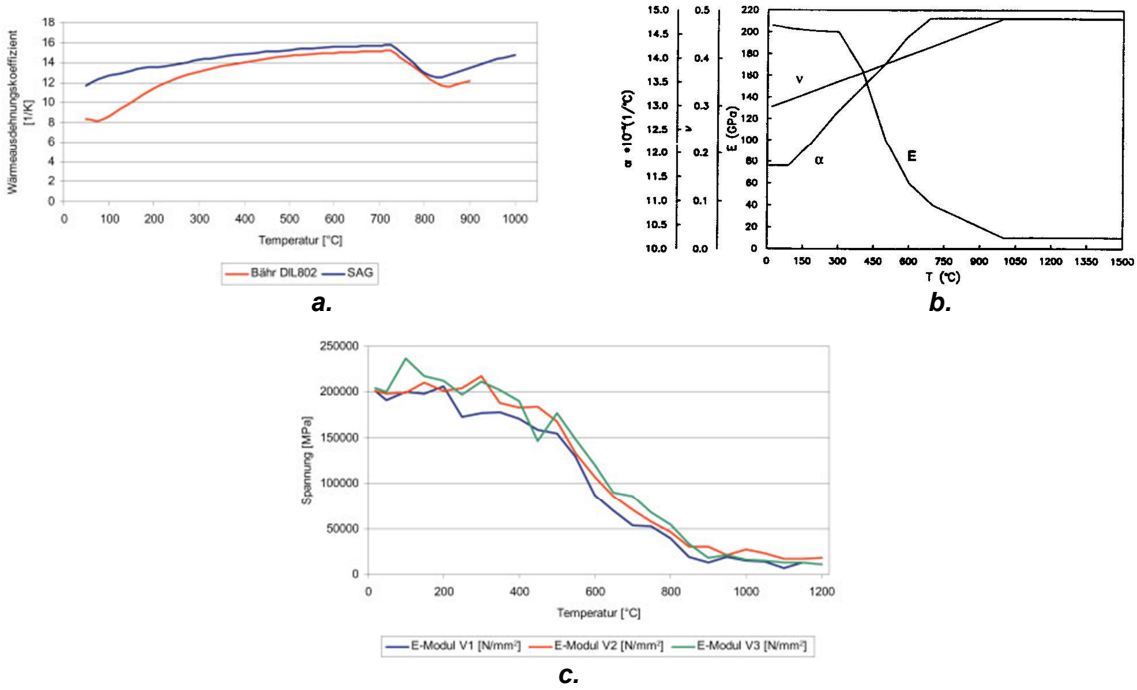

Figure 1-21 Mechanical temperature dependent properties; *a.* Coefficient of linear thermal expansion [132]; *b.* Poisson ration [128]; *c.* Young modulus [132].

Yielding strength

Thermo-mechanical modelling analysis requires appropriate temperature dependent yield strength properties to capture residual stresses generated by the thermal load and different constraint. Peil and Wichers [132] and Outinen *et al.* [134–136], have published the tensile temperature dependent test results for the S355 steel. Unfortunately, the data provided by Outinen *et al.* are in a narrow range close to the yielding point, so the work hardening behaviour cannot be fully appreciated. Figure 1-22 shows tensile test result for different temperatures for S355 J2G3 steel [132]. From the tensile results it is evident how this steel decreases its yielding strength and work hardening while temperature rises. However, between 150 and 350°C the yielding strength and work hardening rose. It is thought that the reason for this is the nucleation of carbides, which eventually grew and lost their reinforcing effect. Between 400

and 750°C the steel lost drastically its yielding strength, and after 750°C it behaved as a virtually perfectly elastic-plastic material.

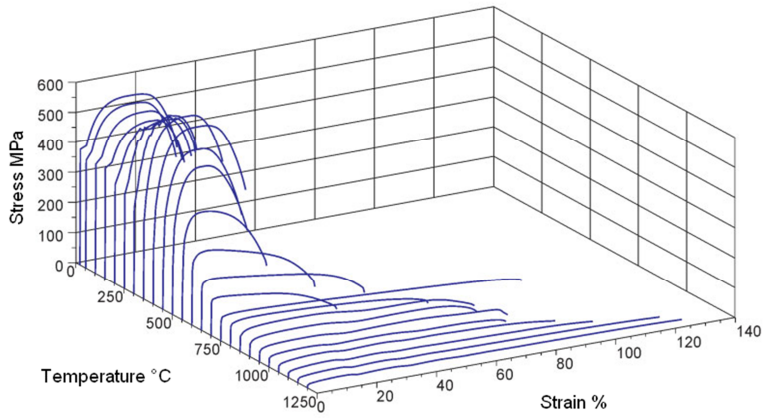

Figure 1-22 Nominal tensile test results at different temperatures [132].

Constitutive modelling of metals

Modelling plasticity is a complex process. There are three fundamental aspects to consider when the material yields, the yielding criteria, the yield strength, and the work-hardening model.

Yielding criteria

In solid mechanics there are several yielding criteria, however, there are two broadly accepted to predict yielding in ductile metals. A good explanation of them is provided by Dieter [137]. The Von Mises or the distortion energy criterion, proposes that yielding would begin when the second invariant of the stress deviator exceeds a critical value, as shown in eq. 1-11. The second, the Tresca or the maximum shear stress criterion, states that the yielding would begin when the maximum shear stress reached the value of the shear stress on the uniaxial tensile test, as shown in eq. 1-12. Where σ_1, σ_2, σ_3, represent the principal stresses, and σ_0 the yield strength of the material.

$$\sigma_0 = \sqrt{\frac{1}{2}[(\sigma_1 - \sigma_2)^2 + (\sigma_1 - \sigma_3)^2 + (\sigma_2 - \sigma_3)^2]} \quad \text{Eq. 1-11}$$

$$\frac{\sigma_0}{2} = \tau_{max} = \frac{\sigma_1 - \sigma_3}{2} \quad \text{Eq. 1-12}$$

Work-hardening models

After the yielding point is exceeded during deformation, metals have the tendency of work-harden. This post yielding behaviour, of elastic-plastic metals, can be usually modelled using different hardening rules, perfectly (elatic-) plastic, isotropic, kinematic (anisotropic), and mixed hardening rules [138]. Note that at high strain rates, dynamic effects can modify the work hardening rules.

The perfectly plastic behaviour occurs when the stress remains the same during the material flow. This behaviour is characteristic of mild steel in the plateau region [139]. In addition, this behaviour is adopted in modelling when the material exceeds the predefine annealing point [140]. It is normally used when small strain is expected to occur in the analysis. In the isotropic rule, the yield surface expands without distortion, owing to a rise in the dislocation density, while the material flows [141], as shown in figure 1-23.

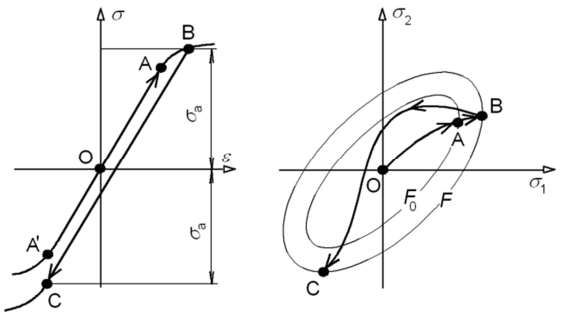

Figure 1-23 Isotropic hardening rule.

The Bauschinger effect is a common phenomenon in polycrystalline metals cyclically loaded. The yielding stress in metals is similar when determined either in tension or in compression. When a metal is loaded in tension and the yielding point is exceeded, some plastic deformation and work-hardening occur. If the

same metal is then loaded in compression its yielding point will be shift to higher values. Figure 1-24 *a.* shows an example of the Bauschinger effect. The 30CrNiMo8 sample had its yielding point at about 900 MPa in tension, while in compression it is increase from about -900 to -400 MPa. The Bauschinger effect can be described by the kinematic rule. It corresponds to the translation of the yielding surface in the stress space [139], as shown in figure 1-24 *b*. This rule is useful to simulate cyclic loads, or in complicated metal stamping shapes were compression and tension can occur at the same time in different part of the workpiece during the same process. With the mixed hardening rule, the yield surface can potentially expand and translate at the same time, as shown in figure 1-24 *c*.

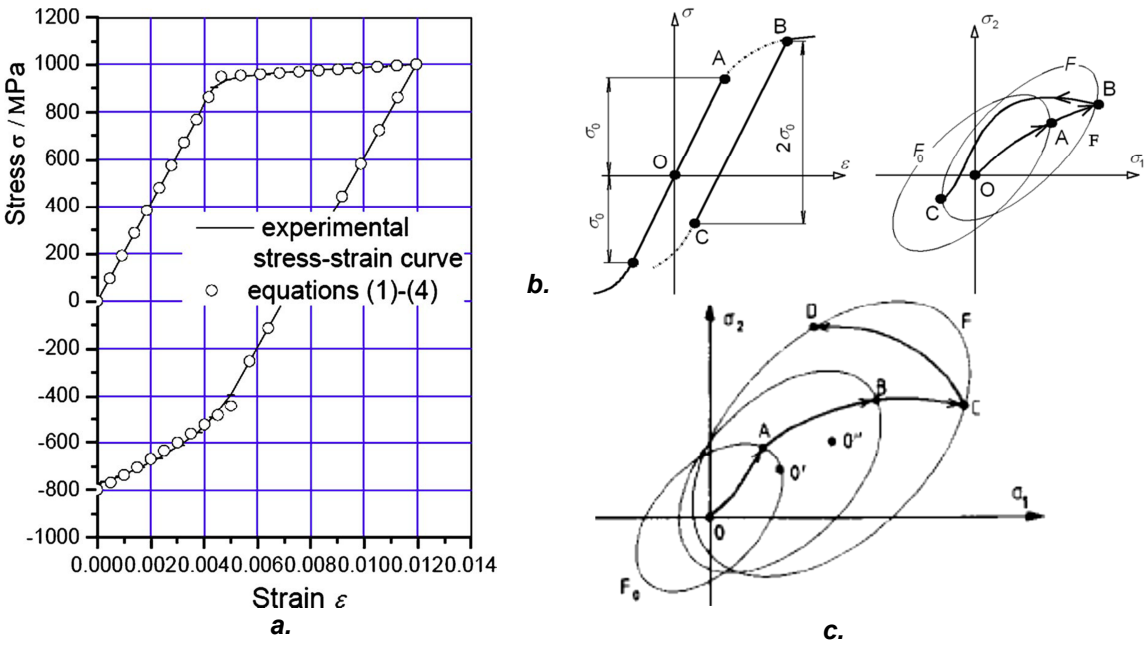

Figure 1-24 ***a.*** **Bauschinger effect in 30CrNiMo8 sample. [142]** ***b.*** **Kinematic, and** ***c.*** **mixed hardening rule [138].**

1.6 Computational welding mechanics simulations (CWM).

Finite element analysis is the dominant tool in CWM. Publication of finite element simulation involving the mechanical effects of welding are present since the beginning of the 70's [129,143]. It was originally applied in the aerospace and nuclear power plant where safety aspects are extremely

important. Nowadays, due to the exponential improvements in computational speed, it is implemented in a wide range of industries such as automotive, and ship and train building.

The CWM focuses on the large scale of welding phenomenon, and not on the particular details of the multi-physics involved in the heat generation of the welding process. CWM deals with the thermo-mechanical behaviour of the material and the changes in its properties due to the thermal cycles in welding. In addition, its role in engineering is not to replace the experiments, but instead CWM is a complementary tool which still needs to be validated against them. However, simulations allow the details of the welding process to be investigated which is impossible to observe by direct measurements made during the experiments.

1.6.1 Numerical aspects of CWM

Coupling physical phenomenon

GMA welding is characterised by the multi-physics nature of the process, which are very challenging to simulate, as they occur in a small portion of the material in relatively small time intervals. However, not all the couplings are of significant importance in the simulation. Consequently, it is not common to analyse all coupled systems in the model at the same time, but instead simulate different physical processes independently, and then link them by simplified assumptions about their interactions [118,129,143,144]. Figure 1-25 shows the important physical couplings in thermo-mechanical welding simulation; consequently, thermal analysis normally takes place before the mechanical analysis.

The fluid flow in the weld pool is normally neglected in the simulation. Instead, the liquid region is approximated with a solid material with low mechanical properties and Poisson's ratio close to incompressible fluid in the mechanical analysis. In the thermal analysis, the heat input is prescribed and usually the thermal conductivity is artificially increased to simulate the convective heat transfer in the weld pool. Therefore, the actual physical phenomenon occurring in the weld pool are simplified by equivalent but simpler assumptions [143].

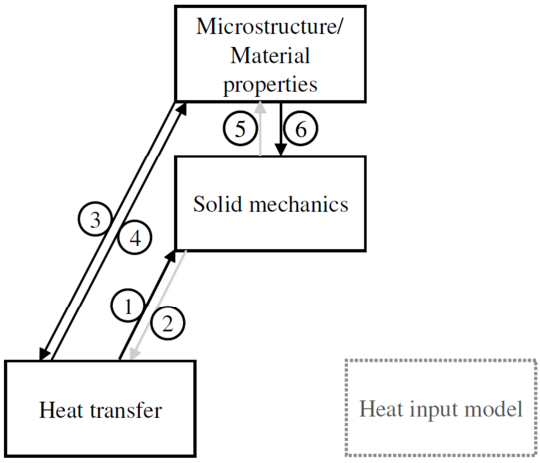

Figure 1-25 Coupling of the important physical processes in thermo-mechanical modelling of weld: less influent couplings are grey, while strong couplings are indicated by black arrows. 1. Thermal expansion drives strain and deformation; 2. heat generation due to deformation; 3. latent heat and thermal material properties depending on temperature and microstructure; 4. temperature inducing microstructure changes; 5. deformation affects microstructure; 6. mechanical properties depend on temperature and microstructure [143].

Reference frame

In CWM two fundamental approaches are commonly used: Lagrangian, in which the heat source moves respect a static frame in the material (transient analysis), and Eulerian, where the static frame is located in the heat source while the material flows though a fixed mesh, to take advantage of the steady-state condition [118,143]. Lagrangian reference frames are more commonly used in CWM simulation, as it is easier to apply with many solvers (*e.g.* Abaqus); nevertheless, the Eulerian frame can reduce significantly the computational time in the simulation [145,146], but particular attention have to be taken in ensuring that the steady-stated was reached in the position where the heat source is placed, as will be described in section 1.6.3.

1.6.2 Modelling aspects of CWM

Model geometry

Brown *et al.* [147–149] recommended the implementation of three dimensional geometries to study the residual stress and distortion caused by welding, to accurately model the coupling between the weld and the large workpiece. The

two dimensional approach can produce faster results; however, the accuracy of the result can be drastically reduced in multi-pass welds [150,151], or in welds of thick material [152] where the temperature gradient through the thickness is significant. On the other hand, in welds with high intensity energy, on thin plates where the thermal gradient through the thickness is negligible, and sufficiently long to reach the steady state, the 2D models could provide accurate predictions [153].

Model mesh

Lindgren [129] recommends the use of elements with one degree of freedom higher in the mechanical analysis than in the thermal one, because the temperature field is directly transform in the thermal strain in the mechanical analysis, and the strain is calculated as the derivative of the displacement field. However, linear brick (hexahedral) elements have produce better results in many cases analysed, such as bending, torsion, and natural frequency, than the quadratic tetrahedral elements, with computational times virtually identical. On the other hand the quadratic tetragonal elements produce better results in the shear analysis [154].

Regarding the element shape, tetrahedrons and hexahedrons (bricks) are commonly used in the FE models. The tetrahedrons are more convenient to use in complex 3D meshes, since the automatic meshing algorithms provided by most of the commercial FE packages can easily generate an adequate mesh. However, hexahedrons are preferred in welding thermo-mechanical studies, because they perform better than the tetrahedrons in terms of accuracy and computational time. Moreover, hexahedrons have a better convergence rate than tetrahedrons [140,155].

“Shear locking” is a problem the fully integrated linear elements can undergo. It causes the under prediction in bending distortion. If an imaginary grid inside the material is consider, as the one shown in figure 1-26 *a*, when a material is subjected to a pure bending moment, it deforms keeping the angle between the internal dashed lines constant (90°), as shown in figure 1-26 *b*. The edges of the linear elements cannot curve; therefore, the deformation under pure

bending moment of a single element is as shown in figure 1-26 *c*, which is not realistic, since the variation between the vertical and horizontal dashed lines is different from the initial 90°, suggesting that the shear stress is non-zero, which is incorrect [140]. Elcoate *et al.* [156] has suggested that for welding mechanical simulation the reduced integration elements are a better option. Figure 1-26 *d* shows the deformed reduced integration linear element. Because it has only one integration point in the centroid of the elements it does not suffer for the problems of the full integrated ones. However, this kind of element tends to be excessively flexible because of the hourglass effect.

The hourglass is an unrealistic deformation which happens with no strain energy involved. The main problem with hourglass is that it can propagate through the mesh causing unexpected results, when the mesh is too coarse [140]. Figure 1-26 *e* shows an example of hourglassing propagating through a small mesh.

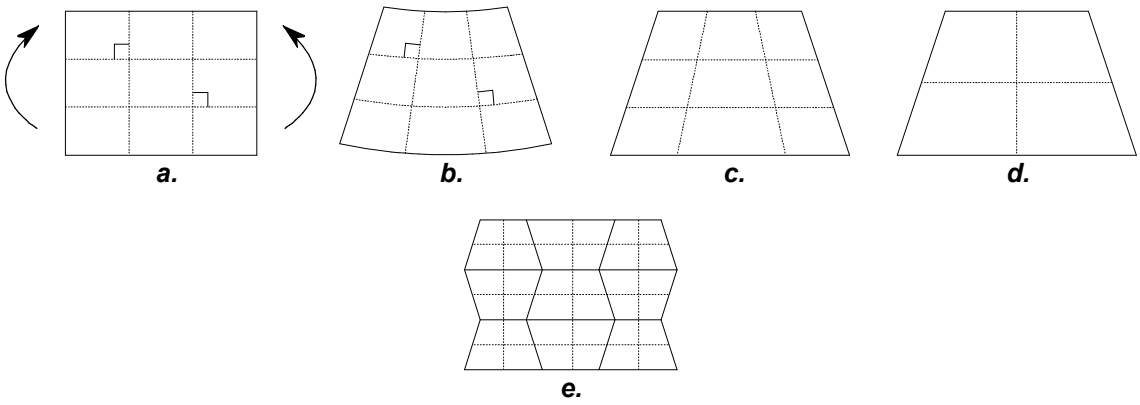

Figure 1-26 Effect of bending deformation in the linear elements. *a.* Small portion of material, and fully integrated single element before deformation; *b.* deformed material; *c.* deformed fully integrated element; *d.* deformed reduced integrated element. *e.* Hourglass effect in reduce integration linear elements.

Model filler material

Different techniques are available to simulate the addition of the filler material in the weld bead. In the element birth technique the elements of the filler material are deactivated until the corresponding filler metal is added [157]. The quiet element has all the elements activated at the start of the welding, but those

corresponding to the not yet laid filler material have artificially modified low strength mechanical properties, so that they do not affect the surrounding elements during the analysis; real material properties are assigned when the fillet material is deposited [158]. In the element movement technique, the elements of the filler material are completely separate from the base metal. As the filler metal is laid, the filler elements are displaced to the base plate, and the nodes of both filler and base metal are linked together to form one body [159]. In the dumped-block method, the filler metal is added from the start of the welding step. It is the most common technique, since is the simplest to implement [152].

Shang *et al*. [152] advise that although the element birth technique could be more accurate than the dumped-block method, it is more computationally time consuming, especially for the mechanical analysis, and the difference in the result is not significant. Fanous *et al.* [159] compared the move elements technique against the element birth one. Although the moving technique performed in half of the time of the element birth one, the results obtained with the latter better matched the experimental results.

1.6.3 Transient and steady state

A process is in a transient state when the different variables which govern that process are changing in time, in other words, when the process has not yet reached the steady state. On the other hand, the steady state is when their variables are non-time dependent.

In welding all the reactions are constrained to take place within very short times in a small volume of metal. For that reason, welding normally is considered a transient process since variables change considerably with time. Nevertheless, as shown in the analytical solution section, Rosenthal proposed a method in which welding can be considered as a pseudo steady state (*"quasi-stationary")*. Grong [108] stated that to reach the steady state it is necessary to overtake a period in transient state.

During welding there is an initial period of time in which there is no steady state. That period is function of the position of the control point, p, whose coordinate

system has its origin in the heat source, and moves with it. Additionally, the pseudo steady state is reached faster when the control point distance is close to the heat source. Travel speed, v, and thermal diffusivity, α, modifies that transient period.

Figure 1-27 *a* and *b* show the variation of the ratio (κ_i) between the transient and the pseudo steady state. Eq. 1-13 shows the dimensionless parameter σ to determine the dimensionless time, τ, from figure 1-27 *a* and *b*. τ is used in eq. 1-14, to find the time required to reach the pseudo steady state. Note that the curves reported in figure 1-27 *a* and *b*, were calculated for aluminium welded plates, and consequently need be recalculated for use with other metals.

$$\sigma_3 \; and \; \sigma_5 = \frac{vp}{2\alpha} \qquad \text{Eq. 1-13}$$

$$t = \frac{2\alpha\tau}{v^2} \qquad \text{Eq. 1-14}$$

Grong [108] showed that the pseudo steady state (for aluminium welded plates reported in the previous paragraphs) was reached faster in thick plates than in thin plates. This was due to the differences in the heat flow conditions involved. However, in his analytical model he did not considered the heat losses, such as the backing-bar which can significantly modify the transient period.

1.6.4 Model heat input

All the CWM simulations only consider the thermo-mechanical phenomena involved in the weld by producing an empirical heat input model which takes into account all the physics of the weld process [143]. There are two main approaches to model the weld heat input in FEM, surface, and volumetric distributions.

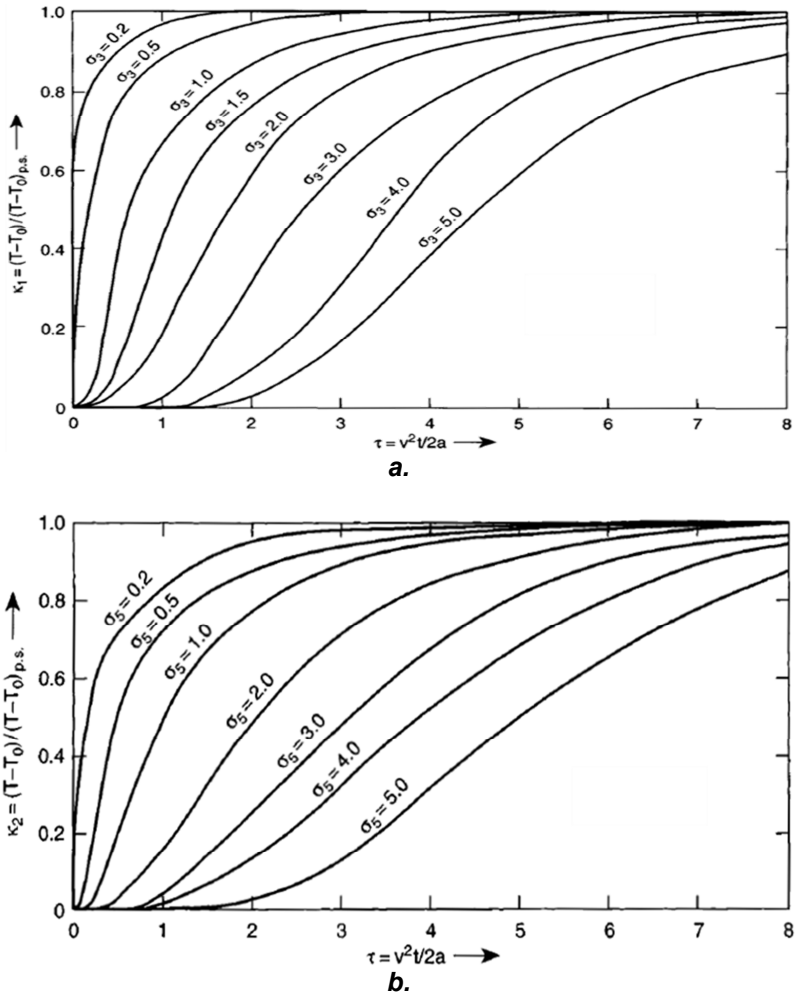

Figure 1-27 Ratio between real and pseudo-steady state temperature in *a.* thick and *b.* thin aluminium welded plates [108].

Gaussian surface heat distribution

A Gaussian heat flux distribution was proposed by Pavelic *et al.* [160]. If the heat source is normal to the surface and it has round shape, the specific heat flux distribution can be expressed by eq. 1-15.

$$q(r) = q(0)e^{-Cr^2} \qquad \text{Eq. 1-15}$$

Where C is the concentration coefficient which determine the amplitude of the Gaussian distribution, and it is related to the actual heat source width; r the radial distance from the centre heat source; $q(0)$ the maximum heat flux at the centre of the source, and $q(r)$ the surface heat flux at the radius r.

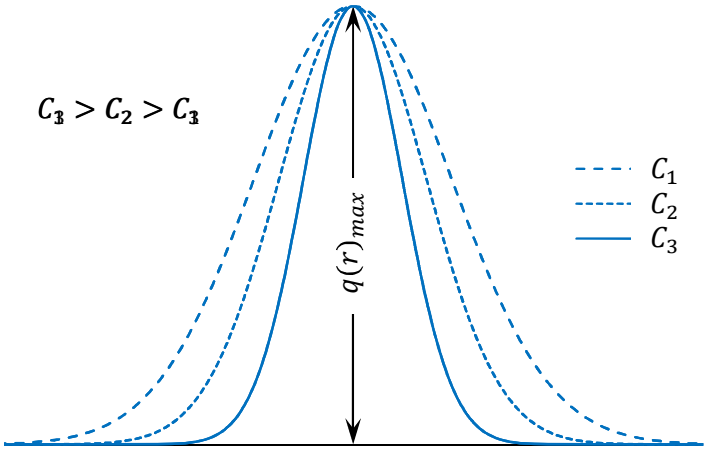

Figure 1-28 Gaussian heat distribution in a circular shape (adapted from [160]).

As shown in figure 1-28, the bigger the value of C the smaller the spot size. In order to know the value of the peak heat input, the total heat input can be integrated as shown in eq. 1-16.

$$q_{Tot} = \eta VI = \int_0^{\infty} q(0)e^{-Cr^2} 2\pi r dr$$

$$q_{Tot} = \eta VI = \frac{q(0)\pi}{C}$$

$$q(0) = \frac{q_{Tot}C}{\pi} \qquad \text{Eq. 1-16}$$

To obtain the value of the concentration coefficient C, eq. 1-15 can be integrated in a defined value, for instance when $q(0)$ is equal to 5 % of the peak, as shown in eq. 1-17

$$q(0)e^{-Cr_{5\%}^2} = 0.05q(0)$$

$$C \approx \frac{3}{r_{5\%}^2} \qquad \text{Eq. 1-17}$$

Volumetric double ellipsoid heat distribution

The double ellipsoid model proposed by Goldak *et al.* [119] has shown to be a more generic case of the disk model developed by Pavelic *et al.* [160] and the

volumetric models of Paley and Hibbert [161] and Westby [162]. As its name suggests, the double ellipsoid heat flux distribution consists in dividing the instantaneous heat input into two parts, and apply them in half of the volume generated by two quarters of ellipsoid (front and rear), as shown in figure 1-29. The heat applied in the frontal, and posterior ellipsoid quadrants are described by eq. 1-18, and eq. 1-19.

$$q(x,y,z,t) = \frac{6\sqrt{3}f_f Q}{a_f bc\pi\sqrt{\pi}} . e^{-3\frac{[x+v(\tau-t)]^2}{a_f^2}} . e^{-3\frac{y^2}{b^2}} . e^{-3\frac{z^2}{c^2}} \qquad \text{Eq. 1-18}$$

$$q(x,y,z,t) = \frac{6\sqrt{3}f_r Q}{a_r bc\pi\sqrt{\pi}} . e^{-3\frac{[x+v(\tau-t)]^2}{a_r^2}} . e^{-3\frac{y^2}{b^2}} . e^{-3\frac{z^2}{c^2}} \qquad \text{Eq. 1-19}$$

The f_f and f_r are the fractional factors of the heat deposited in the front and rear quadrants, where f_f plus f_r equal 2. The value of these two parameters is arbitrary and should be set according the experimental conditions. On the other hand, to avoid discontinuities in the heat distribution between front and rear ellipsoids, f_f and f_r may be determined equalling the heat in the anterior and posterior quadrants of the two ellipsoids, in the intersection surface, as shown in eq. 1-20 [158]. The parameters a_f, a_r, b, c are the geometrical parameters, as shown in figure 1-29, and can be defined from experimental measurements of the weld pool. Goldak and Akhlaghi [118] suggested that good agreement between the predicted and the actual weld pool size can be obtained when the these parameters are about 90 % of the actual weld pool size. Moreover, in the case of welding two different metals it might be necessary to use different values of a, b, c in four octants. x, y, z are the coordinate system fixed in the workpiece, Q is the instantaneous power ($Q = \eta VI$), v is the welding speed, t is the time, and τ is a lag factor to define the position of the source at time t = 0.

$$f_f = \frac{2a_f}{a_f + a_r} \qquad \text{and} \qquad f_r = \frac{2a_r}{a_f + a_r} \qquad \text{Eq. 1-20}$$

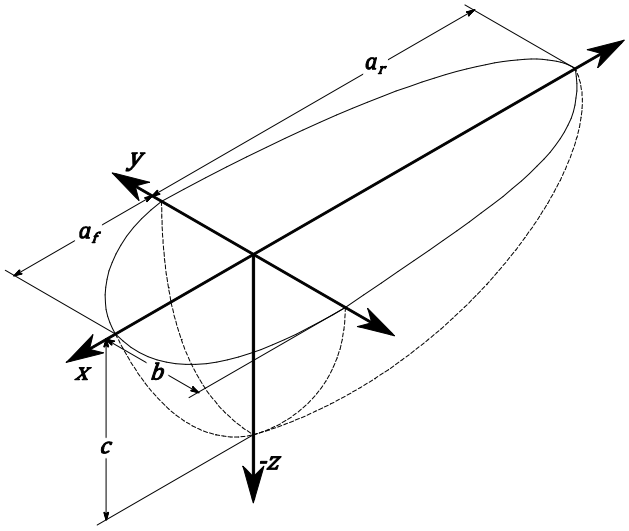

Figure 1-29 Double ellipsoid heat source geometrical parameters.

Backing-bar

The backing-bar is a piece of material placed underneath the weld seam. It is used with two purposes: to avoid the molten metal to go away from the root of the weld, and to modify the thermal distribution in the weldment. There are four types of backing-bar that are commonly used in welding: backing strip, backing weld, metallic backing-bar, and non-metallic backing-bar [163].

A backing strip is a piece of metal underneath the joint. It can be removed after welding or it can be left in place, depending on the requirement of the joint. The strip should be metallurgically compatible with the parent and filler metal. The backing welding is very similar to the backing strip method, but instead of adding a metal strip, a single or multiple welding passes in the back side of the joint are performed, before the first pass is put in the groove of the joint.

A metallic backing-bar is composed by a rectangular cylinder of a high thermal conductive metal, normally copper, in the back of the weld pool, in the root of the joint. Due to the high thermal conductivity of it, it can remove large amounts of heat before melting. To avoid melting of the backing–bar, either it must have enough mass to dissipate the heat, or it can be cooled by a fluid passing through internal holes in the bar.

The non-metallic backing-bar is composed by granular flux or refractory materials like ceramics. As the other techniques, the backing-material should be placed underneath the joint.

During welding thin plates permanent distortion can occur. If a copper backing-bar is used, an adequate clamping system can generate a good contact between the backing-bar and the plates. This increases the thermal conductance between them, and consequently reduces distortion [164]. Rosales *et al.* [165] studied the influence of different backing-bar materials in FSW aluminium plates. They found that with a copper backing-bar the stirred zone was smaller than with a ceramic one. Additionally, they showed that with the ceramic backing-bar there was material losses in the shoulder contact area, presumably generated for the wider hot plastic region affected.

In the welding thermal models the backing-bar can be modelled by two approaches: as a solid body with temperature dependent thermal resistance between the weldment and the backing-bar [166–171], or by modelling its heat sink effect, applying a temperature dependent convective heat sink in the expect contact area [99,146,172–174]. The latter has the advantage of faster computational time; however, to obtain the correct parameters can be time consuming.

1.6.5 Modelling outputs

Modelling allows prediction of details that are impossible to observe during welding experiments. The models can provide details of the temperature and heat propagation during welding, as well as the stress distribution. In section 1.2.3, the techniques to reduce and manage the residual stress were discussed. They showed how models have been used to determine the residual stress reduction as well as distortion mitigation, by mechanical, thermal, and electromagnetical means.

1.7 Conclusions

There is a large amount of work on the aspect related with residual stresses and welding heat effect in the literature. However there are not many models

that combine the effect of stress generated by fusion welding with residual stress mitigation techniques such as stress engineering. There are many advantages of modelling the residual stress mitigation processes. Firstly, it allows a deep understanding of the phenomena involved, and allows exploring conditions that could be physically complicated, or even impossible to perform with the current technology. Secondly, it permits (in some cases) time and material savings in the development of the techniques.

The fundamentals of residual stress formation during welding are well explained in the literature. Modelling of the fusion welding process has been investigated by many authors in the past. All the models have used simplifications to produce accurate but time efficient temperature distribution, and residual stress profiles. One of these simplifications was the thermal losses towards the backing-bar. The literature does not propose a standard approach to model this thermal loss. The most common way to simulate it was by applying force convection in the theoretical contact region. However, the thermal loss though the backing-bar are not constant during the welding process; therefore, the convective coefficient used to simulate the thermal loss had to take into account this phenomenon. In the following chapter different forced convective heat transfer coefficient rules were implemented to address this issue.

To manage the welding residual stress many techniques were found in the literature; however, localised rolling while effective had few references, many of which were 30 to 40 year old. Furthermore, numerical models of the different localised rolling techniques were even less present, and in particular for the pre-weld rolling technique no literature related was found. In addition, the few models available were not particularly applicable to the GMAW process, which was used in the models of this thesis, because they investigated FSW where the weld reinforcements were not present; consequently the effect of rolling the weld toes and the different weld bead shape variation due to rolling has not been investigated. Additionally, the influence of the friction between the roller and the workpiece on the residual stress distribution was not found in the literature survey. These issues were explored and addressed in this thesis.

The effect of different rolling loads have been investigated for different materials, however their effect on the through thickness variation of the residual stress was not explored in the literature. Additionally, most of the literature of the *in situ* rolling was focused on mechanical properties improvements, but not in the management of residual stress; consequently a poor understood of the process was provided.

The literature proposes different ways to model the material properties of the weldments, as well as different values for the same material used in the models of this thesis. This complicated the selection of the appropriate values. In addition, some models used temperature independent material properties, which for the case of welding may not be the most suitable approach.

Therefore, this thesis will address the effect of localised rolling by finite element analysis, and aims to:

- Provide a better understanding of the residual stress distribution after and during localised rolling, and its interaction with the welding residual stress.
- The influence of the roller profiles and rolling parameters such as friction, loads, position, diameter, and width on the residual stress reduction of GMA welded steel plates.
- Validate the predicted results with experimental data.

The thesis is organized in the following way. The next chapter focuses in the temperature distribution of all the models of this investigation, as well as the residual stress distribution due to welding. The influences of different thermal losses through the backing-bar, as well as the influence of the mechanical properties in the residual stress distribution were investigated. The following chapter investigates the pre-weld rolling technique and the effect of different rolling loads, distances from the plate edge, positions (upper or lower surfaces). In addition, the influence on the welding residual stress management of post-weld heating in the rolled areas was investigated. The next two chapters focus in the post-weld and *in situ* rolling methods. In the former, two different roller profiles were investigated, namely, grooved, and dual flat rollers. They

were used to roll the top of the weld bead and next to it, respectively. In addition, the influences of different friction coefficients on the residual stress mitigation were investigated. In the *in situ* method only the grooved roller was used and different rolling trailing distances from the torch were investigated, to analyse the effect of rolling at different temperatures. Most of the models were validated against experimental results.

Chapter 2 Welding Thermal-Mechanical Analysis

2.1 Introduction

Welding is one of the most widely used techniques in metal fabrication such as, shipbuilding, railways, automotive, aerospace, offshore structures, pipelines and every metal manufacture, because it reduces significant the amount of material required in the fabrication. Fusion welding involves uneven heating of the weldments, which causes a characteristic temperature distribution and consequently local plastic strain in the weld and surrounding metal. The mismatch of the plastic strains, between the weld and the parent metal, causes the characteristic welding residual stresses distribution, which have adverse mechanical effects in the weldment.

Finite elements thermal-mechanical welding simulations have been performed since the early 70's [5–7]. However, these models were fairly simple due to the computational resources available at that time. With the advance in computer's performance, welding simulation is nowadays commonly used to determine thermal cycles and residual stresses in academia and industry. However, the current obstacle for implementing welding simulation in industrial practice is the necessity of material properties [175].

Computational welding mechanics focuses in the simulation of the large scale effect of the heat source rather than in the physical phenomena involved in welding [129]. Consequently, many simplifications are adopted, which allows accurate results to be obtained in relatively short time. Additionally, welding simulation can significantly reduce the number of experiments to a few key ones to validate the models, and to test particular design conditions.

In welding simulation the thermal model is generally sequentially coupled from the mechanical one [158], *i.e.* the thermal simulation is performed first, and the temperature history obtained is imported into the mechanical analysis. The consequent thermal dilation, which includes the thermal expansion and the volumetric changes from phase transformation, determines the deformation and consequent residual stress. Therefore, the temperature distribution in the

simulation is one of the most important aspects to produce an accurate residual stress prediction.

In this chapter the thermal and mechanical aspects, as well as the thermo-mechanical results of the all welding models developed in this thesis are discussed.

2.2 Methodology

In this section the features, assumptions, and boundary conditions of the welding thermal-mechanical models for pre-weld, post-weld, and *in situ* rolling geometries are described. The rolling steps for these models are described in subsequent chapters. The first section of the methodology explains the common characteristics for the welding thermal-mechanical analysis used for the different model types presented in this thesis; the second section provides specific details of welding thermal analysis, in which different method to simulate the backing-bar were investigated. The third section describes particular details for the welding mechanical model, where the residual stress were predicted using the three thermal distribution obtained in the previous section. In addition, the effect of different mechanical properties for the S355 mild steel was investigated. In the last section, the buckling eigenvalue analysis is described.

Note that the emphasis of this thesis is the rolling of the welds and understanding how this process affects the residual stress (**RS**) and distortion. Because of this emphasis, full justification for the boundary conditions used in the thermal-mechanical models of the welding process is not provided. In most cases the chapter provides the best values which allowed a good match between the temperature predicted by the model and that measured experimentally. It is recognised that when modelling a welding process there are often many combinations of boundary conditions that provide a good match with experimental data [170,171]. For example, a high heat input and high heat loss from the backing-bar may give a similar result to a lower heat input and lower heat loss from the backing-bar. Therefore, the values presented may not necessary be the correct ones; however, they provide a sufficiently accurate

prediction of the temperature to estimate the RS and deformation caused by welding.

2.2.1 Common characteristics

The models simulate a GMAW process on S355 mild steel plates based on experiments carried out by Coules *et al.* [1–3]. A brief description of the experiments, the equipment implemented, and the experimental residual stress techniques, can be found in appendix d. The models were built with Abaqus Standard version 6.9 using the sequentially coupled thermal-mechanical approach. They are three dimensional and simulate bead-on-plate welds on flat profile plates. Owing to the geometry of the experiments and to reduce computational time, only half of the geometry was modelled. The geometries varied according to the model type, and they are reported on table 2-1.

Table 2-1 Weldment dimensions and element sizes.

Model	Half weldment L×W×T [mm]	Half Reinforcement Ø×H×W [mm]	Element size L×W×T [mm]			
			Welding toes	High density	Medium density	Low density
Pre-weld rolling	500×200×4	11.2×3.1×5.0	1×1×1	1×1×1	2×2×1	6×6×1
Post-weld rolling Long geometry & *In situ* rolling	750×150×6	13.8×2.9×5.6	1×0.5×0.5	1×1×1	2×2×1	6×6×2
Post-weld rolling Short geometry	456×150×6	13.8×2.9×5.6	1×0.5×0.5	1×1×1	2×2×1	6×6×1

A typical mesh used is shown in figure 2-1 *a*. It shows the variation of the mesh density across the width. In general, denser mesh was implemented on the weld bead region and surroundings, and on areas where rolling was applied. The post-weld and *in situ* geometries had meshes with an even higher density mesh around the weld toes to capture the characteristic stress concentration of this region, and is shown in figure 2-1 *b.* The mesh was progressively coarsened in the transverse direction towards the external edge, as shown in

figure 2-1 *a*, and reported in table 2-1. The effect of the mesh density was studied to ensure the result is independent of the mesh size.

The weld reinforcement was simulated as a section of a circle of diameter Ø (see figure 2-1 *b*). Additionally, a 2 mm fillet radius was added on the weld toes of the post-weld and *in situ* geometries, to aid rolling in subsequent steps, as shown in the upper figure 2-1 *b*. The values of Ø, H, and W are provided in table 2-1, and they were estimated from the real welds produced by Coules *et al.* [1,2].

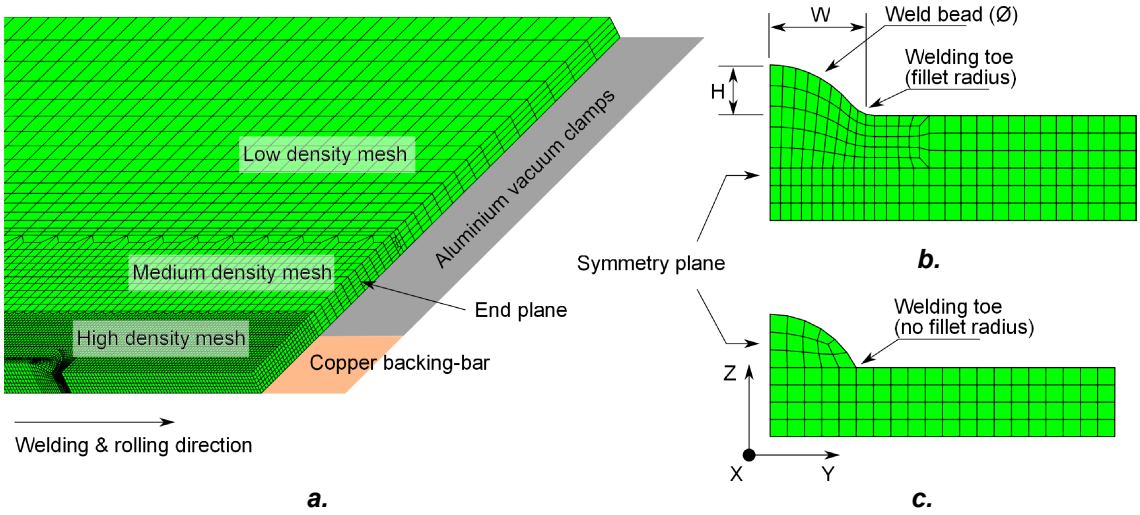

Figure 2-1 ***a.*** **Example of different mesh density through the plate width.** ***b.*** **Weld bead profile in post-weld and *in situ* rolling, and** ***c.*** **in pre-weld rolling.**

Different techniques are available to simulate the addition of the filler material in the weld bead, and they were already discussed in chapter 1. The dumped-block method is the most common technique to model the filler material in welding, because it is the simplest to implement, as it has the whole filler metal added from the start of the welding step [152].

The weld bead in these models was active during the entire welding step as well as the subsequent ones; hence the dumped block method was used. Shang *et al*. [152] advise that although the “bird element” technique could be more accurate than the “dumped-block” method, it is more computationally time

consuming, especially for the mechanical analysis, and the difference in the result is not significant.

When the pre-weld rolling geometry was used, the weld bead was added strain free after rolling, at the start of the welding step (using the keyword “MODEL CHANGE” in the input file). Consequently, it did not affect the rolling process. Additionally, no fillet radius was used on the weld toes in these models, as shown in figure 2-1 *c*, as rolling was not subsequently applied on it.

2.2.2 Welding heat transfer models (without rolling)

All the welding heat transfer models were built with quadratic elements, which have a node at each corner and additional nodes in the middle of each edge. This type of element provided a more accurate temperature prediction. Hexahedral elements were used principally, except for a few wedge elements which were used at the beginning and end of the weld bead in the post-weld and *in situ* rolling models, for geometric reasons. The number of elements, nodes, and Abaqus element types are reported in table 2-2.

Table 2-2 Element and node distribution.

Model Type	Hex elements	Wedge Elements	Analysis type	Nodes	Element Type (Abaqus Code)
Pre-weld rolling	188356	--	Welding heat transfer	898664	Hex. Quad (DC3D20)
			Welding mechanical	236906	Hex Linear (C3D8R)
Post-weld & *in situ* rolling (Longer dimensions)	173890	160	Welding heat transfer	786751	Hex. Quad. (DC3D20) Wedge Quad (DC3D15)
			Welding mechanical	204401	Hex Linear (C3D8R) Wedge Linear (C3D6R)
Post-weld (Smaller dimensions)	163686	--	Welding heat transfer	743600	Hex. Quad. (DC3D20)
			Welding mechanical	193426	Hex Linear (C3D8R)

Figure 2-2 shows the main factors that modify the temperature distribution on the workpiece due to welding. The thermal losses towards the surrounding were modelled by applying free convection and thermal radiation to the free surfaces, except for the lower one. They were modelled with traditional Newton cooling, and Stefan-Boltzmann laws, as shown in eq. 2–1 and eq. 2–2 respectively, using constant parameters.

$$q = hA(T - T_a) \qquad \text{Eq. 2–1}$$

$$q = \sigma\epsilon A((T + 273.15)^4 - (T_a + 273.15)^4) \qquad \text{Eq. 2–2}$$

Where q is the heat transferred per unit time; A is the area; T and T_a are the current and ambient temperatures in °C; h the convective coefficient 10 $W \cdot m^{-2} \cdot °C^{-1}$ [176]; σ the Stefan-Boltzmann constant $5.67 \cdot 10^{-8}$ $J \cdot m^{-2} \cdot s^{-1} \cdot K^{-4}$; and ϵ the emissivity of the workpiece, 0.8 [110].

The backing support was composed of a copper backing-bar underneath the weld, and aluminium vacuum clamps in the far field as shown in figure 2-1 *a*. The thermal losses towards the backing-bar and clamping device were different for each model and will be described separately for each model later in this chapter.

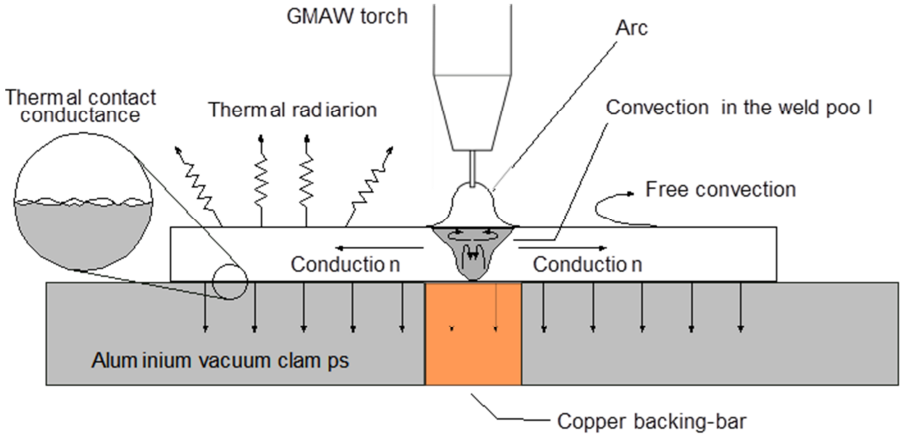

Figure 2-2 Factors which modify the temperature distribution on welding

The welding heat was applied in all the models with a double ellipsoid heat source distribution, as proposed by Goldak *et al.* [119]. The heat is a Gaussian volumetric distribution described by two ellipsoids. Figure 2-3 *a* shows the through thickness heat distribution on half a weldment when the Goldak technique is applied (note 0 mm refers to the upper surface of the weldment – weld bead not considered). The power density shown in figure 2-3 *a* uses the parameters for the post-weld rolling geometry used in the heat transfer analysis shown in table 2-3.

The welding heat distribution, q, is calculated by eq. 2–3.

$$q = \frac{6\sqrt{3}f_f Q}{a_f bc\pi\sqrt{\pi}} e^{-3x^2/a_f^2} e^{-3y^2/b^2} e^{-3z^2/c^2} \qquad if\, x \geq 0$$

$$q = \frac{6\sqrt{3}f_r Q}{a_r bc\pi\sqrt{\pi}} e^{-3x^2/a_r^2} e^{-3y^2/b^2} e^{-3z^2/c^2} \qquad if\, x < 0 \qquad \text{Eq. 2–3}$$

Where Q is the instantaneous power input , a_f, a_r, b, and c are geometrical factors for the ellipsoidal shape; x, y, and z are the coordinates of the geometry, as shown in figure 2-3 *b*; f_f and f_r are the heat input fraction in the front and rear ellipsoid quadrants, which must equal two. Goldak *et al.* [118] explained that the last two are arbitrary factors that depend on the process being modelled. However, in all the models built in this thesis the relation shown in eq. 2–4 was applied.

$$f_f = \frac{2a_f}{a_f + a_r} \qquad \text{Eq. 2–4}$$

This relationship ensures the heat flux with the two parts of eq. 2–3 matches where they meet at x = 0, as Lindgren [129] suggested.

The energy input rate was computed from the welding experiments with eq. 2–5.

$$Q = \eta \frac{\int_0^{t_{Tot}} VIdt}{t_{Tot}} \qquad \text{Eq. 2–5}$$

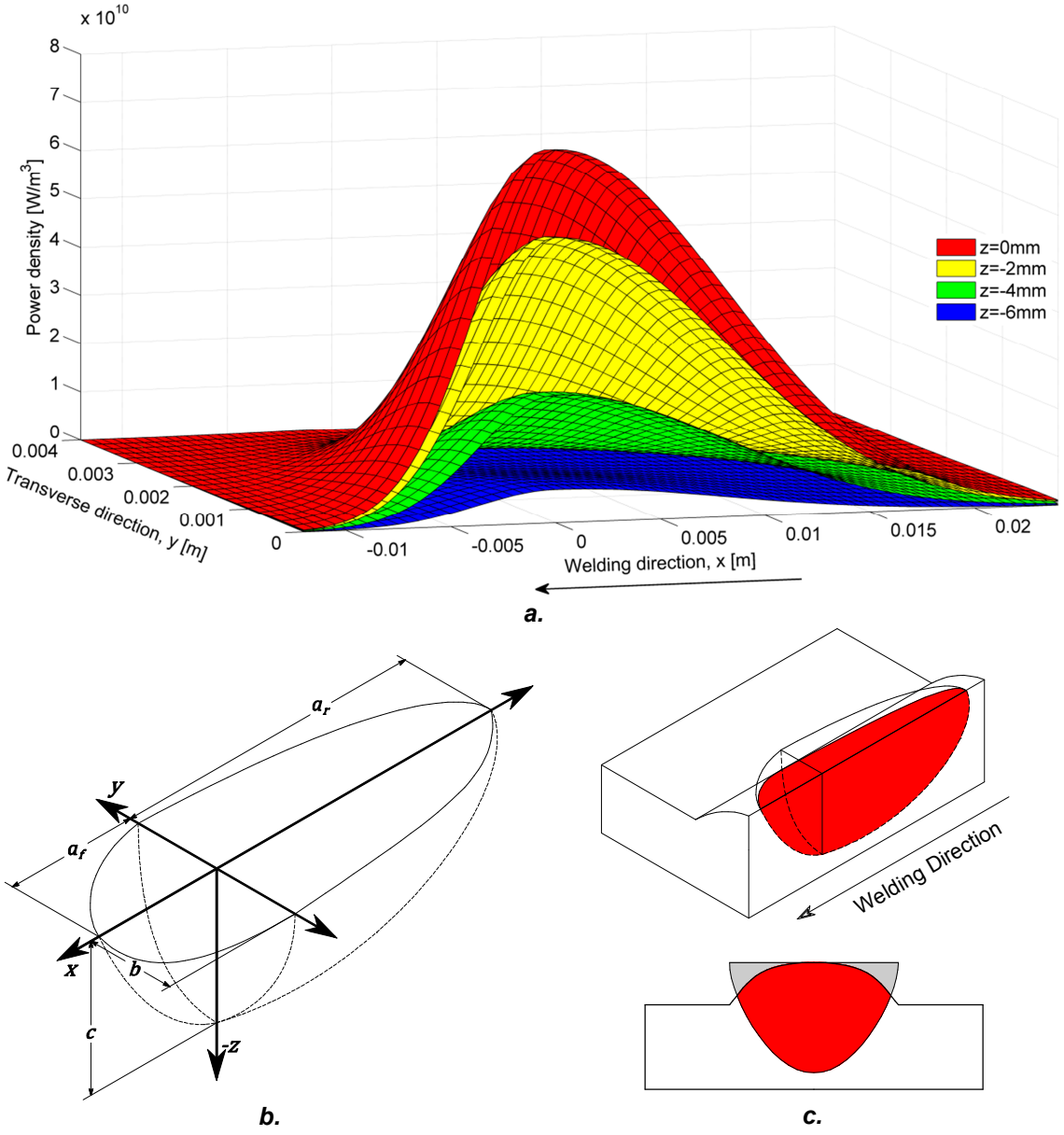

Figure 2-3 ***a.*** **Through thickness heat density distribution of double ellipsoid source (0 mm represents the weldment upper surface).** ***b.*** **Geometrical parameter of the double ellipsoid heat distribution.** ***c.*** **Isometric and transverse views of the heat source which show how it was applied to the weld bead profile.**

The welding current, I, and voltage, V, were obtained experimentally with a AMV 4000 data acquisition system, which measures and records the

instantaneous values during welding. Owing to the variation of these values at the beginning and end of the welds, they were obtained in the middle of the weld where they were relatively steady. Subsequently the instantaneous product of the current and voltage was integrated and divided by the measured time, t_{Tot}, and scaled by an efficiency factor, η, to obtain the welding nominal heat input, Q.

Since the weld bead was entirely present during the welding step, the double ellipsoid heat input was centred on the top of it, as shown in figure 2-3 *c*. Owing to the mismatch between the weld bead and double ellipsoid shapes, not all the heat in the double ellipsoid was actually applied to the weldment. In addition, Lindgren [129] emphasises that even with fine mesh the actual heat in the modelled weldment, Q^*, is less than 90 % of the nominal heat input, Q. The ratio between Q^*, and Q (the former measured by the Abaqus output "RFLE"), was called the "overall model efficiency", ζ, and is reported in table 2-3, as well as the parameters used in the welding heat transfer analyses.

Table 2-3 Heat transfer parameters

		Double ellipsoid parameters						
Model Type	Welding speed [mm·min^{-1}]	a_f [mm]	a_r [mm]	b [mm]	c [mm]	ζ [-]	Q [W]	Q^* [W]
Pre-weld rolling	650	9.0	1.9	4.5	5	0.87	9938	8646
Post-weld & *In situ* rolling	500	9.0	2.0	3.0	6.7	0.96	12096	11612

Figure 2-4 shows the temperature dependent thermal material properties used (supplied by Tata Steel Research Development and Technology, Swinden Technology Centre [177]). The thermal conductivity was artificially increased above the melting point to take into account the stirring present on the weld pool [128]. The latent heat of fusion, 272 kJ·kg^{-1}·K [130], and of vaporisation, 6258 kJ·kg^{-1}·K [130], were included in the analysis between 1500 and 1530°C, and 3090 and 3100, respectively. The solid state transformation latent heat,

7 kJ·kg^{-1}·K [119] (at around 730 °C), was ignored in the analysis since it was significantly smaller than the melting and vaporisation ones.

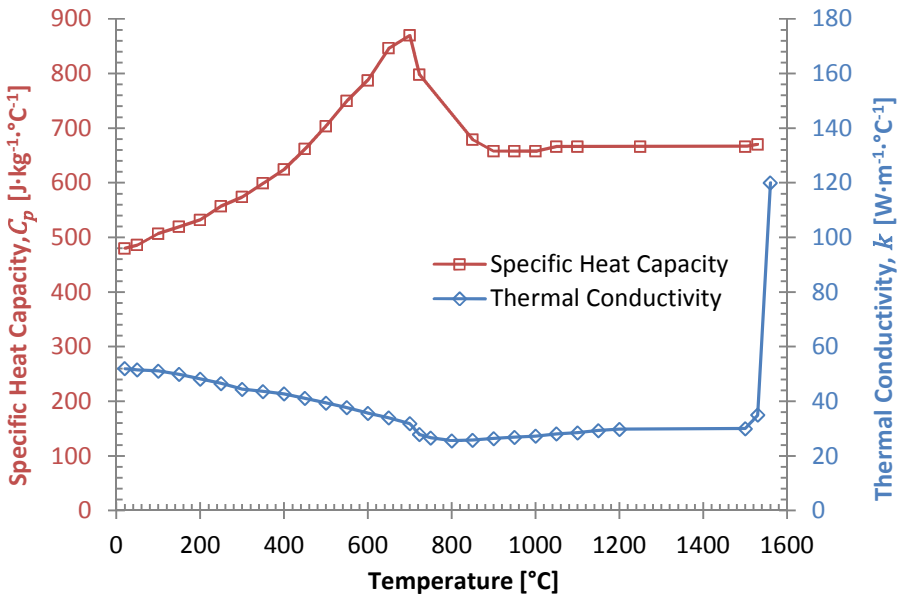

Figure 2-4 Temperature dependent thermal material properties.

After the heat induced by the welding process was finished, an additional 600 seconds cooling step was added to allow the weldment to reach room temperature (about 20 °C). In this step only the cooling mechanisms were active.

Backing-bar boundary condition for Pre-weld rolling geometry

During welding the contact between the workpiece, and backing-bar and vacuum clamps changes because of thermal dilation and distortion; consequently, the thermal contact conductance between them is modified. This phenomenon is difficult to model and it is particularly challenging due to lack of experimental data available. Additionally, modelling conduction between bodies implies longer computational time [174]. To overcome this difficulty, the thermal losses through the lower surface can be modelled by applying forced convective heat sink in that area, as many researchers have already done in the past [99,146,172–174]. In these models, the copper backing-bar and aluminium vacuum clamps were not modelled. Instead, their heat sink effect was taken into

account by adding constant forced convection on the lower surface of the weldment. Two different convective coefficient values, namely, h = 425, and 250 $W \cdot m^{-2} \cdot °C^{-1}$, were applied corresponding to the areas in which the weldment was in contact with the copper backing-bar, and the aluminium vacuum clamps in the experiments, respectively. The copper backing-bar used in these experiments [1] had a rectangular cross section with 20 mm width by 48 mm height; therefore, the forced convective heat sink area due to the copper backing-bar was 10 mm wide under the weld bead (due to the symmetry of the problem), and extended along the entire length of the plate. The forced convective heat sink due to the aluminium vacuum clamps was applied to the rest of the lower surface, as shown in figure 2-1 a, and figure 2-2.

Backing-bar boundary condition for Post-weld rolling geometry

The boundary conditions used for these models were similar to the previous model, except for the backing-bar width, which was 48 mm. The effect of the thermal losses due to the backing-bar, and vacuum clamps was modelled by applying three different convective heat sink rules on the entire lower surface of the weldment, namely, constant, linear, and exponential.

The constant convective heat sink used the same convective coefficients implemented on the pre-weld rolling section (h = 425, and 250 $W \cdot m^{-2} \cdot °C^{-1}$), but applied to the contact area of the backing-bar, and aluminium vacuum clamps used in these models. The linear and exponential functions applied to the lower workpiece surface are shown in figure 2-5, and equations eq. 2–6, and eq. 2–7 respectively*.

$$h(T) = mT + n \qquad \text{Eq. 2–6}$$

$$h(T) = ae^{bT} + c \qquad \text{Eq. 2–7}$$

* The linear and exponential convective heat sink rules were applied by an Abaqus subroutine, “FILM”. This subroutine allows setting the convective coefficient respect to other model parameter such as, temperature, time, or position among others

Where h is the convective heat transfer coefficient, m, and n are the slope and the convective coefficient at 0 °C, respectively, and T is the current temperature at the nodes in the lower surface, in °C. Constants a, b, and c which are used for the exponential curve, determine the horizontal position, the growth rate, and the vertical position of the function, respectively.

Several constant combinations were tested and the best matches were obtained with m = 1.45, and n = 100 for the linear approach, and a = 505.65, b = 158.89 × 10^{-5}, and c = -400 for the exponential one.

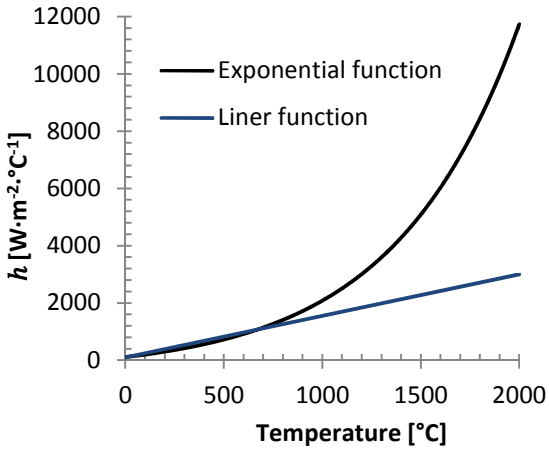

Figure 2-5 Variation of convective heat transfer coefficient against temperature for the linear and exponential functions.

Backing-bar boundary condition for In situ rolling

The backing-bar boundary condition for the *in situ* rolling geometry was very similar to the exponential rule developed for the post-weld rolling analysis. Additionally, the cooling effect generated by the roller was included. In these models two roller trailing distances, namely, 100, and 250 mm were analysed, therefore two different welding heat transfer FE models were built.

The action of the roller will increase heat loss for two reasons: firstly, on the top surface there will be conductive heat loss between the workpiece and the roller; secondly, the load applied by the roller will result in improved heat loss to the backing-bar, as occur in FSW with the welding tool pressure [166–169], hence,

the thermal contact conductance between the workpiece and the backing-bar is increased. Therefore, additional convective heat sink was added on the upper surface in the rolling contact, and in a section on the lower surface, h = 1600 W·m^{-2}·C^{-1}. The later was added to the exponential convective heat sink on the lower surface. These two areas moved with the application of the roller and were activated only during the rolling steps.

The dimensions of the rolling contact on the top surface are shown in figure 2-6, *i.e.* c = 12 mm long in the rolling direction, and extends across of the weld bead width, about 12 mm† (twice of "a" in figure 2-6). The heat sink area on the lower weldment surface was determined by trial and error approach and its dimensions were 2 times the size of the rolling contact length in front of the roller (d = 24 mm), 16 times the rolling contact length behind the roller (e = 192 mm), by 24 mm (twice b) in the transverse direction, as shown in figure 2-6.

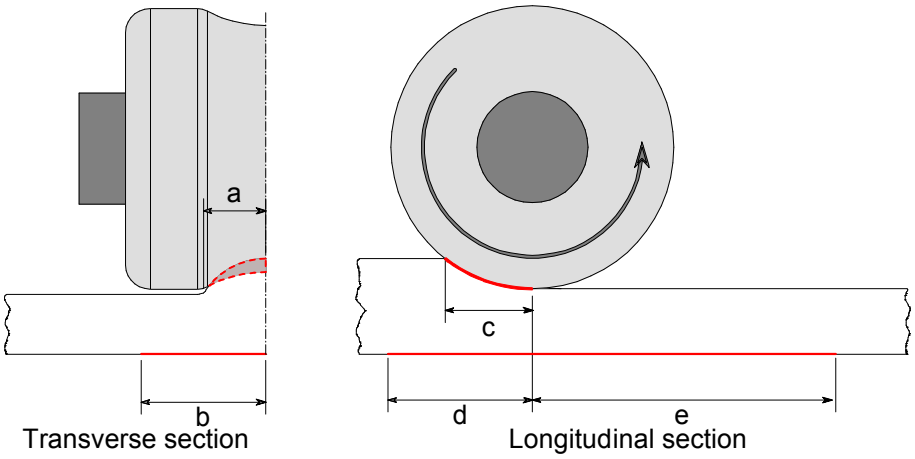

Figure 2-6 **Forced convective heat sink areas to simulate thermal losses due to *in situ* rolling. Where: a = 6, b = 12, c = 12, d = 24, and e = 192. All the dimensions are in millimetres.**

† The total rolling contact width in the top surface is about 12 mm. Since only half geometry has been modelled, the rolling contact width was half too, therefore 6 mm.

2.2.3 Welding mechanical models (without rolling)

In these models, the transient and RS due to welding were investigated. Linear elements with reduced integration were used in these models since they performed faster than the quadratic ones [140]. The mesh used was sufficiently fine to obtain a mesh independent result. The number of nodes and elements, and Abaqus element type are shown in table 2-2.

Temperature dependent material properties for mild steel S355 were used in all models; they were supplied by Tata Steel Research Development and Technology, Swinden Technology Centre [177]. A thorough description of the material used can be found in appendix a. Additionally, an extra model with mechanical material properties from the literature [132] was run for comparison.

Figure 2-7 shows the mechanical material properties implemented in the models. Isotropic elastic-plastic mechanical properties were assumed. The linear thermal expansion coefficient used in the analyses, shown in figure 2-7 *a*, represents the average value of different cooling rates from 429 to 0.4 $°C \cdot s^{-1}$, which represent average welding conditions.

The steel composition and cooling rate determine the presence of the metastable phase, martensite, in the welded metal, and heat affected zone. Martensite has larger volume than the stable phases (ferrite and cementite) [55]; Deng [59] has shown that when martensite is present in the weld and heat affected zones it induce transformation plasticity, and reduce the RS in those zones due to their volumetric expansion. Conversely, he showed also that for steels with low carbon equivalent, such as S355, this effect is negligible, since the amount of the metastable phases at room temperature is low. Therefore, the volumetric fractions of the different phases present during and after welding were ignored. However, the temperature dependent mechanical properties used in the analysis were the result of experimental tests conducted at welding temperature and experimental cooling rates; therefore, the effect of the volumetric fraction of austenite and ferrite was indirectly considered in the simulation.

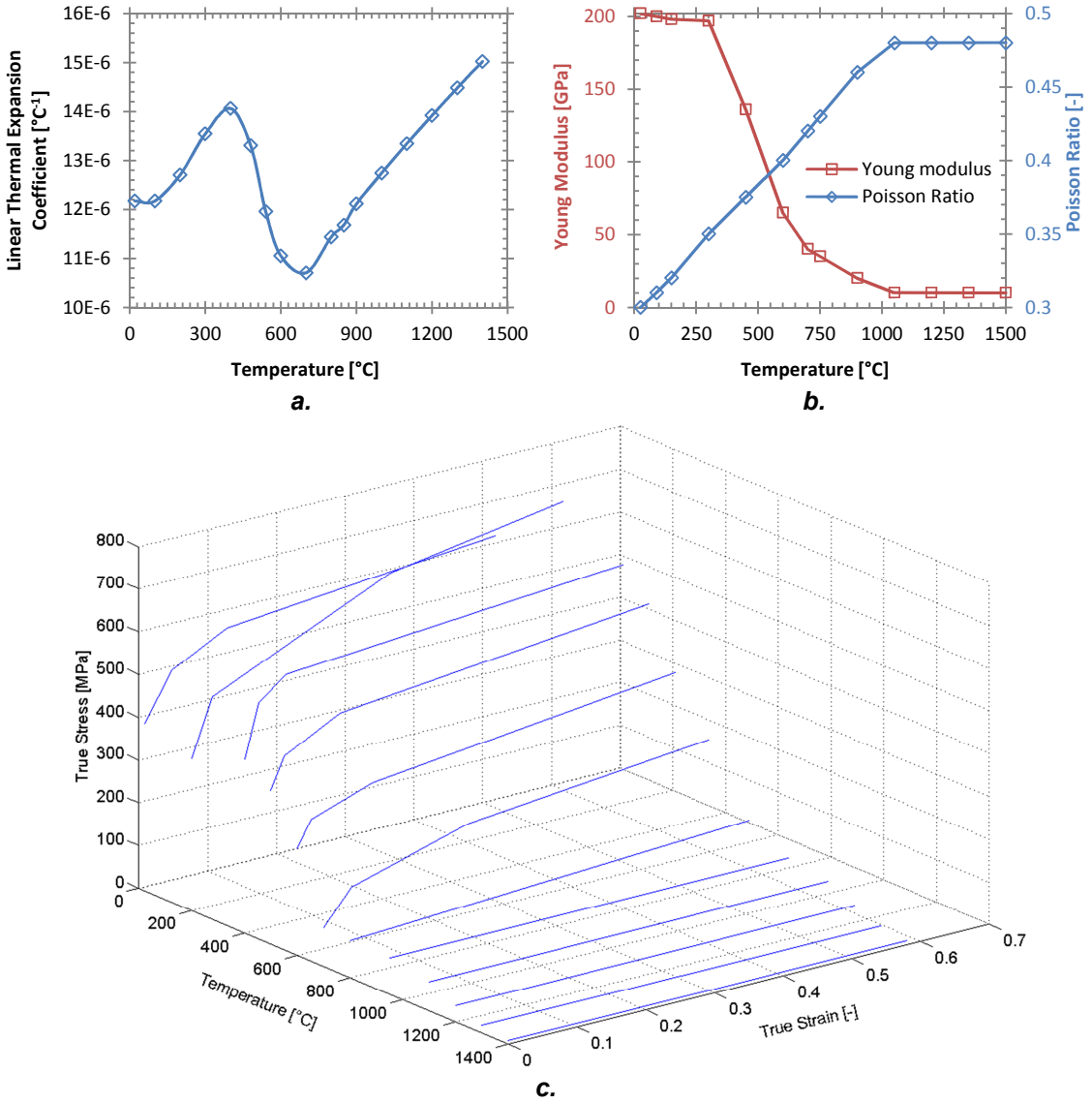

Figure 2-7 **Mechanical properties of S355. *a*. Linear thermal expansion coefficient. *b* Young modulus and Poisson ratio. *c.* True stress—true strain curves [177].**

Leblond *et al.* [178,179] explained that when the material undergoes phase transformation the rearrangement of the dislocations causes partial or total loss of the accumulated strain hardening. In Abaqus the annealing procedure simulates the relaxation of the plastic strain history when a certain temperature is exceeded. Beyond this temperature perfect elastic plastic behaviour was implemented by Abaqus, *i.e.* there was no work hardening above it. Therefore, this procedure is used to model either annealing or fusion of the material [140]. In the mechanical models of this thesis the annealing procedure was

implemented to simulate annealing, and was applied at 950 °C; over that temperature the material exceeds the A_{C3} curve by more than 50 °C, and it was considered perfectly plastic. Appendix A explains with more details the selection of the annealing temperature.

To generate the stress due to welding, the nodal temperature history obtained from the welding heat transfer analysis, described in the previous section, was imported into the welding mechanical model. This caused the expansion of the material and plastic deformation where the yielding criterion was exceeded.

Since only half the geometry was modelled, a symmetric boundary condition was applied to the symmetry plane (see figure 2-1 *b*). This restrained the displacement in the transverse direction, and rotation in the longitudinal and normal directions. Displacement in the longitudinal and normal directions, and the rotation in the transverse direction were allowed. To simulate the vacuum clamping system the displacement in the out-of-plane direction of all the nodes on the lower surface was restrained. To avoid the displacement in the longitudinal direction, all the nodes on the end plane (see figure 2-1 *a*) of the weldment were restrained.

After welding and cooling to room temperature, an extra step was added to simulate unclamping. In this step, one node in the middle length of the symmetry plane was fully restrained in all degrees of freedom (encastré). At the same time all the other mechanical constraints were released, except for the ones on the symmetry plane, allowing the workpiece to deform, when some of the RS were relaxed.

To compare the effect of temperature distribution on the residual stress prediction, three models were built using the three different backing-bar methods, namely, constant, linear, and exponential, and the post-weld rolling geometry. In addition, two different set of mechanical properties for the S355 were used to compare the effect of them on the residual stress prediction.

2.2.4 Buckling Model

Buckling distortion is an elastic failure caused by in-plane compressive load. When a critical load is exceeded the member suddenly collapses losing stiffness. This critical load can be mechanical, thermal or magnetic, and is called critical buckling load (**CBL**). Timoshenko and Gere [180] showed an analytical solution for thin plates compressively loaded by external forces in the plate edges, with some simple boundary conditions to determine the CBL. This method has been modified and used by many researchers [10,35,40,45,181,182] to evaluate analytically the critical buckling load on weldments. However, this approach may not be able to take into account the characteristic longitudinal welding RS distribution. Michaleris and DeBiccari [128] on the other hand, applied a negative thermal load to the material around the weld zone to simulate the tensile stress generated by the welding process. This allowed the critical buckling temperature load to be determined, and from that the CBL was obtained by eq. 2–8.

$$CBL = \frac{\alpha \lambda \Delta T E}{A} \qquad \text{Eq. 2–8}$$

Where α is the linear coefficient of thermal expansion; λ is the eigenvalue obtained by the buckling analysis; ΔT is the unitary temperature load; E, the young modulus; and A, the area in which the thermal load is applied. This approach brings to a more realistic stress distribution in the weldment; therefore, this technique was used to determine the CBL for the models in this thesis.

The eigenvalue buckling analysis performed with Abaqus is a linear perturbation step, which is calculated relative to previous state of the workpiece, and uses temperature independent material properties. This analysis consists in looking for the loads that cause the stiffness matrix to become singular. This is done by defining an incremental load F, which defines the new stiffness matrix K_F, as shown in eq. 2-9. The magnitude of the load is not important because it has to be scaled by the i-th eigenvalue found in the analysis, λ_i. δ_i is the related

buckling displacement shape for the i-th mode. The magnitude of the displacement does not represent the real magnitude of the deformation, because it is a normalised magnitude. However, it shows the shape of the associated buckling mode.

$$|K + \lambda_i K_F|\delta_i = 0 \qquad \text{Eq. 2-9}$$

This analysis was run separately from the welding mechanical analysis assuming that the weld bead was present, and the workpiece material was unstressed. The geometries, mesh densities, and element type implemented were the same as the ones used in the welding mechanical models. Also, the boundary conditions were similar to those used in the unclamping step of those models. Buckling analyses were performed only for the pre-weld, and post-weld rolling analyses. For the *in situ* rolling no buckling analysis was executed because it was assumed to be the same as the post-weld rolling one.

Figure 2-8 *a* shows a typical longitudinal RS distribution after welding across half weldment width, and figure 2-8 *b* shows only the tensile portion of the previous RS distribution. Due to the variation of the longitudinal RS across the width, an equivalent uniform RS distribution was calculated to facilitate and simplify the buckling analysis. The region in which the temperature load was applied in the workpiece was determined by measuring the area below the longitudinal tensile RS portion after unclamping it (grey region in figure 2-8 *b*), and calculating an equivalent width of a rectangular distribution. The height of the former distribution was equal to the average height of the peak of the tensile RS curve (red line in figure 2-8 *b*). The widths of the equivalent tensile region were 18 and 20 mm for the pre-weld and post-weld models respectively.

The eigenvalue λ in the model was obtained by applying a unitary temperature load on the equivalent tensile region along the weld bead length, as shown in figure 2-8 *c* and *d*. The magnitude of the applied temperature load is not important; it is scaled by the eigenvalue found. To compute the CBL, eq. 2–8 is

used with constant linear thermal expansion coefficient, $1.21726 \cdot 10^{-5}$ °C^{-1} and Young modulus, 202 GPa, both of them being at room temperature.

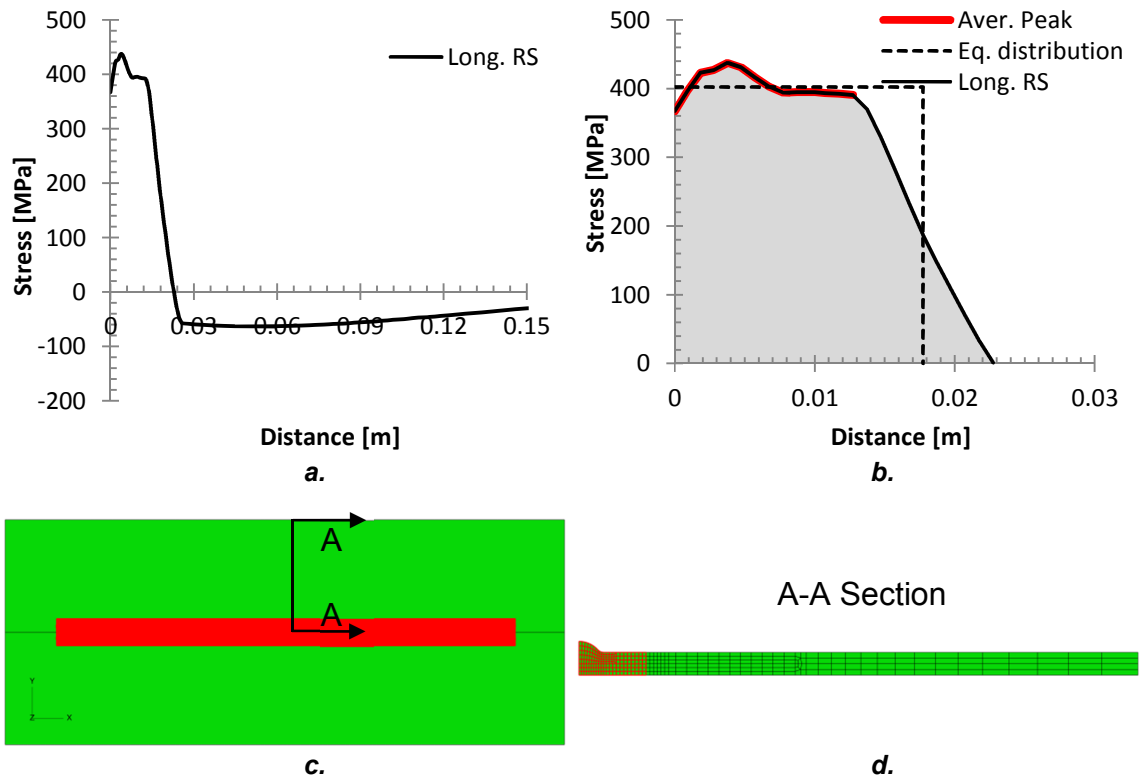

Figure 2-8 ***a.*** **Typical longitudinal RS distribution across half width on the middle thickness of a weldment.** ***b.*** **Tensile portion of the RS of the previous graph to determine the equivalent tensile area.** ***c.*** **Region in which the temperature load was applied in the weldment.** ***d.*** **Transverse section of half of the workpiece showing the applied thermal load.**

The CBL thus calculated needs to be compared with the applied weld load (**AWL**) to determine whether buckling distortion will occur. The AWL is defined as the product of the tensile RS by the area over which it acts [15,42,128]. When the AWL exceeds the CBL, buckling distortion could happen. In FEA this task can be performed by multiplying the tensile RS of each element by its transverse face area, as shown in figure 2-9. The AWL has the advantage that it can be used to compare several rolling parameters in just one chart in an easy and understandable manner.

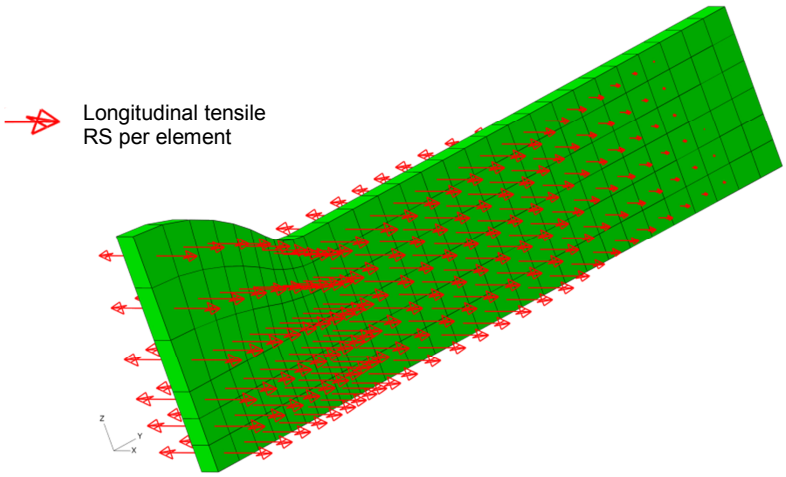

Figure 2-9 Longitudinal tensile RS on the elements of the workpiece transverse section.

2.3 Results and Discussion

2.3.1 Welding heat transfer models

Pre-weld rolling geometry

A contour plot with the temperature distribution after 25 s from the beginning of the weld is shown in figure 2-10. The material was assumed to be molten after 1500 °C, which is represented by the grey region in the figure. As the heat source moves, the heat dissipates across the parent material by conduction, and towards the surroundings by convection and thermal radiation.

Figure 2-11 *a* shows the position of the thermocouples on the welded plates used in the pre-weld rolling experiments conducted by Coules *et al.* [1]. A comparison between the temperature distribution of the welding heat transfer model of the pre-weld rolling geometry analysis and the experimental results is shown in figure 2-11 *b*. Figure 2-11 *c* and *d* show a comparison between the experimental and predicted peak temperatures, and cooling rates from the peak to half height peak temperature, at the thermocouple positions, respectively.

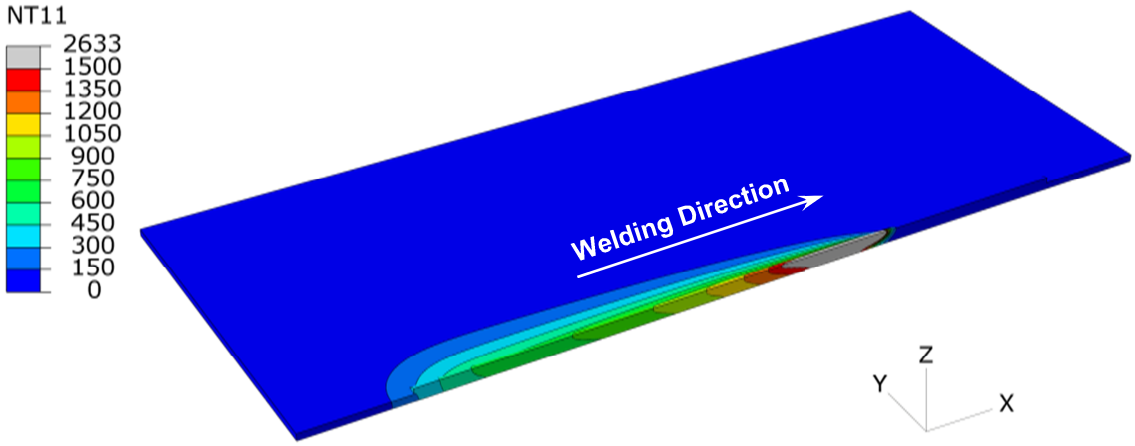

Figure 2-10 Contour plot of the temperature distribution during welding the pre-weld rolling workpiece (with no rolling, and temperatures in °C).

The model overestimates the peak temperature at 10 and 30 mm by 35 and 31 °C respectively, while far away from the welding line, at 70 mm, the match is more accurate, having only 2 °C difference in the peak temperature. The cooling rate was slightly underestimated by the model at 10 mm from the welding line, and marginally overestimated at 30 mm, whereas at the far field it was virtually identical.

Although the results suggested that the heat sink applied in the models in the backing-bar region, as constant convective cooling, underestimates the actual heat removal of the actual backing-bar, and the convective cooling on the vacuum clamp zone predicts the result more accurately, these were the best matches obtained after several attempts with different constant convective coefficients combinations. Moreover, increasing the convective coefficient in the backing-bar yields a reduction of the temperatures in the whole plate, including the far field (70 mm).

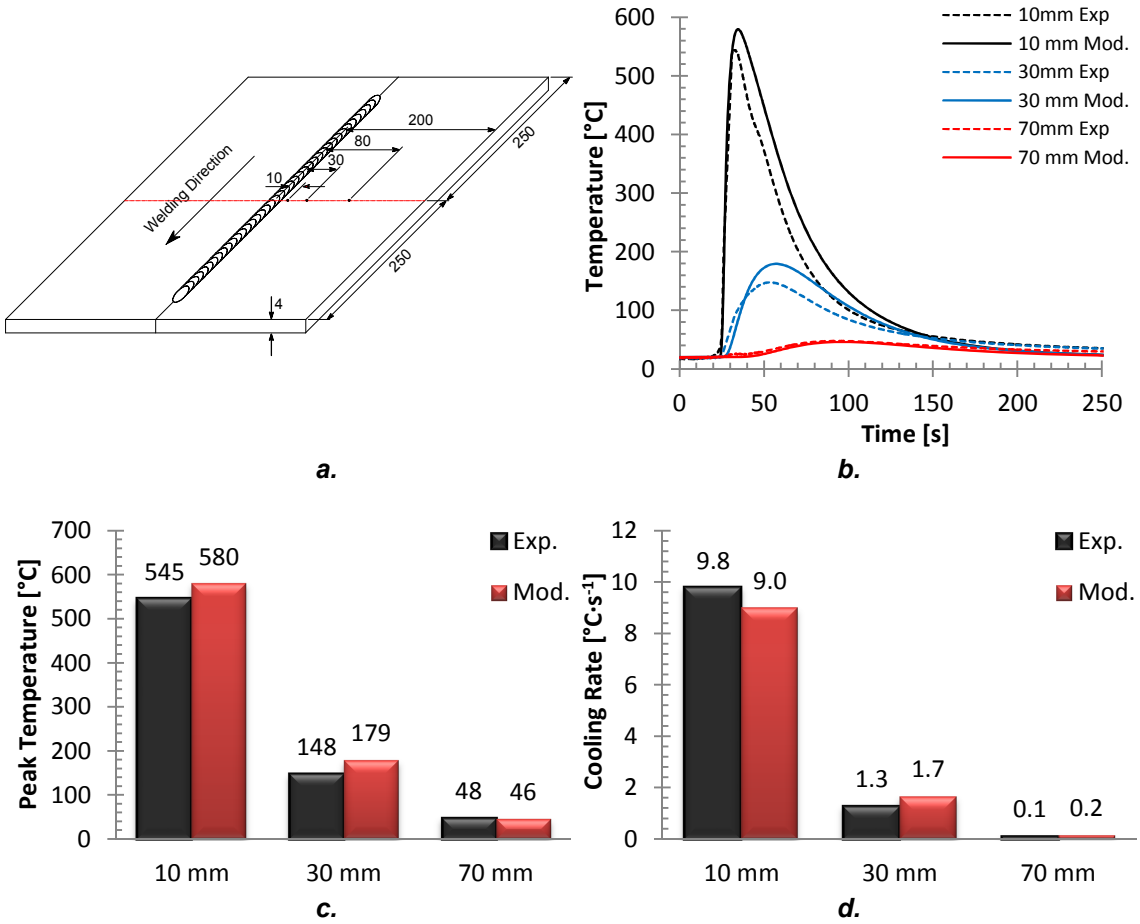

Figure 2-11 ***a.*** **Thermocouples position on the workpiece (all the dimensions in mm). Comparison between the experimental and modelling:** ***b.*** **temperature distribution;** ***c.*** **peak temperature; and** ***d.*** **cooling rates.**

Post-weld rolling geometry

The contour plots of the temperature distribution with different cooling conditions, on the lower surface, namely, constant, linear, and exponential convective coefficient variation, after 60 s from the beginning of the weld, are shown in figure 2-12 *a* to *c*, respectively. As for the pre-weld rolling models the metal was considered melted above 1500 °C, so that the grey region in the figure represents the weld pool. The peak in the molten metal reaches temperatures around 3090 °C in all cases studied, which corresponds to the beginning of the steel vaporisation. Note, however, that these models do not include the internal weld pool convection. Instead, the thermal conductivity was artificially increased above the melting point. With the scale used in these plots

there is little difference in the size of the molten region, although some differences in the far field temperature profile are observed.

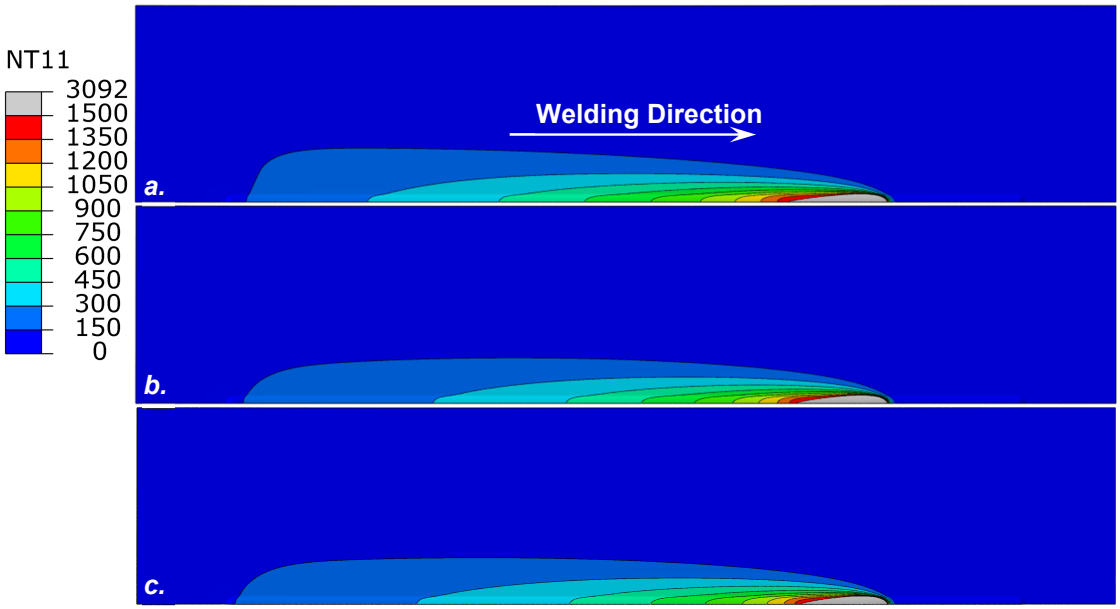

Figure 2-12 Temperature contour plot after 60 s from the beginning of the weld using different cooling convective coefficient rules in the lower surface, namely: *a.* constant; *b.* linear; and *c.* exponential.

Christensen *et al*. [183] measured experimentally the temperature profile in the fusion line in GMA welded mild steel plates. They reported that the temperature right under the arc fluctuates rapidly and erratically; however, they recorded temperature above 3000 °C, which is in agreement with the peak values predicted in these models.

The position of the thermocouples in the experiments conducted by Coules *et al*. [2] is shown in figure 2-13 *a*. Comparisons between the experimental and predicted temperature distribution of the welding heat transfer analysis of the post-weld models using the constant, linear, and exponential convective cooling coefficients are shown in figure 2-13 *b* to *d*, respectively.

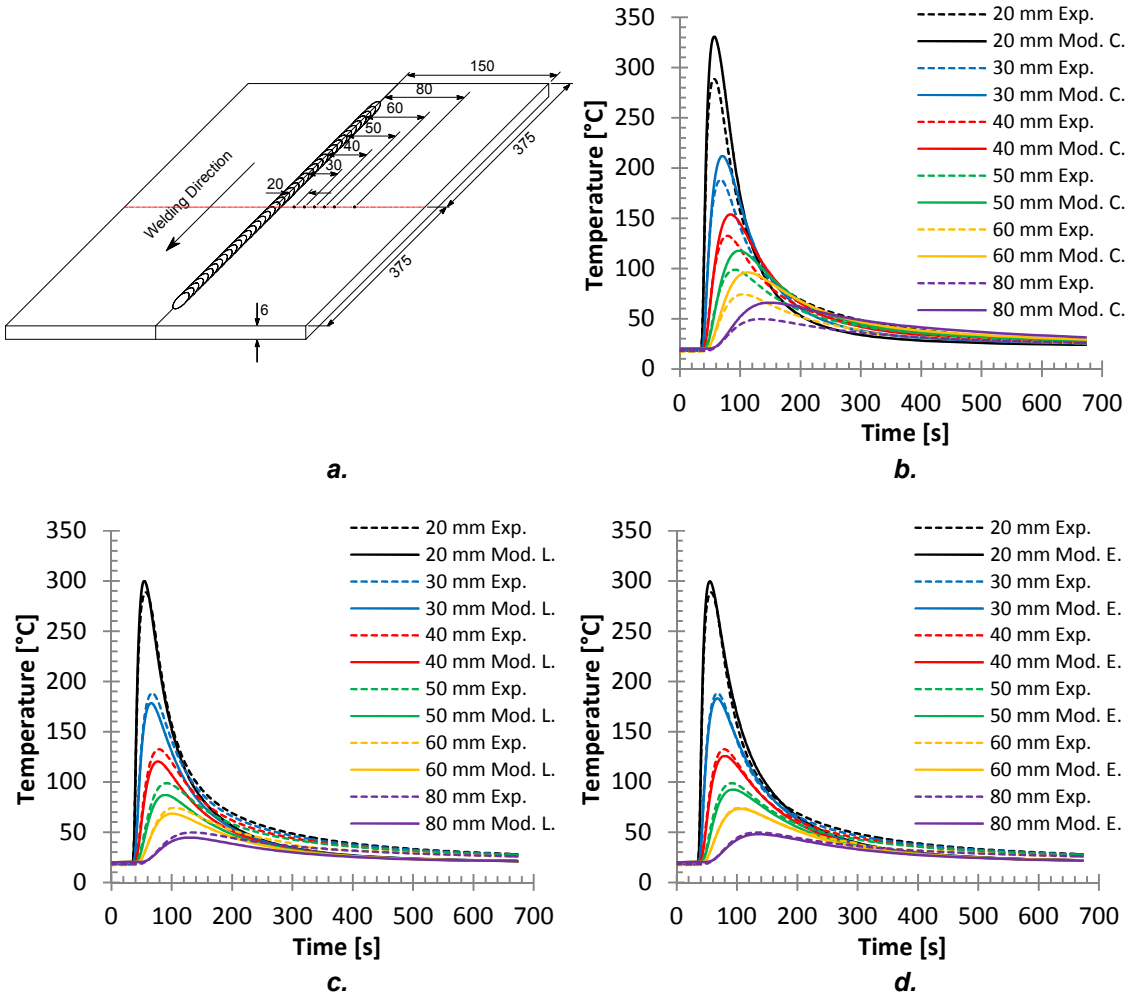

Figure 2-13 ***a.*** **Position of the thermocouples on post-weld rolling experiments [2] (dimensions in millimetres). Comparison between experiments (Exp.) and modelling results when the backing support (copper backing-bar and aluminium vacuum clamps) was model as: *b.* constant values (C.); *c.* linear function (L.); and *d.* exponential function (E.).**

Comparison of the peak temperature and cooling rates, from the peak to half height peak temperature, at the thermocouple position between experimental and predicted results are shown in figure 2-14 *a* and *b*, respectively.

When a constant convective heat transfer coefficient is used to model the backing support (figure 2-13 *b*), the model overestimates the peak temperature in all the positions recorded, and all the predicted cooling rates were higher than the experimental ones. Even though these convective values were suitable for the welding heat transfer analysis of the pre-weld rolling geometry, they did not provide a good prediction for the post-weld rolling geometry for various reasons,

including the unrealistic nature of the boundary condition, different backing-bar widths, and different plate thickness.

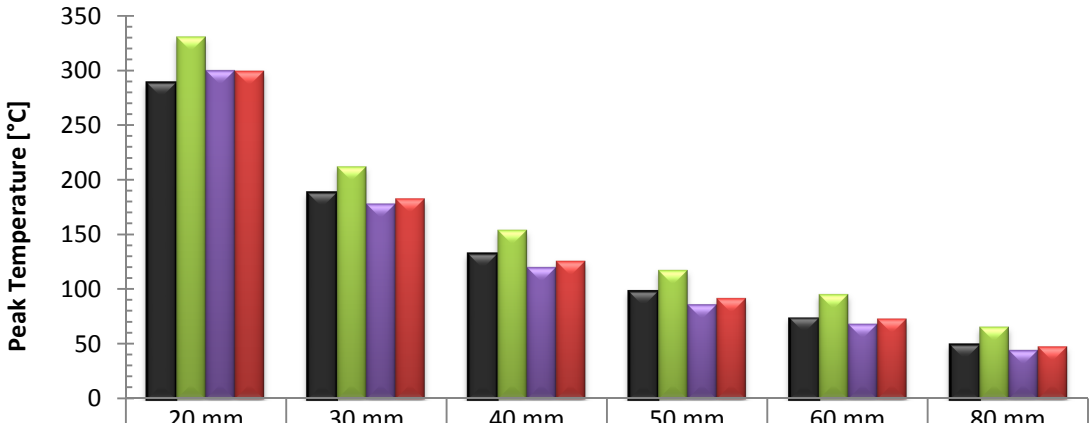

	20 mm	30 mm	40 mm	50 mm	60 mm	80 mm
Exp.	289	188	132	99	74	50
Mod. C.	331	212	154	118	96	66
Mod. L.	300	178	120	87	68	45
Mod. E.	300	183	126	92	73	48

a.

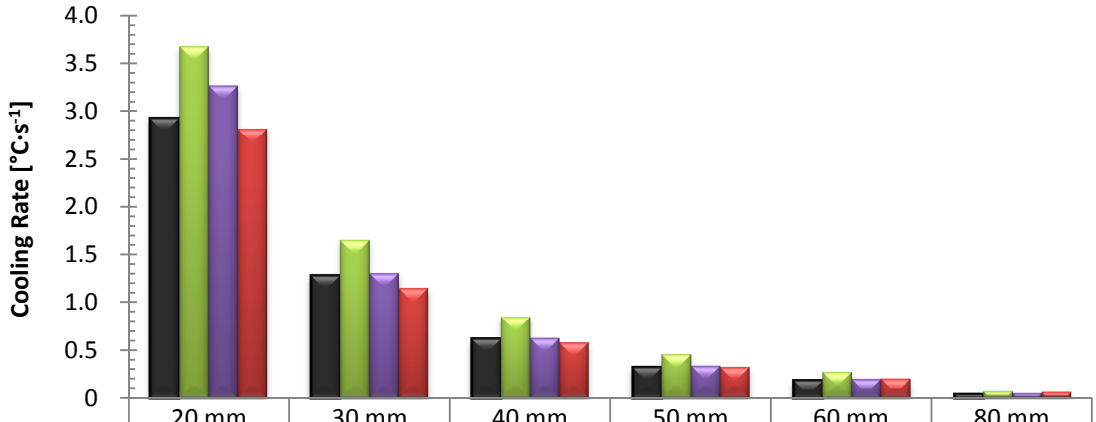

	20 mm	30 mm	40 mm	50 mm	60 mm	80 mm
Exp.	2.9	1.3	0.6	0.3	0.2	0.0
Mod. C.	3.7	1.6	0.8	0.5	0.3	0.1
Mod. L.	3.3	1.3	0.6	0.3	0.2	0.1
Mod. E.	2.8	1.2	0.6	0.3	0.2	0.1

b.

Figure 2-14 **Comparison between experimental (Exp.) and modelled (Mod.): *a.* peak temperatures, and *b.* cooling rates, using different cooling condition on the lower surface such as: constant (C.); linear (L.); and exponential (E.) convective cooling coefficients.**

The models with the linear and exponential variation of the convective cooling coefficient in the lower surface provide a better temperature prediction than the model with constant coefficients. However, the results obtained with the exponential function fit the experimental result slightly more accurately.

The method of using a convective heat transfer coefficient to model the heat loss, caused by the backing-bar, from underneath the weldment is not physically realistic; however, it is more numerically efficient. This is because there is no need to computationally include the backing-bar in the model.

During welding the thermal losses to the backing support are influenced by many factors [173]. For instance, around the weld pool region the material expansion and fluid properties of the molten metal increase the thermal contact conductance between the backing-bar and workpiece, while behind this region the thermal contraction caused by cooling of the workpiece decreases the thermal contact conductance again. Additionally, the uneven pressure performed by the vacuum clamps (larger pressure in the aluminium clamps, and lower pressure in the copper backing-bar), and differences in thermal conduction of the aluminium vacuum clamps and the copper backing-bar complicate further the problem.

Shi *et al*. [167], and more recently Wang *et al.* [170] have shown the relationship between the thermal contact conductance and temperature in fiction stir welding. Shi *et al.* claimed that due to low strength at high temperatures of the aluminium alloy, it conforms better the backing-bar, having higher thermal contact conductance at high temperatures, while Wang *et al.* showed that good agreement between experimental and predicted temperature can be obtained modelling the thermal contact conductance as an exponential function of temperature. In addition, Zhu *et al.* [184] measured experimentally the thermal contact conductance variation between copper and tool steel during solid plastic forming. They showed that the thermal contact conductance at low temperature and pressure was low, and it was high at high temperature and pressure, with an exponential relationship.

In MIG welding of steel plates, the high pressure applied by the welding tool in FSW is not present; nevertheless, the vacuum clamps apply a constant pressure to the workpiece (in the region the vacuum is produced). Additionally, during welding, and due to the uneven heating, the hot metal dilates locally, increasing the thermal contact conductance locally, as for the FSW. Therefore, the thermal loss due to the backing-bar is larger when the temperature is high and vice versa. This phenomenon can be efficiently modelled assuming convection in the lower surface of the weldment; however, it is not physically realistic. The linear and exponential convective cooling coefficient functions allow such variations to be considered, but not the constant convective cooling coefficients. Nevertheless, the high heat exchange from the molten metal to the bucking-bar is better simulated with high convective cooling coefficients such as the ones provided by the exponential function.

In situ rolling

A comparison of temperature distribution, peak temperature, and cooling rate between the post-weld and *in situ* rolling (100 mm trailing distance) experiments carried out by Coules *et al.* [2], is shown if figure 2-15 *a* to *c*, respectively. The position of the thermocouples in the *in situ* rolling experiments was the same as the post-weld rolling analysis shown in figure 2-13 *a*.

The difference in peak temperature at 20 mm from the centreline is not very significant; however, the peak temperature is reached 5 s earlier in the *in situ* experiment. The other thermocouple locations have more prominent peak temperature differences. The cooling rate, conversely, has the opposite behaviour, having the more significant difference closer to the centreline. This difference is gradually dissipated across the workpiece width. Additionally, during heating all the temperature readings of the post-weld rolling experiments virtually overlapped the *in situ* ones, until the peak temperature of the latter was reached, as shown in figure 2-15 *a*.

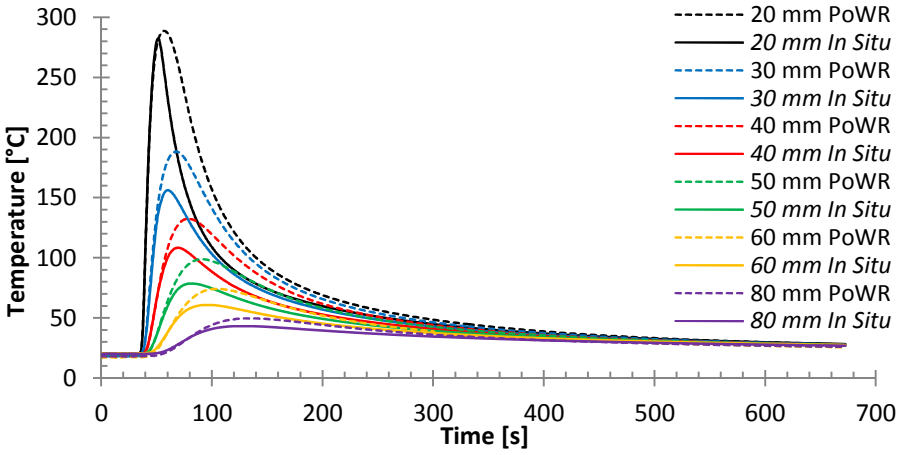

a.

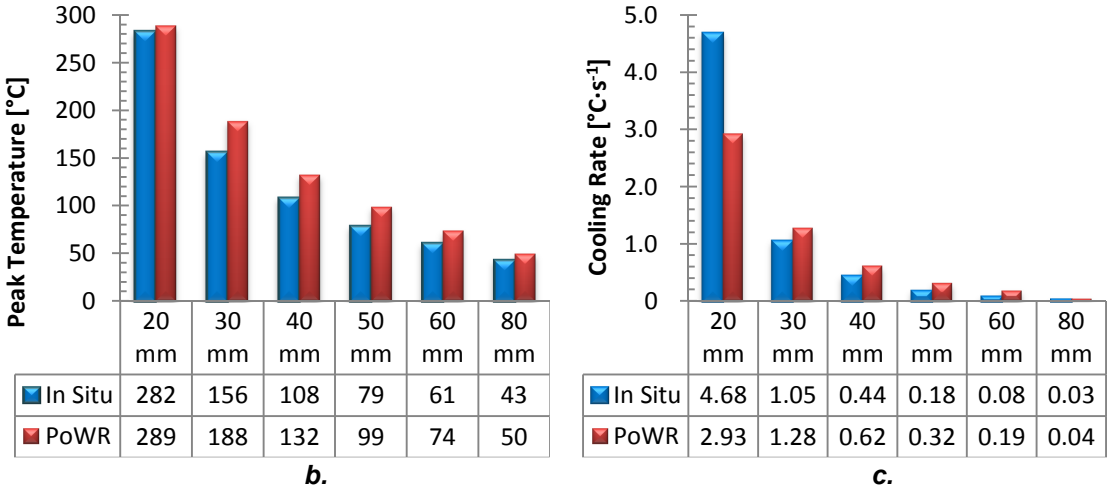

	20 mm	30 mm	40 mm	50 mm	60 mm	80 mm
In Situ	282	156	108	79	61	43
PoWR	289	188	132	99	74	50

b.

	20 mm	30 mm	40 mm	50 mm	60 mm	80 mm
In Situ	4.68	1.05	0.44	0.18	0.08	0.03
PoWR	2.93	1.28	0.62	0.32	0.19	0.04

c.

Figure 2-15 Comparison between experimental measurements from post-weld (PoWR), and *in situ* rolling, in terms of: *a.* temperature distribution; *.b.* peak temperature; and *c.* cooling rate.

The higher cooling rate at 20 mm from the centreline, the almost identical peak temperature, and the virtually identical heating rate until the peak temperature in the *in situ* rolling experiment compared to the post-weld rolling experiments, show that the increase of the thermal contact conductance occurred at certain distance between the welding torch and the roller. However, the experimental measurements do not suggest any information regarding the actual area of the augmented thermal contact conductance in the lower surface of the weldment.

The area where the high convective heat transfer was applied was much greater that the area of contact with the roller. This was done because of two reasons. First, the exponential cooling coefficient could not match the

temperature profile, even when higher convective heat transfer sink were used. In particular, it was not possible to match the peak temperature and cooling rate for the thermocouple at 20 mm from the weld centreline. Secondly, physically when a load is applied at a point, the pressure is redistributed after a certain distance from that point due to the Saint-Venant principal, as explained in Hearn [185]. In the *in situ* rolling models the pressure applied for the roller is redistributed in the weldment lower surface, as shows in figure 2-16; consequently the thermal contact conductance in this region was improved.

Nevertheless, as the material at high temperature has relative low stiffness, its behaviour under the roller is mainly plastic; the addition of frictional interaction between the weldment and the backing-bar makes the determination of the increased thermal contact conductance area complicated, and out of the scope of this thesis. However, the action of the roller in the *in situ* rolling model can be directly compared with the action of the welding tool in FSW, as already discussed in the previous section [166,167,169–171]. Even after the roller has passed, good thermal contact conductance between the backing-bar and workpiece is maintained. This is because the material has been deformed and the asperities between the two surfaces flattened. Hence, good thermal contact is likely to be maintained even after the roller has passed.

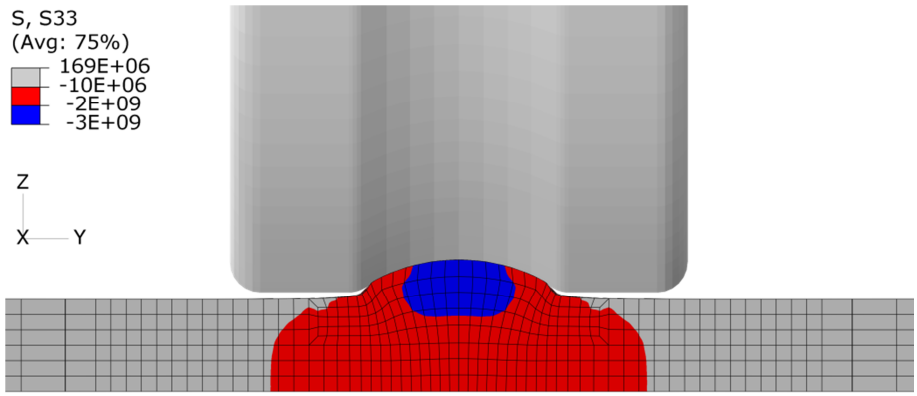

Figure 2-16 Diffusion of the normal stress, from the rolling contact on the weld bead to the lower surface of the workpiece, during rolling with 150 kN vertical load.

The predicted temperature distribution in the *in situ* models with 100 and 250 mm roller trailing distances are shown in figure 2-17 *a* and *b*, respectively;

figure 2-17 *c* shows a comparison of the predicted temperatures between the two trailing distances. Only the 100 mm trailing distance was investigated experimentally. Therefore, no experimental temperature distribution is compared with the 250 mm rolling trailing distance; instead, the data is compared against the predicted post-weld rolling results with the exponential convective cooling function.

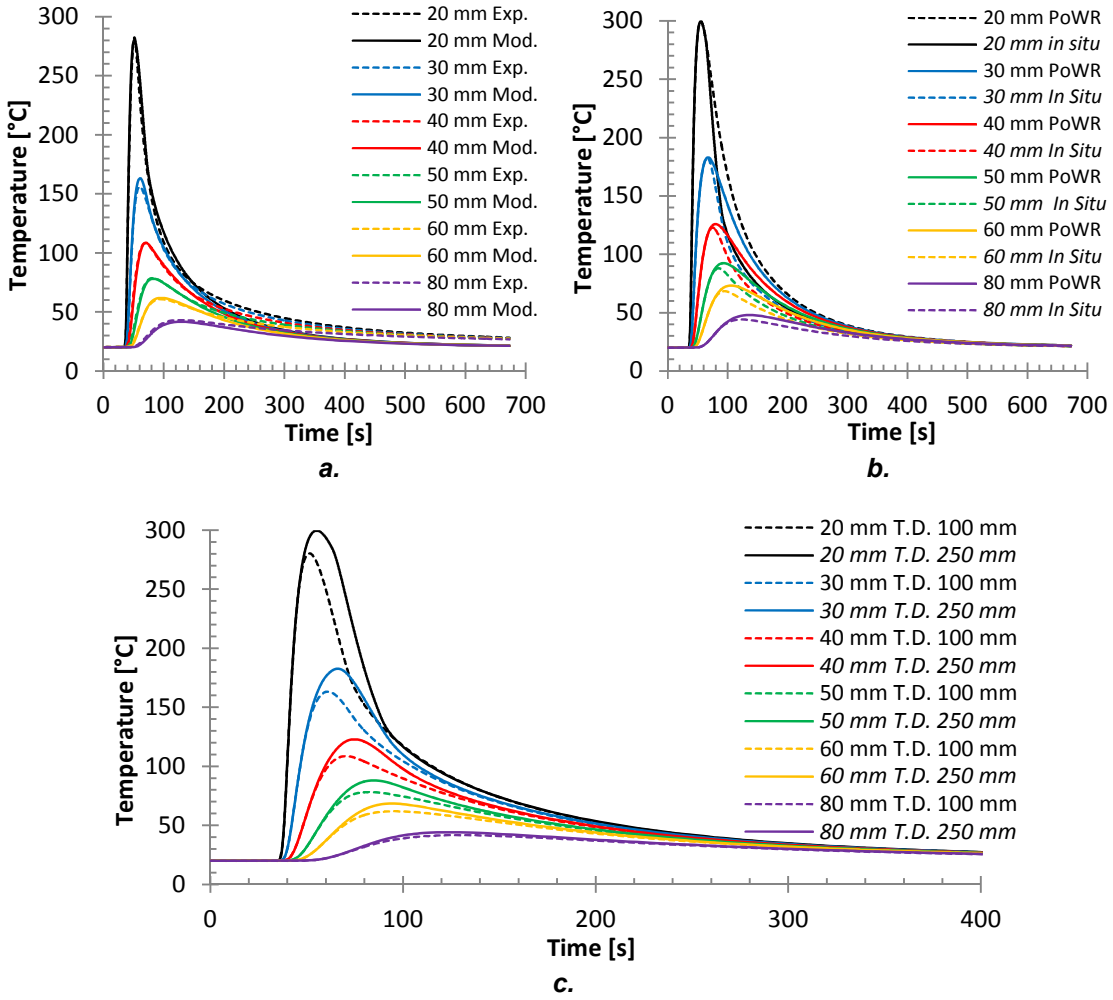

Figure 2-17 Temperature distribution in the *in situ* analysis with a rolling trailing distance of: *a.* 100 mm and a comparison with experimental results; *b.* 250 mm and comparison with predicted post-weld rolling results with exponential cooling function. *c.* Comparison between predicted results with 100 and 250 mm tailing distance.

The predicted temperature distribution with the *in situ* model with 100 mm rolling trailing distance showed a very accurate match in the first 200 s. In the

remaining time the model predicted slightly faster cooling rates; however, due to the low temperatures reached at that time, these small discrepancies are considered not relevant to the subsequent stress prediction.

The predicted temperature distribution in the 250 mm rolling trailing distance showed peak temperatures more similar to the ones observed in the post-weld rolling analysis (see figure 2-17 *b*). In this case the increased thermal contact conductance area is placed farther from the welding heat source, below the rolling contact. Although the temperatures at that region are lower than the previous case, the dimensions of the increased thermal contact conductance were considered the same as the previous case. The effect of the additional heat sink affects the temperature profile later than in the 100 mm trailing distance model, giving virtually the same peak temperature at the 20 to 40 mm positions of the PoWR model. In the far field the temperature peaks are reduced slightly.

The difference in the predicted temperature distribution between the two *in situ* models with the two different trailing distances was observed primarily within 60 mm of the weld bead. The shorter rolling trailing distance showed larger heat sink effect, having smaller temperature peaks. After about 120 s the temperature profile in all the positions analysed was virtually the same. In the far field, after 80 mm the differences can be considered negligible.

The real mechanism of heat sinking in the *in situ* rolling analysis is not fully understood; however, with the approach used in this analysis a fairly accurate temperature distribution was obtained. The advantage of this method is the simplicity and time saving in the model construction compared with more realistic models that include the backing-bar and roller, and the thermal contact conductance with the workpiece material.

2.3.2 Welding mechanical models

Pre-weld rolling geometry – Effect of releasing clamping

The contour plot of the longitudinal RS in half the workpiece is shown in figure 2-18 *a.* The tensile RS are distributed along the weld bead and surroundings,

while the rest of the workpiece is in compression. Figure 2-18 *b* and *c* show the contour plots of the longitudinal RS in half of the transverse section of the workpiece, in the weld bead and surrounding material, before and after unclamping, respectively. Figure 2-18 *d* shows the transverse RS after unclamping.

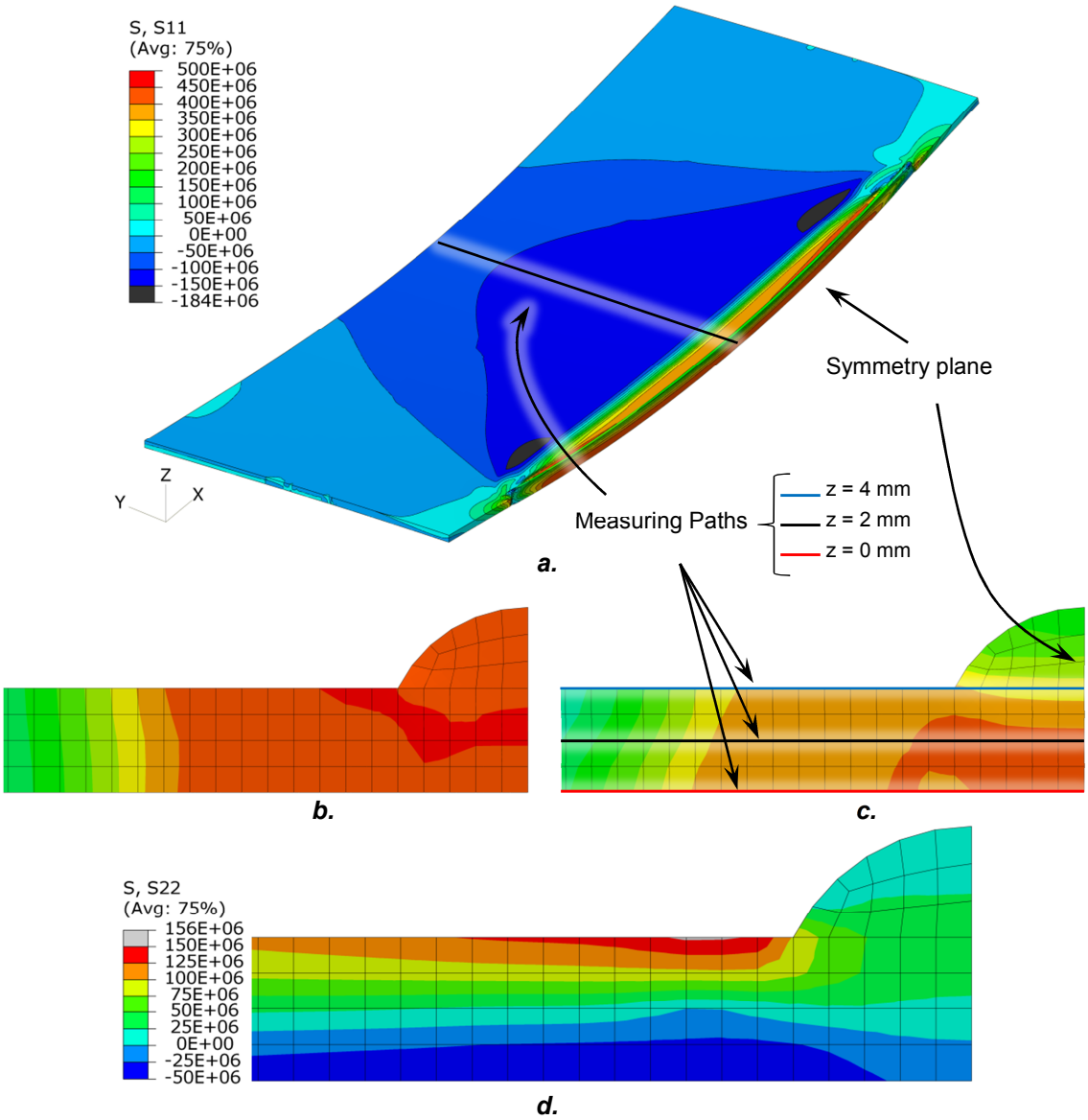

Figure 2-18 Contour plots of the longitudinal RS in half the weldment, and measuring path of the RS. *a.* 5x magnified of the residual distortion; *b.* close up of the weld bead and surrounding region before unclamping; *c.* after unclamping. *d.* Transverse RS in the weld bead and surroundings after unclamping.

Figure 2-19 *a* and *b* show the longitudinal RS before and after unclamping the weldment, respectively. The transverse and normal RSs, after unclamping, are shown in figure 2-19 *c* and *d*, respectively. The RS was taken in the middle length, across half width on the upper (z = 4 mm), and lower (z = 0 mm) surfaces, and in the middle plane (z = 2 mm), as shown in figure 2-18 *a* and *c*. The measurements from the upper surface were through the weld bead reinforcement (z = 4 mm).

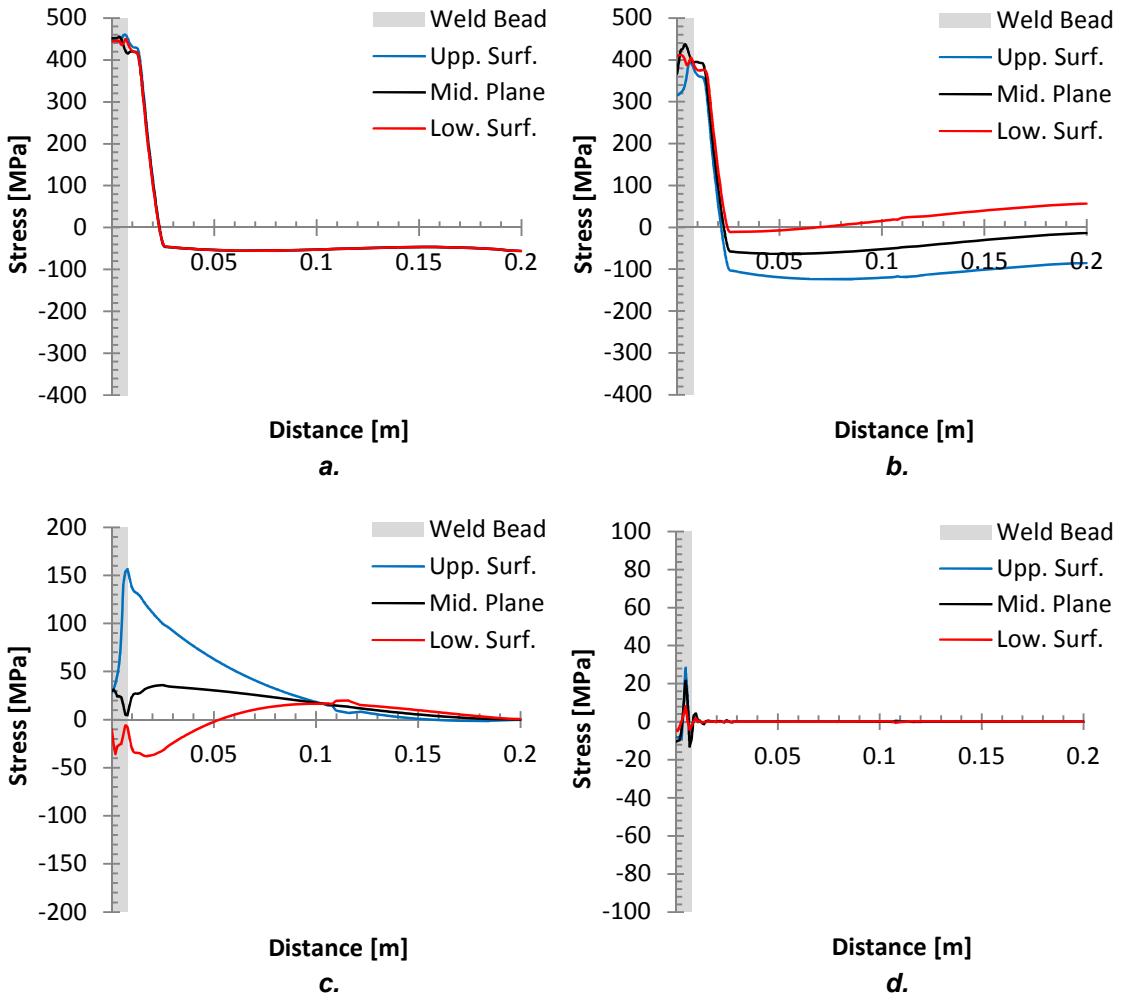

Figure 2-19 RS across half workpiece width in the upper (Upp.), middle (Mid.), and lower (Low.) surfaces in: *a.* the longitudinal direction before unclamping; *b.* the longitudinal direction after unclamping; *c.* and *d.* the transverse and normal directions, respectively, after unclamping.

Figure 2-20 *a* and *b* show the longitudinal plastic strain in the upper and lower surface before and after unclamping the workpiece. The negative values of the

longitudinal plastic strain indicate the shrinkage of the workpiece after welding and cooling.

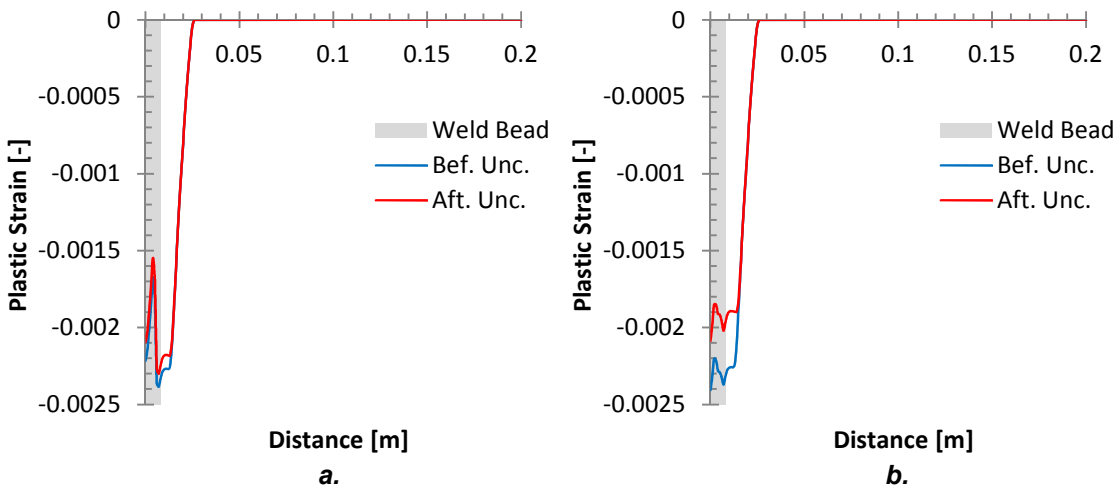

Figure 2-20 Longitudinal plastic strain before and after unclamping the workpiece in the: *a.* upper; and *b.* lower surfaces.

Before unclamping the weldment, the longitudinal RS across the thickness does not have significant variations, as shown in figure 2-18 *b* and figure 2-19 *a*, with a maximum tensile stress in the weld bead, ~ 460 MPa, which is over the yield point of the material (390 MPa). Nevertheless, small differences are observed in the weld bead region. These differences are caused by the inherent uneven heat distribution in bead-on-plate GMA welded plates, which causes uneven plastic strain across the thickness, as shown in figure 2-20 *a* and *b,* and by the concentration of the stress generated by the welding toes.

During unclamping, part of the RS are relaxed, modifying the stress field, as shown in figure 2-18 *c,* and figure 2-19 *b*, allowing the bending moment to find a new equilibrium configuration across the workpiece section [186]. The inherent negative plastic strain in the deposited weld seam causes the workpiece to bend upwards. As the workpiece deforms, the upper surface compresses, and the lower one expands; consequently, the magnitude of the compressive RS in the parent material increases in the upper surface, while decreases in the lower one, leaving the latter virtually entirely in tension, as shown in figure 2-19 *b*. In the weld bead region and surrounding material the longitudinal tensile RS are

slightly reduced in all the planes reported due to distortion and consequent rearrangement of the RS and to a lesser degree due to plastic deformation in that zone, as shown in figure 2-20 *a* and *b*.

The magnitude of transverse and normal RS were significantly lower than the longitudinal one (figure 2-19 *c* and *d*). In the upper surface the transverse RS is slightly tensile in the middle of the weld bead (y = 0 m) and rapidly increases to about 140 MPa in the welding toes, and steadily decreases to zero at the workpiece external edge (y = 0.2 m). The geometrical discontinuity caused by the weld bead in the welding toes acts as a local stress concentrator. This effect is less noticeable in the middle plane and lower surface, as shown in figure 2-18 *d*; consequently no drastic variations are observed across the workpiece close to the lower surface.

Post-weld rolling geometry – Effect of thermal contact conditions

Comparisons among different predicted longitudinal, transverse, and normal RSs, obtained by applying the three different temperature distributions, generated with different cooling sinks in the lower surface, namely, constant (C.), linear (L.), and exponential (E.), are shown in figure 2-21 *a* to *c*, respectively. The RSs were considered after welding, cooling, and unclamping the post-weld rolling modelled workpieces (no rolling applied), and the mechanical properties used were the ones provided by Tata Steel [177]. The main differences in RS field are observed in the longitudinal direction (see figure 2-21 *a*). The longitudinal RSs of the linear and exponential cooling rules are virtually identical, while the constant one is considerably wider (~ 6 mm); however, the peak value is just 20 MPa smaller than the exponential and linear RS. Nevertheless, the transverse and normal RSs have imperceptible differences in the three cases analysed.

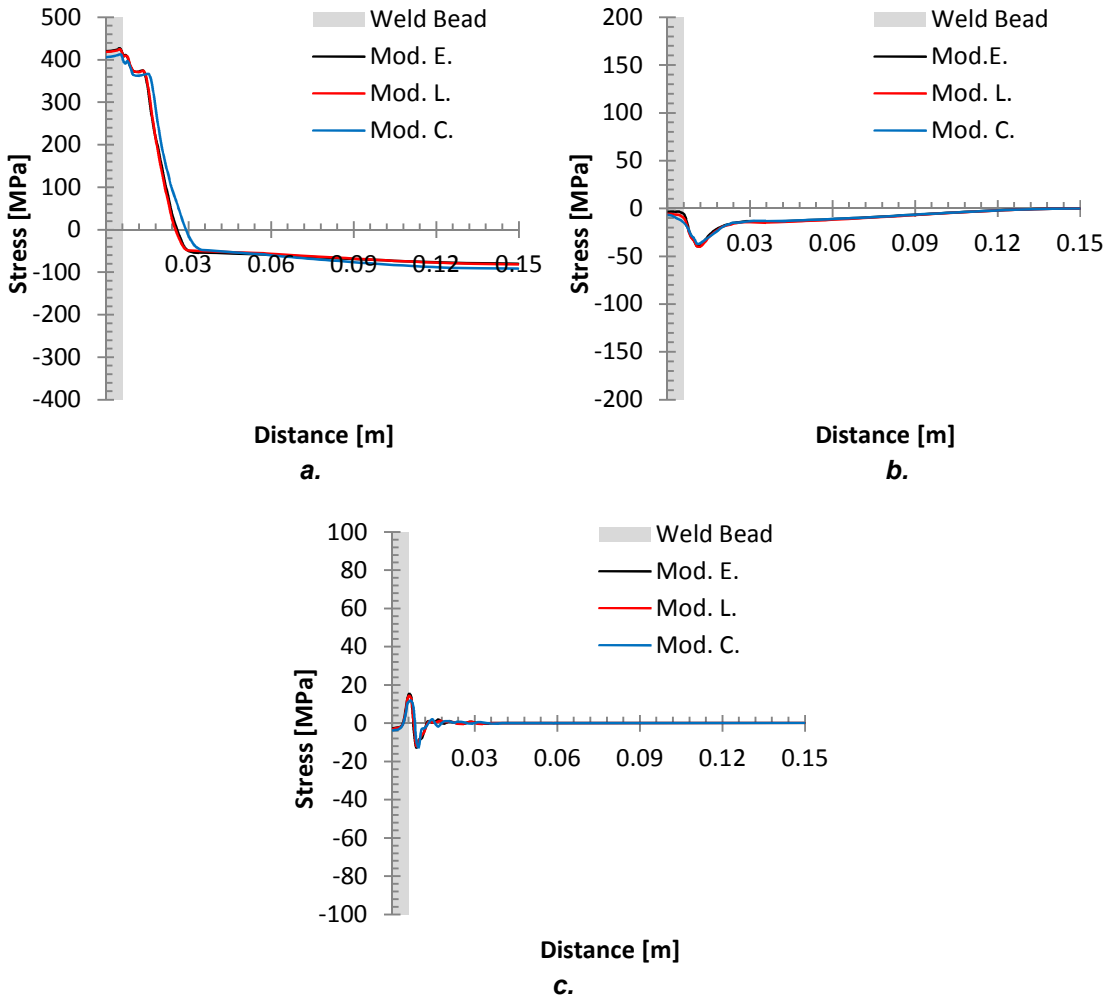

Figure 2-21 Comparison between the predicted RS obtained with different cooling conditions in the lower surface, namely: constant (C.), linear (L.), and exponential (E.) after unclamping in: *a.* longitudinal, *b.* transverse, and *c.* normal directions.

As expected, due to the very similar temperature distribution of the linear and exponential heat sinks, they have virtually identical RS distribution in the three Cartesian directions. In contrast, the constant cooling sink had higher temperatures across the workpiece, generating a wider tensile region. This illustrates how RSs are predominantly a function of the peak temperatures reached during welding along the transverse direction, as described by Camilleri *et al.* [187], and more recently in the numerical models on wire and arc additive manufacturing carried out by Ding *et al.* [188]. As the temperature distribution obtained with the exponential heat sinks approach was the most

similar to the experimental measurements, the RS field obtained with this method will be used in the subsequent investigations.

Post-weld rolling geometry – Effect of mechanical property data

A comparison of the longitudinal, transverse, and normal RSs between experimental measurements [2], and modelling results, obtained with S355 mechanical properties from two different sources, namely, Tata Steel [177] and Peil and Wichers [132], is shown in figure 2-22 *a* to *c* respectively, while figure 2-22 *d* compares the longitudinal plastic strain of the two models. In appendix a a comparison of the two material properties can be found. The longitudinal RS was virtually identical in the far field, after 30 mm from the weld seam, in all the cases analysed. However, the width of the tensile peak was wider in the models with Peil and Wichers mechanical properties, while the one with Tata Steel properties virtually overlaps the experimental RS in most of the measured points.

The mild steel S355, according with the British Standards [189], has a wide range of mechanical properties. It has only a minimum yielding strength, 355 MPa for thickness less than 16 mm, but it has no upper limit. In addition, the tensile strength for thickness between 3 and 100 mm is allowed to vary from 470 to 630 MPa. This variability makes it difficult to find generic mechanical properties for S355 for use in modelling.

Although the two mechanical properties analysed correspond to the same steel grade, they are significantly different. Tata Steel, besides providing the material properties for the models, supplied the steel sheet used in the experiments; consequently, it is more likely to have material properties similar to the actual steel used in the experiments. The material properties provided by Tata Steel were tested using typical welding thermal cycles, as described elsewhere [177], which gave more suitable material properties to be implemented in weld modelling simulations. Additionally, the linear thermal expansion coefficient of the material was obtained using different cooling rates to simulate the cooling conditions at different locations from the weld line in the workpiece, and then

they were averaged. This provides a linear thermal coefficient that can be considered unrealistic; however, the RS obtained with it matched the experimental RS accurately. Therefore, the material properties supplied by Tata Steel were used for the subsequent analysis.

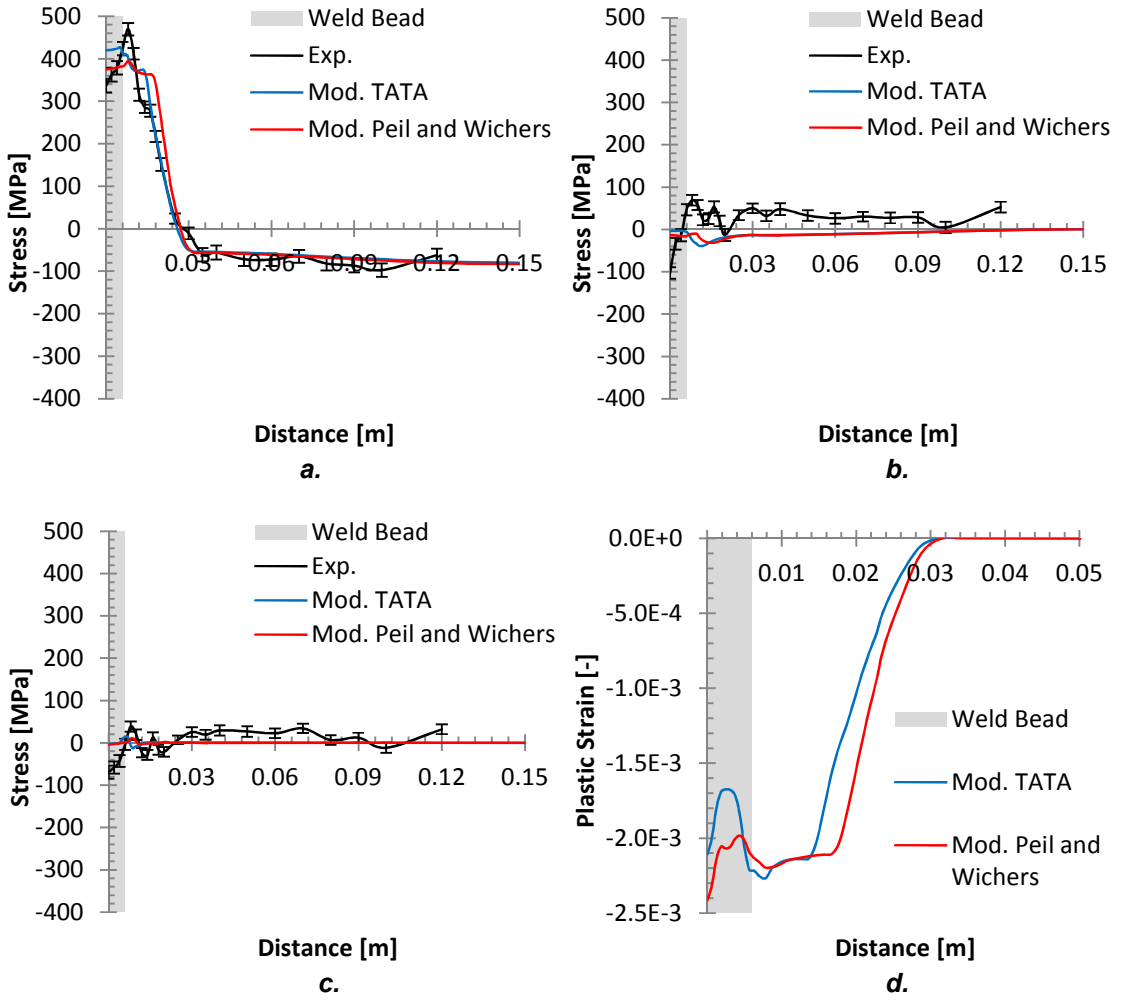

Figure 2-22 Comparison between experimental and predicted RS implementing two different mechanical material sources, namely, TATA [177], and Peil and Wichers [132] in the: *a.* longitudinal; *b.* transverse; *c.* normal direction; and longitudinal plastic strain.

At about 16 mm from the weld centreline, the larger difference in the predicted longitudinal RS, obtained with Tata Steel, and Peil and Wichers mechanical properties, was observed. The peak temperature at that location in the middle thickness was 380 °C. The largest difference between the strength of the two mechanical properties was observed at 400 °C; being the Peil and Wichers

strength being lower (when the true plastic strain was less than 0.1), as shown in appendix a. In addition, the thermal expansion coefficient from Peil and Wichers is slightly larger at that temperature. Consequently, the weldment underwent larger plastic strain at that location, as shown in figure 2-22 *d*, causing larger longitudinal RS.

Post-weld rolling geometry – Spatial variation of residual stress

The transverse and normal RS had smaller magnitude than the longitudinal one, and they were about zero in the parent material. In the weld bead regions the transverse RS is compressive in both experiment and numerical model, but the experimental results turn faster into tension after the welding toes, while the predicted results remain slightly compressive across the entire width. Nevertheless, the magnitude in both experimental and predicted results is very low and the trends are similar. In the normal direction the RS field is very similar to the one observed in the transverse direction. The RS oscillates about zero on the weld bead and HAZ and after 30 mm from the welding line it remains quite steady until the end of the workpiece, in which some small fluctuations around zero are observed.

Figure 2-23 *a* and *b* show the contour plot of the longitudinal RS, in the weld bead region, after welding and unclamping the weldments in the experiments

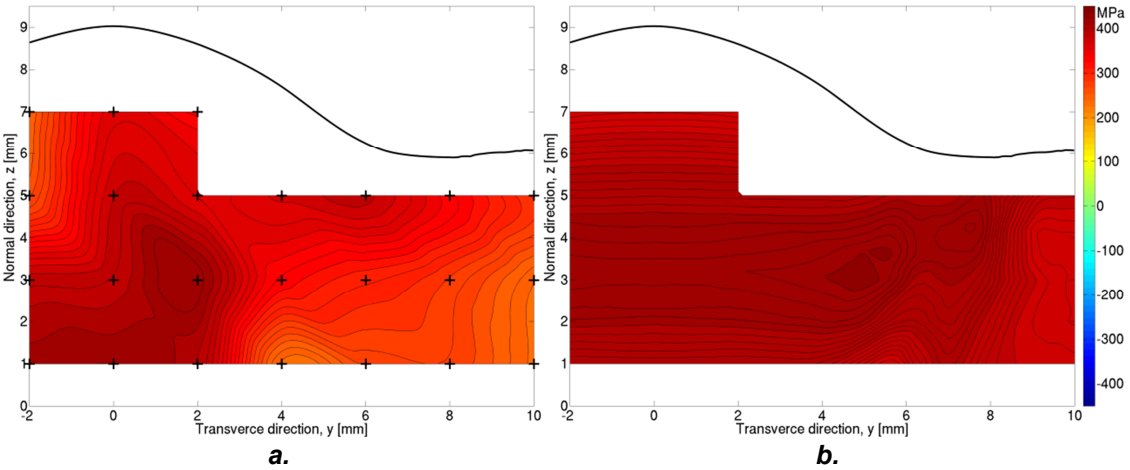

Figure 2-23 Contour plots of the longitudinal stress after welding and unclamping in: *a.* experiments [3], and *b.* modelling results.

carried out by Coules *et al*. [3], and the modelling results, respectively. In both cases the RS was highly tensile; however, the RS in the experiments was less tensile. Note that due to the symmetry of the welding process the RS at each side of the zero position in the experimental measurements, should have been very similar, but this was not observed. It is thought that this variation from side to side can be due either to the inherent uncertainty of the measurements, or slight misplacements of the gauge volume in the measurements.

Figure 2-24 *a* to *c* show the contour plots of half width weldment of the longitudinal transient stress after 16 and 58 s from the beginning of the weld, and the RS after unclamping the workpiece, respectively. The large amount of concentrated heat induced by welding causes the metal to melt. This uneven heating generates a thermal gradient between the parent material and the molten pool, yielding the material in compression at each side and in front of the weld pool, and producing large longitudinal transient compressive stress. As welding continues, the molten metal starts solidifying and shrinking behind the torch, yielding in tension the weld bead and surrounding material, reducing and eventually inverting the compressive stress formed previously beside the weld pool. After welding the stress field continues evolving until the entire workpiece reaches temperatures close to ambient.

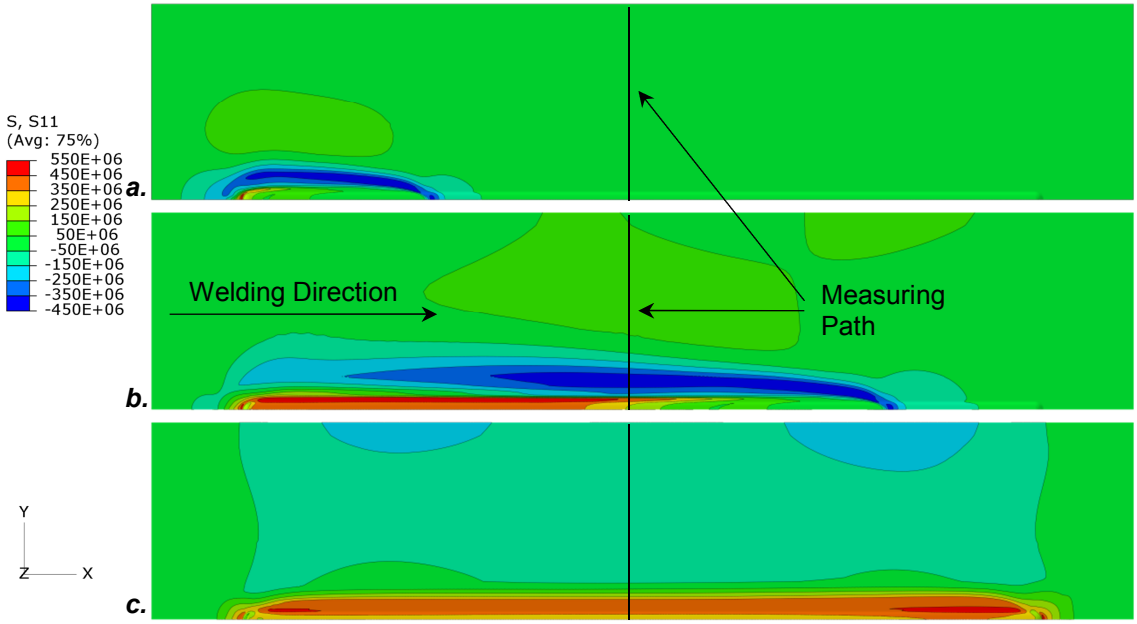

Figure 2-24 Contour plot of the longitudinal stress in post-weld rolling sample (with no rolling), and measuring path, after: *a.* 16 s; *b.* 58 s; and *c.* unclamping (RS)

The longitudinal transient stress field in the middle thickness in the measuring path (shown in figure 2-24) is shown in figure 2-25 *a*. Figure 2-25 *b* shows the transient stress at four different distances from the weld line, on the measuring path, namely, 0, 10, 20, and 30 mm. Two dotted lines were included in the graphs at 36.3, and 72.6 s to indicate the instant where the heat source crosses the measuring path, and the weld end.

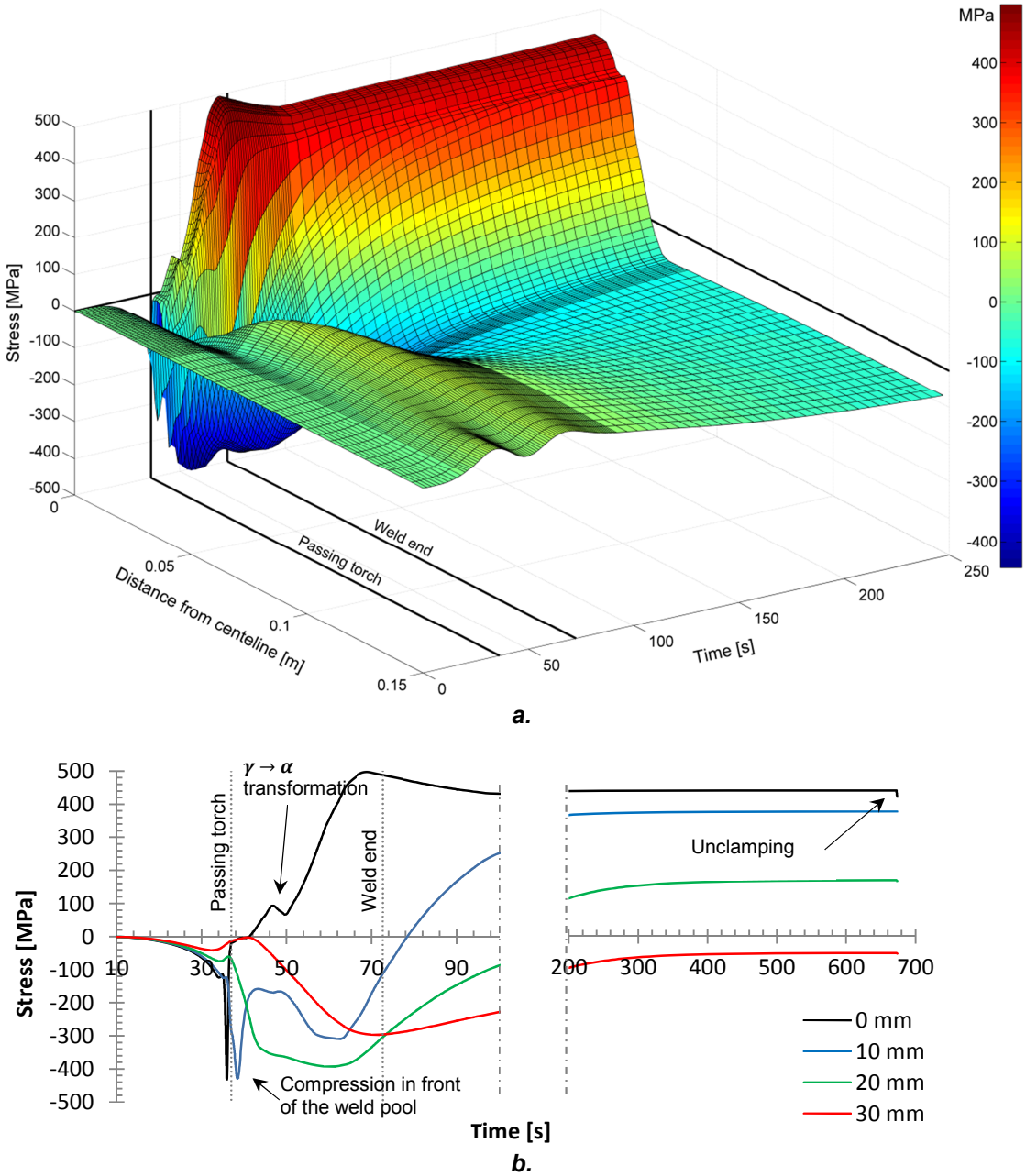

Figure 2-25 Longitudinal transient stress in measuring paths, *a.* across weldment width; *b.* in four location in the measuring path.

As mentioned previously, the material in front of the welding torch (before "passing torch" line) becomes progressively compressive, mainly in the weld bead and surrounding material, as shown at 0, and 10 mm in figure 2-25 *b*. When the heat source reaches the measuring path, the metal in the weld bead region is melted, and no mechanical stress can be supported by it; however, the surrounding material are still dilating and deforming in compression. As the

liquid material solidifies and contracts, tensile stresses start to form. The solid phase transformation austenite (γ) → ferrite (α) slightly reduces the tensile stress during cooling, as shown that at 0 mm in figure 2-25 *b*. Numerical models conducted by Deng [59], have shown that the influence on the RS due to phase transformation in low carbon steel, such as S355, is negligible.

The longitudinal RS in the middle of the weld bead reaches its maximum at 69 s when the temperature is around 400°C. At that temperature the material properties provided by Tata Steel showed higher strength (when the true plastic strain was less than 0.1), as shown in appendix a. A similar behaviour was also observed by Peil and Wichers [132] between 200 and 400 °C, and they claim that it is due to a dynamic strain aging of the material. The tensile RS are created during cooling, when the material contracts and its strength increases. However, below 400 °C the strength of the material decreases, this causes a reduction of the RS. Unfortunately, the lack of experimental data makes difficult to validate this behaviour.

After about 300 s (the weld was ended at 72.6 s), the RS remained virtually unchanged, and only minor variations are observed after this point. At that time the temperatures in the experiments and in the model are about 50°C.

Post-weld rolling geometry – Comparison with in situ strain gauge experiments

Figure 2-26 *a* and *b* show the predicted longitudinal transient stress in the post-weld rolling geometry, and the experimental *in situ* measurements, carried out by Coules *et al.* [190], in bead-on-plate in 750×300×3 mm S355 steel plates. The length and width of the samples in these experiments were the same as the models developed in this section, but the thickness was half (3 mm). Furthermore, the welding speed of the experiment was faster, and the instantaneous power was smaller (6.6 kW). Therefore, the tensile peak was narrower with the thinner plate, as less heat was required to produce the weld. Consequently, only a qualitative comparison between the two results can be made.

The experimental stress measurements are shown between distances from 20 to 80 mm from the centre line. Closer distances were not possible because of the high temperatures close to the welding torch. To facilitate the comparison, a region between 35 and 80 mm from the centreline of the longitudinal transient stress field of the post-weld rolling model, reported in figure 2-25 *a*, was extracted and presented in figure 2-26 *a.*

Both experimental and modelling results showed the same trend, having some compressive stress before the heat source reaches the measuring path, and heavily compressive during cooling. Shanghvi and Michaleri [191], and Richards *et al*. [192] observed the same trend in laser hardening of a steel block, and in aluminium FSW plates, respectively. The thermal dilation of the material around the arc causes compressive stress in the lower temperature material in front and beside it. When the metal in the weld bead starts to cool down behind the weld pool, the tensile stress starts to form. However, the metal next to the weld bead is still increasing its temperature while the heat dissipates across the workpiece. Therefore, the predicted heavily transient compressive stress beside the weld bead at about 65 s is formed for two reasons. Firstly, the tensile transient stress in the weld bead is counterbalance by compressive stress beside it. Secondly, the peak temperature at 30 mm is reached at that time, while the material at the weld bead is already cooling down for about 18 s, causing the maximum dilation of the material at that location; consequently, high transient compressive stresses are formed at that point. At that location only elastic strain occurs, as shown in figure 2-20, hence when the material cools to room temperature the compressive stress reduces in magnitude and at that point it is only depending on the tensile RS in the centreline and surrounding metal.

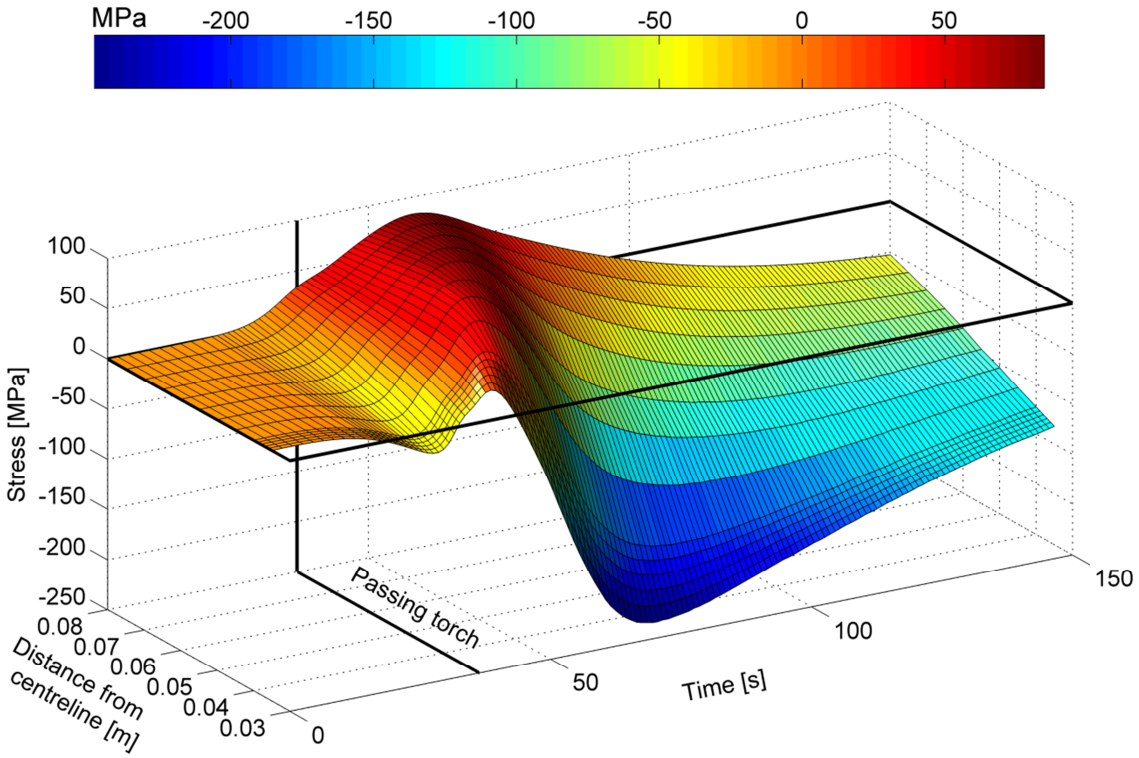

a.

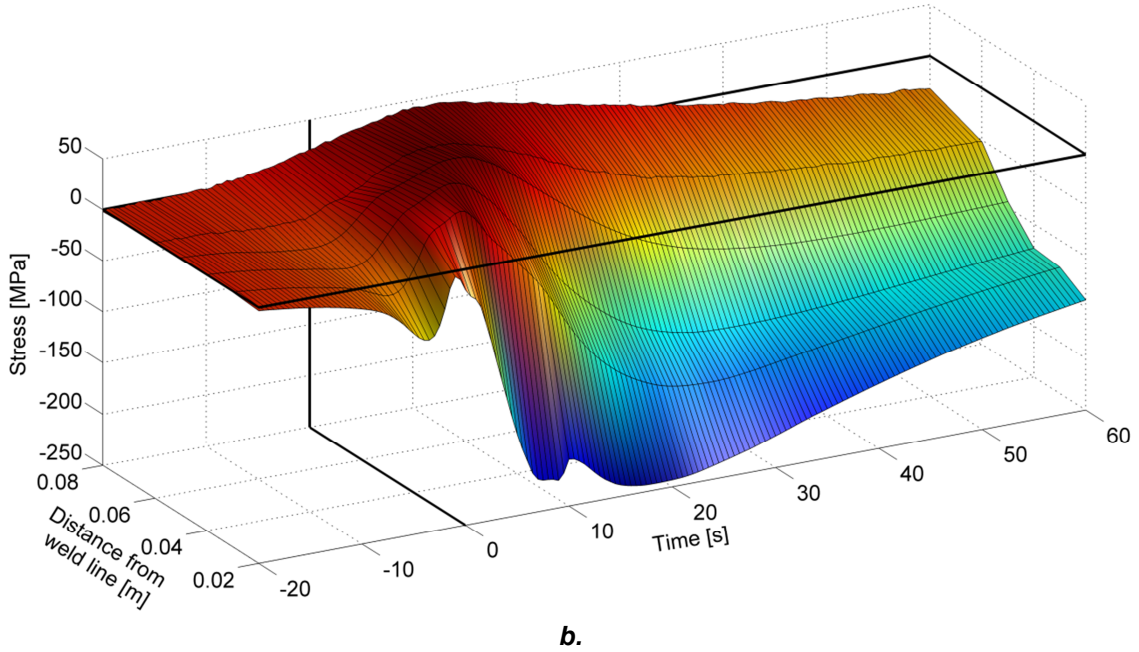

b.

Figure 2-26 ***a.*** **Predicted longitudinal stress field in post-weld rolling analysis.** ***b.*** **Experimental *in situ* strain gauge measurements on the bead-on-plate welding on 3 mm workpiece thickness [193].**

In Coules *et al.* experimental measurements an abrupt change in the transient compressive stress was observed at about 10 s, 20 mm away from the weld

centreline. A similar inflection was observed in the predicted stress, but smaller in magnitude, as shown from 0 to 20 mm from the centreline, at 46 s, in figure 2-25 *b*. This inflection is due to the phase transformation from austenite (γ) to ferrite (α) in the welding line and surroundings during cooling. As the distance from the centreline increases, this effect is less evident, and after a certain distance it is not perceptible. In welding, different cooling rates occur at different parts of the workpiece, as shown in figure 2-14 *b*. Higher cooling rates cause the phase transformation to occur at lower temperatures (supercooling). Consequently, for different cooling rates, different thermal expansion curves need to be considered to capture this effect in the numerical model. However, all the models developed in this thesis used a mean thermal expansion curve, which limits the model's ability to capture the transient stress. Nevertheless, the model is able to predict the overall shape of the RS, which was the main intention as the focus of the work is the rolling process.

2.3.3 Distortion and buckling analysis

Figure 2-27 *a* and *b* show the contour plots of the lower surface of the distorted weldments after welding and unclamping the pre- and post-weld rolling geometries (without rolling), respectively. In all the experiments and models the workpieces after welding and unclamping distort upwards resembling a hyperbolic paraboloid shape (saddle).

The presence of the weld reinforcement and the inherent contraction in the welded region generate a bending moment which induces the upward distortion. In addition, the presence of the weld reinforcement displaces the neutral axis of the weldment from the middle thickness to an upper location which augments the distortion, as shown by Colegrove *et al.* [186]. Their study investigated experimentally and analytically the bending distortion induced by welding in wire and arc additive manufacturing. In that case the effect on bending distortion was greater due to the higher height of the multiple weld beads in the wall built.

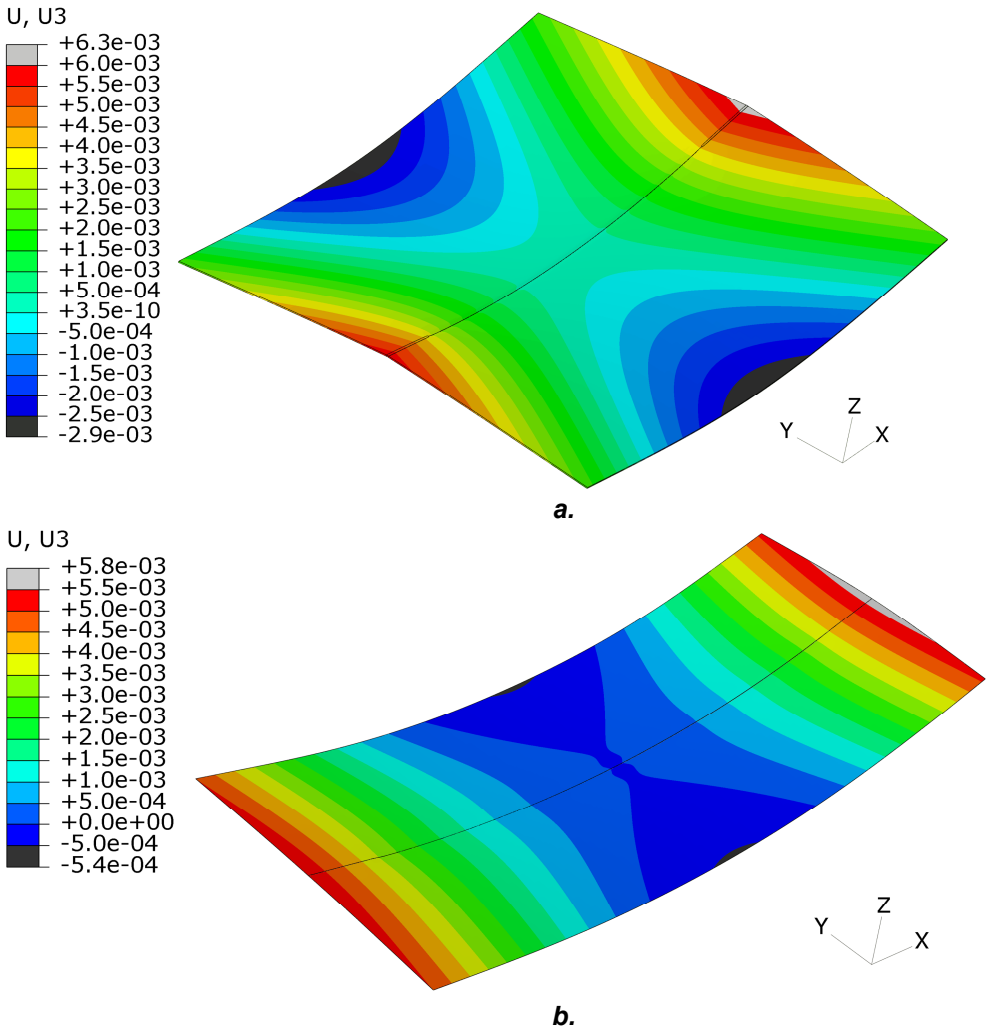

Figure 2-27 Contour plot of the out-of-plane distortion after welding and unclamping *a.* pre-weld rolling (5X magnification), and *b.* post-weld rolling (10X magnification) workpieces (units in meters).

Figure 2-28 *a* shows a comparison between the experimental and predicted out-of-plane peak distortion of the weldments (without rolling) used in the pre- and post-weld rolling studies. In the pre-weld rolling geometry experiments the average out-of-plane peak distortion of 10 samples was about 16.1 mm with 1.1 standard deviation of the population. The post-weld rolling geometry experiments, on the other hand, had an average out-of-plane peak distortion of 10.6 mm and a 1.9 standard deviation of the population, measured on 6 samples. The models underestimated the distortion in both cases having a predicted out-of-plane distortion peak around 9.3 and 6.3 mm in the pre- and post-weld rolling geometry models. The over-predicted weld temperature close

to the weld for the pre-weld rolling geometry models (see figure 2-11 *b*) may have resulted in an incorrect prediction of plastic deformation and consequently the final distortion. On the other hand, the post-weld rolling geometry model had a temperature distribution that better matched the experimental measurements (see figure 2-13 *b*); however, the distortion after clamping was under predicted as well but to a lesser degree.

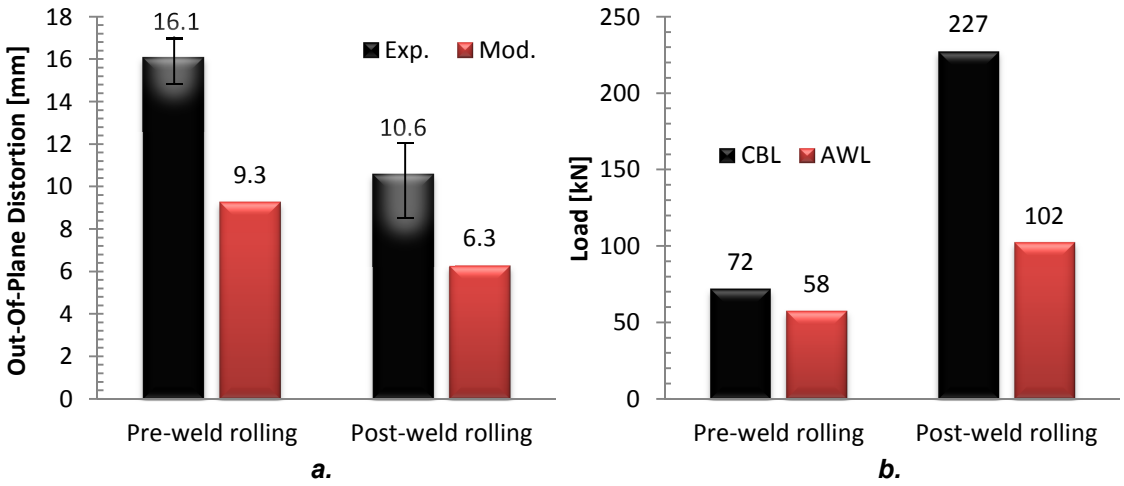

Figure 2-28 ***a.*** **Out-of-plane peak distortion, and** ***b.*** **Critical buckling load and applied weld load, of pre- and post-weld rolling geometry models.**

In the models the plates were considered completely flat and free of any internal pre-existing RS. In the experiments not all the plates were perfectly flat and no RS measurements were made in the virgin material. These factors may exacerbate subsequent distortion in the plate. Similar discrepancies between the distortion prediction by models and that observed in experiments have observed in the literature. Long *et al.* [126] have observed in their simulations on thin butt welded high strength low alloy steel plates (similar to S355) that numerical models can underestimate distortion in butt welds, especially with low welding speeds (< 1 m·min^{-1}). They justified the discrepancies due to inaccuracies in the thermal-mechanical material properties, in the weld bead profile and in the heat input parameters. Masubuchi [194] has reported that inaccuracies in modelling distortion were caused by modelling simplification, inaccuracies in the material properties at high temperature, and the

disregarding of metallurgical phenomena. Additionally, Verhaeghe [195] made a review of different analytical weld distortion predictions and found that none of the methods could predict the exact magnitude of the distortion, but they provided an indication of the magnitude of the expected distortion.

Figure 2-28 *b* shows a comparison between the predicted critical buckling load (CBL) and the predicted applied weld load (AWL) of the pre- and post-weld rolling geometry models. The buckling analysis showed that the CBL of the post-weld rolling geometry weldment is more than twice of its AWL, while in the pre-weld rolling geometry weldment the CBL is only 24 % larger than its related AWL. Buckling distortion is expected to occur when the AWL is larger than the CBL [15,42,128,172,196]. Therefore, in perfect conditions and with a perfect material, no buckling would take place in either weldment. However, imperfections in the material and the weld can reduce the actual CBL causing premature buckling [180].

Watanabe and Satoh [197] studied the influence of geometric variation on buckling distortion in bead-on-plate welded steel plates. Masubuchi [10] rearranged their results to plot the effect of the width-length ratio (B/L) on the critical buckling thickness, as shown in figure 2-29. Therefore, for a given B/L ratio and width (or length) there is a minimum workpiece thickness below which buckling is likely to occur. The pre-weld rolling weldment has B/L ratio equal to (0.4/.05) 0.8, while post-weld rolling one is (0.3/0.75) 0.4, which give critical buckling thickness of about 3.2, and 4.5 mm, respectively. Hence, accordingly to this analysis, buckling distortion is not predicted in both cases which support the CBL analysis done in this work.

To summarise, the relatively large out-of-plane distortion, and the small difference in the CBL and AWL in the pre-weld rolling geometry, suggest that this workpiece may exhibit distortion caused by buckling. On the other hand, the post-weld rolling geometry weldment which used thicker material is unlikely to exhibit buckling distortion; hence, the distortion is predominantly caused by bending.

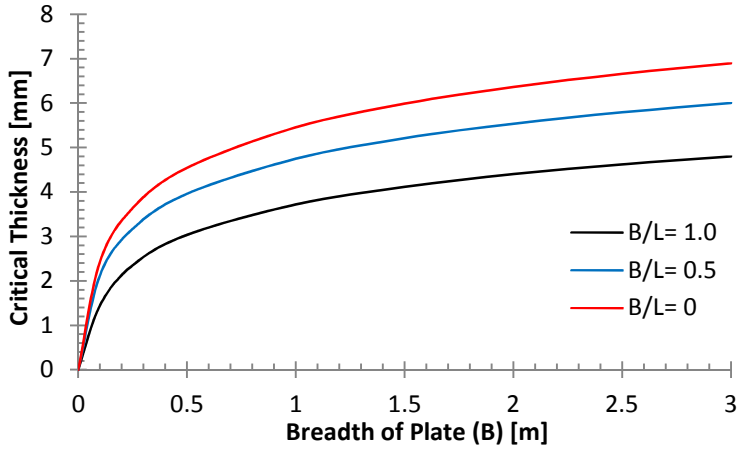

Figure 2-29 Critical thickness for buckling distortion of bead-on-plate welded steel plates(after Watanabe and Satoh [197] in Masubuchi [10]).

2.4 Conclusion

- The cooling effect of the backing support (copper backing-bar, and aluminium vacuum clamps) can be efficiently modelled by applying convective cooling to the lower surface of the weldment.
- It was shown that using a convective cooling coefficient which had an exponential relationship with temperature, provided better prediction of experimental temperature than either constant, of linear values. Note however, that the difference with the linear curve was marginal.
- The effect of *in situ* rolling on the temperature distribution can be effectively modelled by increasing the convective cooling coefficient in the roller – workpiece, and workpiece – backing-bar contact regions. The workpiece – backing-bar region needed to be larger than the roller – workpiece region due to the Saint-Venant principle.
- The longitudinal RS does not present significant variation across the thickness before unclamping. After unclamping, the plates deform, relaxing residual stress, and minor plastic deformation is present in the weld bead and surrounding material. The distortion causes a RS gradient though the thickness, which is more evident far from the weld bead in the parent metal.

- The longitudinal RS showed a significant dependency on the peak temperatures across the weldment width. Increasing the width of the region where high temperatures were observed increased the width of the tensile RS peak. No significant differences were observed in the normal and transverse RSs.
- Two sets of mechanical properties were tested. Using material properties with lower strength and higher linear thermal expansion coefficients around 400 °C, increased the width of the longitudinal tensile RS. Hence to predict RS, particular attention has to be taken to the mechanical properties selection.
- The effect of phase transformation showed an insignificant effect on the RS; however, its effect was observed in the transient stress.
- The models underpredict distortion. It is thought that the presence of pre-existing distortion in the unwelded plates can increase the magnitude of the out-of-plane distortion in the experiments. In addition, there are uncertainties in the material properties and boundary conditions used in the model, which make it difficult to accurately predict the distortion.
- The AWL was compared with the CBL for the two plate geometries investigated in this thesis. For the thinner plate welds, the AWL was comparable to the CBL indicating that buckling distortion may have occurred. The other geometry used thicker plates, and had an AWL less than half of the CBL, so buckling distortion was improbable.

Chapter 3 Pre-Weld Rolling

3.1 Introduction

Pre-weld rolling is a novel technique which aims to induce beneficial Residual Stress (**RS**) before the welding process, to reduce the overall distortion and RS after welding. Other rolling techniques have been investigated in the past, some of them with promising results in terms of RS and distortion reduction. The post-weld rolling has been investigated in aluminium and titanium TIG welded plates [86], as well as in aluminium friction stir welded plates [102,104] with a drastic reduction of the tensile RS in the weld bead area, and with the appropriate load even compressive RS was observed.

The possible advantage of pre-weld rolling over the other rolling techniques is that it can be applied directly by the steel manufacturer prior to being welded by the constructer. In this investigation either the upper or lower surfaces of the plates (relative to the side which is welded) were rolled prior to welding. In addition, the effect of post-weld heating the region that had been rolled was investigated.

3.2 Methodology

In this section the pre-weld rolling models are described. These models are based on the experimental work carried out by Coules *et al.* [1]. A description of the rolling experiments, residual stress measurement, and distortion calculation can be found in appendix d. As for the welding thermal-mechanical models, these models were built with Abaqus Standard version 6.9 as a sequentially coupled thermal-mechanical analysis. The models consist of three main successive steps, namely, rolling, and welding mechanical analyses. The models are divided into three groups. In the first, different roller positions, and rolling loads and sides (*i.e.* upper and lower surfaces) were analysed, ignoring the friction between the components. The second includes the friction between the copper backing-bar and plate, and the roller and plate. Different rolling loads and sides were investigated. In the last group a moving heat source (induction heating) was applied to the region that had been rolled, after the welding step.

The welding heat transfer and the extra moving heat source analyses were run independently of the welding and rolling mechanical analysis. The temperature distributions obtained were imported in the appropriate step to obtain the RS distribution. The welding heat transfer and mechanical models (without rolling) were already described in chapter 2.

As the rolling analysis was performed before welding, each plate was rolled individually, as shown in figure 3-1 *a* and *b*. However, owing to the symmetry of the weldment only half the geometry was modelled; consequently, only one rolled plate was required in the model, which saves computational time and resources. The plates were considered rolled on the upper surface when welding was applied in the same rolled surface, and on the lower one when welding was applied on the opposite surface of the rolled one. The rolling distance was defined as the distance between the plate edge (welding edge), and the roller middle width, as shown in figure 3-1 *a* and *b*. The weld bead was added to the models in the welding step, all at once and strain free, using the block dumped method described by Shan *et al.* [152] , and was not present during rolling.

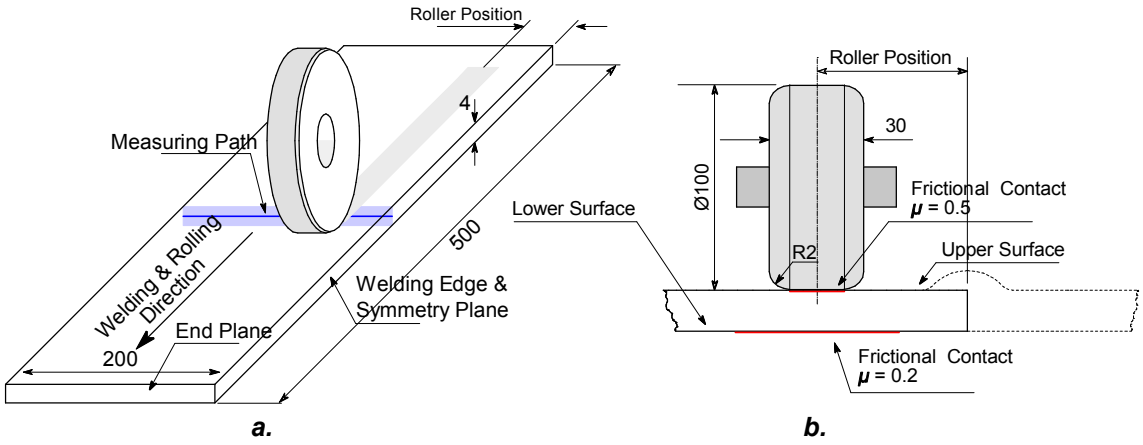

Figure 3-1 ***a.*** **Schematic representation of pre–weld rolling.** ***b.*** **Roller dimensions and position when rolling the upper surface (dimensions in millimetres).**

The roller was modelled as rigid body, so it did not undergo any deformation. Only one cylindrical flat roller was used in all the analysis, whose dimensions are shown in figure 3-1 *b*. The rolling speed was 500 mm·min^{-1}, and no torque

was applied on the roller to drive it. Instead, uniform translation was imposed on the roller axis, and the roller rotation occurred when there was friction interaction with the plate, as occurred in the experiments.

After pre-weld rolling an extra step was added to simulate the unclamping of the weldment. The boundary conditions applied in this step are the same as the ones applied in the homologous unclamping step of the welding mechanical analysis described in chapter 2.

3.2.1 Frictionless models

In this set of models different roller positions, and rolling load and sides (*i.e.* upper and lower surfaces) were investigated. The modelling parameters are shown in table 3-1. No frictional contact was considered in this analysis. To simulate the boundary conditions of the clamped plates, all the nodes in the opposite surface of rolling were restrained against the out-of-plane displacement. To avoid the plate moving in the longitudinal direction during rolling and welding, the end plane (see figure 3-1 *a*) was restrained against displacement in the longitudinal direction (rolling direction). To avoid displacement of the weldment in the transverse direction during rolling, the nodes in the opposite plane to the welding edge were restrained against displacement in that direction, while during the welding step transverse symmetric boundary conditions in the symmetry plane (see figure 3-1 *a*) were applied, which not only restrained the displacement in that direction, but also

Table 3-1 Parameters investigated on the frictionless models set.

Rolling Load [kN]	Rolling Position [mm]	Rolling Side [Upper / Lower]
50	25	Upper & Lower
50	55	Upper
100	15	Lower
100	25; 35; 55	Upper & Lower
100	80	Lower
200	35; 55	Upper & Lower
200	80	Lower

the rotation in the longitudinal and normal directions. The out-of-plane displacement during the welding step was obtained by restraining, all the nodes in the opposite surface to the weld bead, against out-of-plane displacement. On the other hand, during the unclamping step, only one node in the middle of the symmetry plane was fully constrained (encastré), and the transverse symmetric boundary condition applied in the symmetry plane in the welding step was kept, while the rest of the mechanical constraints were removed.

3.2.2 Models with frictional contact

In these models a rigid plane was included to simulate the interaction with the vacuum clamps and a backing-bar on the rolling step. The vacuum clamps were modelled by applying one atmosphere pressure (101325 Pa) on the contact surfaces of the plate towards the rigid plane. An isotropic friction coefficient, μ = 0.2, was added corresponding to the contact area between the plate and the backing-bar, in a 48 mm wide region, along the entire length of the plate, as shown in figure 3-1 *b*. The frictional contact between the roller and the plate was also considered, with μ = 0.5. These coefficients were based on the results obtained in a study performed in chapter 4 about the influence of friction coefficient on post-weld rolled weldments. To prevent the plate moving in the transverse direction during rolling, two nodes on the corners of the plane opposite to the welding edge restrained the plate against displacement in that direction.

During the welding and unclamping steps, the same boundary conditions as for the frictionless models were implemented. Table 3-2 shows the parameters investigated.

Table 3-2 Parameters investigated with frictional contact included, and with post-weld heating.

Rolling Load [kN]	Rolling Position [mm]	Rolling Surface [Upper / Lower]
50	55	Upper
100; 200	55	Upper & Lower

3.2.3 Post–weld heating pre–weld rolling

When the material is heated unevenly, tensile residual stress are produced in the radial direction, if plastic strain occurs, as explained in chapter 1 in the local heating section. Therefore, when a heat source is applied to the rolling paths, the tensile stress induced by rolling can be potentially reduced or even reverted, depending on the magnitude and area of the heat source.

In these models a moving heat source was applied to the rolling path to remove the plastic strain induced by rolling, after the welding process had been applied. The moving heat source was designed to emulate induction heating, as a smaller version of the Terac 25 heating source described by McPherson *et al.* [198]. They showed that with this induction heating system, 6 mm thick plates could be heated through the entire thickness in about 6 s, up to the Curie point of steel (760 °C), for a region of 160 mm long by about 30 mm wide.

The inductive heat source was modelled by applying a uniform volumetric source of 800 $MW \cdot m^{-3}$, throughout the weldment thickness. This was applied in the rolling paths within a rectangular shape, as shown in figure 3-2, and a travel speed of 500 $mm \cdot min^{-1}$ (0.0833 $m \cdot s^{-1}$). Two rectangular heat source sizes were investigated. One was smaller than the roller print, and the other was the same size as the roller print. Both were 20 mm long in the rolling direction. During this heating step, it was assumed that no backing-bar was present, and the weldment was cooled by forced air convection (h = 200 $W \cdot m^{-2} \cdot °C^{-1}$ [110]), and radiation to the surroundings (emissivity ϵ = 0.8 [110]). After the welding step a cooling step of 220 s was added, in which the forced convection and radiation

were propagated, to allow the workpiece to reach room temperature (about 20 °C).

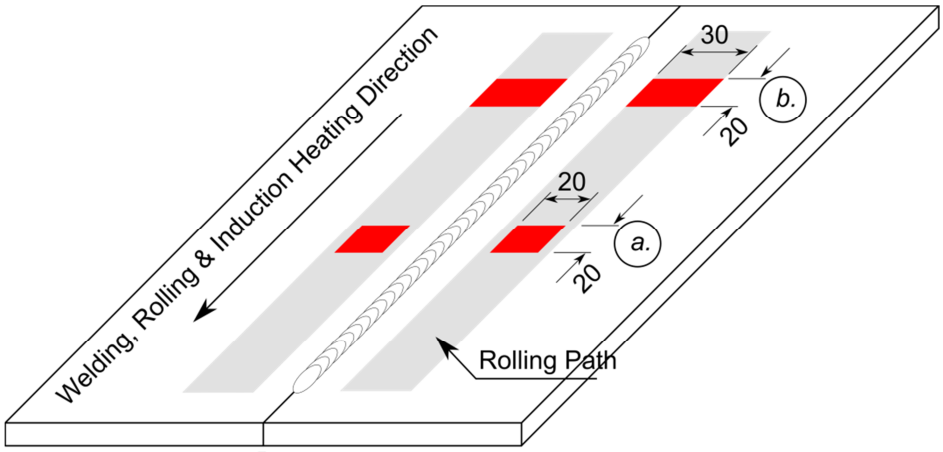

Figure 3-2 **Schematic representation of post-weld induction heating after pre-weld rolling. *a.* Smaller heat source; and *b.* wider size (dimensions in millimetres).**

In the mechanical analysis of the inductive heating model the same boundary condition used for the welding steps, implemented in the frictional models, was used. As for all the previous models, an additional step was added to simulate unclamping with the same boundary conditions already explained.

The parameters investigated were the same as those described in the previous section which are shown in table 3-2.

3.3 Results and Discussion

3.3.1 Results from rolling only (before welding)

Residual stress

Figure 3-3 *a* to *c* show a comparison between the longitudinal RS in the middle thickness along the measuring path (see figure 3-1 *a*) after rolling the plates at 55 mm from the edge with different loads, and after unclamping. The 55 mm distance was chosen because that was the one which produced larger distortion reduction after pre-weld rolling in Coules *et al.* experiments [1], and consequently was the one used in the neutron diffraction measurements. The

results are shown for both the frictionless and with friction models. The longitudinal RS, in the frictionless and with friction models, after rolling with 50 and 100 kN are very similar, as shown in figure 3-3 *a* and *b*. On the contrary, with 200 kN load significant discrepancies were observed. The frictionless model induced large plastic strain in the closer edge (see figure 3-9 *c*), which caused reduction of the longitudinal tensile RS in that region, and lowered the compressive RS under the roller path. On the other hand, in the model with friction included, a slightly reduction of the longitudinal RS in the closer edge was observed, as very small plastic strain was observed in that region (see figure 3-10 *d*). However, in the other part of the plate (from 0.008 to 0.2 m) the longitudinal RSs from the two models virtually overlap each other.

The localised rolling induced large compressive stress in the rolling path, while at each side of the rolling path counterbalanced tensile RS was produced. Since rolling was not applied in the middle width of the plate, but closer to one of its edges, the closer edge had large tensile RS (0 mm in figure 3-3). This tensile RS was a function of the rolling load and rolling position (as will be show in the next paragraphs). However, above a certain rolling load (and below certain rolling distance) the closer edge was plastically deformed, reducing the tensile RS at that location, as shown in figure 3-3 *c*.

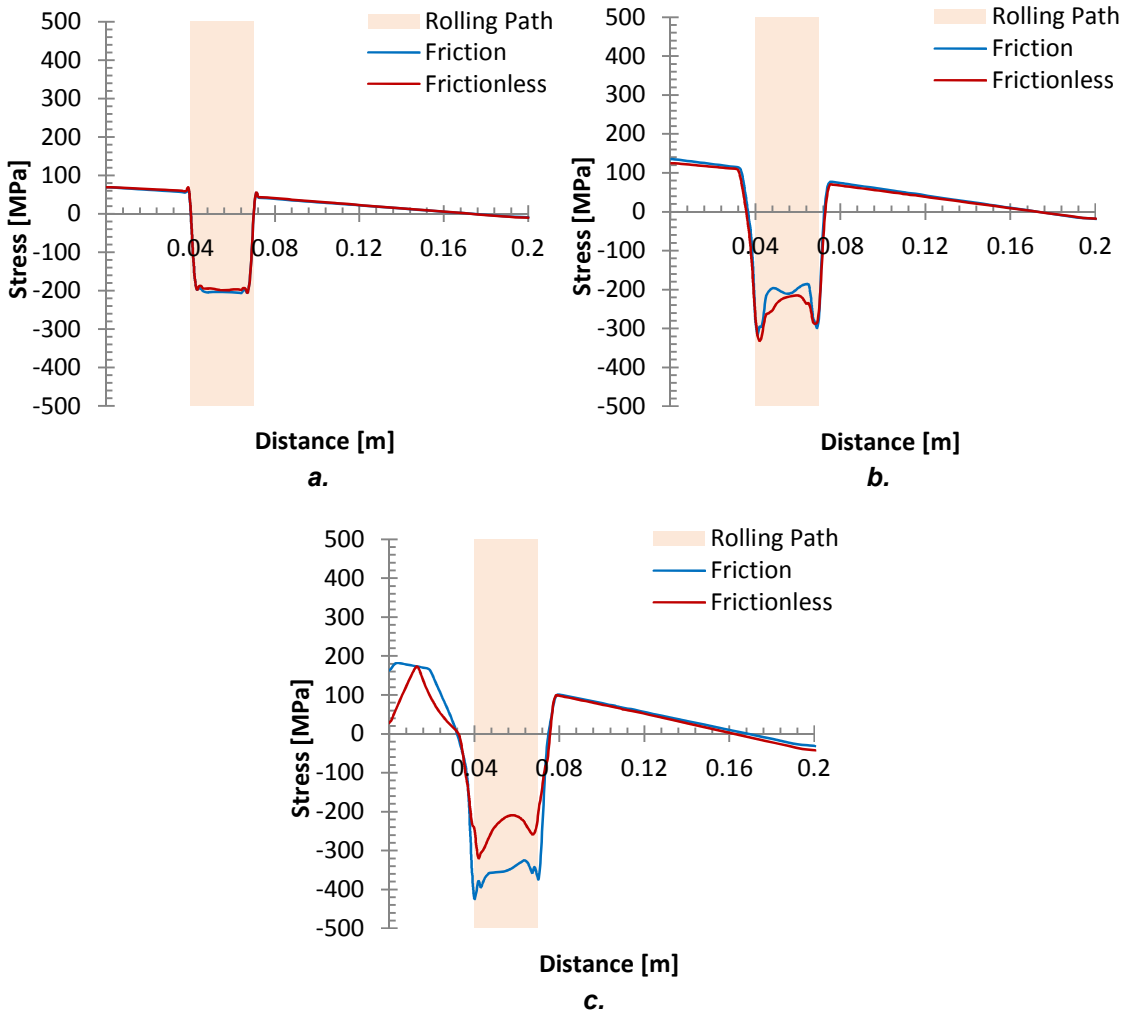

Figure 3-3 **Comparison of the longitudinal RS, between the frictionless and with friction models, in the middle thickness across the measuring path after rolling at 55 mm from the edge with *a.* 50, *b.* 100, and *c.* 200 kN, and unclamping.**

Effect of rolling distance and load on the RS distribution

Figure 3-4 *a* to *e* show the longitudinal RS in the middle thickness, after rolling and unclamping the single plates, at different roller positions, namely, 15, 25, 35, 55 and 80 mm, in the frictionless models. When the edge of the roller was aligned to the edge of the plate (roller centre at 15 mm from the edge) the compressive RS reached the higher values, around -400 MPa, with a rolling load of 100 kN, as shown in figure 3-4 *a*. This compressive peak value was reduced, to about -300 MPa, at farther rolling distances. As the rolling load increased from 50 and 100 kN, the compressive RS, in the roller path,

increased too, as shown in figure 3-4 *b* and *d*. However, from 100 to 200 kN rolling load, the compressive RS magnitude remained virtually constant (as shown in figure 3-4 *d* and *e*, or even reduced its magnitudes, when the roller was close enough to the edge (as shown in figure 3-4 *c*), due to the plastic deformation of the closer edge. Wang and Mote [199] investigated the effect of localised rolling in bandsaw steel strips, and found that compressive RS grew asymptotically as the rolling load increases. Additionally, it was observed that the width of the tensile peak increased with the rolling load, which is in agreement with experimental and modelling results on post-weld rolling of FS welded aluminium plates carried out by Atenkirch *et al.* [98] and Wen *et al.* [200], respectively.

When the plate was rolled at 80 mm from the edge, the RS in the closer edge (0 mm in figure 3-4 *e*) was tensile regardless the rolling load. However, reducing the rolling distance below 55 mm, a drastic reduction of the tensile RS in the plate edge was observed when 200 kN load was used. With large loads the material was plastically deformed in a wider area; therefore, when the roller was sufficiently closed to the plate edge, this was deformed plastically, as shown in figure 3-9 *c*, and consequently the RS reduced its magnitude, as shown in figure 3-4 *d*. This effect was more evident at closer distances from the plate edge, as shown in figure 3-4 *b* and *c*.

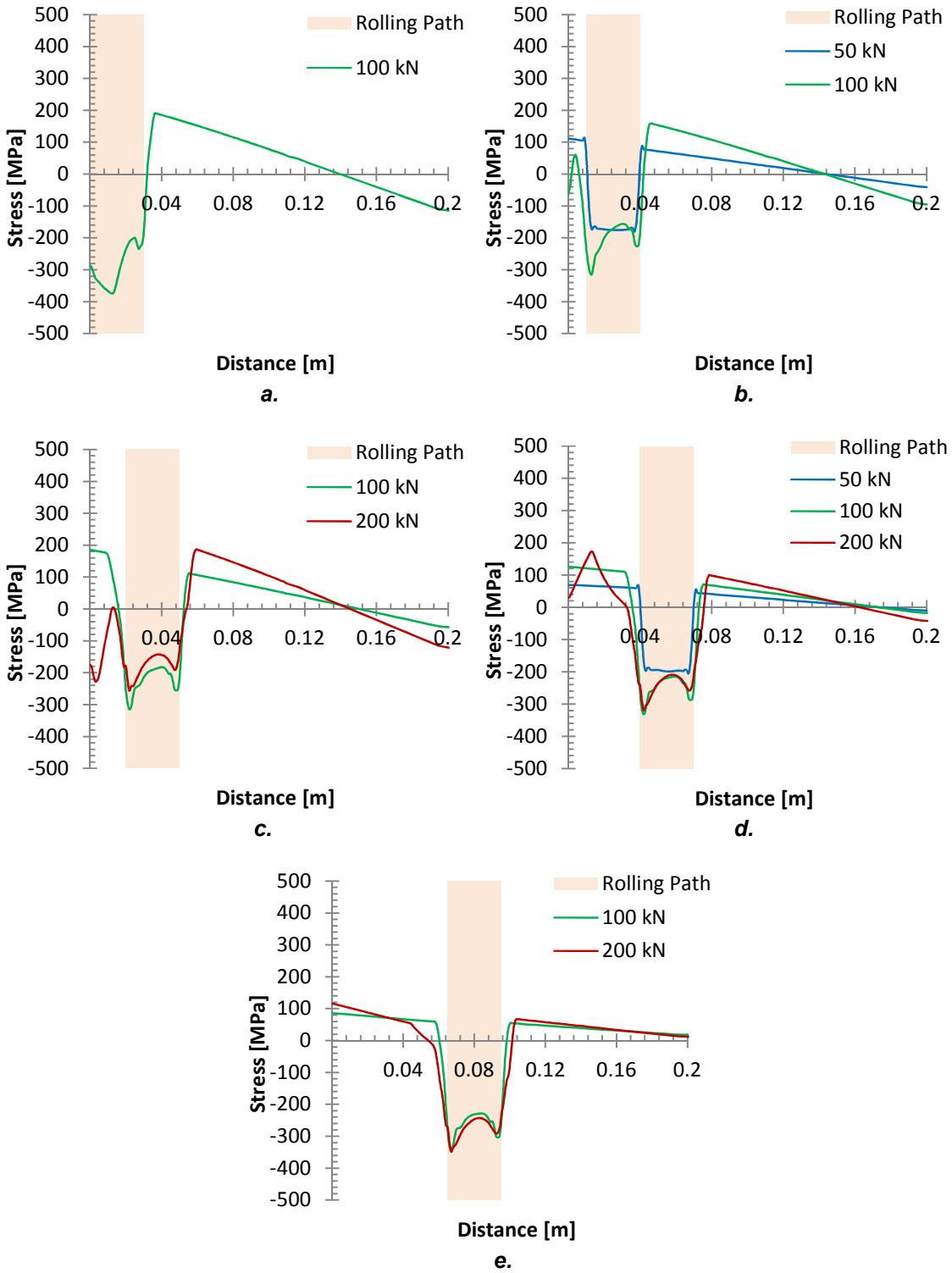

Figure 3-4 **Longitudinal RS after rolling single plates (frictionless models) before welding at: *a.* 15, *b.* 25, *c.* 35, *d.* 55, and *e.* 80 mm from the edge (edge which will be welded).**

Effect of friction on RS distribution

Figure 3-5 *a* and *b* show the predicted RS across the plate width, in the upper and lower surfaces, after rolling with 100 kN load at 55 mm from the edge, before and after unclamping, in the frictionless and with friction models, respectively. Due to the stretching caused by the roller in the longitudinal direction, and the restraint caused by the surrounding material, the portion of material in the rolling path had compressive RS, while tensile RS was present at either side of the rolling path to counterbalance the compressive one.

In the frictionless models the lower surfaces were fully constrained in the out-of-plane direction during rolling; consequently, the RS was largely redistributed after unclamping when the plates bent, as shown in figure 3-5 *a*. Conversely, the models in which friction was included, the out-of-plane displacement was restrained by imposing one atmosphere pressure towards the backing support, to simulate the vacuum clamps used in the experiments; consequently, the RS before and after unclamping were similar, and they slightly redistributes after unclamping, as shown in figure 3-5 *b*. However, after unclamping, the compressive RS in the rolling path reduced its gradient between upper and lower surfaces in both set of models.

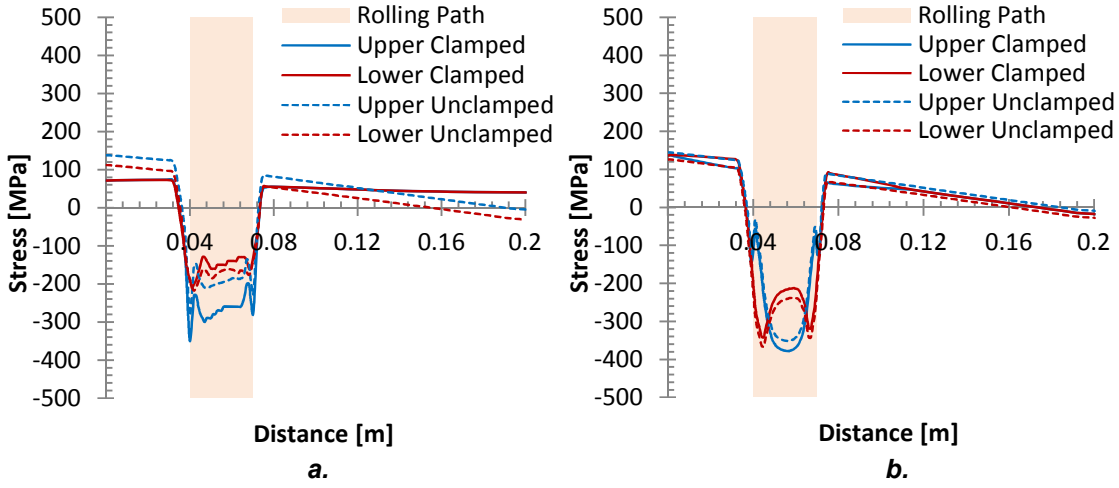

Figure 3-5 **Longitudinal RS, in the upper and lower surfaces, after rolling at 55 mm with 100 kN along the measuring path, before unclamping, and after unclamping, for the *a.* frictionless, and *b.* with friction models.**

Since rolling was not applied in the middle plate width, but always closer to one of the edges, it caused that more tensile RSs were presented in the closer edge (0 mm) rather than in the opposite parallel one, as shown in figure 3-5. When the plates of frictionless models were unclamped, the tensile RS in the closer edge increased slightly its magnitude, while in the farther edge reduced it. However, in the models with friction no significant differences were observed after unclamping in those regions.

Effect of rolling on the through-thickness RS distribution and distortion

Figure 3-6 *a* to *d* show the longitudinal compressive RS across the thickness, in the frictionless and with friction models after 100 and 200 kN rolling models. Only a section of the plates is shown, due to limitation in the space, and to improve resolution. All the plates were clamped when the RSs were obtained. In the models with friction included and large rolling loads applied (200 kN), the peak of the compressive RS was produced between the middle thickness and the upper surface of the workpiece. This was due to the constraints applied by the frictional forces in the surface of the plate during rolling, which reduced the plastic strain in the contact surfaces, forcing the plastic deformation to occur deeper in the core of the material. In the frictionless model on the other hand, the compressive peak RS occurred close to the roller edges due to the high shear forces generated during rolling between the stretched material in the rolling path and the surrounding metal beside that region, in particular in the edge that was close to the welding edge

With 100 kN, the frictionless model produces a compressive region in the rolling path (see figure 3-6 *a*), which is slightly wider close to the lower surface; therefore, when the plate was unclamped, part of this RS was relaxed bending the plate upwards (towards the roller surface). On the other hand, in the model with friction, the 100 kN load caused a compressive region with about the same width across the thickness (see figure 3-6 *b*); however, highly compressive RS was induced in the upper surface, thus, when the plate was unclamped, it deformed downwards (opposite to the rolling surface). With 200 kN the frictionless models induced a wider compressive region close to the upper

surface (see figure 3-6 *c*), causing downwards deformation when the plate was unclamped. In the models with friction and rolled with 200 kN, the compressive RS close to the backing-bar (lower surface) was induced in a larger region than in the upper surface (see figure 3-6 *d*); consequently the plate deformed upwards when it was unclamped.

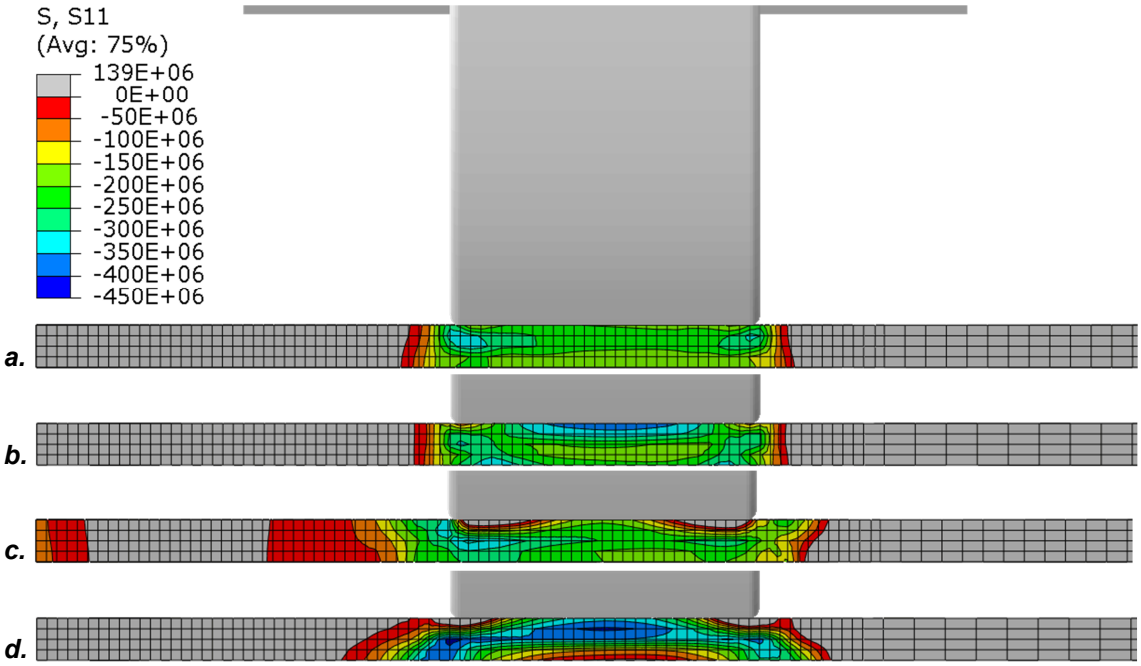

Figure 3-6 **Contour plot of longitudinal compressive RS after rolling the plates with 100 kN load *a.* frictionless, *b.* with friction models; and 200 kN *c.* frictionless and *d.* with friction models (Units is Pa).**

Validation of RS distribution

Figure 3-7 *a* and *b* show a comparison between the experimental and predicted longitudinal RS, of the frictionless and the one with friction models, after rolling and unclamping the steel plates with 100, and 200 kN, respectively. Although both cases were in agreement with the experimental results, some discrepancies were observed. The predicted longitudinal RS after 100 kN rolling were slightly wider than the experiments, while the 200 kN one matched better the width of the compressive region. The compressive RS in the middle of the rolling path was underestimated by the models with 100 kN load. With 200 kN the model with friction matched the RS almost across the entire width, while the

frictionless model underestimates the compressive RS in the middle of the rolling path, and the tensile one near the closer edge (0 mm), as shown in figure 3-7 *b*.

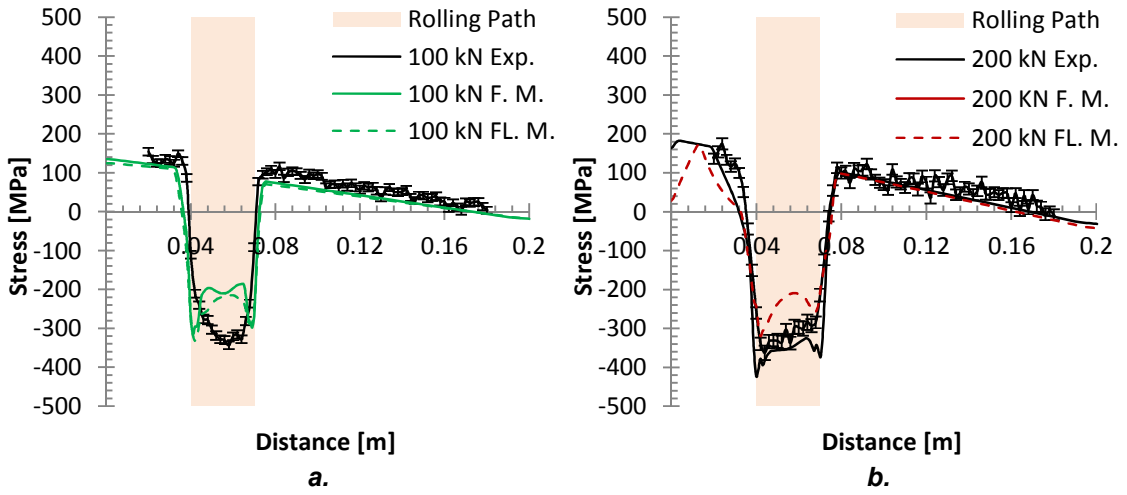

Figure 3-7 **Comparison between experimental (Exp.) and predicted longitudinal RS of the model with friction (F. M.) and frictionless (FL. M.) with two rolling loads: *a.* 100, and *b.* 200 kN**

Distortion

In the pre weld rolling experiments, the rolling process deformed the plates upwards, towards the rolling surface, in all the cases, regardless the rolling distance and the load applied. Figure 3-8 *a* and *b* show the predicted deformed

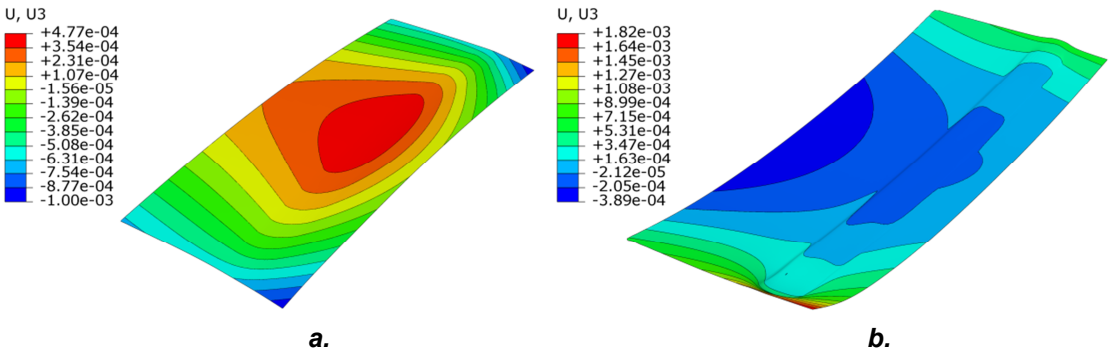

Figure 3-8 **Contour plots of the deformed plates of the models with friction, after rolling with: *a.* 100, and *b.* 200 kN rolling load (both rolled in the upper surface, and magnified X20). Dimensions in millimetres.**

plates, in the models with friction, after rolling the upper surface with 100 and 200 kN, respectively. In those models the behaviour of the experiments was not always observed, *i.e.* the models rolled with 200 kN load, had the same distortion shape of the experiments, deforming towards the rolled surface, while with loads equal or below 100 kN, the plates deformed in the opposite direction, as shown in figure 3-8. The explanation of the distortion in the models was already made in the previous paragraphs; however, the reasons of the discrepancies between experimental and predicted results were not clear, with the experimental data available.

Plastic strain

Figure 3-9 *a* and *b* show the contour plots of the longitudinal plastic strain through the plate thickness, after rolling with different loads and unclamping, in the frictionless and with friction models. The roller was added to the contour plots only to show its position during rolling; the plastic strain was plotted after unclamping, i.e. after rolling was performed. Only the left section of the plates is shown in the figure, due to limitations of space. In the other side of the plates (at the right of the roller), the plastic strain was close to zero, as shown in figure 3-10. The orange band under figure 3-9 *d* represents the position of the backing-bar under the plates (with friction models only).

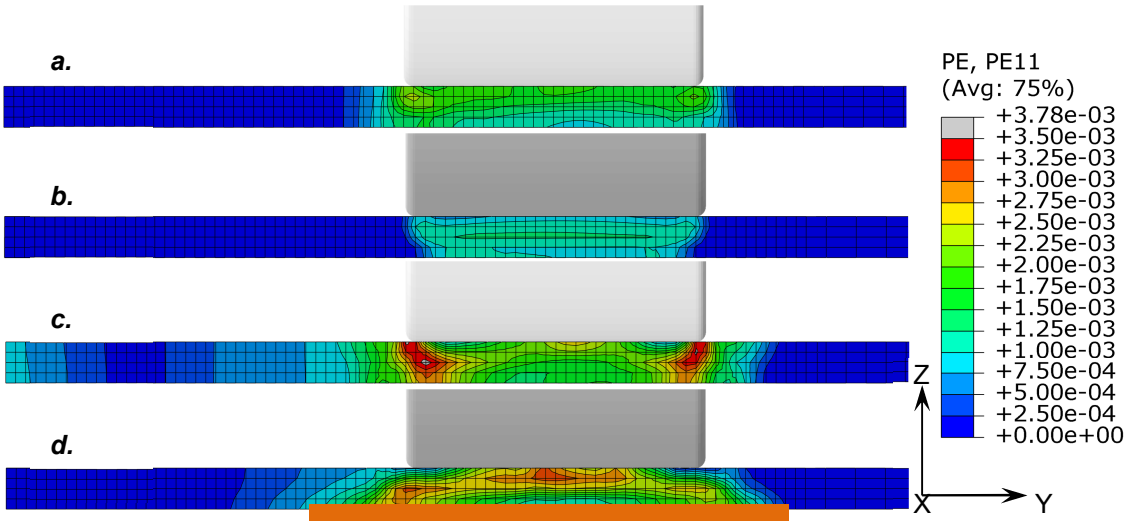

Figure 3-9 Contour plot of longitudinal plastic strain after rolling with 50 kN load *a.* frictionless, *b.* with friction; and 200 kN *c.* frictionless, *d.* with friction.

Figure 3-10 *a* and *b* show comparisons, of the variation of the predicted longitudinal plastic strain in the upper and lower surfaces across the plate width, between the frictionless and with friction models, after rolling at 55 mm from the edge, with 50, and 200 kN load, respectively, and unclamping.

The plastic strain was positive under the rolling path, showing the stretching of the material in the longitudinal (rolling) direction. As rolling was acting only on one surface, it caused an asymmetrical plastic strain through the thickness, as shown in figure 3-9, and figure 3-10. When rolling with relatively low load (50 kN), the longitudinal plastic strain was limited to the rolling path. As rolling load increased, the longitudinal plastic strain increased in magnitude, and a wider region was deformed plastically. With the highest load (200 kN), plastic deformation was observed along the edge that was subsequently welded (see 0 mm in figure 3-10 *b*.).

The low loaded models predicted longitudinal plastic strain which had a similar magnitude for both with friction and frictionless analyses. However, the frictionless model had larger plastic strain in the upper surface than in the lower one (in the rolling path), while the model with friction had the opposite behaviour, as shown in figure 3-10 *a*. This is supported by results from Cook and Larke [201]. They studied the influence of friction in compressive

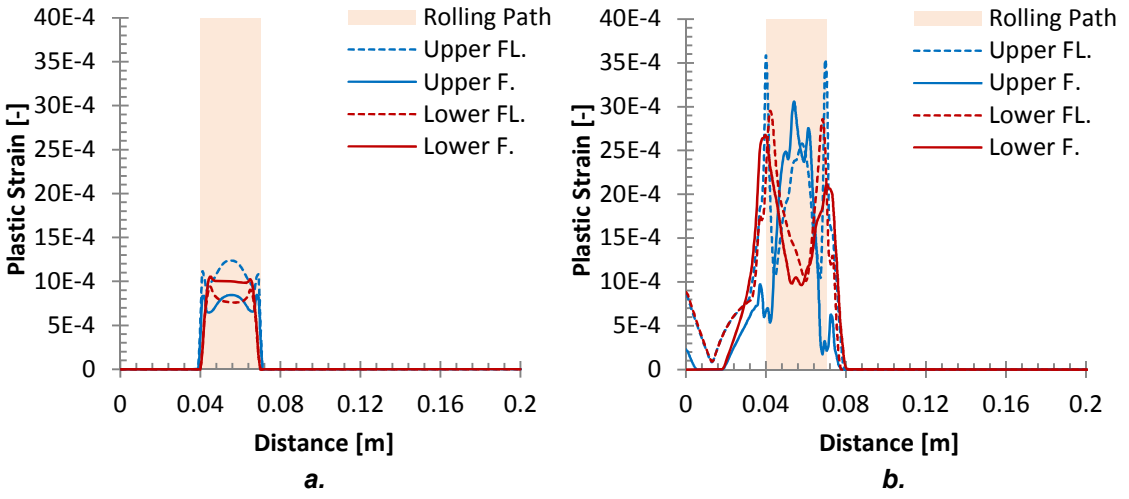

Figure 3-10 Comparison of longitudinal plastic strain in the upper and lower surfaces after rolling at 55 mm between frictionless (FL.) and with friction (F.) models, with different loads: *a.* 50, *b.* 200 kN and unclamping.

deformation of cylindrical samples [202]. A schematic representation of their experiments is shown in figure 3-11 *a* to *c*. Figure 3-11 *d* shows the compression curves of copper cylinders (Ø = 19.05, height = 6.35 in) between different tool surface finishing, namely, turned, ground, and lapped, where lapped has the lowest friction coefficient, and turned the highest one [201].

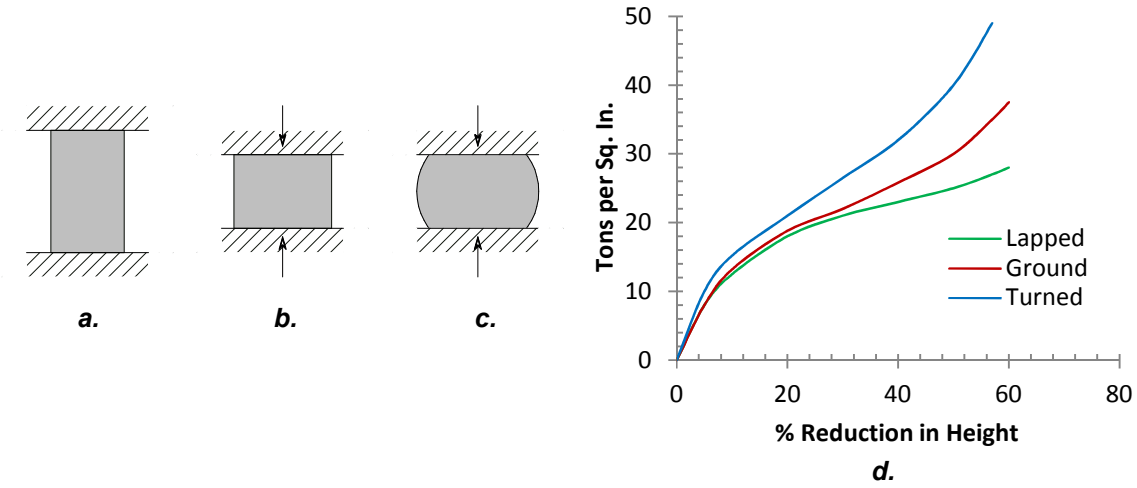

Figure 3-11 Schematic representation of the influence of friction in compressive deformation, *a.* before compression, *b.* frictionless compressed, *c.* sample compressed with friction [202]. *d.* Compression curve for copper cylindrical samples tested between tool with different surfaces finishing, namely, turned, ground, and lapped (adapted from Cook and Larke [201]).

The presence of friction restrains the material in the contact area, reducing the plastic strain in the surface, as shown schematically in figure 3-11 *c*. Since the friction coefficient in the pre-weld rolling model was larger in the upper surfaces, these surfaces were more restrained than the lower ones.

As load increases, friction plays a more important role in the plastic strain, as shown in figure 3-11 *d*. When the load was increased to 200 kN, the longitudinal plastic strain in the upper and lower surface affected a wider portion of the material, as shown in figure 3-10 *b* and figure 3-9 *c* and *d*. The frictionless model increased the longitudinal plastic strain width approximately the same in both surfaces, but the model with friction increased it mainly in the lower surface, as shown in figure 3-10 *b* and figure 3-9 *d*. In addition, the frictionless model causes large plastic deformation in the closer edge (0 mm), while the

model with friction causes minor plastic deformation in that edge, but only in the upper surface. It is thought that the absence of friction and the over-constraint of the boundary conditions, in the frictionless models, increased the plastic strain next to the roller path, causing those peaks observed in figure 3-10 *b* in the upper surface when high pressure was implemented.

Figure 3-12 *a* shows the non-uniform normal plastic strain in the rolling surface after applied the 200 kN rolling load, while figure 3-12 *b* shows the ripple marks observed in the experiments after pre-weld rolling with 200 kN. Figure 3-12 *c* shows the normal plastic strain of one node of the upper surface, in the middle of the weldment length, in the rolling path, after rolling with 200 kN. Figure 3-12 *c* to f show a schematic representation of the formation of ripple marks on the rolled surface.

The larger rolling loads made the roller penetrate deeply in the material during rolling, increasing the built-up material in front of it, as shown in figure 3-12 *c* and *d*. This caused local work hardening in the portion of material in front of the roller. Due to the work-hardened material, the roller was not able to induce the same plastic deformation, since the rolling load was constant, as shown schematically in figure 3-12 *d*. When the material reached a point where it cannot work-harder any further, the roller jumped and then the roller started rolling material that has not been work-hardened to the same degree, as shown in figure 3-12 *e* and *f*. Consequently ripple marks were observed in the surface of the material after rolling with large rolling loads, as shown in figure 3-12 *a* and *b*. Note that this transient rolling process was not observed with lower rolling loads. In addition, numerical simulations conducted by Sun et al. [101], have shown that localised rolling performed with constant rolling penetration (instead of the rolling load), caused variation in the vertical rolling force, which is in agreement with the ripple marks observed in figure 3-12 *a* and *b*.

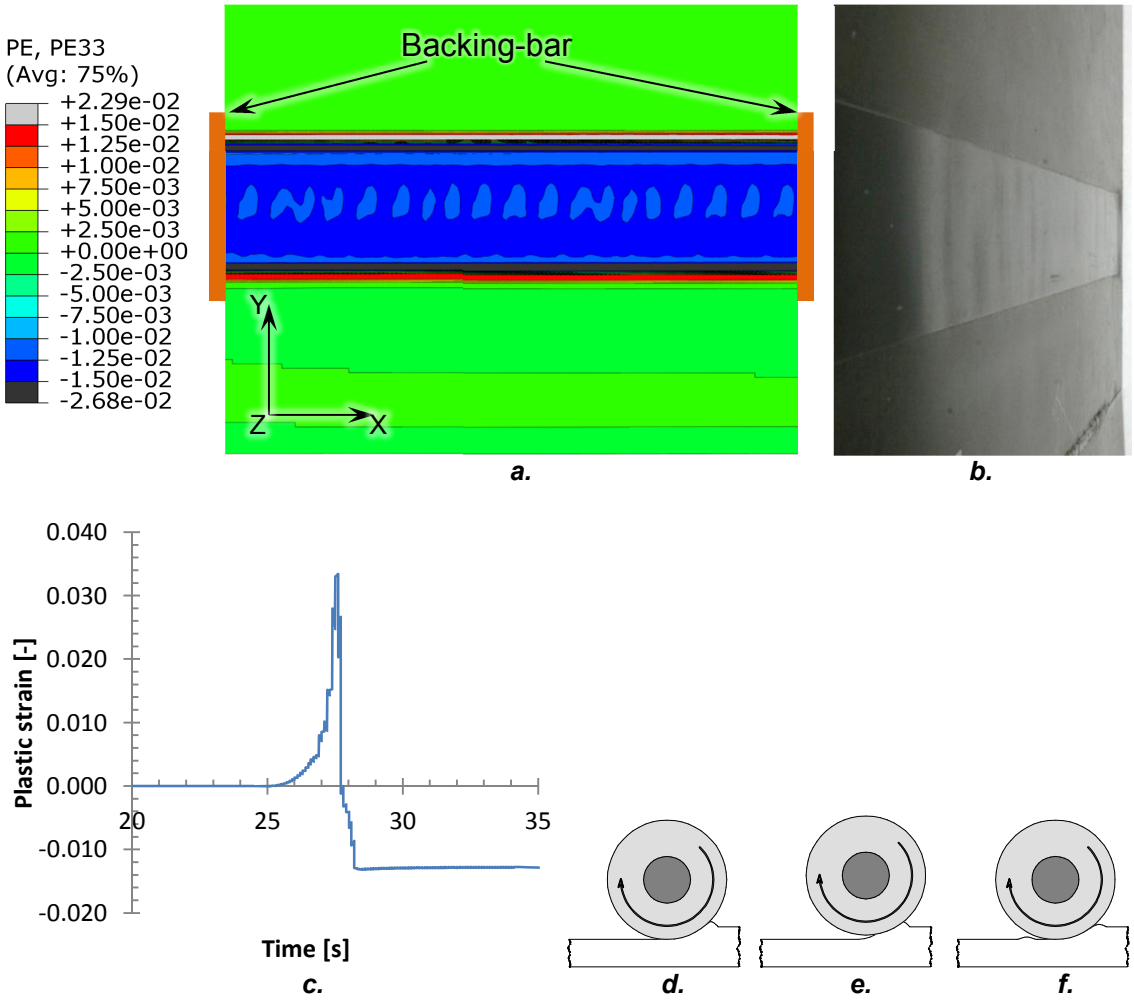

Figure 3-12 ***a.*** **Normal plastic strain in the upper surface after rolling with 200 kN load;** ***b.*** **ripple marks on the rolling surface after 200 kN rolling.** ***c.*** **Normal plastic strain of one surface node in the rolling path in half of the weldment length.** ***d.*** **Built-up of material in front of the roller;** ***e.*** **transient rolling;** ***f.*** **formation of ripple marks on the rolled surface.**

3.3.2 Results from pre-weld rolling (after welding)

Residual stress

Figure 3-13 *a* and *b* show the difference in the longitudinal RS, in the middle plane, after welding and unclamping with no rolling (as-welded), and after pre-weld rolling the upper and lower surfaces with loads of 100 and 200 kN, using the models with friction included. The models had virtually identical RS distribution regardless the surfaces that was pre-weld rolled (upper or lower), when 100 kN was used. In addition, pre-weld rolling with 100 kN seems not to

affect the tensile RS generated by welding. However, with 200 kN the tensile RS peak is slightly reduced when the plate was pre-weld rolled on the lower surface, but no effect was observed when pre-weld rolled in the upper surface.

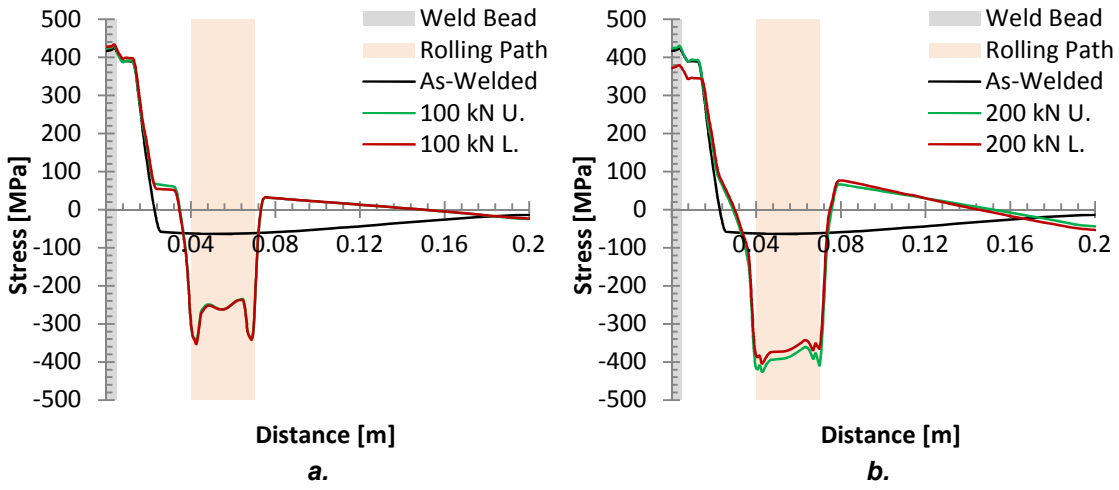

Figure 3-13 Longitudinal RS after pre-weld rolling in the upper (U.), and lower (L.) surfaces in the models with friction included, with: *a.* 100, and *b.* 200 kN, with 55 mm rolling distance.

Figure 3-14 shows the predicted longitudinal RS in the middle thickness of the weldments across the measuring path (see figure 3-1 *a*), in the frictionless models, after pre-weld rolling with different rolling loads and sides (upper and lower surfaces), at different distances from the weld seam. The pre-weld rolled model at 15 mm from the centreline had some reduction of the width of the tensile hill of the RS, but its peak was 100 MPa detrimentally increased respect the as-welded condition, as shown in figure 3-14 *a*. Since rolling at 15 mm from the edge produced tensile RS next to the rolling path (between 0.04 and 0.14 mm in figure 3-4 *a*), and in the same region the weld produced compressive RS; the compressive RS produced by the latter was counteracted by the tensile RS induced by rolling, reducing slightly the tensile peak induced by welding. At all the others rolling positions the tensile peak was marginally altered, but no significant reduction was observed, because the compressive RS induced by rolling was not sufficiently close to modify the RS caused by welding.

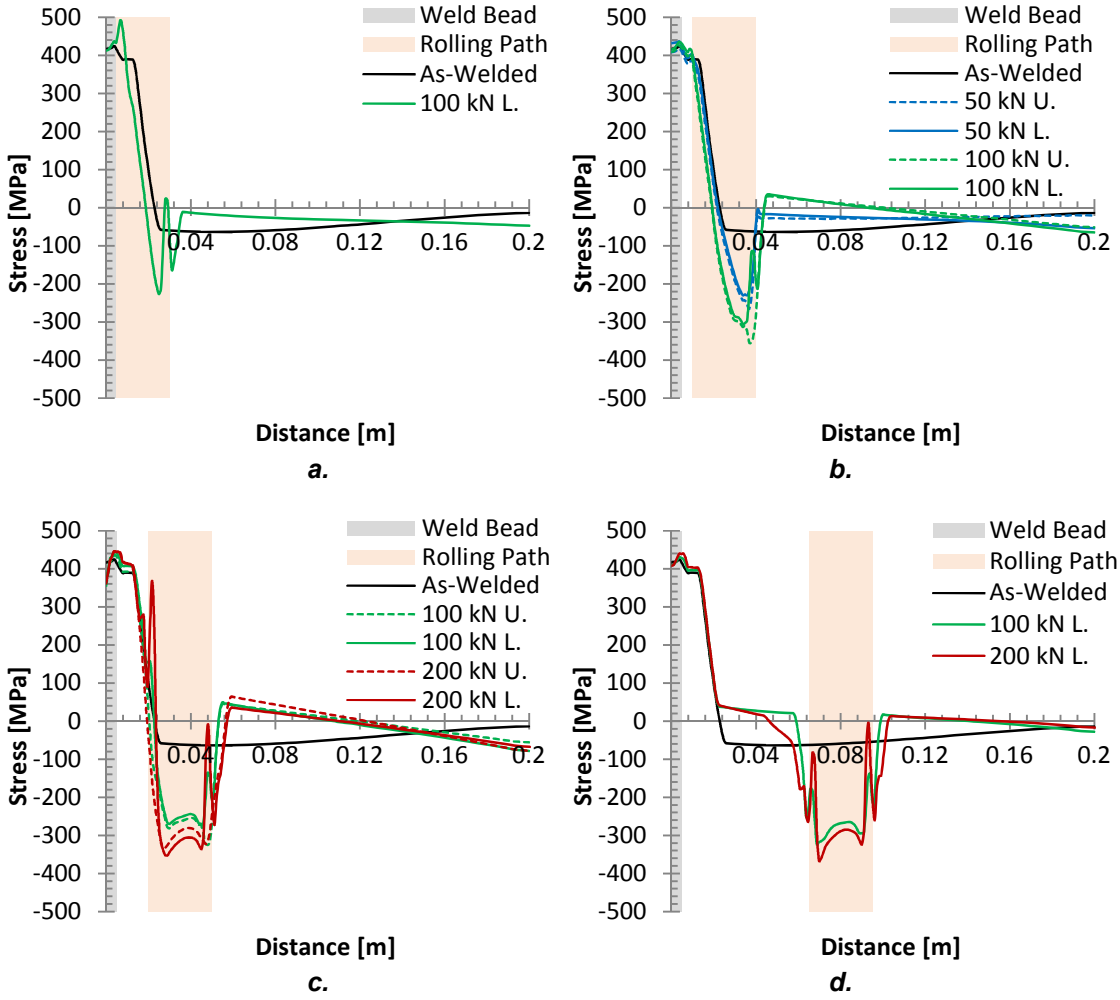

Figure 3-14 Predicted longitudinal RS in frictionless models after pre-weld rolling with different load in the upper (U.) and lower (L.) surfaces at different distances from the weld seam, namely, *a.* 15, *b.* 25, *c.* 35, *d.* 80 mm.

Figure 3-15 shows a comparison of the longitudinal RS between the experimental measurements, and predicted results of the model with friction included, after pre-weld rolling with 200 kN in the lower surface, at 55 mm from the weld centreline. The model was able to predict the compressive RS peak in the rolling path. However, the model was not able to predict the width of the tensile hill. As explained in chapter 2 the predicted temperature distribution did not match accurately the one produced in the experiments; consequently, the tensile peak and width of the welding RS were not precisely predicted. Nevertheless, the model was able to predict qualitatively the longitudinal RS distribution.

The longitudinal RS caused by the welding process is slightly modified by the already present RS induced by rolling. The compressive RS induced by the roller in the rolling path, induced tensile RS in the plate edge, as shown in figure 3-7. This tensile RS interacts with the compressive RS formed in front of the torch during welding, potentially reducing the compressive plastic deformation at that location. However, as that location is melted during welding, there is no beneficial effect in reducing the compressive strain in front of the torch. At the same time, the temperature in the surrounding material increased, and in a certain region close to the weld pool the metal was annealed; therefore, the stress history of the plates was forgotten in those regions.

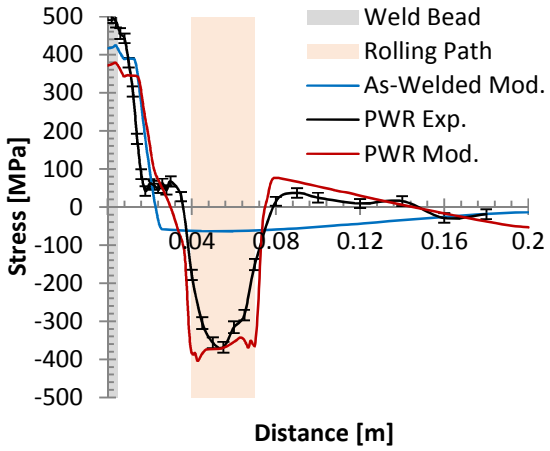

Figure 3-15 Comparison of the longitudinal RS between experimental (Exp.) measurements, and predicted results, after pre-weld rolling with 200 kN in the lower surface, at 55 mm from the centreline (model with friction included only).

Plastic strain

Figure 3-16 shows the longitudinal plastic strain after pre-weld rolling and only rolling the model with friction included, with 200 kN, at 55 mm from the weld centreline, and the as-welded model. Although the longitudinal plastic strain after rolling and subsequent welding was significant reduced, as shown in figure 3-16, the longitudinal RS was not, as shown in figure 3-15. The tensile RS in welding are formed due to the mismatch of the plastic strain in different regions of the weldment [10,34]. When pre-weld rolling was applied, the material was

locally stretched in the rolling direction (parallel to the welding direction). During welding the rolled plates, the material next to and along the torch path, is annealed and melted, reducing the benefit of the localised rolling.

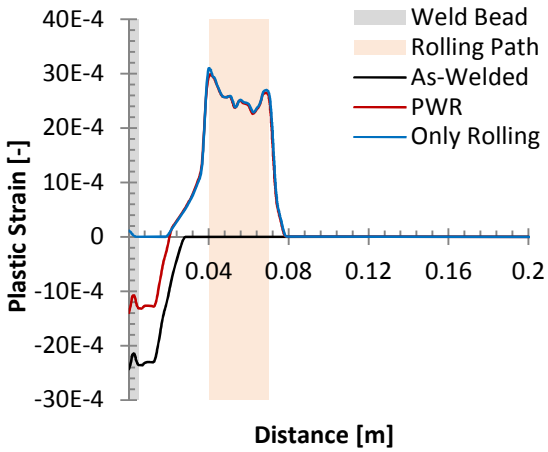

Figure 3-16 Comparison of the predicted longitudinal plastic strain after pre-weld rolling (PWR) and only rolling with 200 kN at 55 mm from the centreline, and the as-welded model (model with friction included only).

Distortion

Figure 3-17 *a* show the predicted and measured peak out-of-plane distortion after pre-weld rolling, with different rolling loads in the upper surface, at different rolling positions, while figure 3-17 *b* in the lower surface. The predicted results underestimate the distortion observed in the experiments in all the cases studied. However, in both experiments and predicted results, the out-of-plane distortion was less significant or even detrimental when the plates were pre-weld rolled in the upper surface (welding and rolling in the same surface), as shown in figure 3-17 *a*. When the plates were pre-weld rolled on the lower surface (rolled in the opposite surface of welding), the out-of-plane distortion was ~36 % reduced with 200 kN at 55 mm from the centreline. Likewise, the models pre-weld rolled in the lower surface showed larger peak out-of-plane distortion reduction, as shown in figure 3-17 *b*. The maximum out-of-plane distortion peak reduction in the models was ~57 % with 100 kN at 55 mm from the centreline in the frictionless models, while in the models with friction was ~62 % with the same rolling conditions.

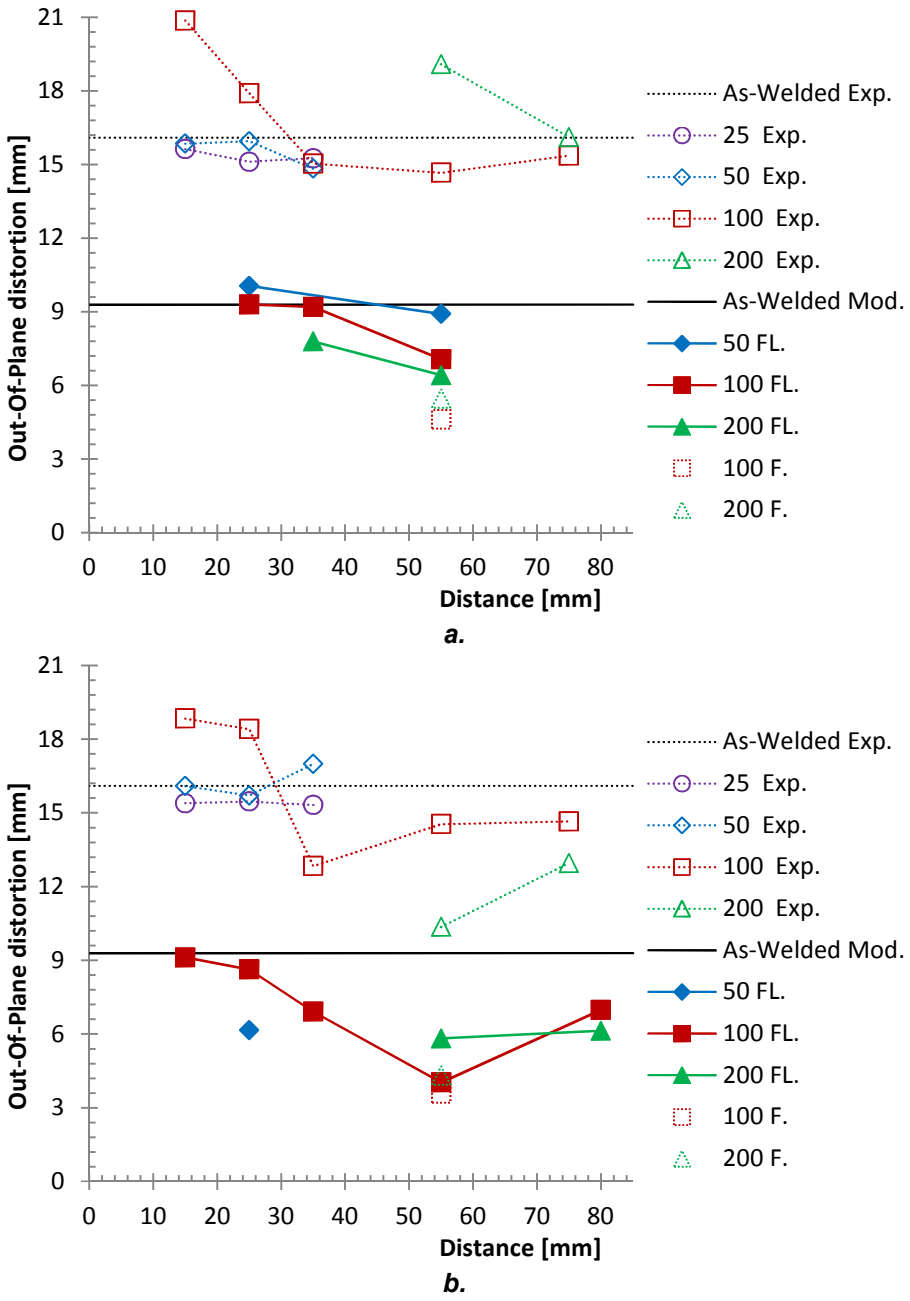

Figure 3-17 **Peak out-of-plane distortion after pre-weld rolling in the experiments (Exp), frictionless (FL), and with friction (F) simulations in: *a.* upper, and *b.* lower surfaces.**

As already explained before, the experimental rolled plates deformed always towards the rolling surface, *i.e.* when the roller was applied in the upper surface the plate bent upwards, while when the plate was rolled in the lower surface the plate bent downwards. On the other hand, the welding process bent the weldment always in the same upwards direction (direction facing the torch).

Therefore, when the welding and rolling were applied in the same surface, the distortion caused for each process (welding and rolling) added up. Conversely, when welding was applied in the opposite surface of the rolled one, the distortions counteracted one another, causing some distortion reduction.

For most of the experimental conditions investigated only one sample was produced with no replications; consequently, no certainty can be provide for a realistic comparison between predicted and experimental measurements.

3.3.3 Results from post-weld heating

Figure 3-18 *a* and *b* show the contour plot of the temperature distribution caused by induction heating with the narrow (20×20 mm), and wide (30×20 mm) heat sources, respectively. As the heat flux was the same in both cases, the peak temperatures are similar and did not exceed the annealing point of the material. An approximation of the minimum temperature required to remove the compressive plastic strain was made with average material properties. It suggested that approximately 250°C can potentially remove the compressive RS induced by 200 kN rolling. The wider heat source produced a 250°C isotherm as wide as the roller prints, while the narrow heat source was smaller.

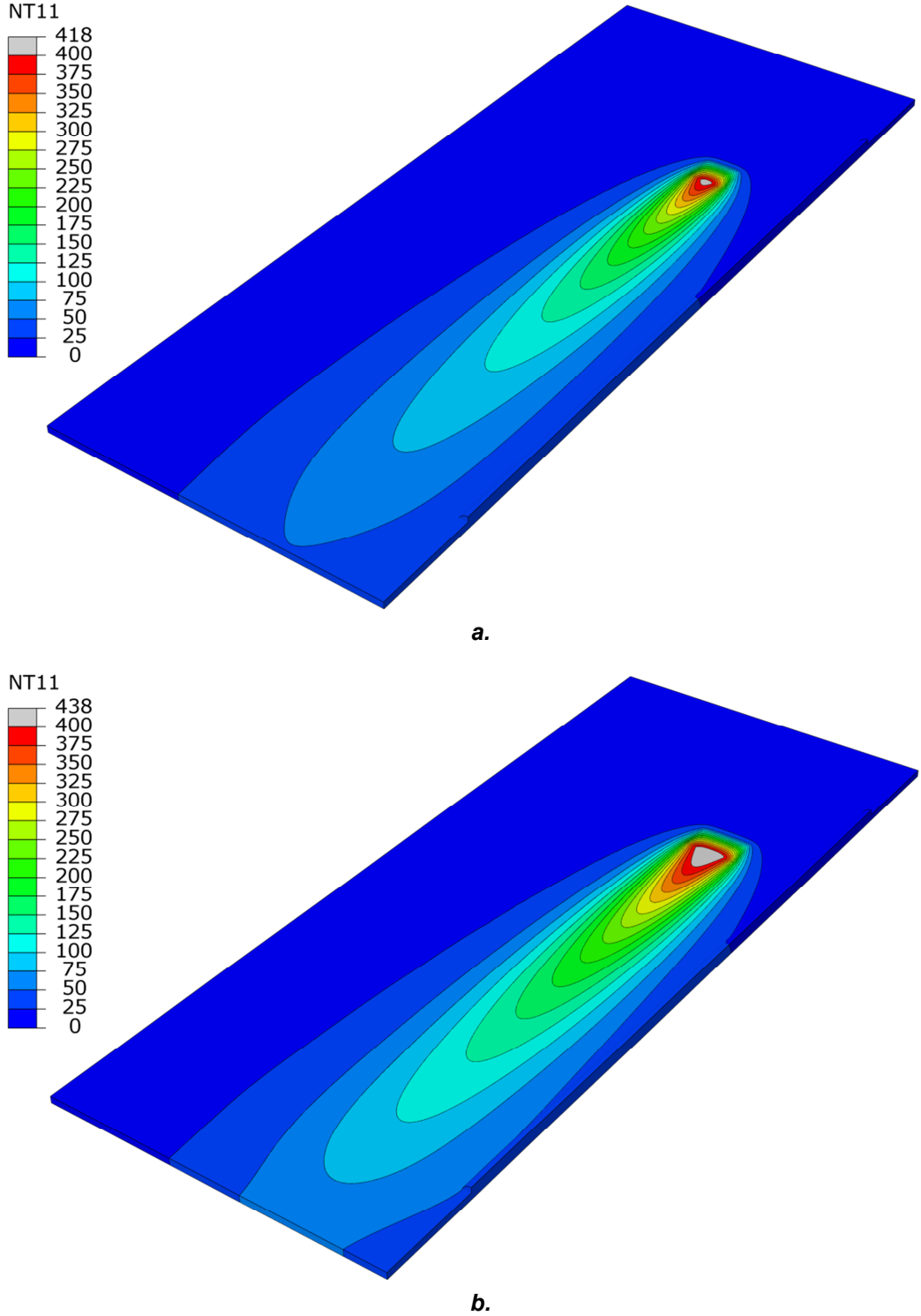

Figure 3-18 Contour plots of temperature distribution with: *a.* narrow, and *b.* wide inducted heat (temperatures in °C).

Figure 3-19 *a* shows a comparison of the longitudinal RS after welding, and after applying the wide induction heating subsequently to welding, without

rolling. The tensile RS peak caused by welding is largely reduced by the post-weld heating step. However, it induces a tensile hill in the induction heating path. Figure 3-19 *b* shows a comparison of the longitudinal RS after pre-weld rolling with 200 kN, and post-weld heating with the narrow and wide heat sources. In all these cases rolling was applied to the lower surface. The narrow heating reduced the welding RS tensile peak to about half, but it left two large compressive RS peaks at each side of the rolling path. The wide heat source, on the other hand, reduced to about a quarter the welding RS tensile peak, and it removed almost completely the compressive RS induced by rolling.

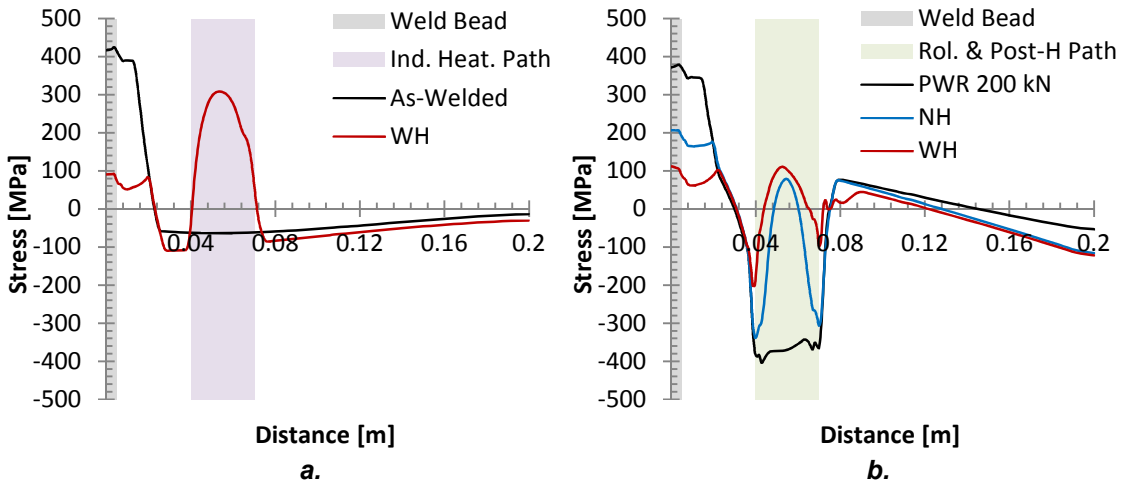

Figure 3-19 Comparison between longitudinal RS after *a.* welding and post-induction heating, and *b.* pre-weld rolling (PWR) and post-induction narrow (NH) and wide (WH) heating.

Figure 3-20 *a* and *b* show the longitudinal RS after pre-weld rolling the upper and lower surface, respectively, and post-weld heating with the wide heating source. Figure 3-20 *c* shows the longitudinal plastic strain after pre-weld rolling, post-weld heating, and only rolling with 200 kN, at 55 mm from the centreline, and the welding alone results. The reduction of the longitudinal RS peak caused by welding was virtually the same, regardless the rolling loads (even with no rolling). However, the models with low loads generate a higher tensile RS hill in the induction heating path. No significant differences were observed in the longitudinal RS distribution of the models rolled in the upper and lower surfaces, when the same load was used.

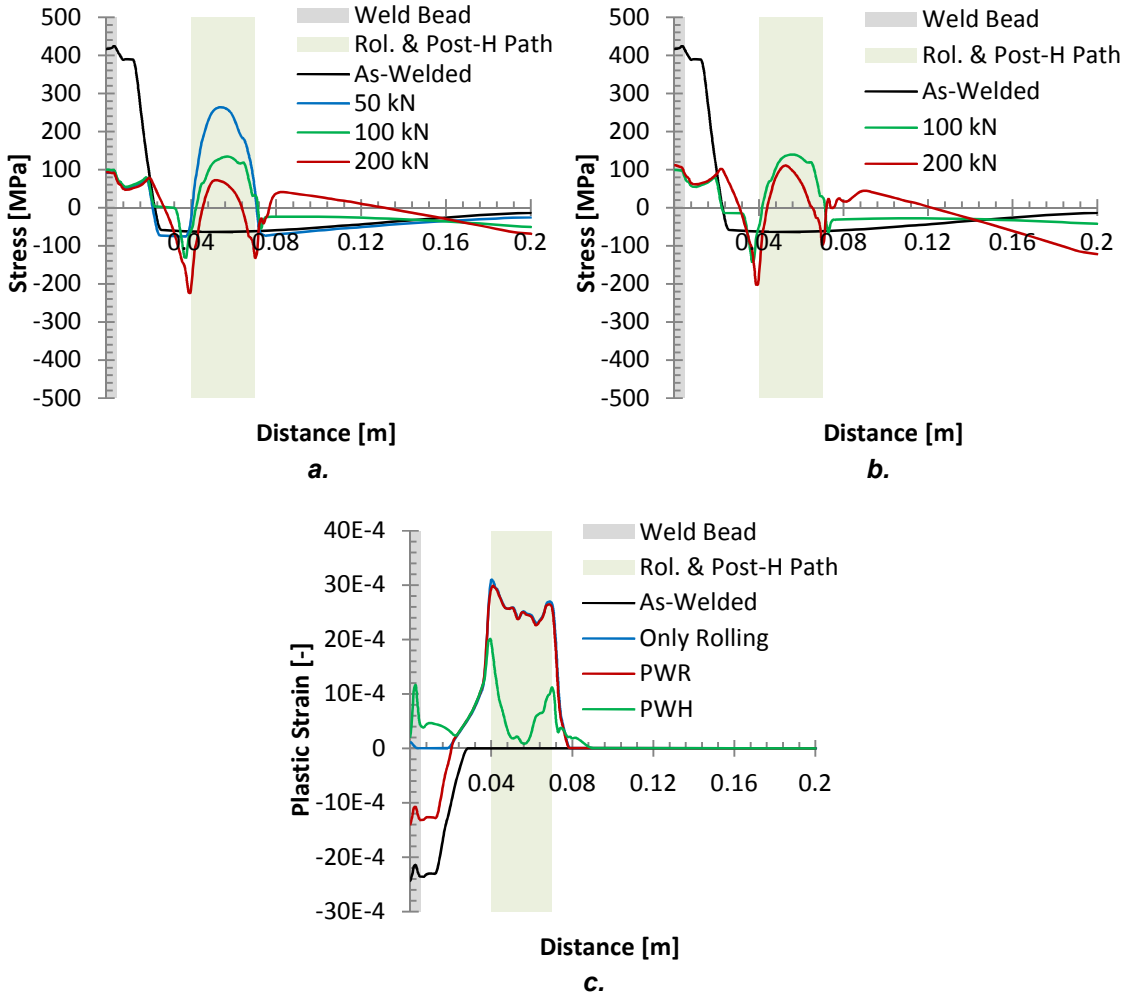

Figure 3-20 **Longitudinal RS after pre-weld rolling in the: *a.* upper, and *b.* lower surface, and post-welding heating with the wide heating source. *c.* Longitudinal plastic strain after pre-weld rolling (PWR) post-weld heating (PWH), and only rolling with 200 kN, at 55 mm from the centreline, and only welding.**

The induction heating as well as the welding process induce negative plastic strain, but in different regions of the weldment, while rolling induces positive one. As explained previously, the pre-weld rolling reduced significantly the plastic strain produced by only welding (see figure 3-16*)*. However, pre-weld rolling by itself did not modify significantly the tensile RS generated by welding (see figure 3-13 and figure 3-14). Post-weld heating on the other hand, induced negative plastic strain in the rolling paths which reduces the magnitude of the positive plastic strain added by rolling (see figure 3-20 *c*). Consequently, the plastic strain in the weld was further reduced, as well as the longitudinal welding RS.

The induction heat step was designed to reduce the welding RS tensile peak and the compressive RS of the 200 kN rolling processes; therefore, when the induction heat step is added to the models rolled with 50, and 100 kN loads, the reduction of the compressive RS region is not optimal. It is thought that comparable RS distribution, to the one obtained in the 200 kN rolling load models, can be obtained in the 50, and 100 kN load models, with lower heat induction power.

Figure 3-21 shows the predicted peak out-of-plane distortion after pre-weld rolling plus post-weld heating with different rolling loads after rolling in the upper and lower surfaces. The out-of-plane distortion peak reduction after post-weld heating the pre-weld rolled models was larger than the only pre-weld rolling results. The maximum out-of-plane peak distortion reduction (~83 %) was obtained by rolling in the lower surface with 100 kN at 55 mm from the centreline. The post-weld heating induced tensile RS in the rolling path, reducing the compressive RS present in that area, and due to the self-balanced nature of the RS, the tensile RS peak in the weld was also reduced, as shown in figure 3-20 *a* and *b*. As the magnitude of the longitudinal RS is reduced, the bending moment which causes the out-of-plane distortion was also reduced. With the post-weld heating, the surface rolled is less important than in the pre-weld rolling analysis, since in the former the RS is redistributed in a beneficial way, while in the later is not.

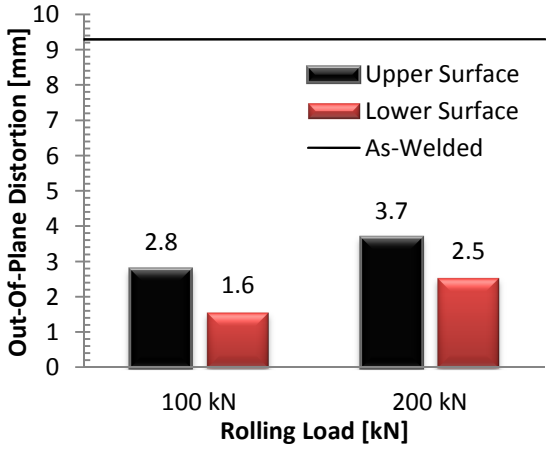

Figure 3-21 Predicted peak out-of-plane distortion after pre-weld rolling plus post-weld heating, and as-welded peak out-of-plane distortion.

3.4 Conclusions

Rolling has been investigated prior to welding to determine whether it could be used to reduce distortion and residual stress. The work showed that:

- The compressive RS induced by rolling in the rolling path are equilibrated by tensile RS beside the rolling path, along the edge that is subsequently welded.
- The rolling models provided a very good estimate of the RS, in particular the models with friction included.
- High rolling loads (200 MPa) can cause ripple marks in the rolling surface due to the build-up of material in front of the roller and the work-hardening of the material.
- Pre-weld rolling does not reduce the tensile RS produced by welding in the weld bead and surroundings.
- Pre-weld rolling can marginally reduce the out-of-plane distortion, when rolling is applied in the lower surface at 55 mm from the centreline. Rolling the lower surface induced bending of the plates in the opposite direction that the bending distortion induced by welding; therefore, the bending moment induced by pre-weld rolling in the lower surface, slightly reduced the distortion caused by welding.
- Post-weld heating the pre-weld rolling samples can potentially reduce the tensile peak produced by welding, and redistribute the RS in a range from 100 to -200 MPa. However, this technique needs to be calibrated to the particular welding and rolling conditions.
- Post-weld heating the pre-weld rolling samples can potentially reduce the out-of-plane distortion by about 83%.

Chapter 4 Post-Weld Rolling

4.1 Introduction

As explained in chapter 1 post-weld rolling (**PoWR**) is one of the stress engineering techniques in which rolling induces positive local plastic strain in the welding direction, counteracting the negative plastic strain generated during welding [93,98,102]. PoWR has been applied on top of the weld or next to it, by means of a single roller applied in the upper or lower surface, as described by Wescott [107]. However, this technique can be applied by using two rollers which roll simultaneously the upper and lower surfaces, as described by Guan [94], and other researchers [101,103]

Rolling to reduce RS has received relatively little attention in the literature. Kurkin and Tsyao [105] analysed its beneficial effect in titanium alloys (OT4-1, VT-1, VT5-1), while Kurkin and Anufriev [86] in aluminium alloys (Amg6 and 1201), obtaining significant RS reduction. Most recently Altenkirch *et al.* [98] experiments have shown its benefit in FSW aluminium plates. In addition, numerical simulation conducted by Wen *et al*. [102], Yang and Dong [103], have obtained results in agreement with the experimental findings. Experiments conducted by Coules *et al.* [2,3,203] demonstrated how PoWR can reduce distortion, and RS in Gas Metal Arc (**GMA)** welded S355 steel plates.

This chapter analyses the PoWR parameters such as, rolling load, roller position and width and their influence on the welding RS and distortion, based on Coules *et al.* experiments. Additionally, the influence of the weld bead reinforcement in the RS distribution, and also the influence of friction between the backing-bar, workpiece, and roller were investigated. The models were divided into two main groups, rolling on top of the weld bead using a grooved roller, and rolling next to the weld bead with a dual flat roller.

4.2 Methodology

All the models of this chapter were based on the experiments and neutron diffraction measurements conducted by Coules *et al.* and described

elsewhere [2,3,203]. A description of the rolling experiments, residual stress measurement, and distortion calculation can be found in appendix d.

The models were built with Abaqus Standard version 6.9 as a sequentially coupled thermal-mechanical analysis. They consist of two main steps, namely, welding thermal-mechanical step, to generate the inherent welding RS, and the rolling step to alter the RS formed in the previous step. The welding heat transfer analysis was run separately, and it was already discussed in chapter 2, as well as the welding mechanical models. The welding mechanical results (before unclamping the weldment) were used as the initial conditions for the rolling mechanical models discussed in this section.

These models were composed of three parts, namely, workpiece or plate, roller(s), and backing support. The workpiece was modelled as a 3D solid deformable body, with mild steel S355 material properties, as for all the models developed in this thesis. A description of the material properties implemented to model the S355 steel can be found in appendix a. The rollers and backing support were modelled as rigid shell bodies; therefore, they were not deformable.

Owing to symmetry, only half geometry was considered in the numerical models, as for the welding heat transfer and mechanical ones, allowing an important reduction of the computational time. Figure 4-1 shows half of the workpiece and the symmetry plane which splits the workpiece. The workpiece adopted the dimensions, mesh, and element types implemented in the welding mechanical analysis, described in chapter 2. The high-density mesh in and around the weld bead regions, as shown in section AA in figure 4-1, was required to obtain good contact behaviour between the rollers and the plate, and it helped to capture details of the stress distribution in these regions. Note that a preliminary mesh dependency study was performed to ensure the mesh was fine enough to have mesh independent results.

The symmetric boundary conditions applied in the welding thermal-mechanical analysis were used for the entire rolling analysis. Unlike the welding thermal-mechanical steps, the vacuum clamps were modelled by applying one

atmosphere pressure (101325 Pa) on the lower surface of the workpiece towards the backing support. In addition, to simulate the friction interaction of the backing-bar and the workpiece, different isotropic constant friction coefficients were considered. These were applied in a strip of 48 mm width in the middle of the workpiece, along its lower surface (represented by the 24 mm wide region in figure 4-1). The remaining area in the bottom plane was considered frictionless. Moreover, different isotropic constant friction coefficients were considered between the rollers and the workpiece.

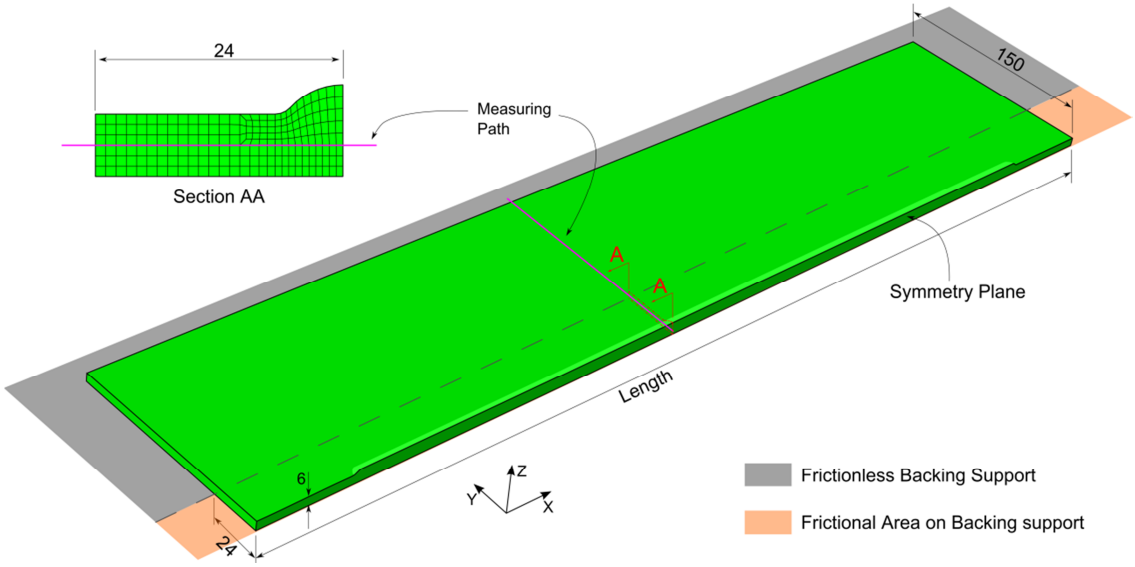

Figure 4-1 Half of workpiece, and transverse section of weld bead and surrounding material (dimensions in mm).

Two types of rollers were investigated; namely, single grooved, and dual flat rollers. The single grooved roller consisted of an 100 mm external diameter roller with a groove radius, as shown in figure 4-2 *a*, which was used to roll the top of the weld bead. The groove radius was larger than the effective mean weld bead radius (measured from Coules *et al.* [2,3,203,204] experiments), allowing accommodation of different weld bead sizes in the practical implementation of the rolling process, to reduce RS and distortion.

The dual flat rollers are composed of twin rollers which rolled both sides of the weld bead simultaneously, as shown in figure 4-2 *b*. These rollers had 2 mm

fillet radius at their corners, and can be used to roll the weld toes to improve their shape, by removing undercuts and geometrical discontinuities, with the objective of improving the fatigue life, as well as reducing the RS, and distortion. With these rollers different roller diameters, widths and positions, and rolling loads were analysed. In addition, all the rolling steps used the same rolling speed, 500 mm·min^{-1}, and no torque was applied to the roller to induce the roller translation (free rolling). The parameters are reported in the appropriate section in which they were used. The roller width and position as they are defined in the analysis are shown in figure 4-2 *b*.

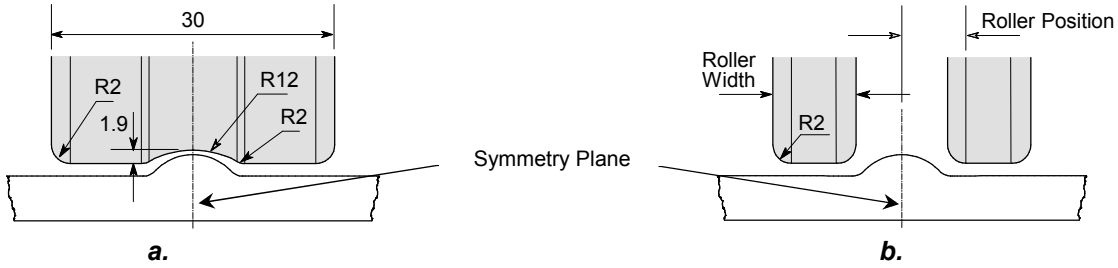

Figure 4-2 Roller profiles. *a.* Single grooved; *b.* Dual flat (dimension in millimetres).

After rolling, an unclamping step was performed with the same boundary conditions describe in homologous unclamping step of the welding mechanical analysis, already described in chapter 2.

4.2.1 Set 1. Rolling on top of the weld bead

In this section, the single grooved roller was used to roll the top of the weld bead along its entire length, as shown in figure 4-3. This set of models focused on the effect of different friction coefficients between the backing-bar and the workpiece, and between the roller and the workpiece, as well as the effect of different rolling loads in the RS distribution. The dimensions of half of the workpiece were 750×150×6 mm, and the weld seam was 600 mm in length.

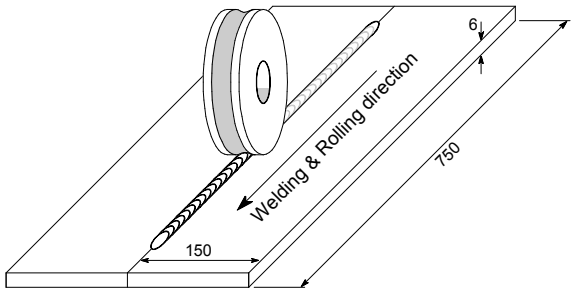

Figure 4-3 Schematic representation of PoWR on top of the weld bead with the grooved roller.

The parameters explored are reported in table 4-1.

Table 4-1 Parameters investigated in set 1.

Rolling Load [kN]	Friction Coefficient Backing-bar – Plate, μ_{BB} [–]	Friction Coefficient Roller – Plate, μ_{R} [–]
25	0.0; 0.5	0.0
25	0.2	0.5
50	0.2	0.5
100	0.2	0.5
150	0.0; 0.2; 0.5; 1.0	0.0
150	0.2	0.2; 0.3; 0.5
150	0.5	0.2; 0.3; 0.5; 0.8

4.2.2 Set 2. Rolling beside the weld bead

To improve fatigue performance it is necessary reduce notch defect at the weld toes. This is difficult to achieve by rolling a weld bead which fluctuates in size due to process variability. In addition, rolling on top of the weld bead exacerbates the notch in the weld toes (as it will be shown). Therefore, rolling beside the weld bead was used because the weld toes may be rolled even with fluctuation in the weld bead shape. The additional objective was the reduction of RS and distortion.

In this section the dual flat rollers were employed to analyse the effect of the roller positions and rolling loads on the welding RS. The total width of the weld bead was approximately 12 mm, and the minimum roller position considered was 7 mm; thus, no contact between the weld bead and roller fillet radius was performed at any roller position. The dimensions of half workpiece were 456×150×6 mm, and the weld bead length was 408 mm. Additionally, only the friction coefficient between the backing-bar and the workpiece (μ_{BB} = 0.5) was considered to reduce computational time.

Different roller widths and distances from the weld centreline, and rolling loads were explored, and are reported in table 4-2. Rolling was only applied to a section in the middle of the workpiece, as shown in figure 4-4 *a*. Tests were performed to verify that rolling the middle 120 mm of the plate gave similar RS on the measuring path as rolling the entire weld bead length. Consequently, computational time was significantly reduced by reducing the rolling length.

Table 4-2 Parameters investigated when rolling beside the weld bead.

Rolling Load [kN]	Roller Width [mm]	Roller Position [mm]
25	9	7; 10; 14; 19; 25
50	7	7
50	9	7; 10; 14; 19; 25
50	18	7; 14
50	24	7
75	7; 9	7
100	9	7; 10; 14; 19; 25
100	18	7; 14
100	24	7
150	9	7; 10; 14; 19; 25
150	18	7; 14
150	24	7

4.2.3 Set 3. Rolling the welding toes

Fatigue cracks usually start from the welding toes [80,205,206], as they act as a stress concentration points. In addition, tensile RS reduces the fatigue life of weldments [205]. PoWR the welding toes can potentially reduce these problems by reshaping the welding toes with a uniform fillet radius, and by inducing compressive RS in the weld bead and surrounding metal.

In this section four sub-sets of models were investigated. The first three sub-set were used to understand the effect of different parameters, while the last sub-set were used to compare against experimental results. Only the 9 mm roller widths were used in these sub-set of models, since this induced the stress deeper in the material. Similar to the previous models, only the friction coefficient between the backing-bar and the workpiece ($\mu_{BB} = 0.5$) was considered to reduce computational time.

In the real GMAW process the weld bead width changes along its length; consequently, rolling the weld toes can be challenging. The first sub-set of models analysed the influence of different roller distances, from 6.5 mm, in which there was virtually no contact between the roller and the weld bead, to 6 mm in which not only the welding toes were rolled, but also the weld bead was significantly deformed too. The dimensions of half workpiece in this sub-set were 456×150×6 mm, and the weld bead length was 408 mm. These models were rolled in the middle by 120 mm, as for the previous section (see figure 4-4 *a*).

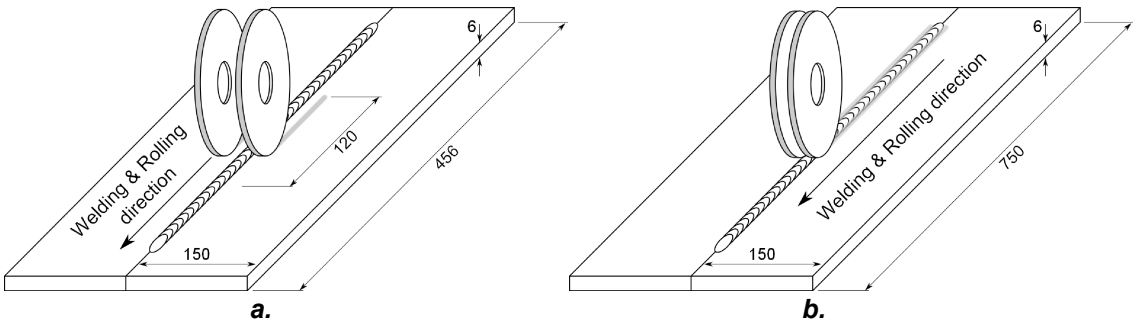

Figure 4-4 Schematic representation of PoWR when rolling with the dual flat roller. *a.* Rolling beside the weld bead. *b.* Rolling the weld toes (Dimensions in mm).

In the second sub-set the influence of rolling loads at 6 mm rolling distance was analysed. The same roller sizes as the first sub-set were implemented. The dimensions of half workpiece were 750×150×6 mm, and the weld bead length was 600 mm. These models were rolled along the entire weld bead length, as shown in figure 4-4 *b*, and they were used to determine the plate distortion.

The third sub-set was focused on the influence of roller diameters. The models used an identical rolling set up as for the second sub-set. The fourth sub-set used a friction coefficient of 0.2 with the backing-bar and 0.5 with the roller. The parameters investigated in all the sub-sets of this section are reported on **Error! Reference source not found.**.

Table 4-3 Parameters investigated when rolling the welding toes.

Model Sub-Set	Rolling Load [kN]	Roller Position [mm]	Roller Diameter [mm]	Plate size L×W×T [mm]	μ_{BB} [–]	μ_R [–]
Sub-Set 1	50	6; 6.1; 6.3; 6.5	100	456×150×6	0.5	0
	75	6; 6.2; 6.5	100	456×150×6	0.5	0
Sub-Set 2	5; 10; 15; 25; 30; 50; 75; 100; 150	6	100	750×150×6	0.5	0
Sub-Set 3	15; 25; 50	6	200	750×150×6	0.5	0
Sub-Set 4 (Validation)	25; 50; 100; 150	6	100	750×150×6	0.2	0.5

4.3 Results

4.3.1 Set 1. Rolling on top of the weld bead

Figure 4-5 shows the longitudinal RS in the measuring path, after PoWR on top of the weld bead with 25 kN rolling load, and different friction coefficients between the roller and the workpiece, μ_R, and between the backing-bar and the workpiece, μ_{BB}. Figure 4-6 *a* to *c* show the contour plots of the longitudinal RS after PoWR on top of the weld bead with 150 kN rolling load, after using different friction coefficients μ_R, and μ_{BB}. Additionally, a model completely

frictionless (no frictional behaviour either in the roller or in the backing-bar) was performed to use as a common reference in the analyses.

The influence of frictional behaviour was significant only when using a large load, such as 150 kN, as shown in figure 4-6, while low loads showed virtually no difference in the RS in the measuring path, as shown in figure 4-5. This phenomenon was already discuss in chapter 3, and explained by Cook and Larke [201]. Consequently, the discussion in this section will be focused on the results obtained with the 150 kN rolling load.

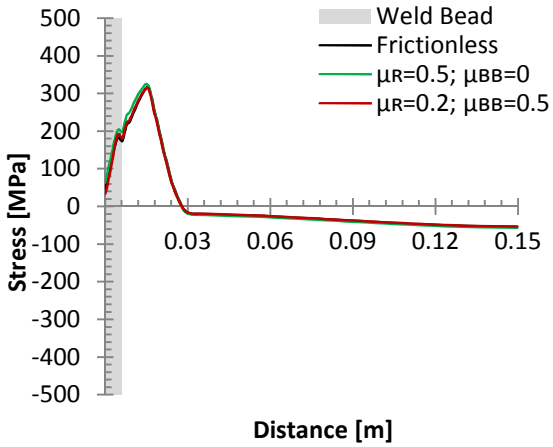

Figure 4-5 Longitudinal RS after PoWR on top of the weld bead using 25 kN load and different friction coefficients in the backing-bar (μ), and in the roller (μR)

With 150 kN rolling load, the longitudinal RS in the far field was marginally modify for the different friction coefficient; however, in the weld bead region and surrounding regions significant differences were observed. In addition, the friction interaction did not change only the RS in the middle thickness (measuring path), but also the complete RS distribution across the thickness. With a frictionless roller (with and without frictional interaction in the backing-bar), the weld bead was largely deformed in the transverse direction, significantly deforming the welding toes, causing sharp edges on the weld bead, and producing longitudinal tensile RS in the top of the weld bead due to the Poisson effect, as shown in figure 4-6. When friction was assumed between the

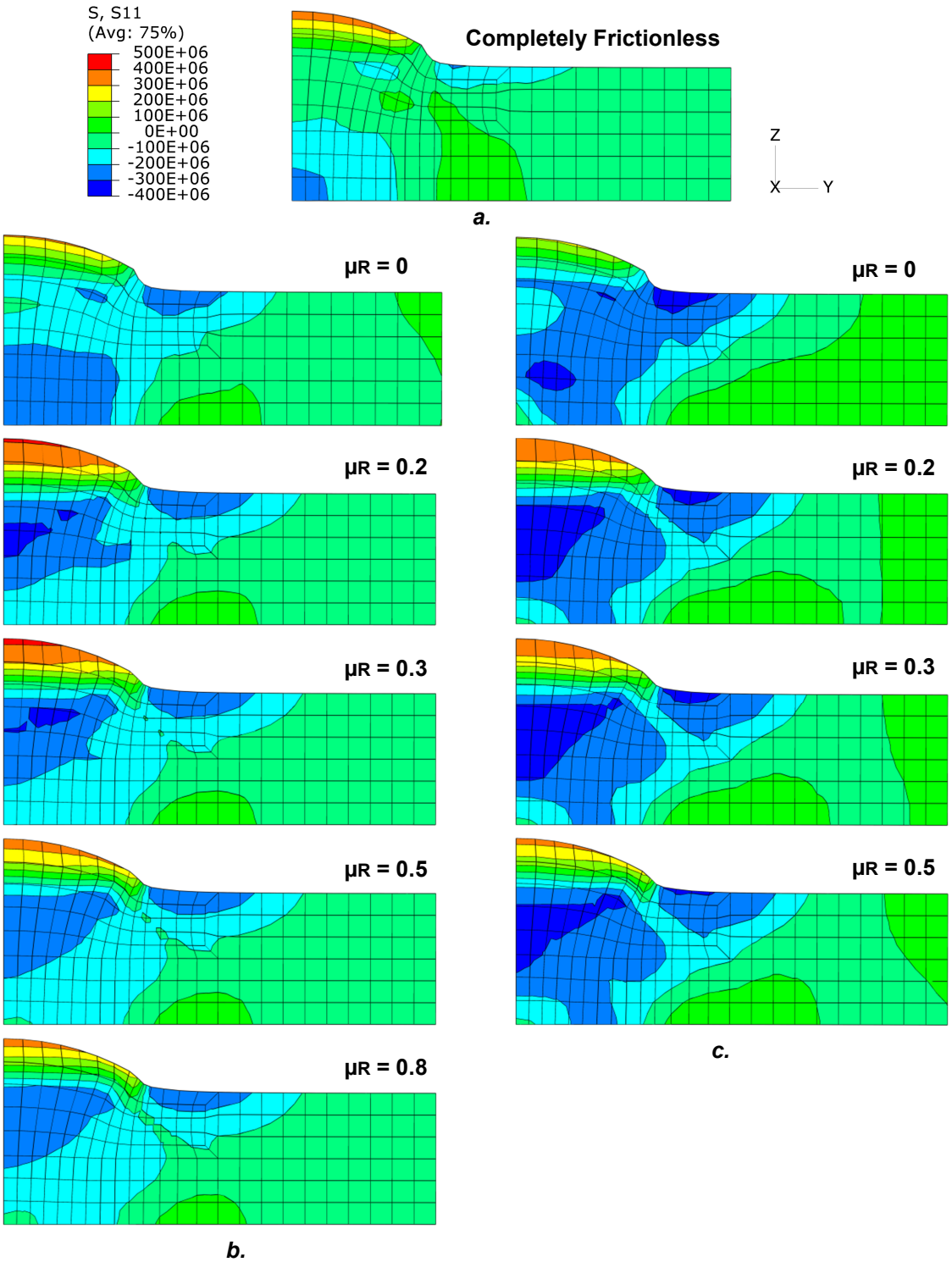

Figure 4-6 **Contour plot of the longitudinal RS within 20 mm from the weld centreline, rolled with 150 kN, with different friction coefficient between workpiece and backing-bar (μ_{BB}), namely, *a.* frictionless, *b.* μ_{BB} = 0.2, and *c.* μ_{BB} = 0.5, and different friction coefficients between the roller and workpiece (μ_R).**

roller and workpiece, the weld bead was deformed more uniformly, and the welding toes deformed having a less sharp profile at their edges, due to the tangential forces induced by friction. Increasing the roller friction coefficient enhanced this effect.

In the complete frictionless model (figure 4-6 *a*), most of the compressive RS was localised close to the lower surface. Adding frictional behaviour in the backing-bar, an area of the lower surface of the weldment was partially restrained to in-plane displacement, causing more compressive RS in a larger region in the weld bead centre. Increasing the friction coefficient on the roller moved that compressive region upwards to the middle of the weld bead.

On the top of the weld bead, tensile RS was observed in all the models. However, in the models with a friction coefficient on the roller of $\mu_R = 0.2$, the region of this RS was larger, as well as its magnitude. When a friction coefficient is applied between the workpiece and the roller, the surface is partially restrained to deform in the contact region with the roller. Consequently, more plastic strain was produced below the top surface generating tensile RS above that region (top of the weld bead surface). The reason for this being greater in magnitude with a friction coefficient of 0.2 than 0.8 is unclear.

Figure 4-7 *a* and *b* show the predicted longitudinal positive and negative plastic strain, respectively, in the middle of the weld seam, during PoWR with 0.2 friction coefficient in the backing-bar and 0.5 in the roller, while figure 4-7 *c* and *d*, show the plastic strain for the transverse and normal directions.

The plastic strain in the top surface was restrained not only for the geometries of the contact areas, but also for the frictional interaction between the roller and the weld bead. As explained in chapter 3 the friction interaction at the surface restrains the plastic strain in that surface, and forces the plastic strain to occur deeper in the workpiece. This phenomenon was present not only in the longitudinal direction (see figure 4-7 *b*), but also in the transverse and normal ones, as shown in figure 4-7 *c* and *d*, respectively. In addition, this increases the load required to produce the same vertical deformation obtained in frictionless conditions [201]. Bijak-Zochowski and Marek [207] studied the influence of

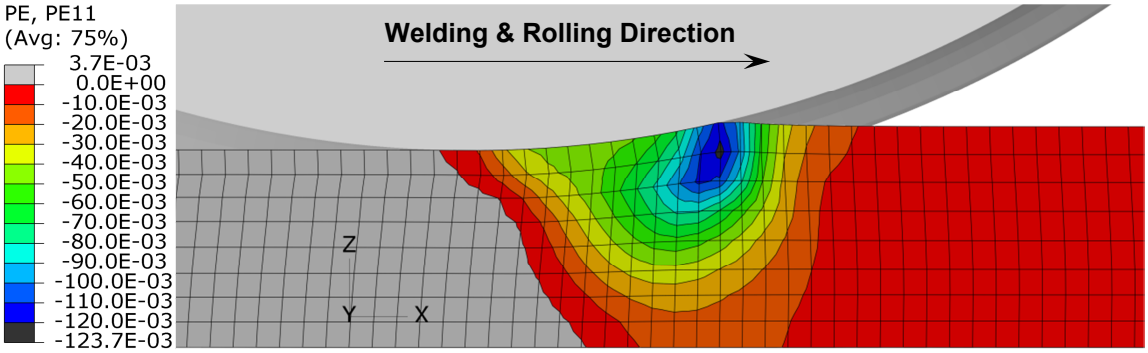

a.

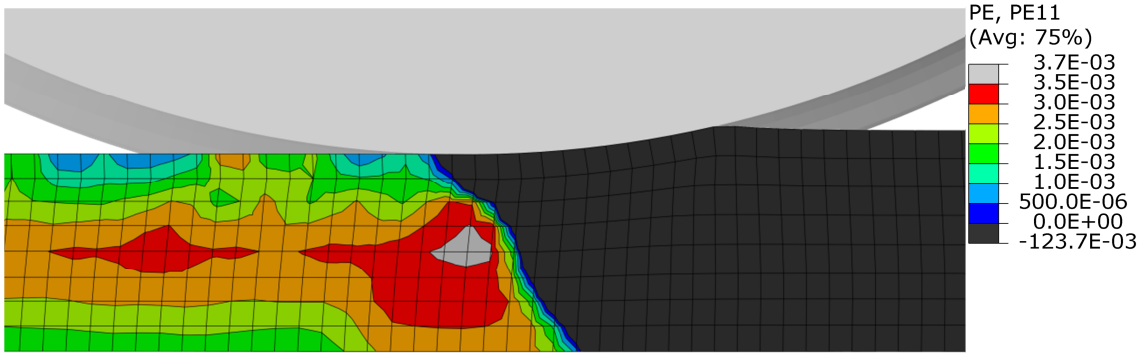

b.

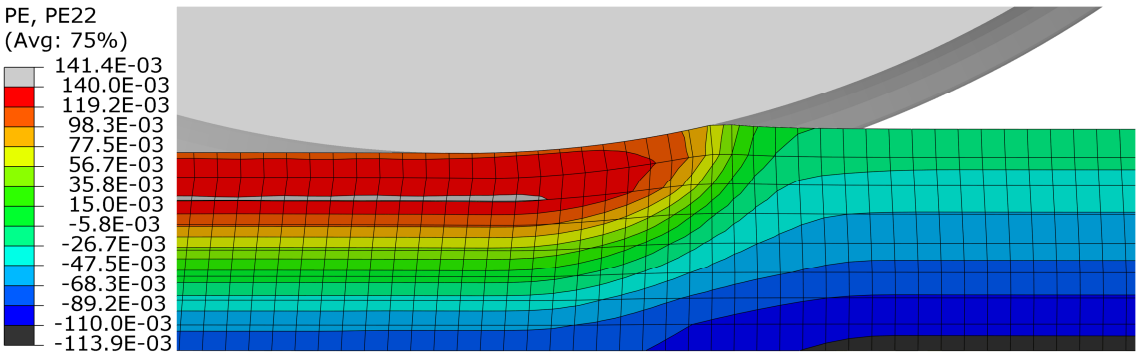

c.

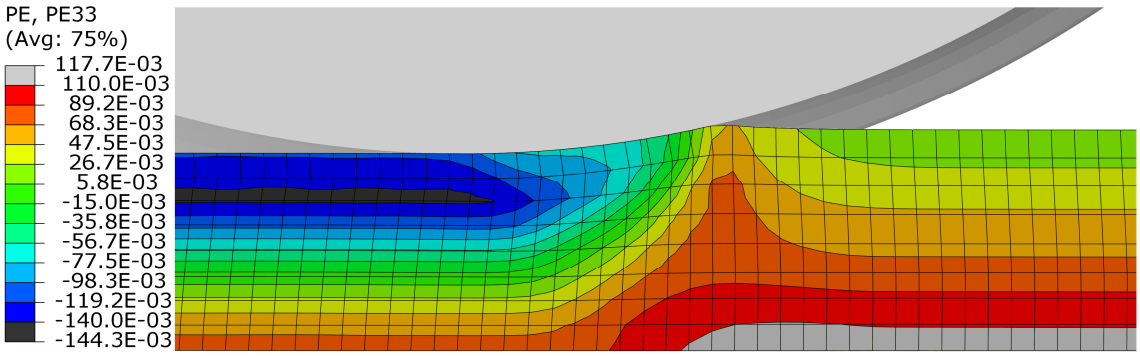

d.

Figure 4-7 **Contour plots of the predicted plastic strain with 0.2 friction coefficient in the backing-bar and 0.5 in the roller, and 150 kN load, *a.* compressive, and *b.* tensile in the longitudinal direction, and *c.* transverse, and *d.* normal directions.**

rolling on steel strips. They reported that for free rolling (with no acceleration or braking, such as the one applied in the models of this thesis) tensile RS are produced in the contact surface, as the maximum plastic strain is produced at some point below the surface, which is in agreement with the model described in this section.

Validation of PoWR the top of the weld bead

The best match between the models and the experimental results were obtained by using a friction coefficient between the backing-bar and the weldment of $\mu_{BB} = 0.2$, and between the roller and the weldment of $\mu_R = 0.5$. Figure 4-8 shows a comparison of the longitudinal RS between experiments and numerical models. The predicted results showed very good agreement with the experiments in all the cases analysed. The results show that the longitudinal tensile peak of the RS is reduced by the action of rolling. As the rolling load increases, the longitudinal tensile RS decreases, and the region affected by the roller is widened.

The roughness of the weld bead was larger than the one on the lower surface in the contact region between the backing-bar and the weldment. Therefore, the assumption of having a larger friction coefficient between the roller and the weld bead than between the backing-bar and the lower surface of the weldment is congruent.

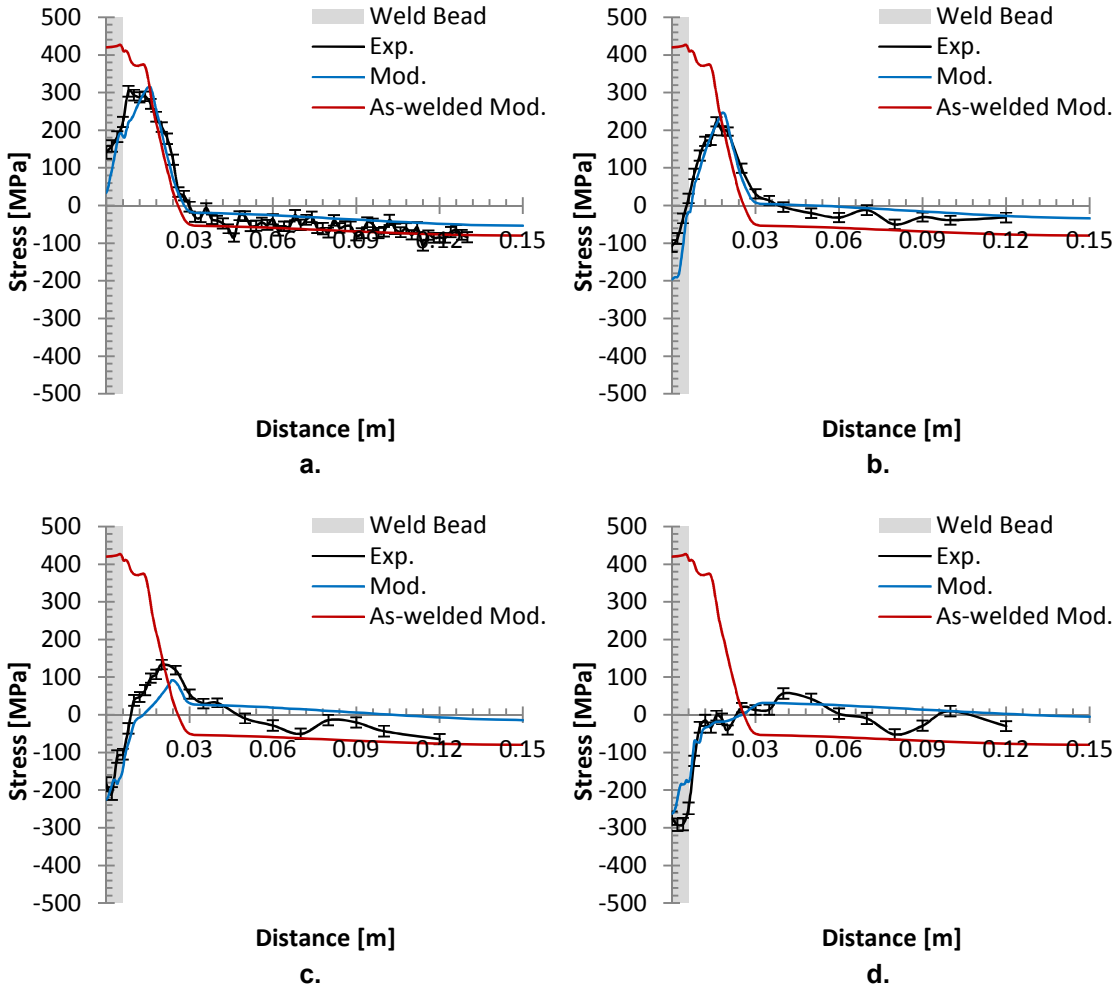

Figure 4-8 **Comparison between predicted and experimental longitudinal RS after PoWR on top of the weld bead with: *a.* 25; *b.* 50; *c.* 100; and *d.* 150 kN.**

Figure 4-9 *a* to *d.* show the longitudinal RS after PoWR the top of the weld bead, with 25, 50, 100, and 150 kN, respectively. Half of the roller was added to the contour plots, to show how the contact sections and the weld bead shapes change with the rolling load. Note that the rollers are shown only for illustrative purposes. To represent the neutron diffraction gauge volume section, a square shape was added to the contour plots. The nodal stress in the FE models on the other hand, relates to an integration of the stress in the adjacent elements, which in these models are smaller than the neutron diffraction gauge volume.

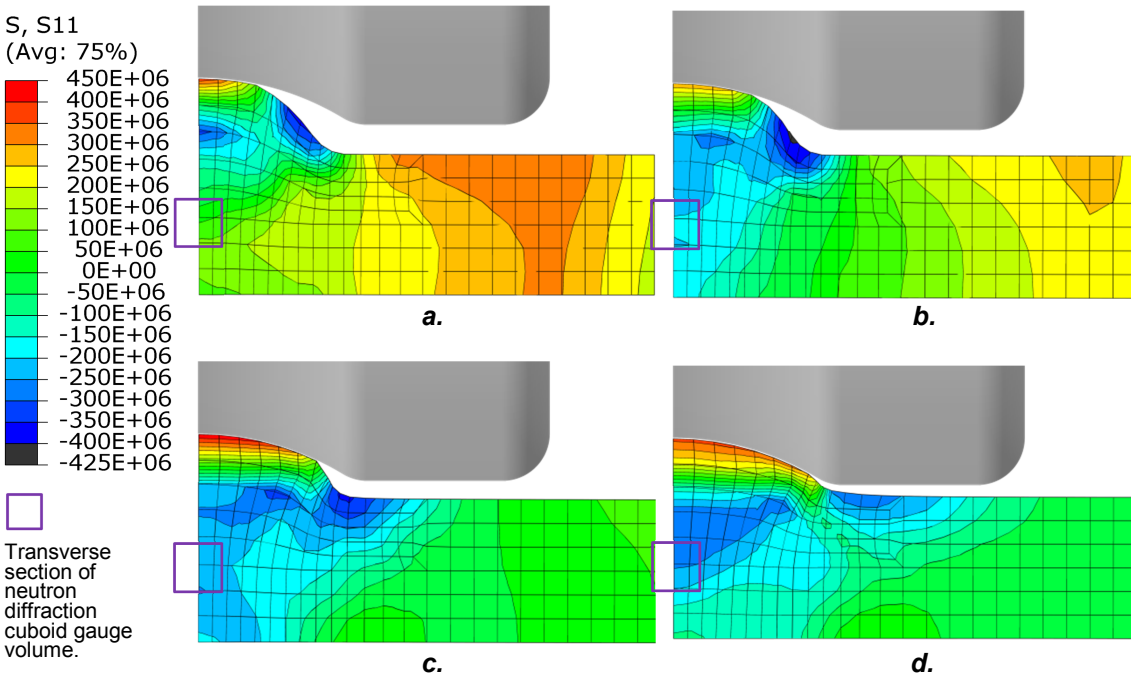

Figure 4-9 **Contour plot of the longitudinal RSs, within 20 mm from the weld centreline, after PoWR on top of the weld bead with: *a.* 25; *b.* 50; *c.* 100; and *d.* 150 kN.**

Although the results are in agreement, some small discrepancies were observed, between predicted and experimental values, as shown in figure 4-8. The experimental measurement were conducted by neutron diffraction with the SALSA instrument [208]. Due to the large variation of the longitudinal RS across the thickness cuboid gauge volumes of 2×2×2 mm were used in that direction, while for the transverse and normal direction 2×20×2 mm ones were used [2]. Consequently, the RS was an average of the stresses inside the gauge volume. Price *et al.* [209] suggested that the differences between the gauge volumes and shapes between the neutron diffraction and FEA, can potentially cause mismatch in the RS results. Therefore, some discrepancies with the experimental measurements were expected, particularly when the gradient is stress is large.

During PoWR the top of the weld bead, the material in contact with the roller tends to be deformed in all the directions, but it is restrained by the roller shape and the tangential forces derived from the frictional contact. With low loads the deformation is limited to the very top of the weld bead, where the curvature of

the roller grove is virtually parallel to the tip of the weld bead, as shown in figure 4-9 *a*, and the transverse plastic deformation is restrained mainly by the small frictional contact region. Therefore, large compressive longitudinal RS is formed in the weld bead next to the welding toes, and at few millimetres underneath the contact region. With large loads, on the other hand, the weld bead is largely deformed, substantially increasing the contact between the roller and weld bead, whilst the weld bead adopted the shape of the roller groove. Consequently, larger frictional tangent forces are produced, increasing the compressive stress in the weld bead core, as shown in figure 4-9 *d.*

Figure 4-10 *a* and *b* shows a comparison between the experimental and predicted longitudinal RS through the thickness on the weld bead region, respectively, after PoWR on top of the weld bead with 150 kN. The modelling results were exported into a Matlab routine to isolate the RS in the approximately same region as the experimental measurements, to ease the comparison between them. The cross marks in the experimental contour plot represent the actual neutron diffraction measurements. In both cases compressive RS was induced in the weld bead region. However, the stress distribution was not exactly the same, particularly below the weld toe, and HAZ.

The experiment has a tensile trend towards the upper surface, and compressive towards the lower surface in the HAZ. Conversely, the numerical model showed the opposite behaviour in that region. In the model the weld bead geometry was the mean of different measurements along the entire weld seam of different samples produced with the same welding parameter and material. Therefore, the model did not take into account the possible weld bead shape variations. A simple model with slightly different weld bead shape, without the fillet radius in the welding toes, was made. In this model only the rolling was performed, and no welding stresses were present. It produced tensile RS in the welding toes, similar to the ones observed in the experiment. This kind of weld bead produced undercuts in welding toes. In addition, the welding toes acted as stress concentrators, as shown in figure 4-10 *c*.

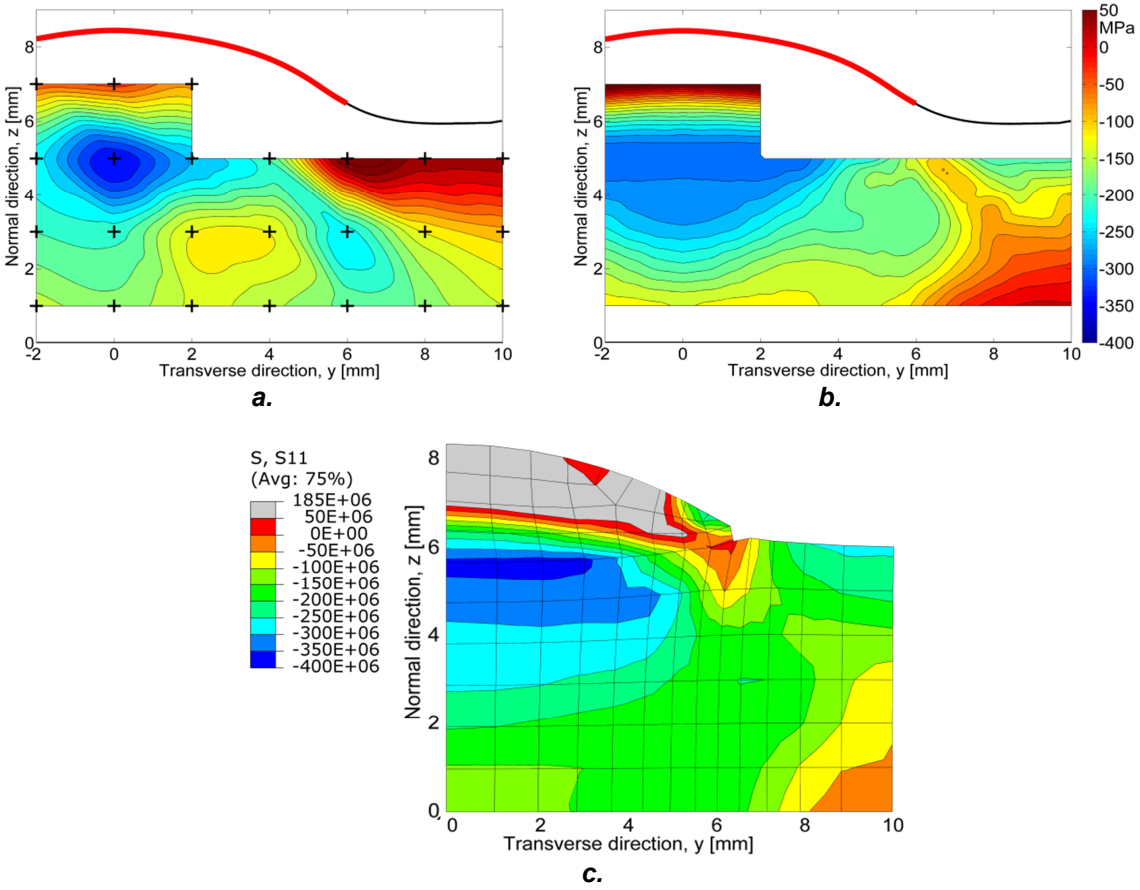

Figure 4-10 **Contour plots of the weld bead sections after PoWR on top of the weld bead with 150 kN load. *a*. Experiment measurements, and *b*. modelling results. *c.* Section of the weldment with modified weld bead to show stress concentration in welding toes and undercut.**

Interestingly, even though the results presented in figure 4-8 *d* and figure 4-10 *a*, both used a rolling load of 150 kN, they were from separate experiments which used different material batches. In addition, they were measured with different instruments, namely, SALSA [208] (batch 1), and ENGIN-X [210] (batch 2), respectively. The two batches had slightly different material properties as reported by Coules [211], and shown in table 4-4, while the yielding point of the material used in the model was 390 MPa at 20 °C, which was lower than the two batches. A comparison of the longitudinal RS in the middle workpiece thickness, measured with the two instruments, and compared with the modelling results is shown in figure 4-11.

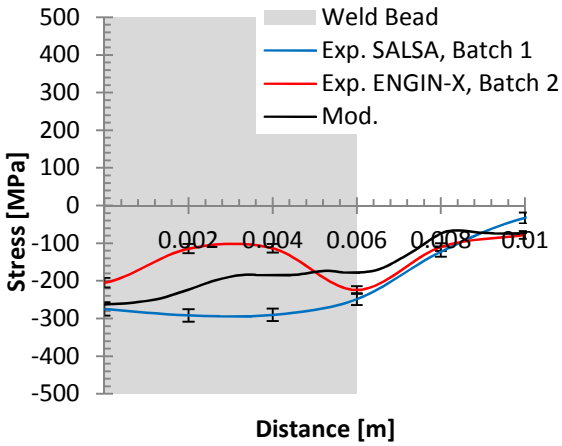

Figure 4-11 Comparison between longitudinal RS on the middle thickness on the weld bead region, after PoWR on top of the weld bead, with 150 kN, using two different batches of S355 plates, and the predicted results.

Although the two samples were built with the same experimental parameters, the longitudinal RS is significantly different, particularly within 6 mm from the centreline. The ENGIN-X measurements were about 200 MPa less compressive than the SALSA ones. The modelling results were more similar to the results obtained with the SALSA instrument. The variations in mechanical properties of the S355 from different batches, and the differences in the gauge volume implemented in the measurements and modelling, make the RS difficult to predict accurately. The RS depends not only on the yielding point of the material at room temperature, but it also depends on the strength of it when the plastic deformation occurs. Therefore, without temperature dependent mechanical properties for the exact plates used in the experiments it is not possible to categorically explain the difference in the two results (assuming that the welding conditions were identical in each experiment).

Table 4-4 Mechanical properties of S355 from different batches [211]

Batch	Yield Strength [MPa]	Ultimate Tensile Strength (UTS) [MPa]	Strain to Fracture [%]
Batch 1	474	520	21
Batch 2	395	520	22

Figure 4-12 *a* to *d* show the transverse RS after PoWR on top of the weld bead with 25, 50, 100, and 150 kN load, while figure 4-13 *a* to *b* show the same results for the normal direction. The transverse RS was modified, from the as-welded condition, primarily in the weld bead region, and its magnitude varied between ± 100 MPa, approximately, in both experiments and models. Hence, the values were much lower than those observed in the longitudinal direction. In the normal direction the RS was even lower than in the transverse one, and they fluctuated around zero in all the experiments and models.

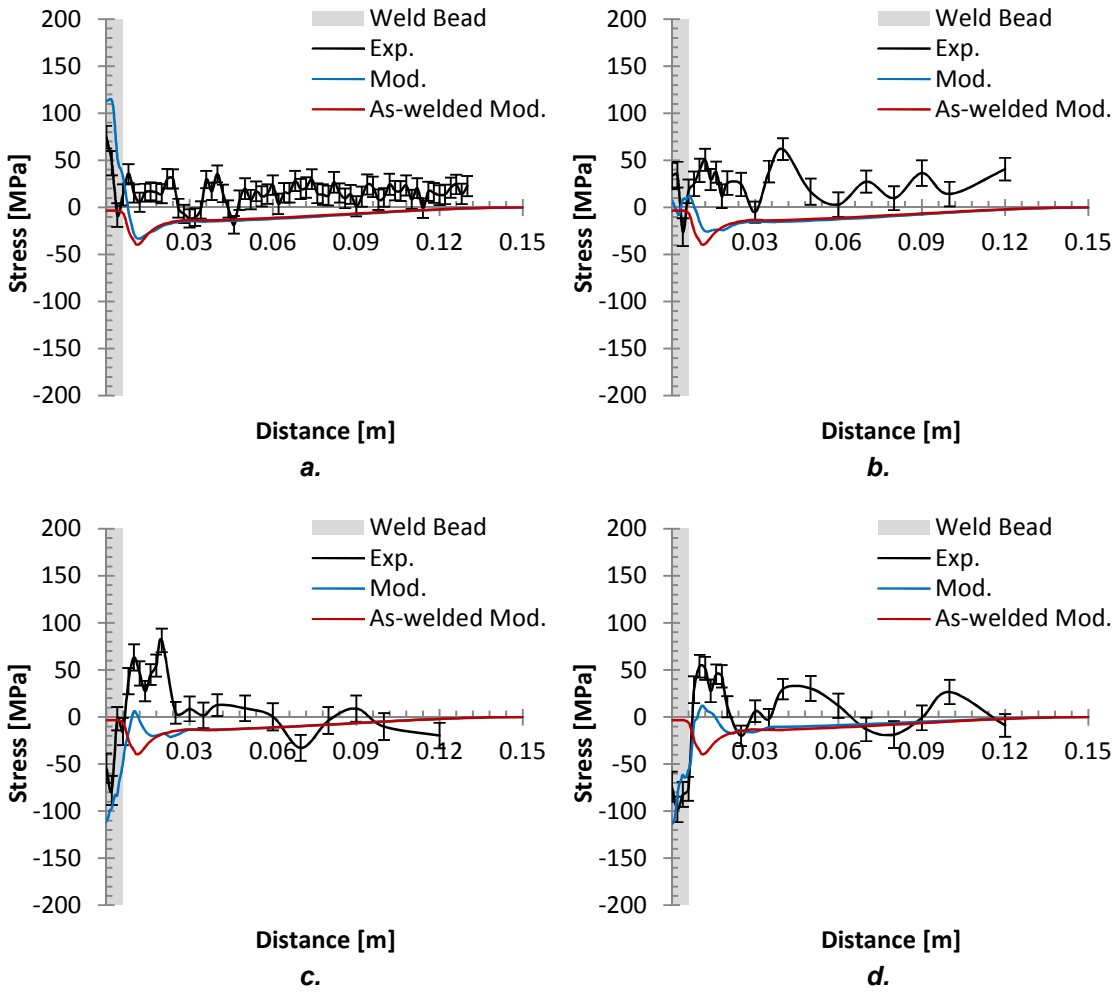

Figure 4-12 Comparison between predicted and experimental transverse RS, after PoWR on top of the weld bead with: *a*. 25; b. 50; *c*. 100; and *d*. 150kN.

The stresses in the transverse direction were greater after rolling with 25 kN than in the as-welded sample. Rolling produces plastic strains which are

non-uniform through the thickness. It is believed that this causes the inversion of the stress observed in the low loaded rolled samples, producing tension when the deformation is localised near the surface, due to the Poisson's effect, and compression with higher loads when the plastic deformation extends through the thickness.

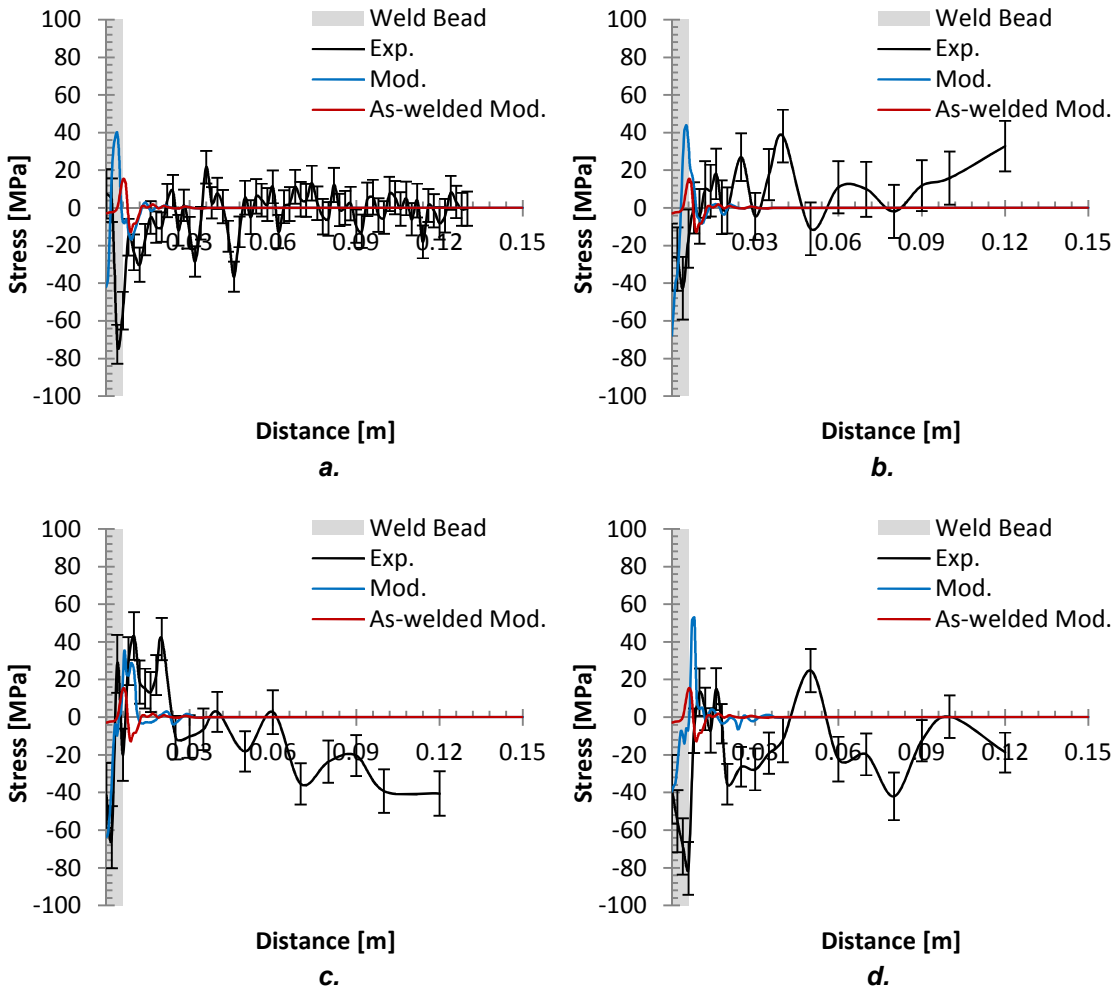

Figure 4-13 Comparison between predicted and experimental normal RS, after PoWR on top of the weld bead with: *a.* 25; *b.* 50; *c.* 100; and *d.* 150kN.

Figure 4-14 *a* shows the contour plots of half weldment[‡], of the out-of-plane distortion with, from top to bottom, 0 (as-welded), 25, 50, 100, and 150 kN rolling loads. The distorted shape of the as-welded condition for both the

[‡] The contour plots show the left side of the weldment, so that the weld seam lies in the right edge of the plots.

predicted and experiment resembled a hyperbolic paraboloid (saddle shape), being concave, and its out-of-plane peaks were 6.30, and 9.89 mm, respectively. In this study this kind of distortion was considered negative. The predicted PoWR weldment distorted in the opposite direction (convex) for all the rolling loads analysed, and this type of distortion was considered positive.

Figure 4-14 *b* shows the out-of-plane distortion peaks as a function of the rolling load for both experiments and models. The contour plot with the red shadow, and the red marker in figure 4-14, *a* and *b*, respectively, represent the minimum out-of-plane displacement obtained, 0.42 mm with 150 kN rolling load. Compared to the as-welded out-of-plane predicted distortion, this represents about 93% distortion reduction. The minimum out-of-plane distortion on the experiments was 1.54 mm, which was obtained with 50 kN rolling load, and it represents about 84% out-of-plane distortion reduction. However, the repeatability of the experimental results was not high.

PoWR the top of the weld bead significantly reduced the distortion in both, the models and experiments. Although the distortion was slightly underestimated in the models, the out-of-plane distortion reduction trend was very similar to the one obtained in the experiments, and it was almost in all the cases within the 95 % of confidence of the experimental results.

As already explained in chapter 2, the presence of the weld bead and the non-uniform tensile RS through the thickness in the weld bead region, displaces the neutral axis of the workpiece from the middle thickness to an upper position, closer to the weld reinforcement. When the workpiece is unclamped the RS redistribute causing a bending moment which distorts the weldment. Rolling on top of the weld bead deforms the weld bead lowering the neutral axis of the workpiece, and induces compressive RS predominantly in the upper part of the workpiece thickness; therefore, when the weldment is unclamped it deforms in the opposite direction of the as-welded sample.

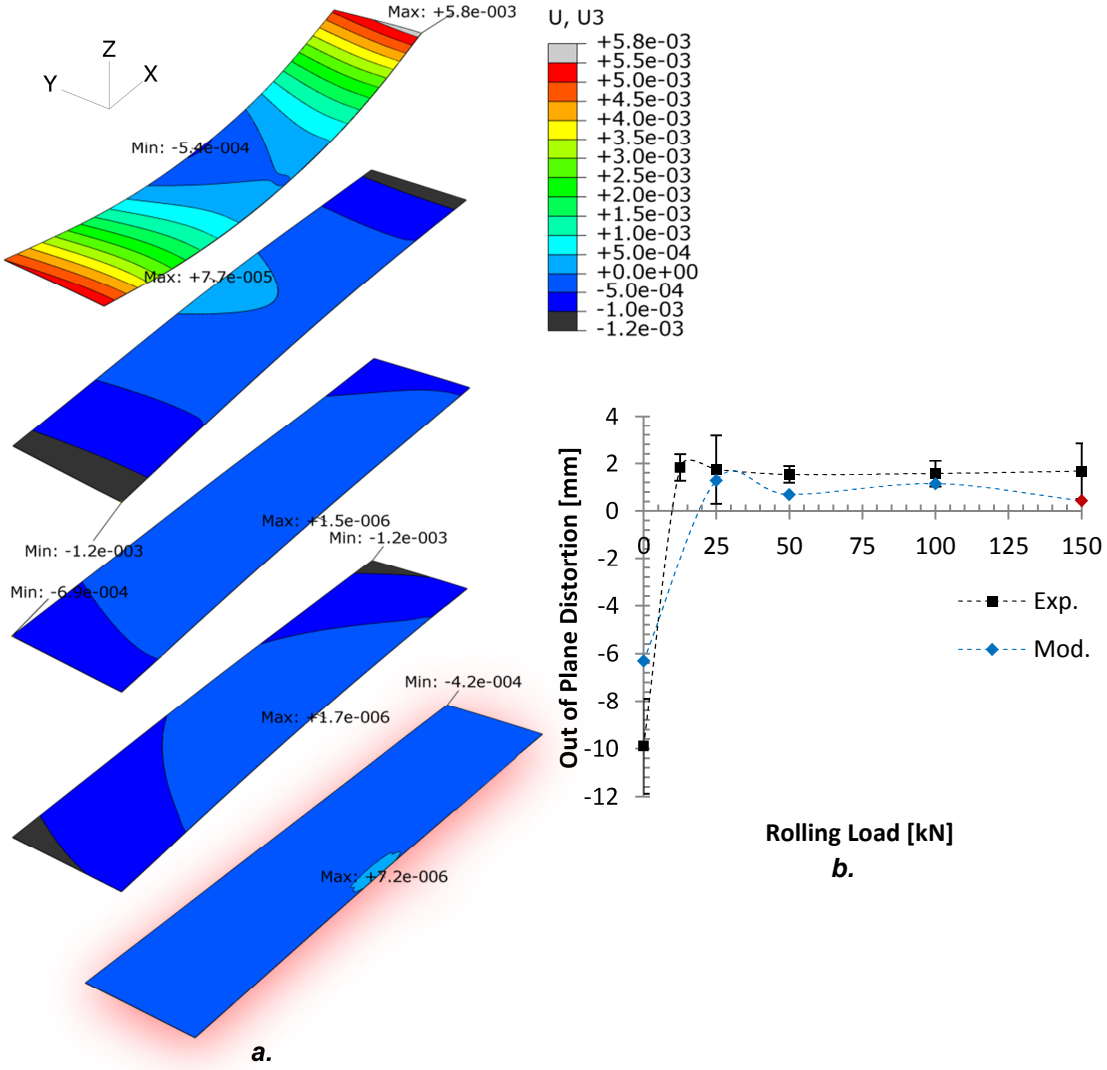

Figure 4-14 ***a.*** **Contour plot of out of plate distortion after PoWR the top of the weld beads, with different loads; from top to bottom: 0 (as-welded), 25, 50, 100, and 150 kN.** ***b.*** **Out-of-plate distortion vs. rolling load.**

4.3.2 Set 2. Rolling beside the weld bead.

Figure 4-15 *a* and *b* show the longitudinal RS across the half workpiece width in the middle thickness (measuring path shown in figure 4-1), after PoWR beside the weld bead with a 9 mm roller width at different roller positions, and 25 and 100 kN rolling loads, respectively. Figure 4-15 *c* and *d* show on the other hand, the longitudinal RS after PoWR beside the weld bead with different loads at 7 mm from the weld centreline, with a 18 and a 24 mm roller widths, respectively.

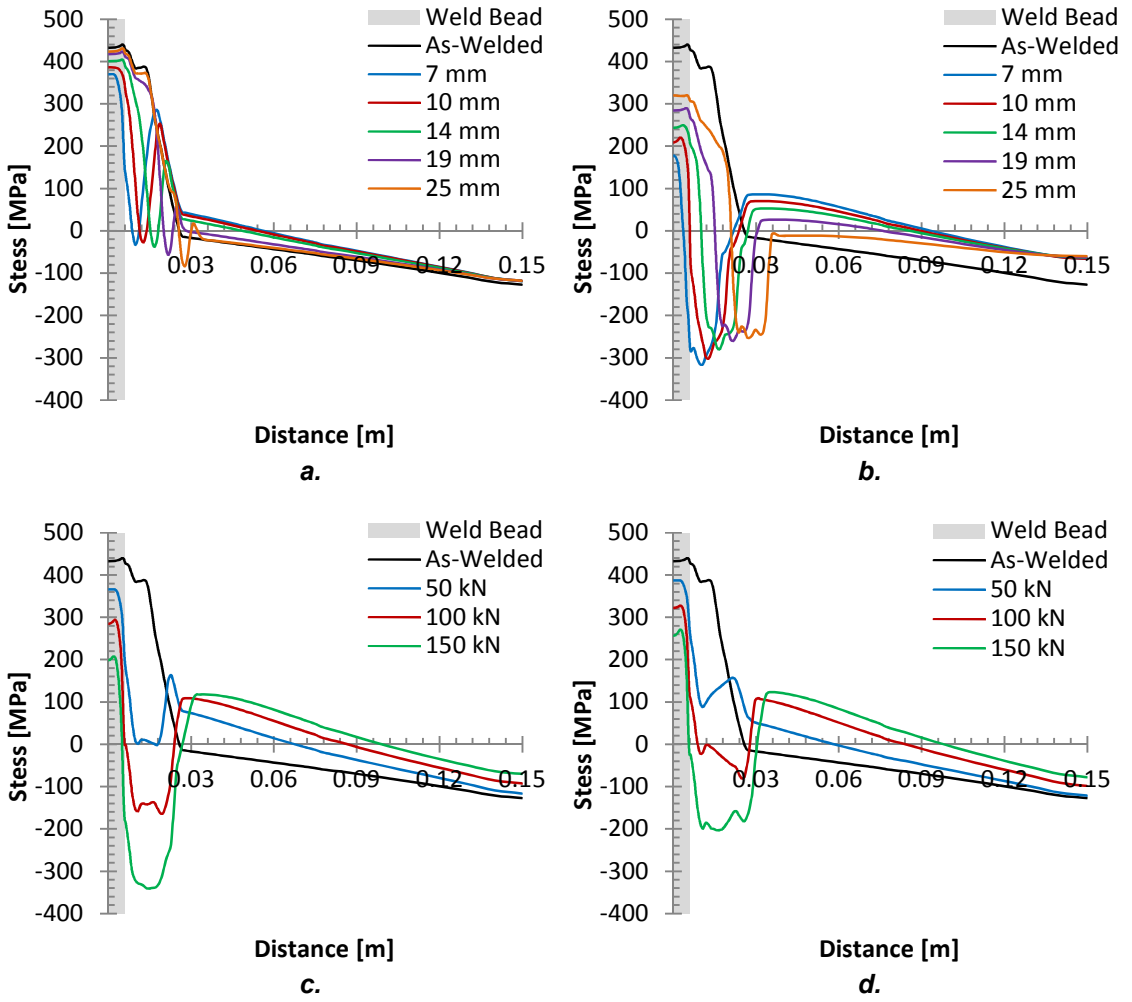

Figure 4-15 Longitudinal RS after PoWR beside the weld bead with a 9 mm roller width, different roller positions *a.* 25, and *b.* 100 kN rolling loads. Rolled at 7 mm from the weld centreline with different loads, using *c.* 18, and *d.* 24 mm width rollers.

The results show that the longitudinal RS can be potentially reduced in most of the conditions modelled. With a thin roller and low loads (9 mm roller width and 25 kN load), the RS reduction was less prominent than the one obtained with the same roller but with larger loads, as shown in figure 4-15 *a* and *b*, respectively. However, when the thin roller is applied far from the welding toes (farther than 19 mm) with low loads, there is no significant reduction of the RS, as shown in figure 4-15 *a*. Nevertheless, when larger loads are applied farther than 19 mm, a significant longitudinal RS reduction can be obtained, as shown in figure 4-15 *b* at 25 mm from the weld centreline. In any case, the larger RS reductions were observed when rolling was performed at 7 mm from the weld

centreline, for each load applied. Note that at that distance the welding toes are not in contact with the roller, so that small variation in the weld bead width should not significantly affect the RS profile obtained after rolling.

When larger width rollers are used, the longitudinal tensile RS peak can be largely reduced in the weld bead region and in the surrounding metal, as shown in figure 4-15 *c* and *d*. With the 18 mm roller width the tensile peak is almost completely removed next to the weld bead, when 50 kN load was used. However, in the weld bead region the tensile peak was reduced by about only 60 MPa. With larger rollers loads, and the same roller width, heavily compressive longitudinal RS can be induced next to the weld bead, and larger reduction of the RS in the weld bead can be obtained. With a larger roller width the longitudinal compressive region was wider, but its magnitude smaller, as shown in figure 4-15 *d*.

The Applied Weld Load (**AWL**) is a useful criterion that can be used to estimate an average of the magnitude of the tensile RS in the region in which it is acting (weld bead and HAZ), as described in chapter 2. However, it is only useful in the case of buckling distortion. Since the geometry of these weldments produced bending distortion, the AWL will not predict reduction in distortion.

Figure 4-16 *a* and *b* show the AWL after PoWR with the dual flat roller with the 9 and 18 mm roller widths, respectively, at several roller positions. In figure 4-16 *c* and *d*, the AWL is shown as a function of roller width at constant roller position, at 7 and 14 mm from the weld centreline, respectively. There was a strong relationship between the rolling loads, roller positions, with the AWL reduction, for each roller widths analysed. The larger AWL reduction was observed with higher load in the closer roller position to the centreline using the thinner rollers, as shown in figure 4-16 *a* and *c*. As the roller position increased, less AWL reduction was observed, for all the loads studied, for the roller width studied, as shown in figure 4-16 *a* and *b*. As the roller width increased, less AWL reduction was obtained for each rolling load, for each roller position. The lowest AWL was obtained with 150 kN, for all the roller widths and a 7 mm roller position (Green line in Figure 4-16 *c*).

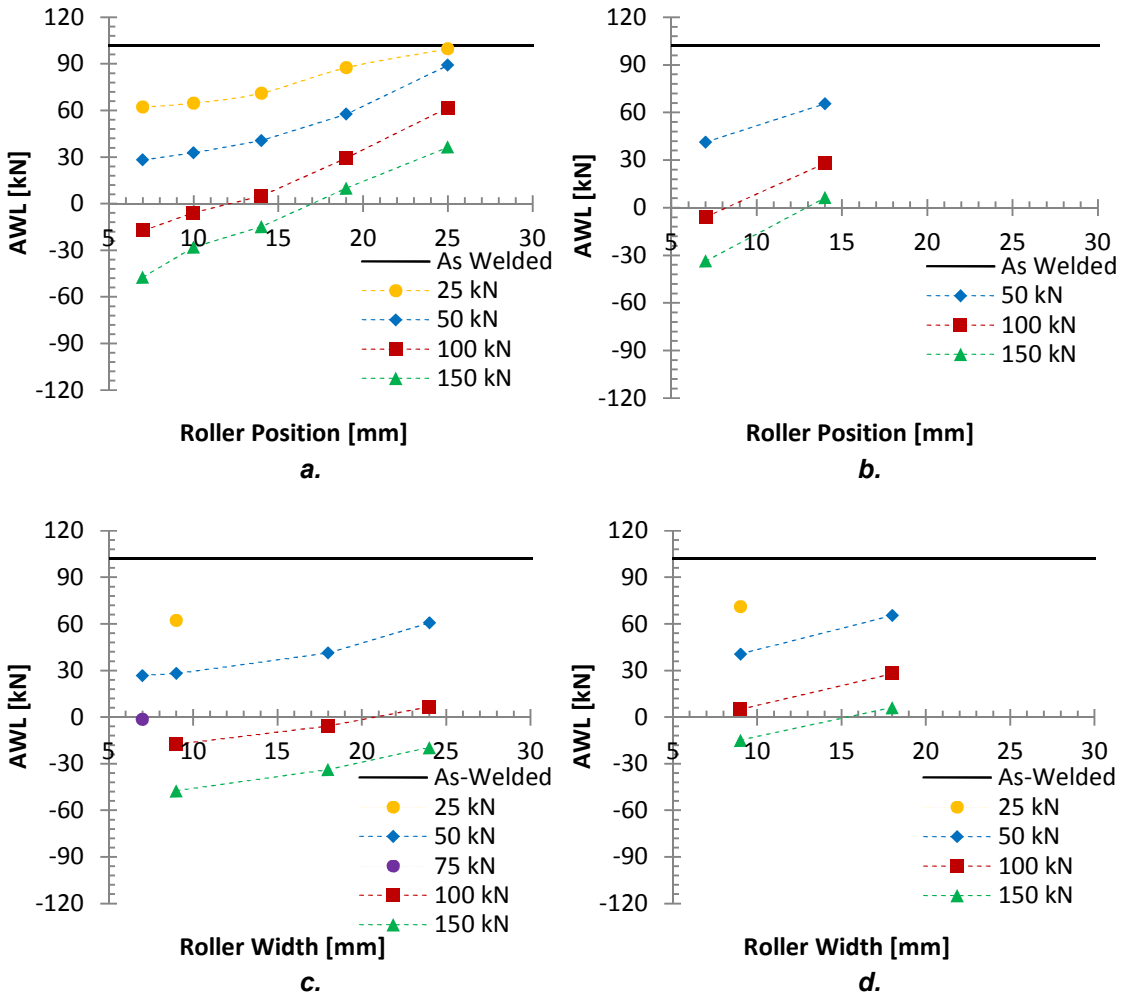

Figure 4-16 AWL after PoWR with different loads, and distances from the welding centre line with roller width of *a*. 9 and *b* 18 mm; and different roller width at *c*. 7, and *d*. 14 mm roller position.

The use of wider rollers produced a reduction of the longitudinal tensile RS peak in a wider area, but the magnitude of the compressive stress induced was smaller than the one produced by thinner rollers using the same load. The wider rollers distribute the vertical load applied in a larger contact area, which is not particularly useful in this application, as the longitudinal tensile RS peak is relatively narrow. However, in other welding processes, which involve larger heat input and consequently wider tensile RS regions, the wider roller can be an appropriate option. On the other hand, it is thought that the use of very thin rollers, such as the 7 mm one, can cause practical problems due to low

stiffness. Consequently, the 9 mm roller width was chosen to analyse the influence of rolling the welding toes in the next section.

The contour plots of the longitudinal and transverse stress within 35 mm from the centreline, (from top to bottom) before, during, and after PoWR, with 100 kN load, 9 mm roller width, at 7 mm roller position, are shown in figure 4-17 *a* and *b*, respectively. The magnitude of the longitudinal stress on the weld bead region was larger than the transverse one in the three stages shown. When rolling occurs, it causes a high hydrostatic compressive region underneath its contact zone; it induces highly compressive transient stress and a transient reduction of the tensile longitudinal and transverse stress in the weld bead. After rolling, the longitudinal RS was largely reduced in the weld and HAZ, and the transverse stress became slightly compressive in those regions.

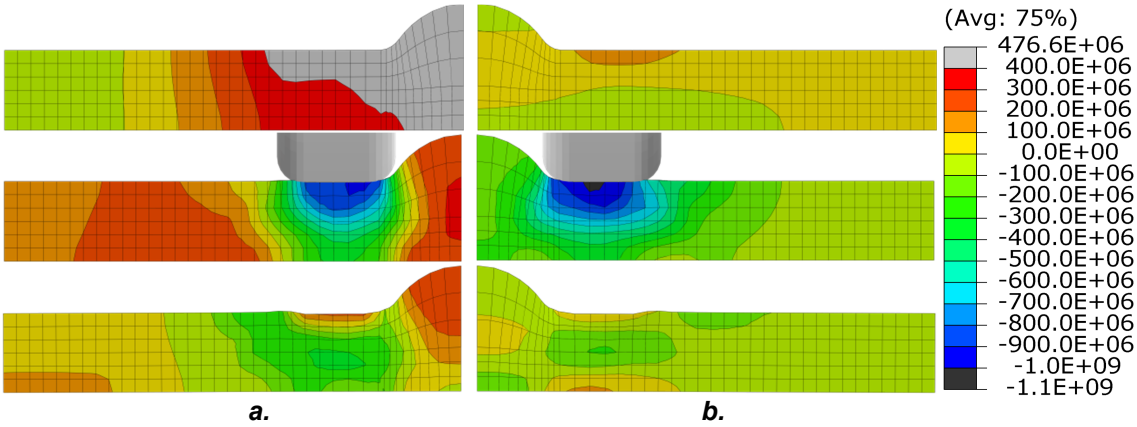

Figure 4-17 Contour plots of the stress distribution within 35 mm from the centreline, rolling load 100 kN, roller position 7 mm, and 9 mm roller width. From top to bottom, as-welded, during PoWR, unclamped after PoWR. *a*. Longitudinal stress; *b*. Transverse stress.

4.3.3 Set 3. Rolling the welding toes

Figure 4-18 shows the longitudinal RS, after PoWR the welding toes with the dual flat roller, at different roller positions, with the 9 mm roller width, and 50 and 75 kN load. The longitudinal RS at 7 mm belongs to the previous set of models, rolling beside the weld bead, since at that roller position the welding toes are not rolled. This was added to the plots in this section because it is one

of the extreme conditions that can occur when the actual rolling is performed, due to the weld bead width variation.

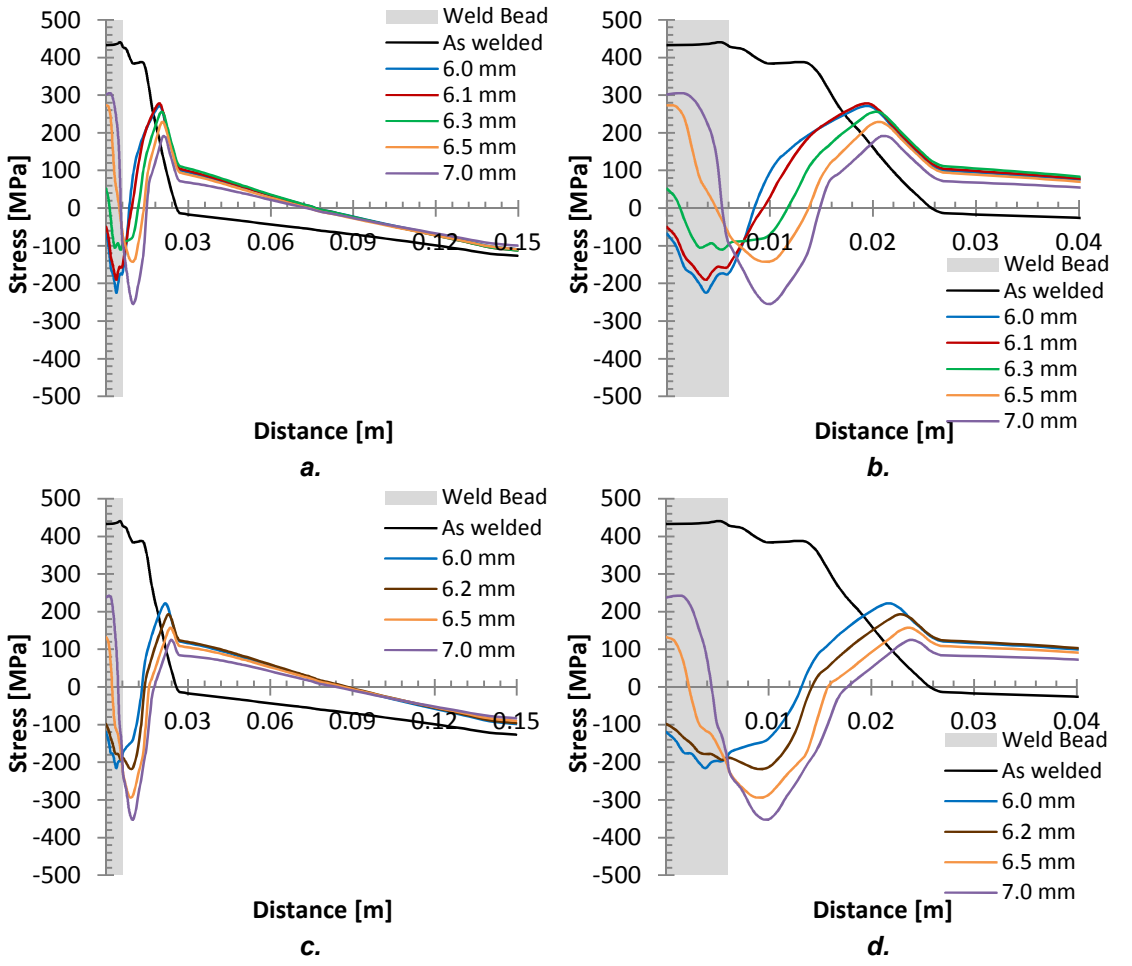

Figure 4-18 Longitudinal residual stress after PoWR on the welding toes, at different roller position, with a 9 mm roller width and two different rolling loads: *a.* 50, and *c.* 75kN; and a close-up of the first 40 mm from the welding centreline with *b.* 50, and *d.* 75 kN.

All cases analysed in this section generated high reductions of the longitudinal tensile RS peak and width. The dual flat roller caused longitudinal compressive RS regions along its path (at each side of the weld bead). On the weld bead region, the longitudinal welding RS was significantly reduced, while on the other sides of the rolling paths, in the parent metal, the longitudinal tensile RS was increased from the as-welded original distribution, particularly with 50 kN load. The 75 kN load caused a bigger reduction of the tensile peak at the centreline, and larger reduction of the tensile RS peak width, than the 50 kN one.

At 6 mm from the centreline the longitudinal RS in the weld bead region was compressive with both, 50 and 75 kN rolling loads, as shown in figure 4-18. Increasing this distance reduced the compressive RS induced by rolling, and at 6.5 mm the longitudinal RS was tensile in the weld bead. The effect of RS reduction in the weld bead region was much greater than the one when rolling was applied further than 7 mm, as shown in figure 4-15 *a* and *b*. This is due to the roller squeezing the weld metal between the two sided of the roller, producing more deformation of the weld metal and reducing the RS. Consequently, physical variations in the weld bead width would yield varying longitudinal RS regions along the weld, as well as the out-of-plane distortion. Nevertheless, the AWL variation with the different distances was relatively small.

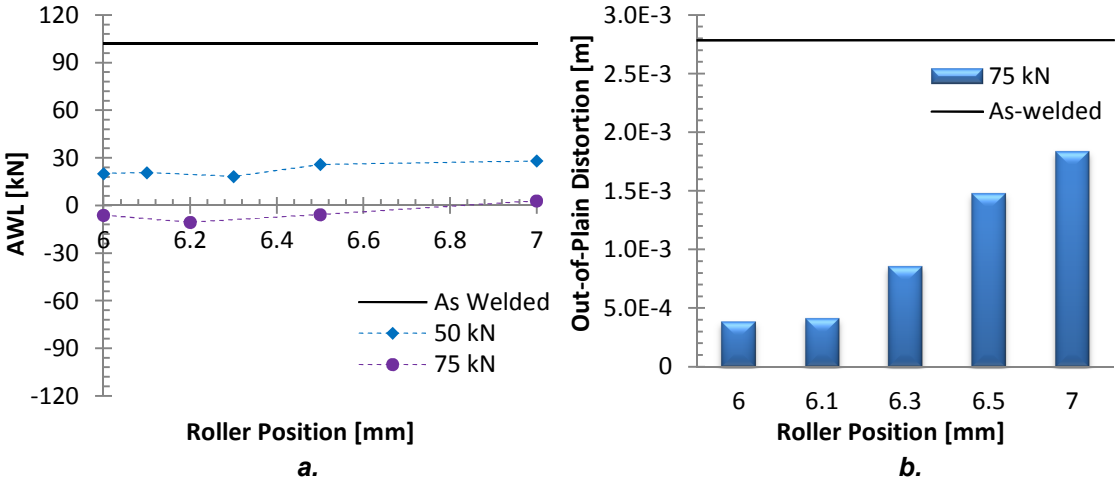

Figure 4-19 ***a*. AWL after PoWR the welding toes at different roller positions, from the centreline, with 9 mm roller width, and 50 and 75 kN rolling loads. *b.* Out-of-plain distortion after PoWR with 75 kN at different rolling positions.**

Figure 4-19 *a* shows the AWL versus the roller position, after PoWR the welding toes with 50 and 75 kN load, with the 9 mm roller width, while figure 4-19 *b* shows the out-of-plane distortion of the weldments PoWR with 75 kN. The AWL reduction was virtually constant with respect to the roller position. Therefore, the result of 50 kN rolling load was virtually parallel to those of 75 kN. On the other hand, the out-of-plane distortion had very small variation when the roller

position changed from 6 to 6.1 mm; however, for farther roller positions the out-of-plane distortion increased significantly.

The effect of varying the rolling load on the longitudinal RS profile is shown in figure 4-20. This plot shows the result at the measuring path, after PoWR at 6 mm from the weld centreline, the 750 mm length models, using a friction coefficient between the weldment and the backing-bar of $\mu_{BB} = 0.5$, and completely frictionless between the roller the weldment. The grey shadow area represents the weld bead width, while the orange one represents the roller contact path. All the loads applied caused reduction in the longitudinal welding RS tensile peak, and its width, and the reduction increased with the increase of the rolling load. Farther from the weld bead, in the parent material, the counterbalanced compressive RS caused by welding was reduced in magnitude and became tensile with rolling load larger than 50 kN. With 5 kN load the RS reduction was marginal, however with 25 kN or higher loads larger RS reductions were observed.

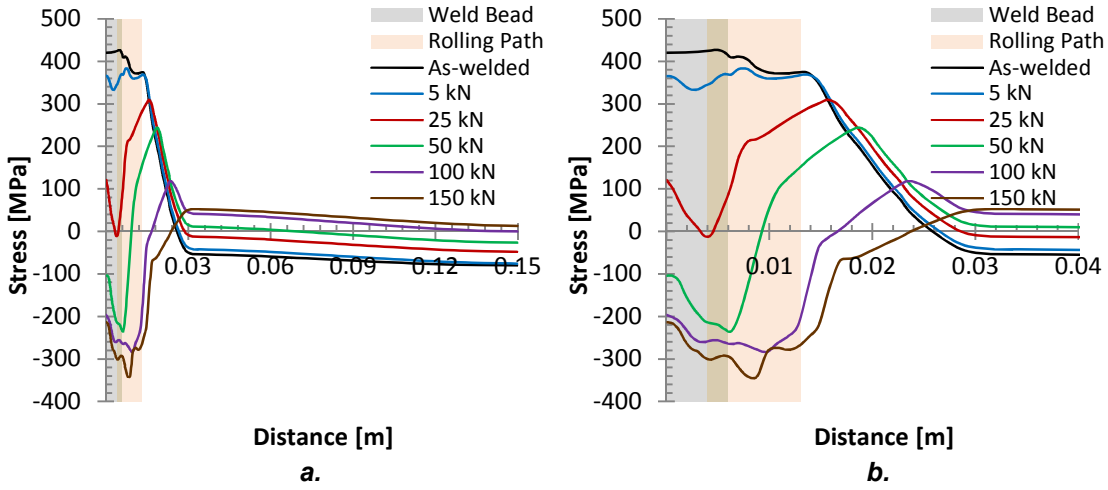

Figure 4-20 ***a.*** **Longitudinal RS after PoWR the welding toes at 6 mm from the centreline with a 9 mm width roller.** ***b.*** **Close-up of** ***a.*** **in the first 40 mm.**

Figure 4-21 shows a comparison of PoWR the welding toes at 6 mm from the weld centreline, with 100 and 200 mm roller diameters, 9 mm roller width, and different rolling loads. Larger roller diameters induced less compressive RS on the weld bead and rolling path regions compared with the smaller roller with the

same loads. Farther away from the rolling region, in the parent metal, the reduction of the welding compressive RS is slightly lower than that caused by the smaller rollers, for all the loads analysed. As the roller diameter increases, the contact region increases. Consequently, the compressive stress induced by rolling with the larger roller is smaller than the one induced by smaller roller with the same load.

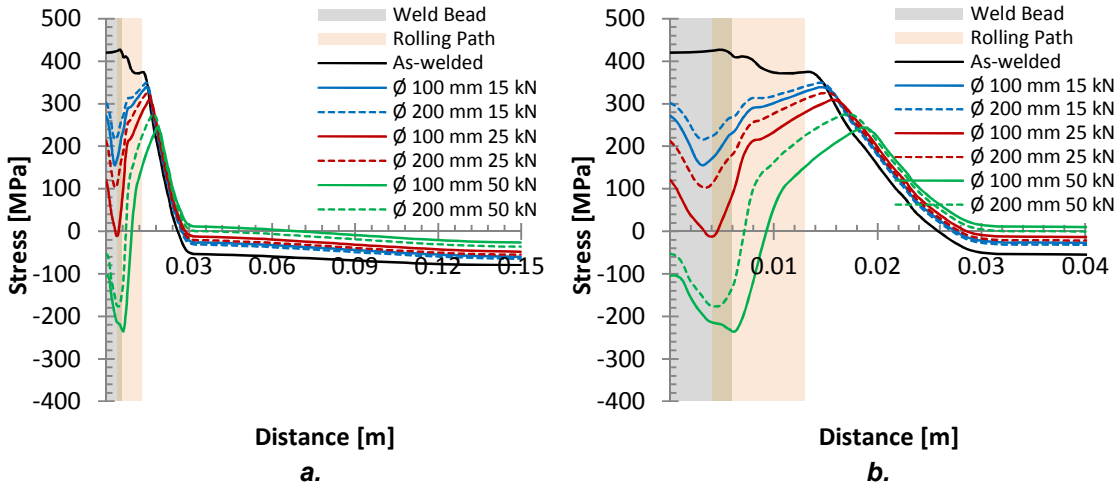

Figure 4-21 Longitudinal RS after PoWR with 100 and 200 mm diameter roller, at 6 mm from the centreline. *a.* Half workpiece width; *b.* close-up of the first 40 mm from the weld bead.

Figure 4-22 *a* and *b* shows the contour plot of the longitudinal RS, within 30 mm from the centreline, after PoWR with 100 and 200 mm roller diameters, respectively, (from top to bottom) with 15, 25, 50 kN load. The 100 mm roller diameter induced deeper compressive residual stress than the 200 mm one, for the same rolling load. Therefore, the 100 mm roller diameter was able to remove the welding tensile RS close to the lower surface with less rolling load. On the other hand, the 100 mm roller caused a shallow tensile RS field in the weld toes when 50 kN load was applied, while with the 200 mm diameter roller this tensile region was not observed. Baldwin [212,213] explained that the relationship between roller radius, workpiece thickness and deformation ratio can determine whether there is either tensile or compressive RS in the surface of the workpiece after rolling. However, in these models the interaction between the roller and the workpiece was simulated frictionless, therefore, the tensile RS

field close to the surface is unlikely to be realistic. This is investigated further in the subsequent section.

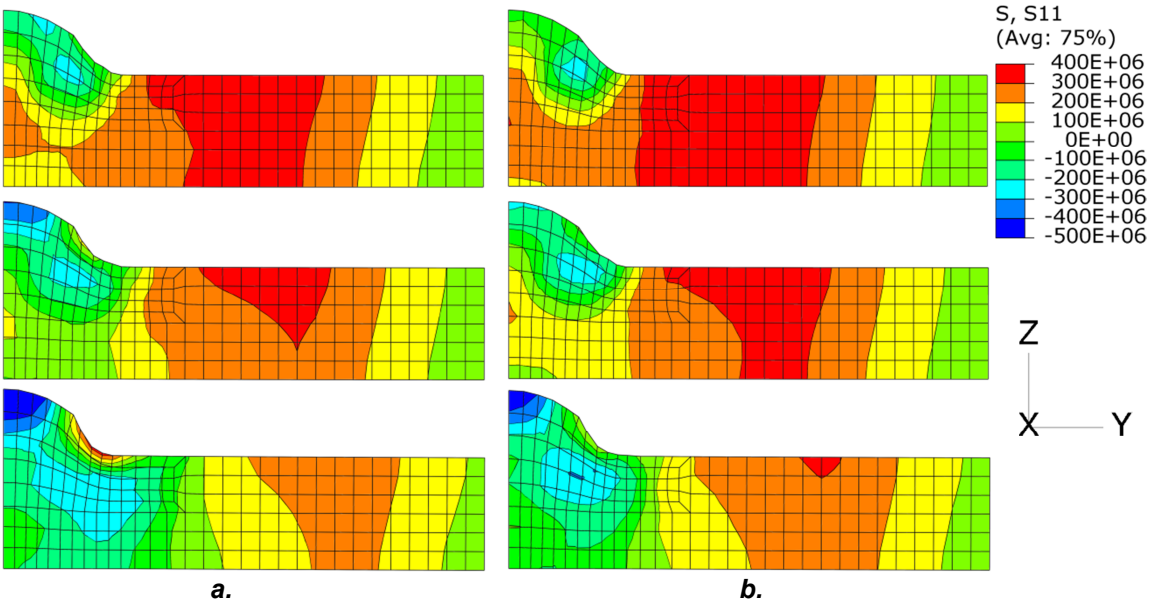

Figure 4-22 Contour plots of the longitudinal residual stress, within 25 mm from the centreline, after PoWR the welding toes with: *a.* 100 mm; *b.* 200 mm roller diameter. From top to bottom, 15, 25, 50 kN rolling load.

Figure 4-23 *a* shows the contour plots of the out-of-plane displacement after PoWR the welding toes, with a 9 mm roller width, and the 100 mm roller diameter, using different rolling loads. While, figure 4-23 *d* shows the contour plot of the longitudinal RS when 5 kN load was used. The out-of-plane displacement peak versus the rolling load, using the 100 and 200 mm roller diameters, is reported in figure 4-23 *b*, while the AWL as a function of the rolling load, for the 100 mm roller diameter, is shown in figure 4-23 *c*.

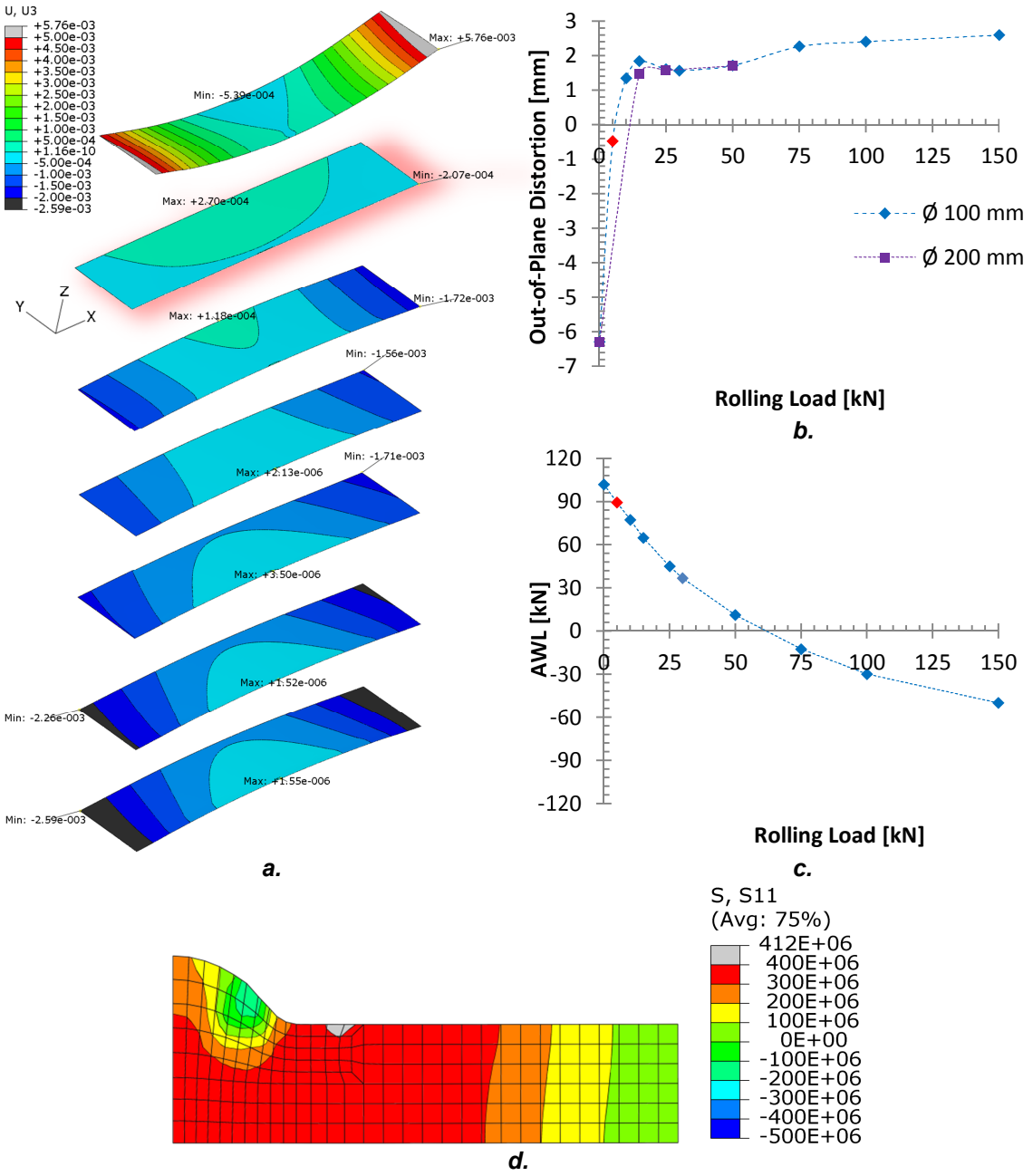

Figure 4-23 ***a.*** **Counter plots after PoWR on the welding toes with different rolling load, magnified 10×. From top to bottom 0 (as welded), 5, 15, 30, 50, 75, and 150 kN;** ***b.*** **Peak out-of-plane distortion vs. rolling load;** ***c.*** **AWL reduction vs. rolling load; contour plot of the longitudinal RS after 5 kN rolling load.**

The contour plot with the red shadow shown in figure 4-23 *a*, and the red markers in figure 4-23 *b* and *c*, represent the minimum predicted out-of-plane distortion (0.48 mm). This was obtained with the 100 mm roller diameter, and with 5 kN load. However, with that low load the reduction of the longitudinal RS was marginal as shown in figure 4-20 *a*. and figure 4-23 *c* and *d*. In addition,

with 5 kN load the larger RS reduction occurs in the weld reinforcement, leaving the longitudinal RS in the base plate virtually unaffected. Consequently, the possible benefit of having compressive RS in the weld bead was not obtained. In addition, with this highly tensile RS field in the weld bead region, a relatively small external force could buckle the weldment, if the critical buckling load is exceeded.

Almost all the loads analysed caused a change in the deformation shape (from negative to positive, except with 5 kN load), and a significant reduction of the out-of-plane peak distortion, from above 6 to approximately 2 mm. The AWL was reduced as the load increased, and it became negative after about 60 kN of rolling load. However, the larger out-of-plane distortion reductions were observed with loads between 5 and 50 kN. At that interval the AWL was still positive, but its magnitude changed significantly between the two ends of the interval. As explained before the AWL it is useful only for estimating buckling distortion; since the distortion with this geometry is primarily bending the changes in AWL do not indicate changes in distortion.

The out-of-plane distortion in these weldments is caused by a bending moment which finds a new self-equilibrated configuration when the weldment is unclamped, distorting the workpiece. With the 5 kN load, only the longitudinal RS in the weld reinforcement are reduced, while the RS in the base plate was virtually unaffected. Consequently the new self-balancing bending moment is equilibrated in a shape virtually flat, as shown in figure 4-23 *a*.

The out-of-plane distortion reduction produced with the 200 mm roller diameter was very similar to the ones produced with the 100 mm roller diameter.

Validation of PoWR the welding toes

Figure 4-24 *a* and *b* show a comparison between the experimental and predicted longitudinal RS, after PoWR with a load of 150 kN in the longitudinal direction, within 20 mm from the weld centreline. Figure 4-25 *a* and *b* show the same results for the transverse direction. This models were produced using friction coefficients between the roller and the weldment of $\mu_R = 0.5$, and

between the weldment and the backing-bar of μBB = 0.2. The longitudinal RS had discrepancies mainly in the first 10 mm from the weld centreline. Farther from 10 mm the predicted longitudinal RS are more similar to the one in the experiments. The experiments showed a slightly tensile region in the weld bead zone, while the predicted results showed a very compressive RS in the same region. Below the region rolled (showed with the red line) the experiments showed a compressive region close to the upper surface, whereas in the model, the compressive region was more uniform through the thickness. On the other hand, in the parent metal the RS of both, experiment and model, was between ±50 MPa.

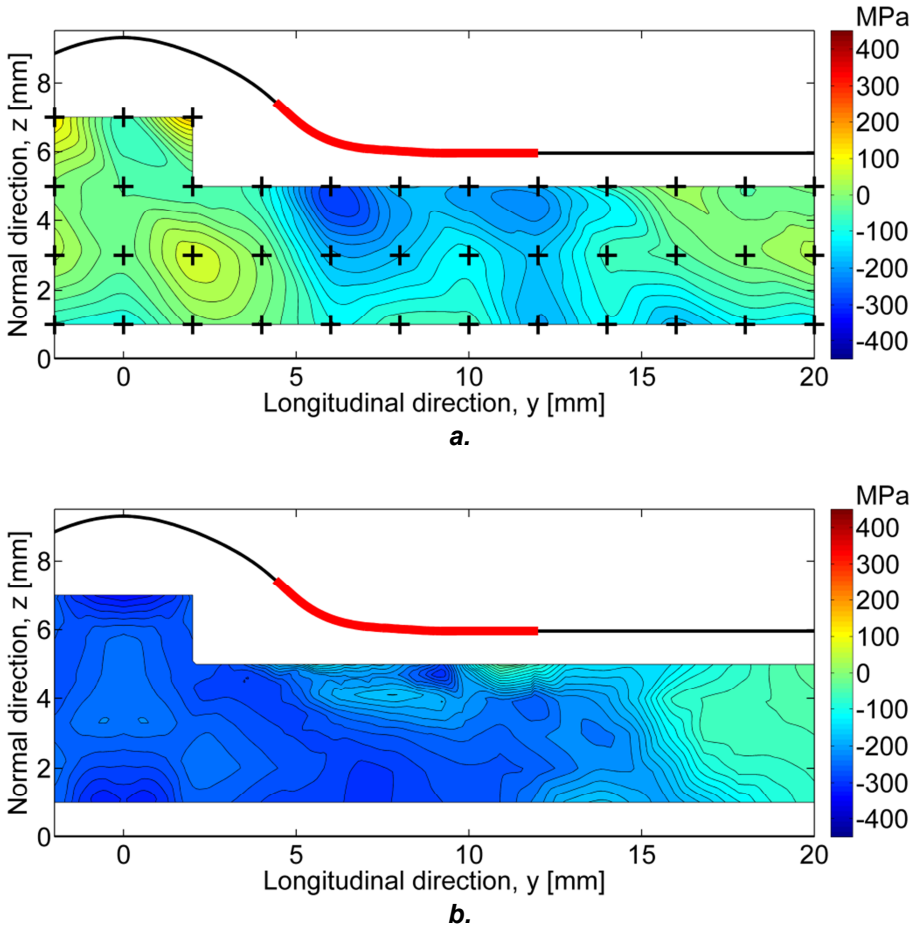

Figure 4-24 Contour of the longitudinal RS after PoWR the welding toes, with 150 kN. *a.* Experimental, and *b.* modelling results. Red line represents the roller contact.

The predicted transverse RS had a more similar behaviour to the experimental measurements. In the weld bead region the RS were slightly tensile, while under the roller print, it was compressive. In the parent material, after 15 mm from the weld centreline, the transverse RS was again slightly tensile in the middle thickness.

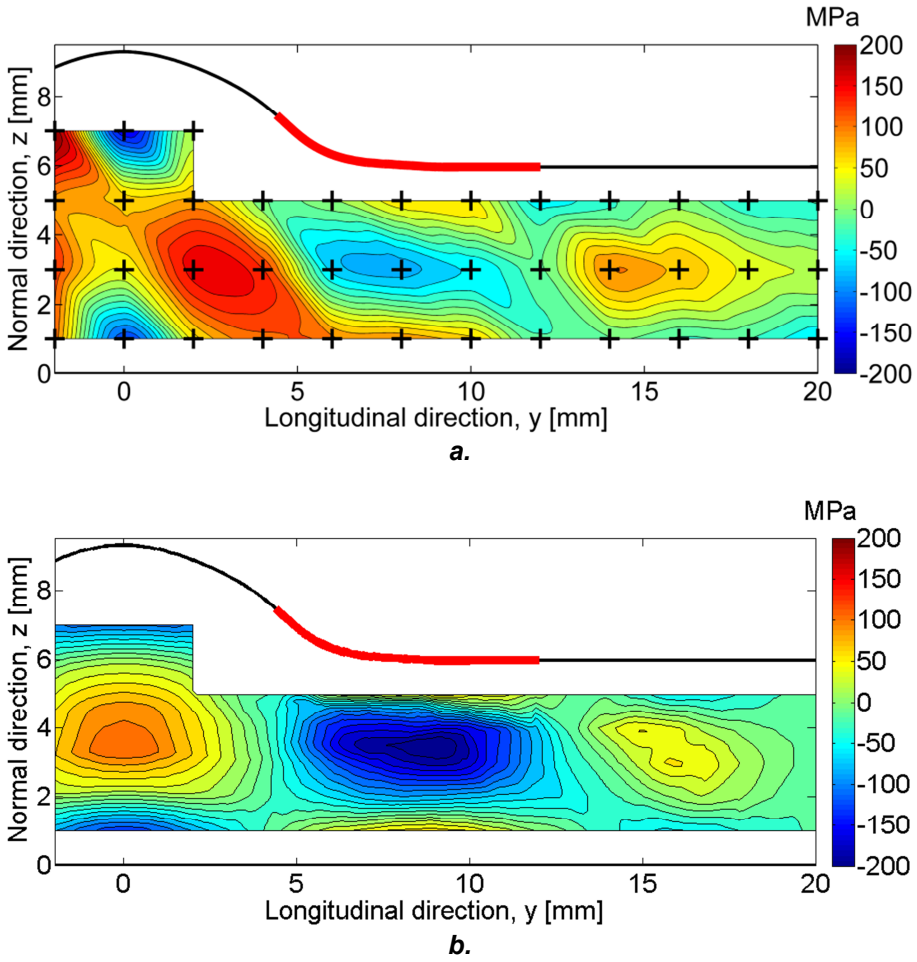

Figure 4-25 Contour of the transverse RS after PoWR the welding toes, with 150 kN. *a.* Experimental, and *b.* modelling results. Red line represents the roller contact.

The discrepancies in the longitudinal RS between the experiment and model, is thought to be due to the weld bead width variation along the weld seam. This is substantiated by the asymmetric RS distribution observed at each side of the weld bead (figure 4-24 *a*, and figure 4-25 *a*). In addition, figure 4-18 shows that when the rolling position increases by 0.5 mm (from 6 to 6.5 mm), the tensile

RS in the weld bead is not completely removed, as observed in the experiment. Although, the longitudinal RS reduction was overestimated by the model, it showed that PoWR the welding toes caused a large reduction to the longitudinal RS which was also observed in the experiment.

Figure 4-26 shows the out-of-plane peak distortion after PoWR the welding toes. Although the RS was largely reduced with this technique in the experiments, the distortion was not reduced significantly. The predicted out-of-plate peak distortion was much less than the one observed in the experiments. It is thought that the weld bead width variation along the weld, did not allow the roller to remove the RS homogeneously along the seam, hence, most of the original distortion remained. Figure 4-18 and figure 4-19 *b* showed that different roller positions can significantly modify the RS distribution and out-of-plate distortion. The model used a constant weld bead shape and width, based in the mean of many experimental observations of Coules *et al*. [2] experiments. Consequently, it does not take into account the actual variations and their effect in the RS and distortion. However, PoWR the welding toes can be used as a subsequent process after a pre-forming of the weld bead shape step, as for example with *in situ* rolling (explained in the next chapter), in which a virtually constant weld bead shape can be obtained.

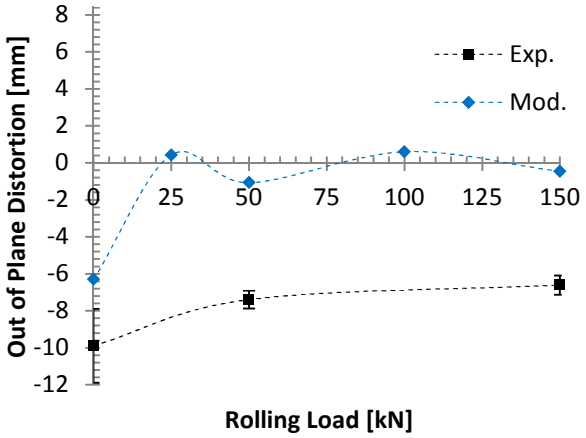

Figure 4-26 Peak out-of-plate distortion vs. rolling load, after PoWR the welding toes.

4.4 Conclusions

Rolling has been investigated after welding to determine its influence in reducing distortion and residual stress. The work showed that:

- Friction coefficients between roller and workpiece, and backing-bar and workpiece are important with high load. For low loads the frictionless and with friction models produce virtually the same RS distribution. In the frictionless models the material deforms more uniformly through the thickness, while in the models with friction the surface constraint imposed by the frictional interaction produces more compressive RS in the core of the weld bead. Therefore, there can be greater tensile stress at the upper surface.

- PoWR the top of the weld bead reduces RS and distortion, providing a very compressive RS region in the weld bead and surrounding material, when loads larger than 50 kN were used.

- The modelling results of the PoWR the top of the weld bead were in very good agreement with the experimental results, in terms of RS and out-of-plate distortion reduction.

- The longitudinal RS can be theoretically reduced by rolling the weldments beside the weld beads. Large RS reductions were produced with the 9 mm roller width, 100 mm diameter, and 100 kN rolling load, rolling at 7 mm from the weld centreline, in which no contact between the roller and the weld bead was produced at any moment. However, some tensile RS remained in the weld bead after rolling, but its magnitude was less than half of the RS produced by welding, and its width was narrower than the weld bead width.
- The wider rollers cause a wider compressive RS in region, but the magnitude of it was less than the compressive RS obtained with narrower rollers for the same rolling loads and positions.

- When rolling the weld toes the RS reduction was sensitive to the precise location of the roller. Therefore, when rolling a weld bead that varies in shape, the RS reduction will vary along the length.
- When rolling the welding toes with the dual flat roller, the longitudinal tensile RS were virtually removed when large loads were applied (higher than 100 kN), at 6 mm from the centreline. However, at distances farther than 6.5 mm the longitudinal RS was tensile in the weld bead. Consequently, physical variations of the weld bead width can yield compressive and tensile longitudinal RS along the weld seam, which can be undesirable.
- The reduction of the welding tensile RS obtained with the 200 mm roller diameter, was less significant than the one produced by the 100 mm one for the same rolling loads. In addition, the RS profile obtained with larger rolling load, and diameter was very similar to the one produce with lower load and small roller diameter.

- The models showed that PoWR the welding toes can efficiently reduce distortion with a wide range of loads, as well as the longitudinal RS. On the other hand in the experiments, the RS was significantly reduced, but not the out-of-plane distortion.

- The AWL was not a useful parameter to determine the appropriate load to reduce distortion. The AWL can be a useful criterion to determine if the weldment is buckled, but it is not suitable for other types of distortions. Therefore, for the weldment geometry and the thermal load induced by welding in the models, bending was the main type of distortion produced, and for that the AWL did not provide any valuable information.

- Variation of the material properties of the actual material can generate significant difference in the RS.

- The RS and distortion predictions with the dual-flat roller were highly sensitive to the position of the roller relative to the weld bead. Therefore,

obtaining a good match with the experiments, where the weld bead size varied, was difficult.

Chapter 5 *In Situ* Rolling

5.1 Introduction.

Many techniques are available to reduce RS and distortion caused by welding. They can be divided into stress engineering techniques, which can be applied before [1,214], during [40,73,215] or after welding [2,81,98], and in-process techniques [10,15,49,54] in which the welding parameters, and other boundary conditions are tuned to reduce distortion and/or RS. *In situ* rolling is not a new technique. Kurkin *et al.* [106] studied its influence on TIG welded aluminium plates (AMg6), by rolling on top of the weld seam at different distances from the weld torch, while most recently, Altenkirch *et al.* [98] (experimentally), and Wen *et al.* [102] (numerically) studied its influence on FSW aluminium plates. They all found that the RS reduction was not significant.

In situ rolling has the potential advantage over the other rolling process in the low load required to induce plastic strain in the weld due to the relatively high temperature in which rolling occurs. In addition, it potentially can reduce time in production as it is not necessary to wait until the weldment cools down. In this chapter the *in situ* rolling models are described. These models were based on the experimental work, and neutron diffraction measurements carried out by Coules *et al.* [2].

5.2 Methodology

As for all the models explained in previous chapters, these models were built with Abaqus Standard version 6.9 as a sequentially coupled thermal-mechanical analysis. The models consist of one main step, in which welding and rolling were performed simultaneously, so that the RS caused by welding was modified by the roller when the material was still hot. Different rolling loads and trailing distances were investigated. The welding heat transfer analysis was run independently of the welding-rolling mechanical analysis, and was already discussed in chapter 2. The temperature distributions obtained in those analyses were imported in the welding-rolling mechanical analyses to obtain the RS distribution produced by welding. In addition, the heat transfer

analysis considered the thermal losses caused by rolling contact and thermal resistance reduction between the backing-bar and the weldment. Figure 5-1 shows a schematic representation of the *in situ* rolling technique.

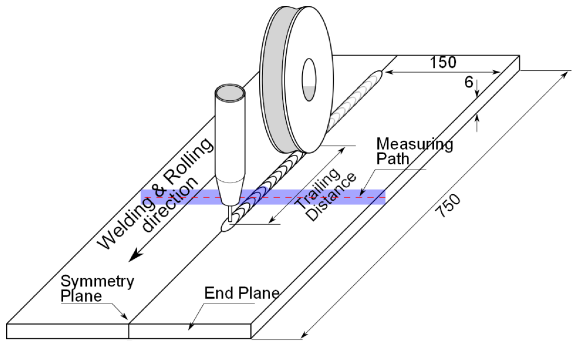

Figure 5-1 Schematic representation of the *in situ* rolling method.

The *in situ* rolling models were based on the post-weld rolling models already explained in chapter 4. In these models the same boundary conditions, element types and number, and plate dimensions of the post-weld rolling models were used. However, the friction coefficient implemented was 0.5 between the backing-bar and the weldment, and frictionless between the roller and workpiece, to reduce computational time.

The *in situ* rolling models investigated the influence of different rolling trailing distances and loads on the welding RS. The trailing distance was considered as the distance between the welding torch axis to the roller centre, as shown in figure 5-1. Table 5-1 shows the parameters investigated in the *in situ* rolling models. The RS were mainly measured across the weldment width, in the middle of it, as shown in figure 5-1.

Table 5-1 Parameters investigated in the *in situ* models

Rolling trailing distance [mm]	Rolling Load [kN]
100	25; 50; 100
250	25; 100

5.3 Results

Figure 5-2 *a* to *c* show a comparison between the predicted and measured longitudinal RS, after welding, and after *in situ* rolling with different loads, with 100 mm trailing distance. Although there is good agreement with the experimental results, some discrepancies were observed in the weld bead region, in particular, after rolling with 100 kN. Farther from the weld bead, the longitudinal predicted RS virtually overlapped the measured values with the three rolling loads.

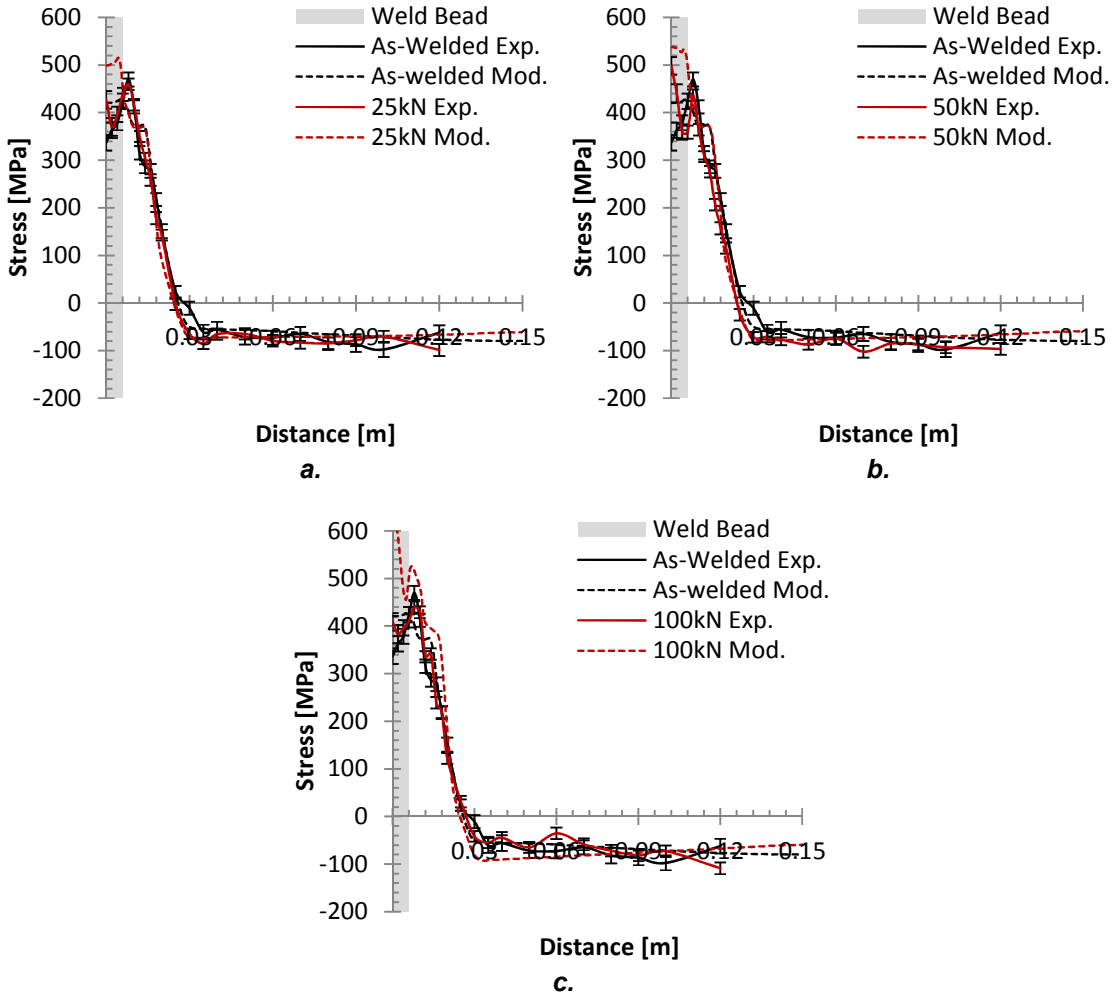

Figure 5-2 Comparison between predicted and experimental results after only welding, and *in situ* rolling with: *a.* 25, *b.* 50, *c.* 100 kN, and 100 mm trailing distance.

Figure 5-3 *a* shows a comparison of the longitudinal transient stress, and transient temperature, in the middle of the weld bead, between the as-welded,

and *in situ* rolling models with different loads, and with 100 mm trailing distance. The results show that *in situ* rolling has a detrimental influence in the longitudinal RSs, generating larger RSs than the ones observed in the as-welded condition. This dependency was proportional to the rolling load used, producing larger RS in the weld bead with larger rolling loads.

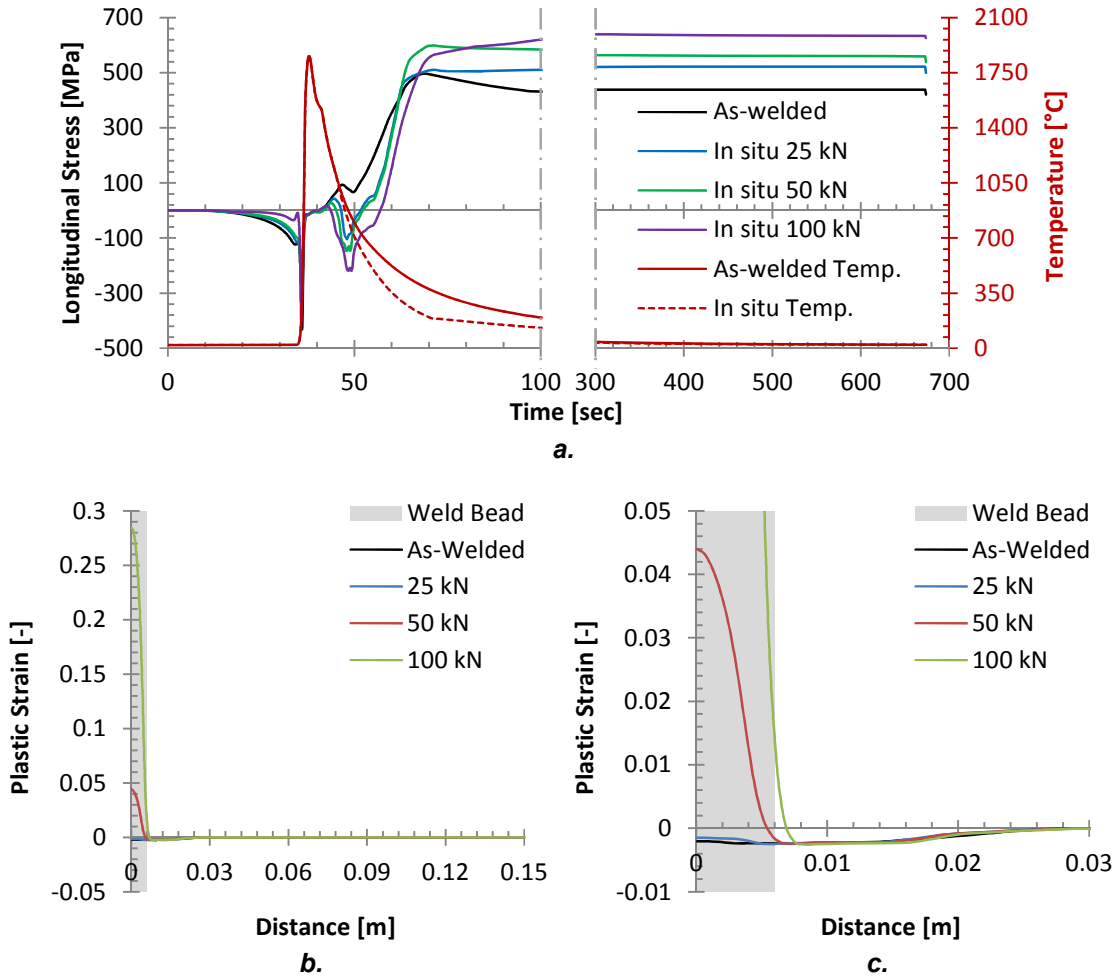

Figure 5-3 ***a.*** **Comparison of longitudinal transient stress, and transient temperature, in the middle of the weld bead, between the as-welded and the *in situ* rolling models with different loads, and 100 mm trailing distance.** ***b.*** **Comparison of the longitudinal plastic strain in the measuring path, after *in situ* rolling with different loads, with 100 mm trailing distance, and** ***c.*** **the same results shown in *b.* but with smaller axial scale.**

Figure 5-3 *b* shows the longitudinal plastic strain in the measuring path after the *in situ* rolling with different loads at 100 mm trailing distance, while figure 5-3 *c* shows a closer view of the previous figure, to display the longitudinal plastic

strain produced with 50 kN and lower loads, as well as the one produced by only welding. Despite the very large plastic strain induced by rolling, especially with 100 kN, the longitudinal RS induced by welding was not reduced, and even increased.

The annealing point of the material in these models was assumed at 950 °C. Above that temperature the material was considered completely annealed, and no work hardening was possible in the models. However, in metals the annealing depends on many factors, such as, amount of previous work hardening, time, temperature, original grain size, and composition [216]; consequently it cannot be defined as a precise temperature. In the *in situ* rolling models the material under the roller was around the annealing point; thus, it induced some work hardening at high temperature, when the metal strength was relatively low. When the material cooled down, it shrank and tensile RSs were formed despite the compression induced by rolling. As rolling load increases, more work hardening was induced and consequently an increase of the tensile RS was observed.

Rolling induces negative plastic strains, in the longitudinal (rolling) direction, as the material is compressed in front of the roller, then positive ones when the material is stretched behind it and hence it reduces the longitudinal tensile RS caused by welding, as described in the post-weld rolling the top of the weld bead section in chapter 4 (see figure 4-7 *a* and *b*, and figure 4-8). In the *in situ* rolling models due to the low strength of the material at high temperature, it produces relatively low compressive stress, as shown at 50 s in figure 5-3 *a.* During cooling, the material contracts, reducing slightly the plastic strain induced by rolling. However, as the temperature decreases the strength of the material increases, so that small variation in the strain produces larger stress. Consequently, when the material reaches room temperature, the RS is similar or even higher than the RS produced by only welding, as shown in the predicted results in figure 5-2 in the weld bead region, and in figure 5-3 *a* when the weldment was at room temperature. The *in situ* rolling with 100 mm trailing distance is not an effective technique to reduce longitudinal RS, since the

tensile RS due to the metal contraction occurs after rolling. However, longer trailing distances can have the beneficial RS reduction of the post-weld rolling the top of the weld bead method, within a single process.

FE prediction of *in situ* rolling on FSW aluminium plates, conducted by Wen *et al.* [102], suggested that longitudinal RS are reduced when the rolling trailing distance was 25 mm, and the RS reduction increased with the rolling load, as shown in figure 5-4, which disagrees with what was observed experimentally in GMA welded S355 plates shown in figure 5-2 *a* to *c*. There are many differences between the *in situ* rolling present in Wen *et al.* and the current study. Firstly the material type, aluminium, has much higher conductivity, lower strength, lower elastic modulus, and much lower welding temperature. Therefore, this may explain why it was possible to get stress reduction so close to the welding tool. Nevertheless, another study by Kurkin and Anufriev [86], conducted in GMA welded aluminium alloy plates (AMg6 and 1201) *in situ* rolled, showed that it was necessary for the material to cool down to 90 °C before stress reduction was possible, seemingly contradicting the results of Wen *et al.*

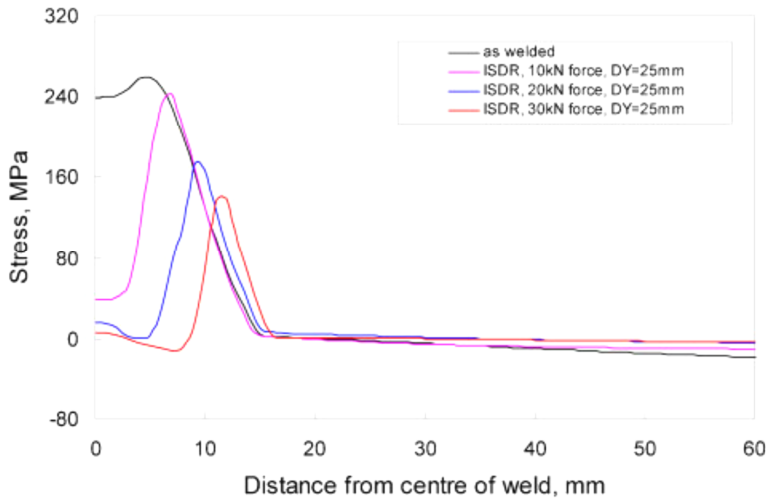

Figure 5-4 Predicted longitudinal RS, after Wen *et al.* [102] (ISDR stands for in situ direct rolling which the same technique applied the models of this thesis).

Kondakov [88] studied the effect of *in situ* rolling in titanium (VT1-1) alloy, and austenitic steel (12Kh18N10T) TIG welded plates. He investigated the influence

of the weld bead height reduction on the RS, distortion, and mechanical properties, by *in situ* rolling with a flat profile roller close to the weld pool. He observed that at those close distances there was no significant effect in the longitudinal RS reduction in the titanium weldments, however, in the austenitic steel weldment, the RS was about 20 % increased after *in situ* rolling. This is in perfect agreement with the results found by Coules *et al.* [2], and with the models developed in this section.

Kondakov and Martynov [87] studied the effect of dual tandem rolling in GMA butt welded aluminium alloy (V92) plates. They found that when the first roller was applied between 370 and 490 °C with strain of 10-23 %, the RS distribution was virtually the same as the as-welded sample. In addition, they claimed that to reduce the RS a lower rolling temperature must be used (cold deformation), which is in agreement with what observed in the modelling results produced in this thesis.

Figure 5-5 *a* shows a comparison of the longitudinal transient stress and transient temperature between the as-welded and the *in situ* models with 25 and 100 kN loads, with 250 mm trailing distance. While, figure 5-5 *b* shows the longitudinal RS in the measuring path for the same conditions.

When the roller axis was aligned with the measuring path (see figure 5-1), the torch was at 48 s from the starting position, in the *in situ* rolling with 100 mm trailing distance, while the torch was at 66 s in the 250 mm trailing distance one. The post weld rolling (**PoWR**) models can be considered as a particular condition of the *in situ* rolling, when the trailing distance tends to infinity. Figure 5-6 shows a comparison of the longitudinal stress in the measuring path at various distances from the welding torch in the as-welded condition, and *in situ* rolling. This shows the effect of rolling on the residual stress field.

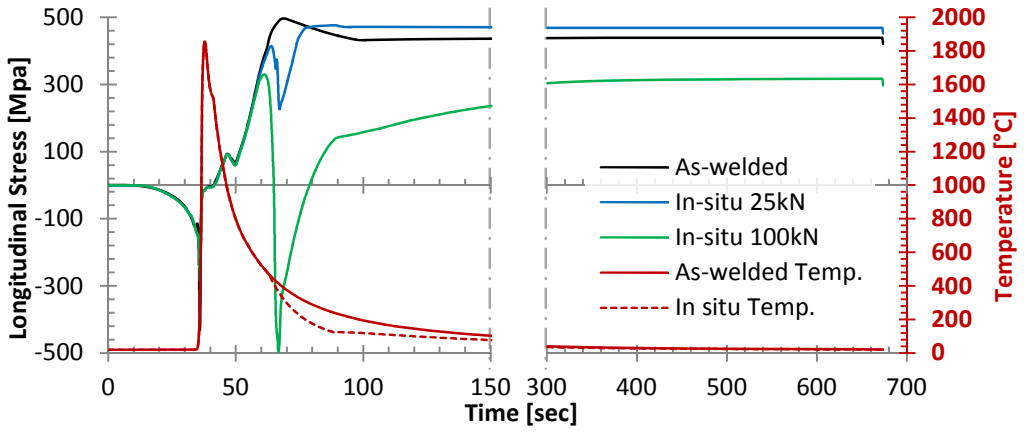

a.

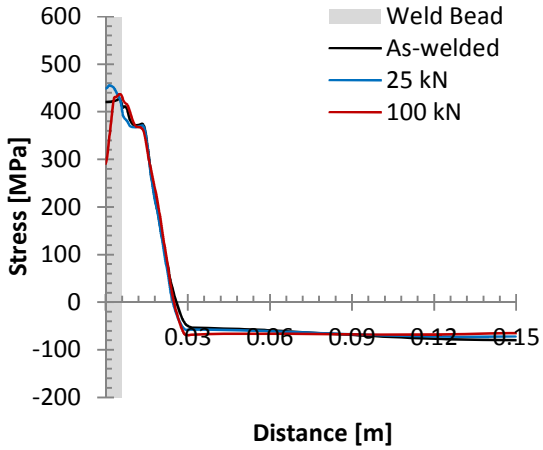

b.

Figure 5-5 ***a.*** **Comparison of the temperature and longitudinal transient stress between as-welded and *in situ* rolling with 250 mm trailing distance models.** ***b.*** **Comparison of the longitudinal RS along the measuring path after *in situ* rolling with 250 mm trailing distance and different loads.**

The 250 mm trailing distance rolling process (T = 66 s) induced larger compressive stress in the weld bead region, which is proportional to the load applied. The temperature in the weld bead below the roller was around 370 °C, and the RS at that point was virtually completed developed, as shown in figure 5-5 *a*. However, next to the weld bead, the RS were not completely set, as shown in figure 5-6 (green dashed line); consequently, no significant reduction of the RS was obtained, as shown in figure 5-5 *b*.

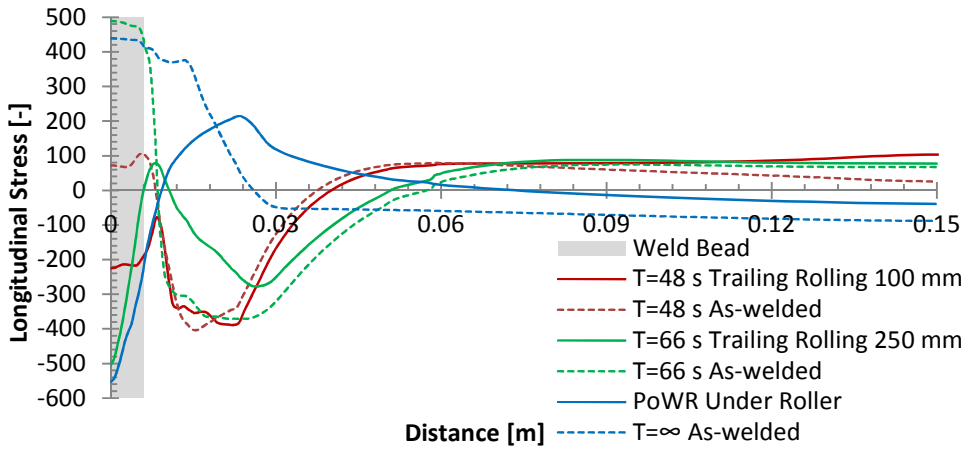

Figure 5-6 **Comparison between the longitudinal transient stress of the *in situ* rolling models with 100 kN, and different trailing distances, against the equivalent transient stress with no rolling.**

When the welding torch was 48 s from the starting position in the as-welded model, the longitudinal tensile transient stress was relatively low (around 100 MPa) in the weld bead region, and large compressive stresses were present next to the weld bead, as shown by the dashed red line in figure 5-6. At the same time, in the *in situ* rolling model, with 100 mm trailing distance, the roller was above the measuring path inducing compressive stress in the weld bead, while next to the weld bead the transient stress was not significant altered (see solid red line in figure 5-6). The temperatures across the weld bead were around the annealing temperature of the material (950 °C), so that some part of it underwent work hardening while the other was perfectly elastic-plastic. However, in both cases (below and above the annealing point) the lower strength of the material at high temperature can only induce low stress.

When the torch was at 66 s from the starting position in the as-welded model, the longitudinal transient stress was very tensile in the weld bead region, and largely compressive next to it in the parent metal, as shown by the green dashed line in figure 5-6. At the same time in the *in situ* rolling model, with 250 mm trailing distance, the temperature under the roller, across the weld bead thickness, was around 370 °C; hence, the material underwent large compressive stress under the roller, and to counterbalance it, the compressive stress present next to the weld bead reduced its magnitude. However, after

rolling the weldment continues cooling and some tensile stress are reformed, as shown in figure 5-5 *b*.

In the PoWR, the RS is fully developed, and the longitudinal tensile peak covers about 52 mm in the middle of the weldment (26 mm in figure 5-6). In this case, when rolling is performed, the tensile RS is reduced about the same amount as the *in situ* rolling model with 250 mm in the weld bead region; however in the PoWR the RS beside the weld bead are fully developed, so that the RS reduction is permanent in the weldment.

Figure 5-7 *a* and *b* show the contour plots of the longitudinal transient stress across the weldment thickness, in the longitudinal section of the weld bead, during rolling with 100 kN, with two different trailing distances, namely, 100, and 250 mm, respectively. The 100 mm trailing distance model induced large deformation in the weld bead; however, the longitudinal transient stress did not exceed 622 MPa underneath the roller, as shown in figure 5-7 *a*. In addition, due to the low strength, and high plasticity of the material at high temperature, the weld bead is largely deformed, building up material in front of the roller.

On the other hand, when 250 mm trailing distance was used, the deformation of the weld bead was much less, and the longitudinal transient stress was larger (reaching about 900 MPa below the roller, see figure 5-7 *b*), because of the lower temperature, and high strength material at that point.

Figure 5-8 *a* shows the contour plot of the typical out-of-plane distortion after *in situ* rolling (100 kN rolling load, and 250 trailing distance). The deformed shape was similar to the one produced by only welding model (see figure 2-27 *b*); therefore it was considered negative. Figure 5-8 *b* shows the predicted out-of-plane peak distortion after *in situ* rolling with different rolling trailing distances and loads, and the experimental results of Coules *et al.* with 100 mm rolling trailing distance. Some of the *in situ* rolling experiments did not have replicates; consequently no error bars were present at all the loads investigated. A reduction of about 42 % of the out-of-plane peak distortion was observed in the experiments, when *in situ* rolled with 25 kN. The reduction with the other loads was less significant. The predicted out-of-plane peak distortion was not

very similar to the one observed in the experiments, however with 100 kN load all the results were very similar. In FE models, the prediction of distortion is very complicated because the models did not take into account all the metallurgical phenomena in the material present during welding and post weld heating, as the recovery and the recrystallization.

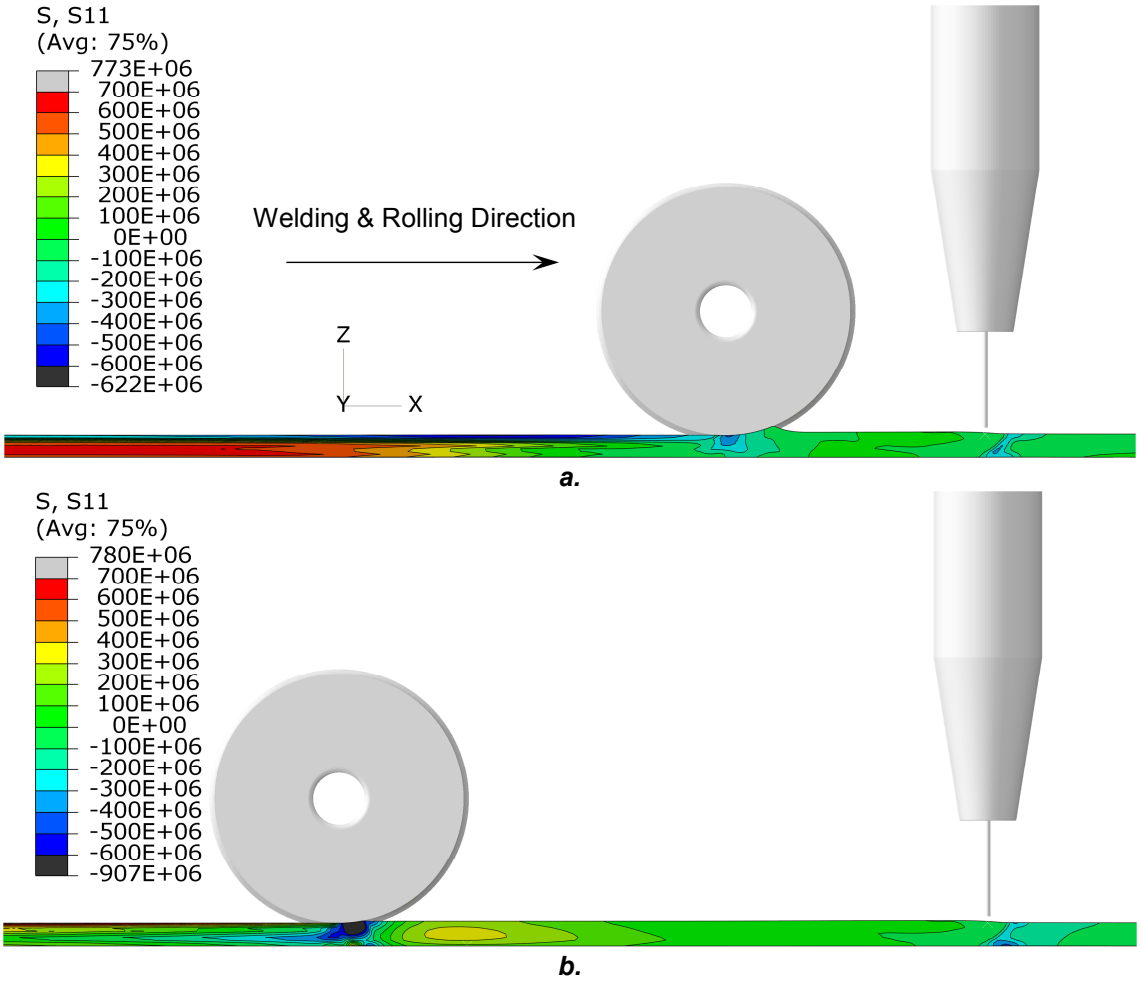

Figure 5-7 Contour plots of the longitudinal transient stress in the *in* situ rolling with 100 kN, and: *a*. 100 mm, and *b.* 250 mm trailing distance.

The thermal cycle the weldment undergoes during welding causes plastic strain in the weld and nearby metal, producing RS. The internal forces due to the RS interact to distort the weldment in different modes, being the bending mode the principal in this case. The *in situ* rolling induced plastic strain which counteracted the inherent plastic strain due to welding. However, due to the low

strength of the material at high temperature, the plastic strain induced by rolling is localised to the weld bead. In addition, when rolling was performed, the material was still contracting, so that the plastic strain continued after rolling. Consequently, RS and distortion formed after *in situ* rolling. This was observed with the two rolling trailing distances, regardless of the rolling load. To obtain significant distortion reduction either the rolling trailing distance should have been larger than 250 mm for the current welding conditions, or the temperature of the weld bead in the rolling contact should have been lower than 370 °C.

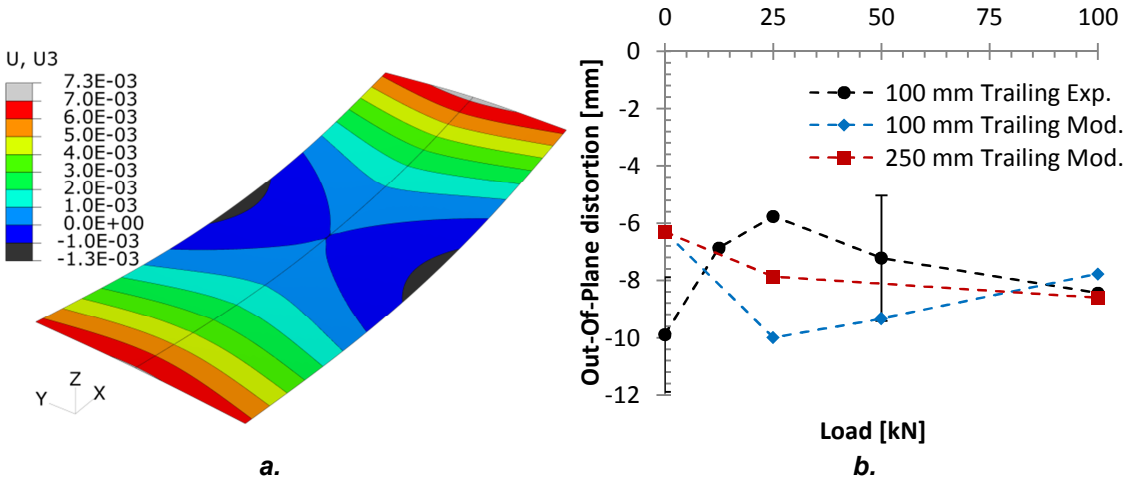

Figure 5-8 ***a.*** **Contour plot of the out-of plane distortion after *in situ* rolling with 100 kN rolling load, and 250 mm trailing distance (magnified 5×).** ***b.*** **Out-of plane distortion after *in situ* rolling with different rolling loads and trailing distances.**

5.4 Conclusions

- The *in situ* rolling is not an effective technique to reduce RS and distortion caused by welding, because the tensile RS are recreated on the last stage of cooling, reverting the compressive RS induced by rolling.
- With 250 mm trailing distance the longitudinal RS in the weld bead is slightly reduced, however, the RS in the rest of the cross section was virtually unmodified.
- *In situ* rolling can induce larger plastic strain; however, it is contained within a region underneath the roller. Consequently, it can reduce the

plastic mismatch caused by welding, but no significant RS reduction can be obtained by this method. Nevertheless, there was a small increase in the peak tensile RS which was not clearly observed in the experiments conducted by Coules *et al.* [2].

Chapter 6 General Conclusions and Future Work

6.1 Conclusions

The main objective of the present investigation was to provide a deep understanding of the localised rolling to reduce the residual stress induced by welding, as well as the reduction of the distortion. In this thesis the advantages and down sides of different localised rolling processes have been shown. In addition different approaches to simulate the thermal losses due to the backing-bar were investigated. Three different localised rolling techniques were investigated. *Pre-weld rolling* (**PWR**) consists in rolling the individual plates before welding, at certain distance from the welding edge. An additional post-weld heating treatment in the roller prints was also investigated. *Post-weld rolling* (**PoWR**) was investigated with two different roller profiles, a radius grooved, and a dual flat roller. The grooved roller was used to roll the top of the weld bead, while the dual flat rolled the weld toes and the parent material next to the weld bead. The *in situ rolling* used the grooved roller to roll the weld bead top a short period after being deposit, when the material was still hot.

Even though PWR induced heavily compressive residual stress in the roller path, and tensile residual stress in the edge in which the weld seam was subsequently applied, neither significantly reduced the welding residual stress nor the distortion. The tensile residual stress in the welding edge (before welding), can reduce the transient compressive stress in front of the torch during welding, however, above a certain temperature the material is annealed and hence it forgets its work-hardening history. Therefore, no reduction of the longitudinal tensile welding residual stress was obtained by this technique. On the other hand, when post-weld heating was applied in the roller prints, massive longitudinal residual stress reduction was obtained. As for the welding process, the induction heating induces longitudinal tensile residual stress along the heating path. When the moving induction heating was applied to the region that had been rolled, the compressive residual stress present in those regions was reduced, and consequently the welding tensile residual stress (which was in

equilibrium with the rolling compressive stress) was reduced too. As a consequence the distortion was also reduced.

Pre-weld rolling has the advantage over the other rolling techniques in that it can be potentially performed directly by the steel manufacturer or in a separate location from the place in which the plates are going to be welded. In addition, induction moving heating used as a distortion reduction method in shipyards [198] relies on contracting the structure; residual stresses are redistributed generating a new tensile peak. The pre-weld rolling followed by induction heating reduces the overall levels of RS. Therefore, it can be particularly effective when applied to thin plate structures where buckling distortion occurs.

The PoWR induced large longitudinal compressive residual stress in the rolling path. When applied on top of the weld bead, it reduced or even reverted the welding tensile residual stress. However, it can detrimentally modify the shape of the weld toes, increasing the stress concentration in those regions.

When PoWR is applied in the weld toes, a reduction of the welding tensile residual stress was observed. In addition, due to the curvature of the roller in the contact with the weld bead, it improves the shape of the weld toes, removing undercuts and smoothing those regions. This may improve the fatigue performance. The stress reduction obtained when rolling the weld toes was strongly dependent in the position of the roller from the weld centreline. Therefore, in a practical weld where weld shape variability occurs, there will be a varying stress profile along the weld length.

The frictional interaction between roller and workpiece, and backing-bar and workpiece showed strong effects on the RS distribution when large rolling loads were used. With low loads the frictionless and with friction models produce virtually the same RS distribution. In the frictionless models the material deforms more uniformly through the thickness, while in the models with friction the surface constraint imposed by the frictional interaction produces more compressive RS below the contact surface in the core of the weld bead. Note that when the roller was modelled as frictionless, the weld toes were largely deformed, increasing the stress concentration shape in those regions.

Using the dual flat roller to roll the weld toes, the longitudinal tensile RS were almost completely removed when large loads were applied (higher than 100 kN), at a rolling distance of 6 mm from the centreline. On the other hand, at distances farther than 6.5 mm the longitudinal RS was tensile in the weld bead. Consequently, physical variations of the weld bead width, due to normal process fluctuation, can yield compressive and tensile longitudinal RS along the weld seam, which can be undesirable.

In situ rolling takes advantage of the high temperature of the weld bead to obtain large plastic deformation of it with relatively low loads. However, when rolling was applied the surrounding material was at lower temperature than the weld bead, and hence their strength was higher than in the weld bead. Consequently, the plastic deformation was localised to the weld bead. The welding longitudinal residual stresses are formed during cooling; therefore, they are formed after rolling was performed. Thus, *in situ* rolling did not reduce the welding tensile residual stress. Even when the weld bead was warm (370 °C) the welding longitudinal residual stress reduction was marginal (a reduction of about 100 MPa), and limited to a small part of the weld bead. On the other hand, *in situ* rolling has the advantage of reshaping the weld bead profile, which could improve the stress concentration normally present in the weld toes. In addition, due to the plastic deformation at high temperature, it could induce recrystallization of the microstructure of the weld bead, improving the mechanical properties.

6.2 Prospect for future work

- More work has to be done on applications where buckling distortion is an issue such as in thinner and narrower materials.
- Experimentally validate post-weld heating method on pre-weld rolled plates.
- Experimental validation of dual flat rollers with low loads to investigate their influence in distortion reduction and fatigue life.
- Experimental influence of friction interaction in the residual stress reduction in weldments.

Appendix A Material properties of mild steel S355

S355 is a high-strength low-alloy structural steel, commonly used in construction. Its composition and different delivery conditions are regulated in the UK by the British Standards BS EN 10025-1-6:2004 [120,189,217–220].

Temperature dependant material properties for S355 and similar steel grades can be found in the literature [119,127,128,132,134–136,221]. A remarkable work was performed by Outinen *et al.* [134–136], and Peil and Wichers [132] in the temperature dependent mechanical properties. However, the data used primarily in the numerical models presented in this thesis were supplied by Tata Steel Research Development and Technology, Swinden Technology Centre. Table A-1 shows the chemical composition of the steel used in the experiments carried out by Coules *et al.* [1,2].

Table A-1 Chemical composition. Analysed by Tata R, D&T Swinden Technology Centre

C	Si	Mn	P	S	Cr	Mo	Ni
0.12	0.35	1.37	0.017	0.007	0.016	0.002	0.019
Al	Sn	B	Cu	N	Nb	Ti	V
0.034	0.032	0.0001	0.01	0.004	0.028	0.001	0.002

Figure A-1 shows the temperature dependent specific heat capacity, C_p, and thermal conductivity, k, of S355. To take into account the convective heat transfer mechanism in the weld pool [222], the thermal conductivity can be increased [7] or reduced [6] artificially. While increasing the thermal conductivity after the melting point can be justified by the stirring forces present in the molten pool, the reason for decreasing the thermal conductivity after the melting point is not clear. It is thought that such an assumption can be made only when stirring forces are not significant in the molten pool, or when the thermal conductivity of the liquid metal drops heavily as occurs in pure aluminium,

where such property drops from about 210 to 90 $W \cdot m^{-1} \cdot K^{-1}$ when the metal melts [127]. In this thesis the value of thermal conductivity was artificially increased.

The specific heat capacity of the S355 has local maximums at the Curie, and state transformation regions [223]. These maximums are difficult to capture and are not included in the graph. Some authors [125] use constant value of specific heat capacity after the first local maximum, corresponding to the ferrite-austenite transformation, to simplify calculation and reduce computational time in modelling, but there is no physical reason for that assumption.

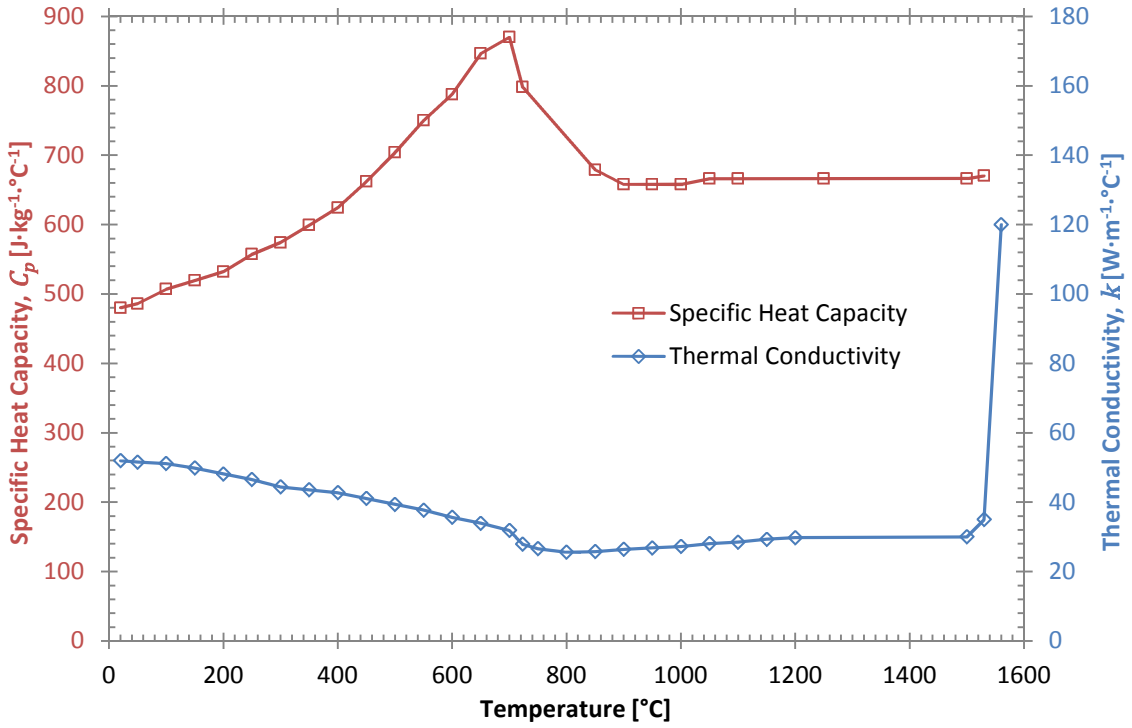

Figure A-1 Heat transfer properties of S355.

The energy required to induce the phase changes at constant temperature is called the latent heat. Since the latent heat of solid phase transformation was much lower than the fusion and vaporisation ones, it was ignored in the model built in this thesis. Only the latent heat of fusion and vaporisation were included in the numerical models. The different values of latent heat for S355 are

reported in table A-2 with their respective start and finish temperature for each transformation.

Table A-2 S355 Latent heat and Density

	Solid phase transformation $\alpha \leftrightarrow \gamma$ [119]	Fusion [130]	Vaporization [130]	Density
Temperature range [°C]	723—870	1500—1530	3090—3100	Room temperature
Latent heat $[kJ \cdot kg^{-1} \cdot K]$	7	272	6258	
Density $[kg \cdot m^{-3}]$				7850

Although density changes with temperature, Abaqus Standards version 6.9, does not update the density when the temperature changes during the analysis (except for acoustic analysis). Instead, Abaqus Standard recalculates the density based on the volume changes, calculated from the thermal expansion coefficient (figure A-2 *a.)*, and the original density. Consequently, temperature dependent density is not required in the analysis.

Figure A-2 shows the linear thermal expansion, Young modulus, Poisson ratio, and True stress of S355. This data was provided by Tata Steel Research Development and Technology, Swinden Technology Centre. The data was adapted from the mechanical properties presented on SYNFAN report [177,224].

The linear thermal expansion curve reported in figure A-2 *a* represents an average value after measuring the thermal expansion with a dilatometer at different cooling rates from 0.4 to 430 °C·s^{-1} (the heating rate was 90 °C·s^{-1}). The true stress and the rest of the mechanical properties were measured in compression using a process simulator, Gleeble. The tested material was first heated up to 1400 °C and then cooled down to the testing temperature in which the compressive test was performed.

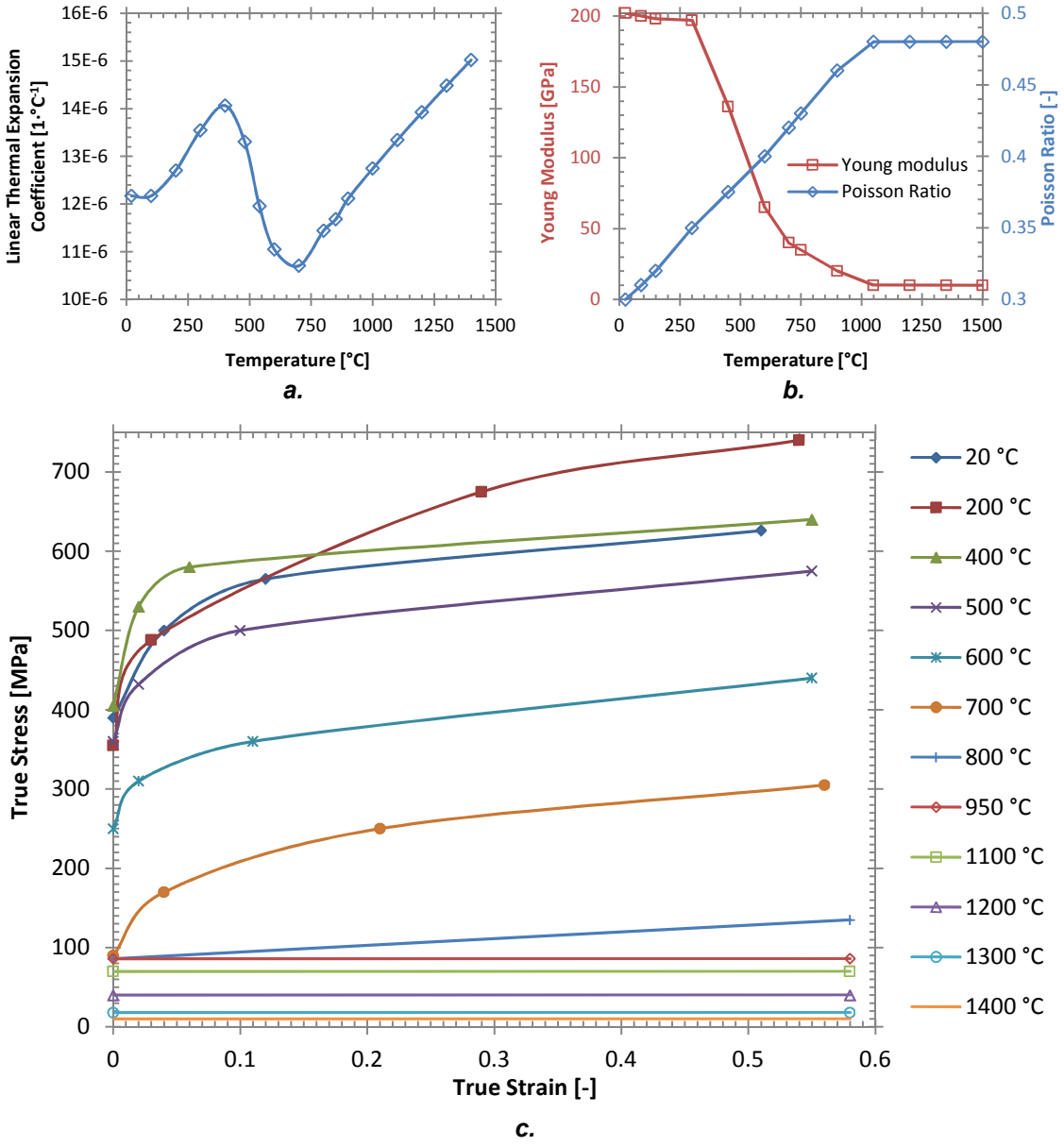

Figure A-2 **Mechanical properties of S355. a. Linear thermal expansion coefficient. b. Young modulus and Poisson ratio. c. True stresses. (Provided by Tata Steel Research Development and Technology, Swinden Technology Centre).**

Figure A-3 show the tensile test results conducted in S355 by Peil and Wichers [132], in a wide range of temperature. The true stress of both, Tata Steel, and Peil and Wichers showed higher work hardening behaviour between 200 and 400 °C than the room temperature test. Peil and Wichers claim that this behaviour is owed to a dynamic strain aging. At this range of temperature the diffusion of carbon and nitrogen atoms in the BCC ferritic matrix to preferential locations, and the formation of Cottrell atmospheres, difficult the dislocation

motion; consequently, an increment of the work hardening, and serrated behaviour was observed in the tensile test at those temperatures. Figure A-4 *a* to *c* show a comparison of true stresses at 20, 200, 400 °C, between Tata Steel and Peil and Wichers. The result shows good agreement at 20, and 200°C in the rage of strain compared (rage reported on Peil and Wichers paper). However, at 400°C the yielding strength is about 100°MPa higher than Peil and Wichers. It is thought that the discrepancies are related with the way how the strength curves were conducted. Peil and Wichers tested the S355 in heating and in tension, while Tata Steel did it in cooling and in compression. Consequently, the kinetic of the formation of the carbonitrides is different hence the yielding strength.

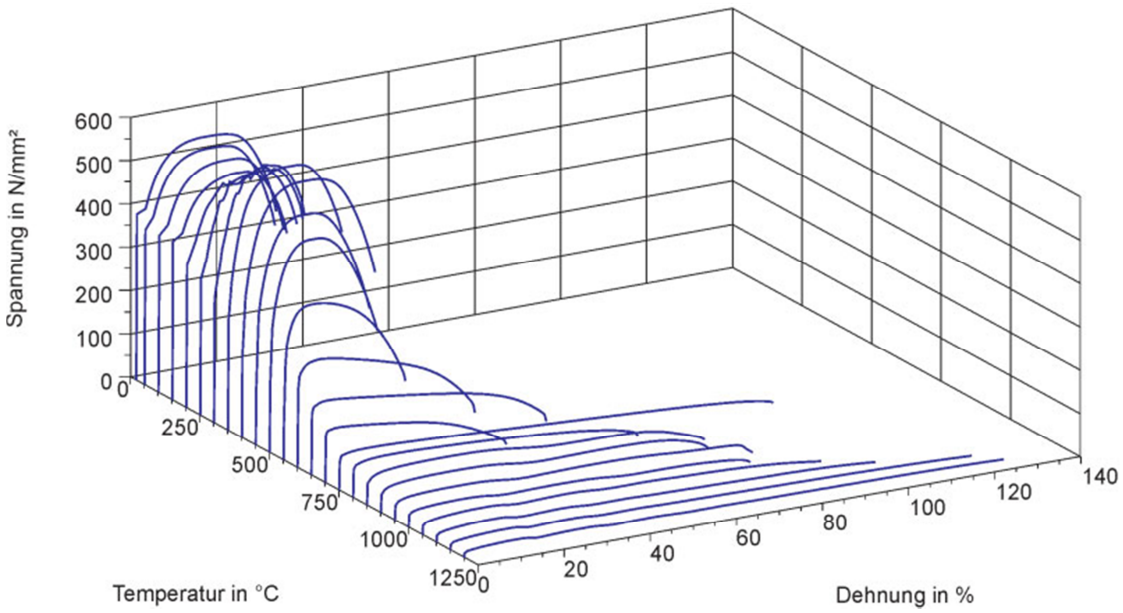

Figure A-3 Results of a series of tensile tests conducted from 20 to 1200 °C by Peil and Wichers [132]

The plastic deformation induced during welding and accumulated by the workpiece is relaxed when the material melts. Moreover, when a ferritic steel undergoes phase transformation the rearrangement of the dislocations causes partial or total loss of the accumulated plastic strain with probably the exception of the martensitic transformation, which only involves a shear movement of the

atoms non affecting the dislocation density [143,178,179]. This phenomenon commonly called in welding annealing [225].

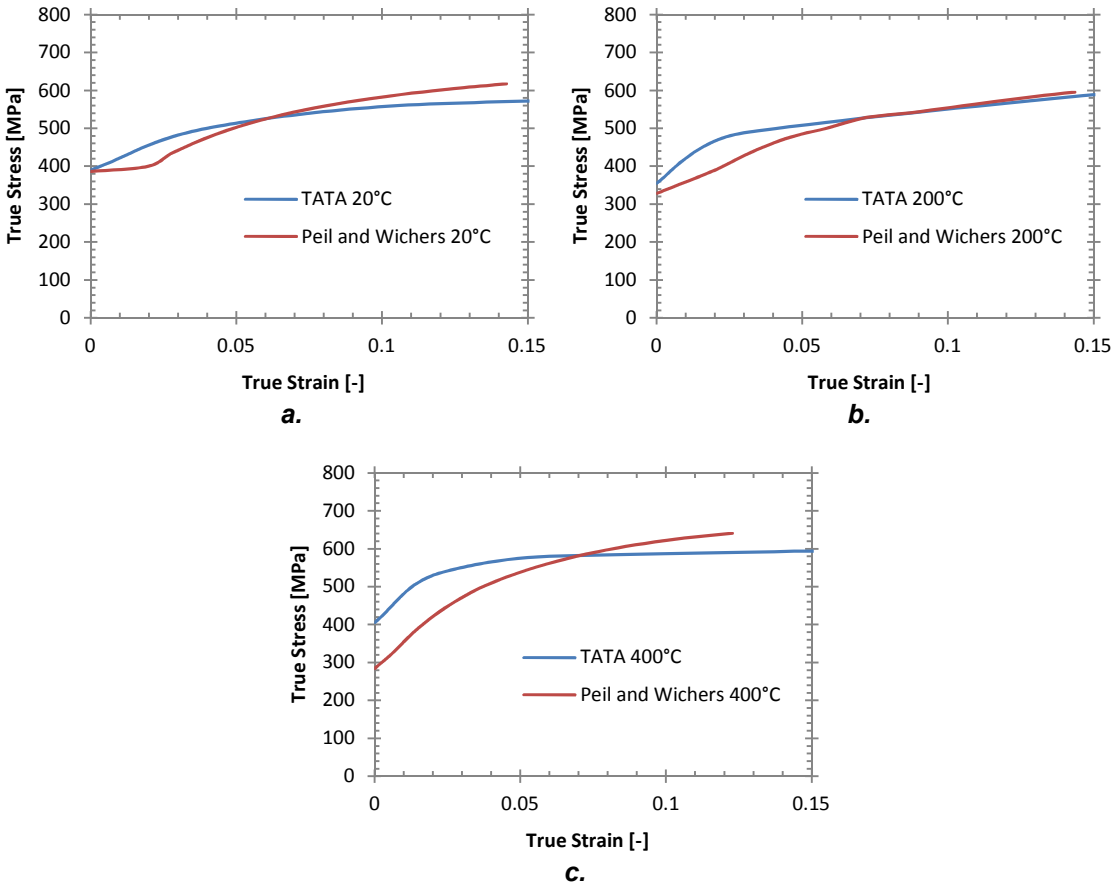

Figure A-4 Comparison of some true stress at different temperatures between Tata and Peil and Wichers [132]. *a.* to *c.* True stress at 20, 200, and 400 °C respectively.

In Abaqus the anneal procedure simulates the relaxation of the accumulated stresses and plastic strains when certain temperature is exceeded. Therefore, it is used to model either annealing or fusion of the material [140]. In the literature annealing is used at different temperatures [143,225]; however, assuming that the plastic strain history is deleted only after melting could overestimate the work hardening induced on the material. Consequently, in the models developed in this thesis the material was considered full annealed when it was above the upper critical temperature, A_{C3}, by more than 50 °C [226,227]. The

upper critical temperature, A_{C3}, was calculated by the empirical equation proposed by Andrews [228] and showed in eq. A–1.

$$A_{C3} = 910 - 203\sqrt{\%C} - 15.2(\%Ni) + 44.7(\%Si) + 104(\%V) + 31.5(\%Mo) + 13.1(\%W)$$

Standard deviation = ± 16.7°C

Eq. A–1

The austenitization temperature is expected to occur in quasi-equilibrium conditions since superheating effects can be ignored for most welding situations [223]. The calculated A_{C3} temperature was 855.3°C; therefore, the annealing point of the material was assumed at 950°C. Above this temperature perfect plastic behaviour was assumed, *i.e.* no work hardening occurred beyond the annealing temperature.

In appendix b can be found the Abaqus coding for the material properties implemented in the models of this thesis.

Appendix B Material properties Abaqus keywords

```
** MATERIALS
**
*Material,  name="S355
TATA STEEL"
*Conductivity
 51.956,  20.
 51.537,  50.
 51.118, 100.
 49.856, 150.
 48.148, 200.
 46.509, 250.
 44.414, 300.
 43.576, 350.
 42.738, 400.
 41.062, 450.
 39.386, 500.
  37.71, 550.
 35.615, 600.
 33.939, 650.
 31.844, 700.
 27.864, 723.
 26.607, 750.
 25.559, 800.
 25.769, 850.
 26.397, 900.
 26.816, 950.
 27.235,1000.
 28.073,1050.
 28.492,1100.
  29.33,1150.
 29.749,1200.
    30.,1500.
    35.,1530.
   120.,1560.
*Density
7850.,
*Elastic
 2.02e+11, 0.3, 25.
 2e+11, 0.31, 90.
 1.98e+11, 0.32, 150.
 1.97e+11, 0.35, 300.
1.36e+11, 0.375, 450.
 6.5e+10, 0.4, 600.
 4e+10, 0.42, 700.
 3.5e+10, 0.43, 750.
 2e+10, 0.46, 900.
 1e+10, 0.48, 1050.
 1e+10, 0.48, 1200.
 1e+10, 0.48, 1350.
*Expansion
 1.21726e-05,  20.
 1.21726e-05, 100.
 1.27052e-05, 200.
 1.35446e-05, 300.
 1.40638e-05, 400.
 1.33026e-05, 480.
 1.19539e-05, 540.
 1.10511e-05, 600.
 1.07067e-05, 700.
 1.14403e-05, 800.
 1.16815e-05, 850.
 1.21137e-05, 900.
 1.27448e-05,1000.
 1.33448e-05,1100.
 1.39213e-05,1200.
 1.44792e-05,1300.
 1.50222e-05,1400.
*Latent Heat

272000.,1500,1530.

6.25815e+06,3090,3100

*Plastic
  3.9e+08,   0.,  20.
    5e+08, 0.04,  20.
 5.65e+08, 0.12,  20.
 6.26e+08, 0.51,  20.
 3.55e+08,   0., 200.
 4.88e+08, 0.03, 200.
 6.75e+08, 0.29, 200.
  7.4e+08, 0.54, 200.
 4.05e+08,   0., 400.
  5.3e+08, 0.02, 400.
  5.8e+08, 0.06, 400.
  6.4e+08, 0.55, 400.
  3.6e+08,   0., 500.
 4.32e+08, 0.02, 500.
    5e+08,  0.1, 500.
 5.75e+08, 0.55, 500.
  2.5e+08,   0., 600.
  3.1e+08, 0.02, 600.
  3.6e+08, 0.11, 600.
  4.4e+08, 0.55, 600.
    9e+07,   0., 700.
  1.7e+08, 0.04, 700.
  2.5e+08, 0.21, 700.
 3.05e+08, 0.56, 700.
    5e+07,   0., 800.
  8.2e+07, 0.09, 800.
 1.35e+08, 0.58, 800.
  8.6e+07,   0., 950.
    7e+07,   0.,1100.
    4e+07,   0.,1200.
  1.8e+07,   0.,1300.
    1e+07,   0.,1400.
*Anneal Temperature
950.,
*Specific Heat
   480.,  20.
 486.04,  50.
 506.99, 100.
 519.56, 150.
 532.13, 200.
 557.27, 250.
 574.03, 300.
 599.17, 350.
 624.31, 400.
 662.02, 450.
 703.92, 500.
 750.01, 550.
 787.72, 600.
 846.38, 650.
   870., 700.
  798.2, 723.
 678.78, 850.
 657.83, 900.
 657.83, 950.
 657.83,1000.
 666.21,1050.
 666.21,1100.
 666.21,1250.
 666.21,1500.
  670.4,1530.
```

Appendix C Numerical solutions

Finite differences method (FDM).

Finite differences method is a classical way to solve numerically partial differential equations (PDE). The method consists in passing from a continuous function (within a certain domain) to a discrete distribution of points in a mesh or grid, transforming the PDE in a group of finite difference approximation with the appropriate boundary conditions. This finite difference approximation is often obtained from the Euler method or truncated Taylor series.

The numerical solution for PDE and ordinary differential equations is done by the limit when h tends to zero, as shown in eq. C–1. Since in finite differences there is no continuum of values to reduce the increment to zero, the limit cannot be applied and h has to be a finite value [229].

$$\frac{dU}{dx} = \lim_{h \to 0} \frac{U(x+h) - U(x)}{h} \qquad \text{Eq. C–1}$$

Therefore eq. C– can be written as shown in eq. C–2, when h is small enough.

$$\frac{dU}{dx} \approx \frac{U(x+h) - U(x)}{h} \qquad \text{Eq. C–2}$$

The first order derivative can be approximated by three methods:

$$U'^{(x)} = \frac{U(x+h) - U(x)}{h} \qquad \text{Forward difference}$$

$$= \frac{U(x) - U(x+h)}{h} \qquad \text{Backward difference}$$

$$= \frac{U(x+h) - U(x-h)}{2h} \qquad \text{Central difference}$$

The second order derivative can be approximated as shown below.

$$U''(x) = \frac{U(x+h) - 2U(x) - U(x-h)}{h^2}$$ Central difference

After that, a set of equations is generated and distributed in a grid that can be solved by numerical methods such as Newton-Raphson, Euler or others.

Finite volume method

The finite volume method is a way to calculate partial differential equations by transformation in algebraic equations. It uses the conservation equations of Navier-Stokes and Euler. Finite volume method consists in discretising the constitutive equations of flow in a grid, similar to finite difference, generating an amount of arbitrary polyhedral control volumes. The surface integral of the total volume is approximated to the sum of the fluxes that are going through the surfaces of each control volume [230].

An advantage of the finite volume respect finite difference method is that the former is more flexible, and may be simply used on complex grids. For this reason the finite volume method is one of the most widely applied techniques to calculate flows in complex geometries [230].

Finite element method (FEM)

The FEM, sometimes called finite element analysis (FEA), is a numerical technique normally used to find approximate solutions of PDE. To understand how the method works, the description provided by Oran and Boris [229] was used. Consider an initial PDE, as shown in eq. C–3, where u is a dependent variable defined by the continuity equation, $\mathcal{L}$ is generally a nonlinear operator and represents the spatial derivative operator in the continuity equation, and f is another function with the same parameters used by u.

$$\frac{\partial u(x,t)}{\partial t} = \mathcal{L}[u(x,t)] + f(x,t)$$ Eq. C–3

An approximate solution of the function u is reached in eq. C–4, by a superposition of N functions $v_n(x)$, which satisfies the boundary conditions of the problem.

$$u(x,t) \equiv \sum_{n=1}^{N} a_n(t) v_n(x) \qquad \text{Eq. C–4}$$

There are two ways to see FEM as a solution of PDE: the first way is global, where the independent variable u is developed through the complete region, as shown in eq. C–4. A common choice for v_n is given by eq. C–5.

$$v_n(x) = \begin{cases} \dfrac{x - x_{n-1}}{x_n - x_{n-1}} & \text{if } x_{n-1} \leq x \leq x_n \\ \dfrac{x_{n+1} - x}{x_{n+1} - x_n} & \text{if } x_n \geq x \geq x_{n+1} \\ 0 & \text{Otherwise} \end{cases} \qquad \text{Eq. C–5}$$

Each value of x_n is called node and the straight line between two consecutive nodes is an element. The second method is named local, where each element is expanded in a polynomial, as shown in eq. C–6.

$$v_e(x) = \sum_{i=1}^{I} a_{e,i} x^i \qquad \text{Eq. C–6}$$

Where $a_{e,i}$ is the coefficient of the i^{th} term of the polynomial of the element e [229].

Appendix D Description of the experimental work

This appendix describes all the parameter implemented in the preparation of the samples produced by Coules *et al*. [1–3], in the pre- and post-weld rolling, *in situ* rolling, and the as-welded conditions for the pre- and post-weld rolling geometries. In addition, a brief description of the implemented equipment is provided.

D.1 Equipment description

All the experimental welds were performed with a Fronius TransPuls Synergic 5000 welding machine (see figure D-1 *f*), using a pulsed Gas Metal Arc Welding (**GMAW**) process.

The rolling and welding equipment is shown in figure D-1. The sample plates were fixed during welding and rolling by a vacuum clamping system. The rolling load was performed by lowering the roller assembly with a hydraulic piston, while the linear crossbeam translation was performed by the feed motor. The equipment had a maximum travel speed of 25 $mm \cdot s^{-1}$. The welding process was performed by attaching a welding torch to the crossbeam, and moving the crossbeam with the feed motor.

The machine can potentially operate in two modes, namely, constant and dynamic force modes. In the constant force mode, the oscillating mass is fixed to the crossbeam and the rolling load is provided by the piston pressure between the workpiece and the crossbeam. In this mode the maximum load that can be provided is 200 ± 4 kN. In the dynamic force mode, the oscillating mass is free to move vertically. The load is applied dynamically by a high speed pressure applied by the piston. Then the peak load is determined by the acceleration of the oscillating mass. In the models of this thesis only the constant force mode was considered.

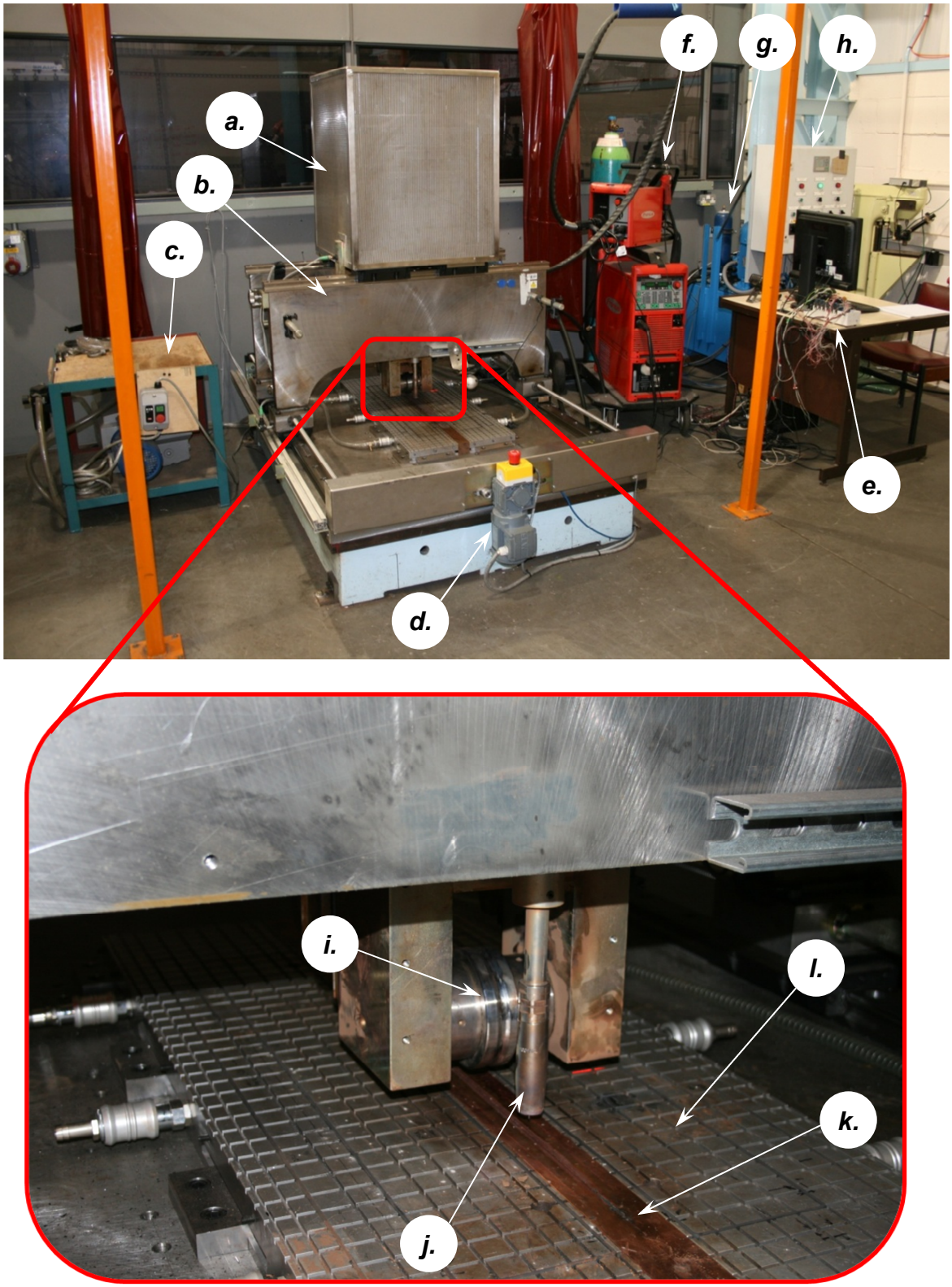

Figure D-1 Experimental equipment [211]. *a.* Oscillating mass; *b.* Crossbeam; *c.* Vacuum pump; *d.* Feed motor; *e.* Computer and National Instruments DAQ-mx modular data acquisition unit; *f.* Fronius TransPuls Synergic 5000; *g.* Main hydraulic system; *h.* Controls; *i.* Roller assembly; *j.* Welding torch; *k.* Copper backing-bar; and *l.* Aluminium vacuum clamp system.

The roller assembly can be dissembled and the roller can be changed for the appropriate roller profile. The fork can work with either a single axle roller or two individual shorter axles with two separate rollers, to roll fillet welds (fillet stiffness between the two rollers). The roller profiles can vary between 100 to 200 mm diameter, and a maximum width of 30 mm. The rollers were produced with tool steel and heat treated to obtain 540 HV.

D.2 Experimental parameters

The pre-weld rolling geometry of the plates used in this set of experiments was 500 × 200 × 4 mm, being the longer distance the rolled and welded directions. All the plates were rolled with a flat profile roller of 30 mm width and 100 mm diameter, at different distances from the edge and with different loads (see figure 3-1). In addition, the plates were roller either in the upper or lower surfaces with a rolling speed of 8.33 mm·s^{-1}. The welding and rolling parameters are shown in table D-1 and table D-2.

Table D-1 Welding parameters implemented in the experiments

Experiment	Wire feed speed [mm·s-1]	Travel speed [mm·s^{-1}]	Nominal heat [W]	Wire diameter [mm]	Gas flow rate [l·min^{-1}]	Gas composition
Pre-weld rolling	242	10.8	9938	1	14	5% CO2, 2% O2, balance Ar
Post-weld rolling and *In situ* rolling	250	8.33	12096	1	10	20% CO2, 2% O2, balance Ar

The post-weld rolling weldments were 750 × 300 × 6 mm, being the longer distance the rolled and welded directions. Two different set of rollers were implemented; both of 100 mm diameter and a rolling speed of 8.33 mm·s^{-1}. The first, grooved roller, had a 12 mm radius groove (see figure 4-2 *a*), which was larger than the weld bead profile, used to roll the top of the weld beads. The second, double flat roller (see figure 4-2 *b*), was conformed by two flat rollers of 9 mm width and a space between them of 8 mm.

Table D-2 Pre-weld rolling parameter

Rolling Load [kN]	Rolling Position [mm]
25	15; 25; 35
50	15; 25; 35
100	15; 25; 35; 55; 75
200	55; 75

Table D-3 show the rolling parameters implemented in the post weld rolling experiments.

Table D-3 Post-weld rolling parameter

Roller Profile	Rolling Load [kN]
Grooved	25; 50; 100; 150
Double flat	150

The *in situ* rolling specimens had the same geometry of the post-weld rolling ones. They were rolled using the grooved roller described above at the same rolling speed as the post-weld samples. The trailing distance of the roller axis from the torch was 100 mm. The loads investigated were 20, 50, and 100 kN.

D.3 Experimental measurements

In this section a brief description of the experimental measurement techniques is provided. A detailed description of the measurement technique can be found in Coules *et al.* [2,4].

Laser scans to measure distortion

All the samples were scanned by a Laser coordinate system in the upper surface, as shown in figure D-2 *a* and *b*. The raw data produced by the scanning was processed by a Matlab algorithm, which interpolated and fit the

out-of-plane distortion in a grid of 10 × 10 mm as shown in figure D-2 *c*. The data corresponding to the weld bead was removed and the peak out-of-plane distortion was determined.

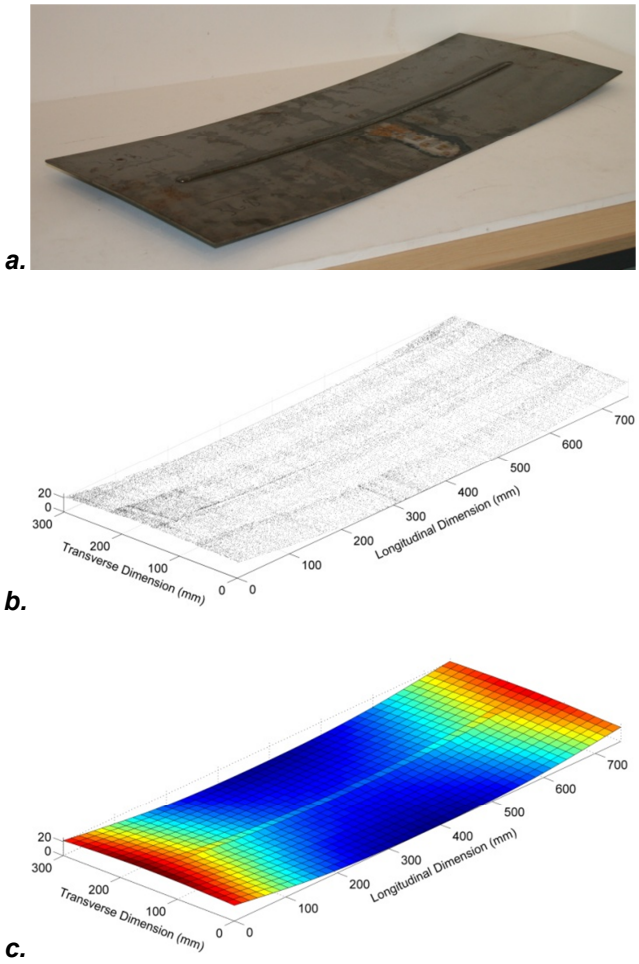

Figure D-2 Measurement of the out-of-plane distortion [4]. *a.* as-welded sample; *b.* Laser scanning data before filtering; *c.* filtered mesh.

Neutron diffraction measurements

This strain measurements were performed at Institut Laue-Langevin in France, with the SALSA instrument [208], and with the ENGIN-X instrument, at the ISIS neutron source, Rutherford Appleton Laboratory, UK [231]. The SALSA measurements were performed using a cuboid gauge volume of 2 × 2 × 2 mm in the longitudinal direction, while 2 × 20 × 2 mm in the transverse and normal ones. A neutron wavelength of 1.644 Å was used to measure the interplanar

spacing of the ferritic plane {211}, across the middle of the sample as shown in figure D-4 and figure D-3. Unstressed measurements of the lattice parameter (d0) were taken in all the direction to counteract the texture effect. These measurements were used to determine the elastic strain in the three orthogonal directions in the middle thickness of the samples.

The measurements provided by the SALSA instrument were used to validate the RS distribution on the middle plane across the sample width of:

- the as-welded condition of the post-weld rolling geometry,
- the pre-weld rolling plates before welding, with 100 and 200 kN load at 55 mm from the edge,
- the pre-weld rolling after welding with 200 kN at 55 mm from the centreline,
- the post-weld rolling with 25, 50, 100, and 150 kN, with the grooved roller,
- the *in situ* rolling with a trailing distance of 100 mm and 25, 50, and 100 kN.

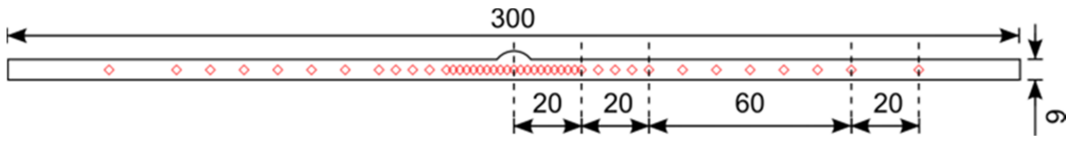

Figure D-3 Cross section of the of the post-weld rolling and *in situ* geometries, tested with the SALSA instrument, showing the location of the neutron diffraction measurements [2].

The ENGIN-X measurements on the other hand, were performed using a gauge volume of 1 × 2 × 1 mm in the longitudinal direction, while 1 × 15 × 1 mm in the transverse and normal ones. Each measurement was taken with a spacing of 2 mm. The actual positions of the measurement are represented as crosses in the appropriate figures (see the validation sections in chapter 4).

The ENGIN-X measurement, were used to validate the RS through the sample thickness generating a topography of the residual stress in the orthogonal directions in the weld bead and heat affected zones of:

- the post-weld rolling with 150 kN, with the grooved roller,
- the post-weld rolling with 150 kN, with the double flat roller.

The residual stress was calculated by assuming isotropic elastic properties in a triaxial stress state, as shown in eq. D-1 [232].

$$\sigma_{xx} = \frac{\nu E}{(1+\nu)(1-2\nu)}\{\varepsilon_{xx} + \varepsilon_{yy} + \varepsilon_{zz}\} + \frac{E}{1+\nu}\varepsilon_{xx} \qquad \text{Eq. D-1}$$

Where σ_{ii} and ε_{ii} are the stress and strain in the i-th direction, ν and E are the Poisson ratio and Young's modulus, respectively. The predicted elastic constants by Kröner [23] were used in the calculations (E = 225.5 GPa, and ν = 0.28).

D.4 Strain gauges measurement

Resistance strain gauge foils (3.2 × 2.0 mm) were used to measure the elastic strain of welded samples (3 mm thickness), as shown in figure D-4 *a*. The welding parameters are shown in table D-4. The welded samples were held flat during welding by a vacuum clamping system, and were unclamped after 600 s of accomplishment of the weld. Temperature and strain measurement were performed during welding and cooling. The strain measurements were compensated against temperature effect. The strain gauge at the 20 and 30 mm from the weld seam were elevated-temperature Ni-Cr strain gauges, while the rest of them were general-purpose constantan (copper-nickel alloy, usually 55% copper, 45% nickel) gauges.

Table D-4 Welding parameters implemented in the strain gauge experiments with the 3 mm thick plates

Wire feed speed [mm·s^{-1}]	Travel speed [mm·s^{-1}]	Nominal heat [W]	Wire diameter [mm]	Gas flow rate [l·min^{-1}]	Gas composition
173	10.8	5509	1	12	20% CO2, 2% O2, balance Ar

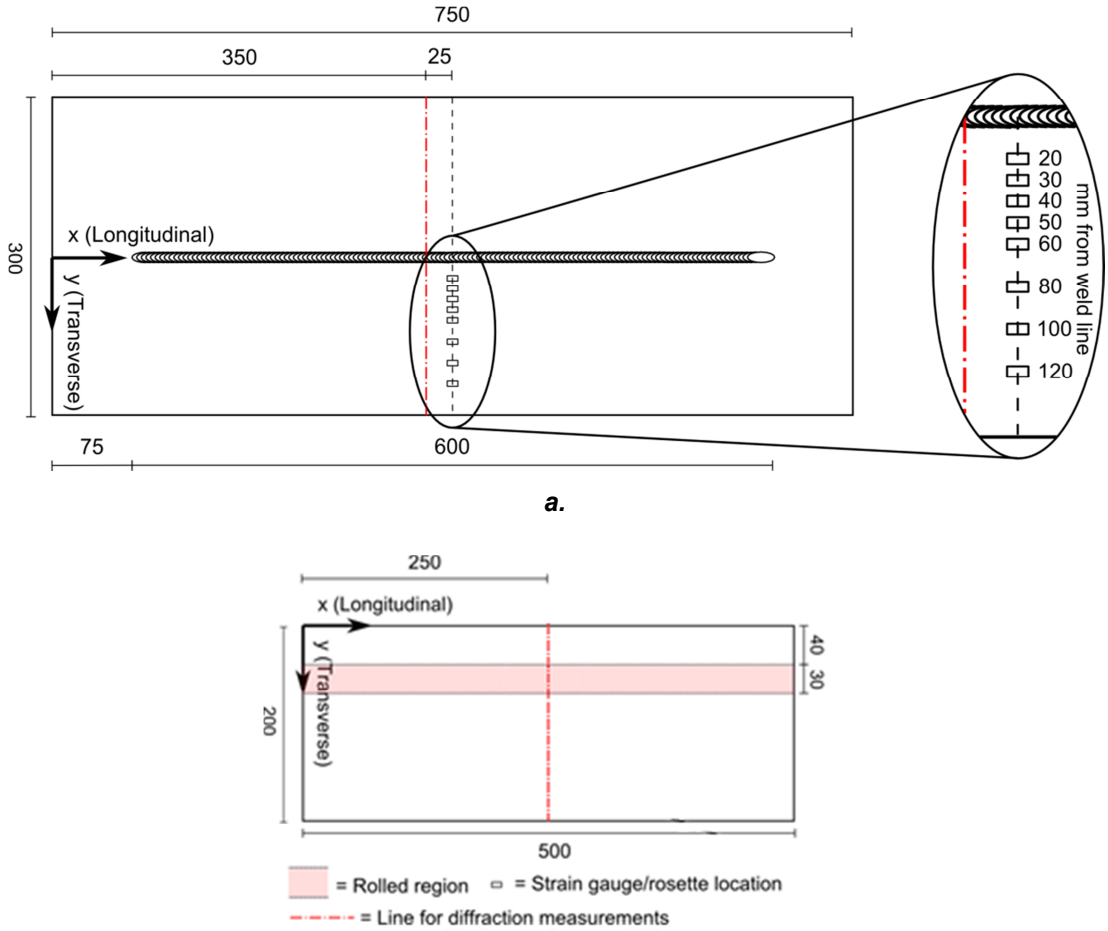

Figure D-4 Strain measurement locations [4]: *a.* welded sample with 3 mm thick plate; *b.* pre-weld rolling plate.

This technique was used to measure the elastic stress of the weldment and pre-weld rolling plate geometries. The absence of yielding was verified by comparison against the von Mises stress at the strain gauge locations.

References

[1] Coules H. E., Cozzolino L. D., Colegrove P., and Wen S. W., 2011, “The effect of pre-weld rolling on distortion and residual stress in fusion welded steel plate,” Materials Science Forum, Trans Tech Publ, pp. 486–491.

[2] Coules H. E., Colegrove P., Cozzolino L. D., Wen S. W., Ganguly S., and Pirling T., 2012, “Effect of high pressure rolling on weld-induced residual stresses,” Sci. Technol. Weld. Join., **17**(5), pp. 394–401.

[3] Coules H. E., Colegrove P., Cozzolino L. D., Wen S. W., and Kelleher J. F., 2013, “High pressure rolling of low carbon steel weld seams: Part 2 - Roller geometry and residual stress,” Sci. Technol. Weld. Join., **18**(1), pp. 84–90.

[4] Coules H. E., Cozzolino L. D., Colegrove P., Ganguly S., Wen S. W., and Pirling T., 2012, “Residual strain measurement for arc welding and localised high-pressure rolling using resistance strain gauges and neutron diffraction,” J. Strain Anal. Eng. Des., **47**(8), pp. 576–586.

[5] Ueda Y., and Yamakawa T., 1971, “Analysis of thermal elastic-plastic stress and strain during welding by finite element method,” Trans. Japan Weld. Soc., **2**(2), pp. 186–196.

[6] Hibbitt H. D., and Marcal P. V., 1973, “A numerical, thermo-mechanical model for the welding and subsequent loading of a fabricated structure,” Comput. Struct., **3**(5), pp. 1145–1174.

[7] Friedman E., 1975, “Thermomechanical Analysis of the Welding Process Using the Finite Element Method,” J. Press. Vessel Technol., **97**(3), p. 206.

[8] Withers P. J., and Bhadeshia H. K. D. H., 2001, “Residual stress part 1 - Measurement techniques,” Mater. Sci. Technol., **17**(4), pp. 355–365.

[9] Totten G., Howes M., and Inoue T., eds., 2002, Handbook of residual stress and deformation of steel, ASM International.

[10] Masubuchi K., 1980, Analysis of welded structures, Pergamon Press.

[11] Williams S. W., 2009, “Residual stress in friction stir welding,” Friction Stir Welding: From Basics to Applications, Z.C. D. Lohwasser, ed., Woodhead Publishing Limited, pp. 215–244.

[12] Wilson W. M., and Hao C.-C., 1946, Residual stresses in welded structures, Elsevier, Illinois, USA.

[13] Masubuchi K., 2005, “Residual Stresses and Distortion in Welds,” Encycl. Mater. Sci. Technol., pp. 8121–8126.

[14] McPherson N. A., Suarez-Fernandez N., Moon D. W., Tan C. P. H., Lee C. K., and Baker T. N., 2005, “Laser and laser assisted arc welding processes for DH 36 microalloyed steel ship plate,” Sci. Technol. Weld. Join., **10**(4), pp. 460–467.

[15] Colegrove P., Ikeagu C., Thistlethwaite A., Williams S. W., Nagy T., Suder W., Steuwer A., and Pirling T., 2009, “Welding process impact on residual stress and distortion,” Sci. Technol. Weld. Join., **14**(8), pp. 717–725.

[16] Rossini N. S., Dassisti M., Benyounis K. Y., and Olabi a. G., 2012, “Methods of measuring residual stresses in components,” Mater. Des., **35**, pp. 572–588.

[17] Withers P. J., Turski M., Edwards L., Bouchard P. J., and Buttle D. J., 2008, “Recent advances in residual stress measurement,” Int. J. Press. Vessel. Pip., **85**(3), pp. 118–127.

[18] Leggatt R. H., Smith D. J., Smith S. D., and Faure F., 1996, “Development and experimental validation of the deep hole method for residual stress measurement,” J. Strain, **31**(3), pp. 177–186.

[19] Kelsey R., 1956, “Measuring non-uniform residual stresses by the hole drilling method,” Proc. SESA, **14**(1), pp. 181–194.

[20] Treuting R. G., and Read W. T., 1951, “A Mechanical Determination of Biaxial Residual Stress in Sheet Materials,” J. Appl. Phys., **22**(2), p. 130.

[21] Cullity B. D., 1956, Elements of X-ray Diffraction, ADDISON-WESLEY.

[22] Noyan I. C., and Cohen J. B., 1987, Residual Stress Measurement by Diffraction and Interpretation, Springer New York, New York, NY.

[23] Hutchings M. T., Withers P. J., Holden T. M., and Lorentzen T., 2005, Introduction to the characterization of residual stress by neutron diffraction, Taylor and Francis CRC ebook account.

[24] Webster P. J., Djapic Oosterkamp L., Browne P. A., Hughes D. J., Kang W. P., Withers P. J., and Vaughan G. B. M., 2001, “Synchrotron X-ray residual strain scanning of a friction stir weld,” J. Strain Anal. Eng. Des., **36**(1), pp. 61–70.

[25] Withers P. J., and Webster P. J., 2001, “Neutron and synchrotron X-ray strain scanning,” Strain, **37**(1), pp. 19–33.

[26] Nierlich W., and Gegner J., 2008, “X-Ray diffraction residual stress analysis: One of the few advanced physical measuring techniques that have established themselves for routine application in industry,” Adv. Solid State Phys., **47**, pp. 301–314.

[27] Ohanian H. C., 1989, Physics, W W Norton & Company Incorporated, London.

[28] Hauk V., ed., 1997, Structural and Residual Stress Analysis by Nondestructive Methods, Elsevier Science, Amsterdam.

[29] Bray D. E., and Dietrich M., 1997, “Stress Evaluation in High Speed Rotating Machinery with the LCR Ultrasonic Technique,” Proceedings of the 26th Turbo Machinery Symposium, pp. 143–149.

[30] Ilker Yelbay H., Cam I., and Hakan Gür C., 2010, “Non-destructive determination of residual stress state in steel weldments by Magnetic Barkhausen Noise technique,” NDT E Int., **43**(1), pp. 29–33.

[31] Prime M. B., 2001, “Cross-Sectional Mapping of Residual Stresses by Measuring the Surface Contour After a Cut,” J. Eng. Mater. Technol., **123**(2), p. 162.

[32] Prime M. B., Hill M. R., DeWald A. T., Sebring R. J., Dave V. R., and Cola M. J., 2002, “Residual stress mapping in welds using the contour method,” Trends in Welding Research, Proceedings of the 6th International Conference, S.A. David, ed., ASM International, Pine Mountain, GA, pp. 891–896.

[33] Prime M. B., 2009, “The Contour Method: A New Approach in Experimental Mechanics,” Proceedings of the SEM Annual Conference, New Mexico, USA.

[34] Radaj D., 1992, Heat effects of welding: temperature field, residual stress, distortion, Springer-Verlag, Berlin.

[35] Papazoglou V. J., and Masubuchi K., 1978, “Analysis and control of distortion in welded aluminum structures,” Weld. Journal, Res. Suppl., (September), p. 251s–262s.

[36] Feng Z., ed., 2005, Processes And Mechanisms of Welding Residual Stress And Distortion, CRC Press.

[37] Dong P., 2005, “Residual stresses and distortions in welded structures: a perspective for engineering applications,” Sci. Technol. Weld. Join., **10**(4), pp. 389–398.

[38] Yang Y. P., Dong P., Brust F. W., Zhang J., and Cao Z., 2000, “Numerical prediction of welding-induced buckling distortion and buckling mechanisms,” Adv. Comput. Eng. Sci.

[39] Messler R. W., 1999, Principles of Welding: Processes, Physics, Chemistry, and Metallurgy, Wiley-VCH.

[40] Van der Aa E. M., 2007, “Local cooling during welding: prediction and control of residual stresses and buckling distortion,” Delft University of Technology.

[41] Pilipenko A., 2001, “Computer simulation of residual stress and distortion of thick plates in multi-electrode submerged arc welding. Their mitigation techniques,” Norwegian University of Science and Technology.

[42] Dydo R. J., Castner H. R., and Koppenhoefer K., 1999, Guidelines for The Control of Distortion in Thin Ship Structures, Columbus, Ohio.

[43] Vinokurov V. A., 1977, Welding stresses and distortion: determination and elimination, British Library Lending Division.

[44] Rajendran P., Sivakumar V. R., and Gunaraj V., 2011, “STATISTICAL ANALYSIS ON ANGULAR DISTORTION OF WELDED STRUCTURAL STEEL PLATES,” Int. J. Eng. Sci. Technol., **3**(4), pp. 3404–3421.

[45] Watanabe M., and Satoh K., 1961, “Effect of welding conditions on the shrinkage and distortion in welded structures,” Weld. J., **40**(8), p. 377s–384s.

[46] Tsai C. L., Park S. C., and Cheng W. T., 1999, “Welding distortion of a thin-plate panel structure,” Weld. JOURNAL-NEW YORK-, **78**(May), p. 156s–165s.

[47] Schenk T., Richardson I. M., Kraska M., and Ohnimus S., 2009, “A study on the influence of clamping on welding distortion,” Comput. Mater. Sci., **45**(4), pp. 999–1005.

[48] Gannon L., Liu Y., Pegg N., and Smith M., 2010, “Effect of welding sequence on residual stress and distortion in flat-bar stiffened plates,” Mar. Struct., **23**(3), pp. 385–404.

[49] Schenk T., Richardson I. M., Kraska M., and Ohnimus S., 2009, “Influence of clamping on distortion of welded S355 T-joints,” Sci. Technol. Weld. Join., **14**(4), pp. 369–375.

[50] Mochizuki M., Hayashi M., and Hattori T., 2000, “Residual Stress Distribution Depending on Welding Sequence in Multi-Pass Welded Joints With X-Shaped Groove,” J. Press. Vessel Technol., **122**(1), pp. 27–32.

[51] Kadivar M. H., Jafarpur K., and Baradaran G. H., 2000, “Optimizing welding sequence with genetic algorithm,” Comput. Mech., **26**(6), pp. 514–519.

[52] The Welding Institute (TWI), 2010, “Knowledge for welders. Distortion - prevention by design.”

[53] Kou S., 2003, Welding Metallurgy, John Wiley and Sons.

[54] Nitschke-Pagel T., and Wohlfahrt H., 2002, “Residual Stresses in Welded Joints – Sources and Consequences,” Mater. Sci. Forum, **404-407**, pp. 215–226.

[55] Bhadeshia H. K. D. H., 2004, “Developments in martensitic and bainitic steels: role of the shape deformation,” Mater. Sci. Eng. A, **378**(1-2), pp. 34–39.

[56] Francis J. a., Bhadeshia H. K. D. H., and Withers P. J., 2007, “Welding residual stresses in ferritic power plant steels,” Mater. Sci. Technol., **23**(9), pp. 1009–1020.

[57] Withers P. J., and Bhadeshia H. K. D. H., 2001, “Residual stress part 2 - Nature and origins,” Mater. Sci. Technol., **17**(4), pp. 366–375.

[58] Leblond J. B., Devaux J., and Devaux J. C., 1989, “Mathematical modelling of transformation plasticity in steels I: case of ideal-plastic phases,” Int. J. Plast., **5**, pp. 551–572.

[59] Deng D., 2009, “FEM prediction of welding residual stress and distortion in carbon steel considering phase transformation effects,” Mater. Des., **30**(2), pp. 359–366.

[60] Kumose T., Yoshida T., Abe T., and Onoue H., 1954, “Prediction of angular distortion caused by one-pass fillet welding,” Weld. J., **33**(10), pp. 945–956.

[61] Henry R. W., 1974, “Reduction of out-of-plane distortion in fillet welded high strength aluminum.,” MIT.

[62] Mrvar P., Medved J., and Kastelic S., 2011, “Welding Sequence Definition Using Numerical Calculation,” Weld. J., **7**, pp. 5–8.

[63] Guan Q., 1994, “Dynamic control of welding distortion by moving spot heat sink,” Weld. World.

[64] Gabzdyl J., Johnson A., Williams S. W., and Price D. A., 2003, “Laser weld distortion control by cryogenic cooling,” Proceedings of SPIE, Spie, pp. 269–274.

[65] Pazooki A. M. A., 2010, “Transient Thermal Tensioning during Welding of AISI 316 L and DP 600 Steel Sheets,” TMS 2010 Annual Meeting & Exhibition, Minerals, Metals and Materials Society/AIME, Seattle, WA (USA).

[66] Han W. T., Wan F. R., Li G., Dong C. L., and Tong J. H., 2011, “Effect of trailing heat sink on residual stresses and welding distortion in friction stir welding Al sheets,” Sci. Technol. Weld. Join., **16**(5), pp. 453–458.

[67] Nagy T., 2012, “Investigation of thermal techniques to mitigate buckling distortion in welding panels,” Cranfield University.

[68] Pazooki A. M. A., Hermans M. J. M., and Richardson I. M., 2011, “Reduction of welding distortion in DP600 steel by manipulation of temperature distribution during welding,” Proceedings of the IWOTE’11: International Workshop on Thermal Forming and Welding Distortion, F. Vollertsen, ed., Bias Verlang, Bremen, Germany, pp. 181–202.

[69] Nagy T., Williams S. W., Colegrove P., Ikeagu C., and Fafiolu I., 2008, “Distortion Mitigation in Welded Ship Panels,” International Workshop on Thermal Forming and Welding Distortion, F. Vollertsen, and J. Sakkiettibutra, eds., Bias Verlang, Bremen, Germany, pp. 265–275.

[70] Ohata M., Toda Y., Toyoda M., and Takeno S., 1999, “Control of welding distortion in fillet welds of aluminium alloy thin plates,” Weld. Int., **13**(12), pp. 967–976.

[71] Takeno S., and Takada H., 1999, “Investigation on the correction of distortion of MIG fillet welds in aluminum alloy,” Joints in Aluminium - INALCO ’98: Seventh International Conference, Woodhead Publishing, Cambridge, UK, pp. 345–353.

[72] Vinokurov V. A., 1987, “Mechanical aspect of stress relieving by heat and non-heat treatment,” Proceedings of the International Conference: Stress Relieving Heat Treatments of Welded Steel Construcions, Elsevier Science Limited, Sofia, Bulgaria, pp. 1–11.

[73] Price D. A., Williams S. W., Wescott A., Harrison C. J. C., Rezai A., Steuwer A., Peel M., Staron P., and Koçak M., 2007, “Distortion control in welding by mechanical tensioning,” Sci. Technol. Weld. Join., **12**(7), pp. 620–633.

[74] Huther I., Lieurade H. P., Souissi R., and Nussbaumer A., 1996, “Analysis of results on improved welded joints,” Weld. World, **37**(5), pp. 242–66.

[75] Branco C., Infante V., and Baptista R., 2004, “Fatigue behaviour of welded joints with cracks, repaired by hammer peening,” Fatigue Fract. Eng. Mater. Struct., **27**(9), pp. 785–798.

[76] Günther H.-P., and Kuhlmann U., 2009, “Nachweiskonzepte zur Bemessung ermüdungsbeanspruchter Bauteile unter Berücksichtigung von Schweißnahtnachbehandlungsverfahren durch höherfrequentes Hämmern (Fatigue design concepts for post-weld treated joints improved by high frequency hammer peening met,” Stahlbau, **78**(9), pp. 613–621.

[77] Trufiakov V. I., Mikheev P. P., and Kudryavtsev Y. F., 1995, “Fatigue Strength of Welded Structures. Residual Stresses and Strengthening Treatments,” Weld. Surf. Rev., **3, Part 2**, p. 102.

[78] Gurney T. R., 1979, Fatigue of welded structures, Cambridge Univ. Pr., Cambridge, UK.

[79] Booth G. S., 1983, A review of fatigue strength improvement techniques, Abingdon, UK.

[80] Kirkhope K. J., Bell R., Caron L., and Basu R. I., 1997, Weld detail fatigue life improvement techniques.

[81] Munsi A. S. M. Y., Waddell A. J., and Walker C. A., 2001, “The Influence of Vibratory Treatment on the Fatigue Life of Welds: A Comparison with Thermal Stress Relief,” Strain, **37**(4), pp. 141–149.

[82] Walker C., 2011, “A theoretical review of the operation of vibratory stress relief with particular reference to the stabilization of large-scale fabrications,” Proc. Inst. Mech. Eng. Part L J. Mater. Des. Appl., **225**(3), pp. 195–204.

[83] Siddiqui M. A., Correia J. P. M., Ahzi S., and Belouettar S., 2009, “Electromagnetic forming process: estimation of magnetic pressure in tube expansion and numerical simulation,” Int. J. Mater. Form., **2**(S1), pp. 649–652.

[84] Xu D., Liu X. S., Wang P., Yang J. G., and Fang H. Y., 2009, “New technique to control welding buckling distortion and residual stress with non-contact electromagnetic impact,” Sci. Technol. Weld. Join., **14**(8), pp. 753–759.

[85] Harvey G. W., Jolla L., and Brower D. F., 1961, “Metal Forming Device and Method,” US Pat. 2,976,907.

[86] Kurkin S. A., and Anufriev V. I., 1984, “Preventing Distortion of Welded Thin-Walled Members of AMg 6 and 1201 Aluminum Alloys by Rolling the Weld With a Roller Behind the Welding Arc,” Weld. Prod. (English Transl. Svarochnoe Proizv., **31**(10), pp. 52–55.

[87] Kondakov G. F., and Martynov A. N., 1986, “Effect of methods of local deformation on residual stresses and properties of welded joints,” Weld. Prod. (English Transl. Svarochnoe Proizv., **33**(5), pp. 28–30.

[88] Kondakov T. F., 1988, “High temperature rolling in welding butt joints,” Weld. Int., **34**(2), pp. 172–175.

[89] Pavlovsky V. I., and Masubuchi K., 1994, “Research in the USSR on residual stresses and distortion in welded structures,” Weld. Res. Counc. Bull., (388), p. 62.

[90] Kondakov G. F., 1995, “Calculating the solidification front in the thickness of the material in high-temperature rolling during welding,” Weld. Int., **9**(11), pp. 917–920.

[91] Kondakov G. F., and Bantserzh N. E., 1996, “Quantitative analysis of defects in arc butt welded joints in titanium alloys,” Weld. Int., **10**(3), pp. 246–248.

[92] Liu W., Tian X., and Zhang X., 1996, “Preventing weld hot cracking by synchronous rolling during welding,” Weld. J., **75**(9), p. 297s–304s.

[93] Yang Y. P., Dong P., Tian X., and Zhang Z., 1998, “Prevention of Welding Hot Cracking of High Strength Aluminum Alloys by Mechanical Rolling,” ASM Proceedings of the International Conference: Trends in Welding Research, J.J.A.S.H.B.D.T. Vitek J.M. David S.A., ed., Pine Mountain, GA, pp. 700–705.

[94] Guan Q., 1999, “A survey of development in welding stress and distortion controlling in aerospace manufacturing engineering in China,” Weld. World, **43**(1), pp. 64–74.

[95] Yang Y. P., Dong P., Zhang J., and Tian X., 2000, “A hot-cracking mitigation technique for welding high-strength aluminum alloy,” Weld. J., **79**(1), p. 9s–17s.

[96] Xu W., Fan C., Fang H., and Tian X., 2004, “New development in welding thin-shell aluminum alloy structures with high strength,” China Weld., **13**(1), pp. 27–30.

[97] Wen S. W., 2007, Development and Evaluation of a Roller System for Mitigation of Weld Residual Stress and Distortion.

[98] Zhu D.-C., Zhang L.-W., Pei J.-B., Zhang G.-L., and Wei R.-X., 2009, “Residual stress engineering in friction stir welds by roller tensioning,” Sci. Technol. Weld. Join., **14**(2), pp. 185–192.

[99] Sun Y.-J., Zang Y., and Shi Q.-Y., 2009, “High Precision Modeling of Welding and Post Welding Cold Rolling Continuous Process in Numerical Simulation,” Proceedings of The Second International Conference on Modelling and Simulation, Manchester, England, pp. 312–318.

[100] Threadgill P. L., Leonard A. J., Shercliff H. R., and Withers P. J., 2009, “Friction stir welding of aluminium alloys,” Int. Mater. Rev., **54**(2), pp. 49–93.

[101] Sun Y.-J., Zang Y., and Shi Q.-Y., 2010, “Numerical Simulations of Friction Stir Welding Process and Subsequent Post Weld Cold Rolling Process,” Key Eng. Mater., **419**, pp. 433–436.

[102] Wen S. W., Colegrove P., Williams S. W., Morgan S. A., Wescott A., and Poad M., 2010, “Rolling to control residual stress and distortion in friction stir welds,” Sci. Technol. Weld. Join., **15**(6), pp. 440–447.

[103] Yang Y. P., and Dong P., 2011, “Buckling Distortions and Mitigation Techniques for Thin-Section Structures,” J. Mater. Eng. Perform., **21**(2), pp. 153–160.

[104] Altenkirch J., Steuwer a., Withers P. J., Williams S. W., Poad M., and Wen S. W., 2009, “Residual stress engineering in friction stir welds by roller tensioning,” Sci. Technol. Weld. Join., **14**(2), pp. 185–192.

[105] Kurkin S. A., and Tsyao G., 1962, “Reduction of Residual Stresses in Thin-Walled Members of Titanium Alloys,” Weld. Prod. (English Transl. Svarochnoe Proizv., **10**, p. 1.

[106] Kurkin S. A., Anufriev V. I., and Milekhin E. S., 1980, “Improving the Mechanical Properties of Welded Joints in the AMg6 Alloy by Plastic Deformation During Arc Welding,” Weld. Prod. (English Transl. Svarochnoe Proizv., **27**(3), pp. 20–24.

[107] Wescott A., 2009, “Residual stress and distortion control of weldments by applying local mechanical tensioning methods,” Cranfield University.

[108] Grong Ø., 1997, Metallurgical modelling of welding, Maney Publishing, London.

[109] Fourier J. B., 1822, “Theorie analytique de la chaleur (The Analytical Theory of Heat).”

[110] Simonson J. R., 1967, An introduction to engineering heat transfer, McGRAW-HILL International, London.

[111] Holman J. P., 2009, Heat Transfer, McGraw Hill Higher Education.

[112] Rosenthal D., 1941, “Mathematical theory of heat distribution during welding and cutting,” Weld. J., **20**(5), pp. 220–234.

[113] Rosenthal D., 1946, “The theory of moving sources of heat and its application to metal treatments,” Trans. ASME, **68**(11), pp. 849–866.

[114] Adams Jr C. M., 1958, “Cooling rates and peak temperatures in fusion welding,” Weld. J., **37**, p. 210s–215s.

[115] Eagar T. W., and Tsai N.-S., 1983, “Temperature Fields Produced by Traveling Distributed Heat Sources,” Weld.J., **162**(12), p. 346–s–355–s.

[116] Rykalin N. N., 1976, “Energy Sources for Welding,” Rev. Sold., **6**(3), pp. 125–140.

[117] Myers P. S., Uyehara O. A., and Borman G. L., 1967, “Fundamentals of heat flow in welding,” Weld. Res. Counc. Bull., **123**(123), pp. 1–46.

[118] Goldak J., and Akhlaghi M., 2005, Computational welding mechanics, Springer.

[119] Goldak J., Chakravarti A., and Bibby M., 1984, “A new finite element model for welding heat sources,” Metall. Trans. B, **15**(2), pp. 299–305.

[120] British Standards, 2004, “Hot rolled products of structural steels— Part 2: Technical delivery conditions for non-alloy structural steels,” BS EN 10025-22004, **10025-1: 2**.

[121] Komanduri R., and Hou Z. B., 2001, “Thermal analysis of the arc welding process: Part II. effect of variation of thermophysical properties with temperature,” Metall. Mater. Trans. B, **32**(3), pp. 483–499.

[122] McDILL J. M. J., Oddy A. S., Goldak J., and Bennison S., 1990, “Finite element analysis of weld distortion in carbon and stainless steels,” J. Strain Anal. Eng. Des., **25**(1), pp. 51–53.

[123] Thistlethwaite A., 2007, “Evaluating the effect of welding parameters on residual stress magnitude using a simplified finite element analysis mode,” MsC. Thesis. Cranfield University.

[124] Zhu X. K., and Chao Y. J., 2002, “Effects of temperature-dependent material properties on welding simulation,” Comput. Struct., **80**(11), pp. 967–976.

[125] Tekriwal P., Stitt M., and Mazumder J., 1987, “Finite element modelling of heat transfer for gas tungsten arc welding.,” Met. Constr., **19**(10), p. 599R–606R.

[126] Long H., Gery D., Carlier A., and Maropoulos P. G., 2009, “Prediction of welding distortion in butt joint of thin plates,” Mater. Des., **30**(10), pp. 4126–4135.

[127] Mills K. C., 2002, Recommended values of thermophysical properties for selected commercial alloys, Woodhead Publishing and ASM International.

[128] Michaleris P., and Debiccari A., 1997, “Prediction of welding distortion,” Weld. J. (Miami, Fla), **76**(12), p. 172s–180s.

[129] Lindgren L.-E., 2007, Computational Welding Mechanics Thermomechanical and Microstructural Simulations, Woodhead Publishing.

[130] Al-Sulaiman F., Yilbas B. S., Karatas C., Keles O., Uslan I., Usta Y., Ahsan M., and Bazoune A., 2007, “Laser cutting of kevlar and mild steel composite structure: End product quality assessment,” J. Mater. Eng. Perform., **16**(1), pp. 22–29.

[131] Lindgren L.-E., 2001, “Finite element modeling and simulation of welding. part 2: Improved material modeling,” J. Therm. Stress., **24**(3), pp. 195–231.

[132] Peil U., and Wichers M., 2004, “Schweißen unter Betriebsbeanspruchung– Werkstoffkennwerte für einen S 355 J2G3 unter Temperaturen bis 1200°C,” Stahlbau, **73**(6), pp. 400–415.

[133] Tekriwal P., and Mazumder J., 1991, “Transient and residual thermal strain-stress analysis of GMAW,” J. Eng. Mater. Technol. Trans. ASME, **113**(3), pp. 336–343.

[134] Outinen J., 2007, “Mechanical properties of structural steels at high temperatures and after cooling down,” Helsinki University of Technology Laboratory of Steel Structures Publications.

[135] Outinen J., Kaitila O., and Mäkeläinen P., 2001, High-temperature testing of structural steel and modelling of structures at fire temperatures, Espoo, Finland.

[136] Outinen J., and Mäkeläinen P., 2004, “Mechanical properties of structural steel at elevated temperatures and after cooling down,” Fire Mater., **28**(24), pp. 237–251.

[137] Dieter G. E., 1961, Mechanical metallurgy, McGRAW-HILL International.

[138] Hinton E., 1992, NAFEMS: Introduction to nonlinear finite element analysis, Nafems.

[139] Lemaitre J., and Chaboche J.-L., 1994, Mechanics of solid materials, Cambridge University Press, Cambridge, UK.

[140] Dessault Systemes, 2009, “Abaqus 6.9/Documentation,” Abaqus Analysis User’s Manual.

[141] Barlat F., 2007, “Constitutive modeling for metals,” Adv. Methods Mater. Form., pp. 1–18.

[142] Huang X. P., and Cui W. C., 2006, “Effect of Bauschinger Effect and Yield Criterion on Residual Stress Distribution of Autofrettaged Tube,” J. Press. Vessel Technol., **128**(2), p. 212.

[143] Lindgren L.-E., 2006, “Numerical modelling of welding,” Comput. Met. Form., **195**(48-49), pp. 6710–6736.

[144] Felippa C. A., Park K. C., and Farhat C., 2001, “Partitioned analysis of coupled mechanical systems,” Comput. Methods Appl. Mech. Eng., **190**(24-25), pp. 3247–3270.

[145] Balagangadhar D., Dorai G. A., and Tortorelli D. A., 1999, “A displacement-based reference frame formulation for steady-state thermo-elasto-plastic material processes,” Int. J. Solids Struct., **36**, pp. 2397–2.

[146] Ding J., Colegrove P., Mehnen J., Ganguly S., Sequeira Almeida P. M., Wang F., and Williams S. W., 2011, “Thermo-mechanical analysis of Wire and Arc Additive Layer Manufacturing process on large multi-layer parts,” Comput. Mater. Sci., **50**, pp. 3315–3322.

[147] Brown S. B., and Song H., 1992, “Implications of three-dimensional numerical simulations of welding of large structures,” Weld. J.

[148] Brown S. B., and Song H., 1992, “Finite element simulation of welding of large structures,” J. Eng. Ind., **114**(4), pp. 441–451.

[149] Brown S. B., Christie K., and Song H., 1991, “Mechanical Effects of Welding,” Mechanical Effects of Welding, L. Karlsson, L.-E. Lindgren, and M. Jonsson, eds., Springer-Verlag, Lulea, Sweden, pp. 181–188.

[150] Mughal M. P., Fawad H., and Mufti R., 2006, “Finite element prediction of thermal stresses and deformations in layered manufacturing of metallic parts,” Acta Mech., **183**(1-2), pp. 61–79.

[151] Michaleris P., Feng Z., and Campbell G., 1997, “Evaluation of 2D and 3D FEA models for predicting residual stress and distortion,” ASME-PUBLICATIONS-PVP, **347**, pp. 91–104.

[152] Shan X. Y., Tan M. J., and O'Dowd N. P., 2007, "Developing a realistic FE analysis method for the welding of a NET single-bead-on-plate test specimen," J. Mater. Process. Technol., **192-193**, pp. 497–503.

[153] Michaleris P., Zhang L., Bhide S. R., and Marugabandhu P., 2006, "Evaluation of 2D, 3D and applied plastic strain methods for predicting buckling welding distortion and residual stress," Sci. Technol. Weld. Join., **11**(6), pp. 707–716.

[154] Cifuentes A. O., and Kalbag A., 1992, "A performance study of tetrahedral and hexahedral elements in 3-D finite element structural analysis," Finite Elem. Anal. Des., **12**, pp. 313–318.

[155] Benzley S. E., Perry E., Merkley K., Clark B., and Sjaardema G., 1995, "A comparison of all hexagonal and all tetrahedral finite element meshes for elastic and elasto-plastic analysis," 4th International Meshing Roundtable, pp. 179–191.

[156] Elcoate C. D., Bouchard P. J., and Smith M. C., 2003, "3-Dimensional Repair Weld Simulations–Bead-on-plate Comparisons," ABAQUS World Users' Conference, Munich.

[157] Shan X., Davies C., Wangsdan T., Odowd N., and Nikbin K., 2009, "Thermo-mechanical modelling of a single-bead-on-plate weld using the finite element method," Int. J. Press. Vessel. Pip., **86**(1), pp. 110–121.

[158] Lindgren L.-E., 2001, "Finite Element Modeling and Simulation of Welding Part 1: Increased Complexity," J. Therm. Stress., **24**(2), pp. 141–192.

[159] Fanous I. F. Z., Younan M. Y. A., and Wifi A. S., 2003, "3-D Finite Element Modeling of the Welding Process Using Element Birth and Element Movement Techniques," J. Press. Vessel Technol., **125**(2), pp. 144–150.

[160] Pavelic V., Tanbakuchi R., Uyehara O. A., and Myers P. S., 1969, "Experimental and computed temperature histories in gas tungsten-arc welding of thin plates," Weld. J., **48**(7), p. 295–s–305–s.

[161] Paley Z., and Hibbert P. D., 1975, "Computation of temperatures in actual weld designs.," Weld. J. (Miami, Fla), **54**(11).

[162] Westby O., 1968, Temperature distribution in the work-piece by welding, Marine Technology Centre, Trondheim, Norway.

[163] O'Brien R. L., ed., 1991, "Welding process," Weld. Handb., **2**.

[164] Schwenk C., Rethmeier M., Dilger K., and Michailov V., 2005, “Schweißsimulation im Fahrzeugbau - Möglichkeiten, Grenzen und Herausforderungen,” Schweißen und Schneid., **237**, pp. 353–358.

[165] Rosales M. J. C., Alcantara N. G., Santos J., and Zettler R., 2010, “The Backing Bar Role in Heat Transfer on Aluminium Alloys Friction Stir Welding,” Mater. Sci. Forum, **636-637**, pp. 459–464.

[166] Simar A., Pardoen T., and de Meester B., 2007, “Effect of rotational material flow on temperature distribution in friction stir welds,” Sci. Technol. Weld. Join., **12**(4), pp. 324–333.

[167] Shi Q.-Y., Dickerson T., and Shercliff H. R., 2003, “Thermo-mechanical FE modelling of friction stir welding of Al-2024 including tool loads,” 4th International Symposium on Friction Stir Welding, Park City, Utah, USA, p. 12.

[168] Shi Q.-Y., Dickerson T., and Shercliff H. R., 2003, “Thermo-mechanical Analyses of Welding Aluminium Alloy with TIG and Friction Stir Welding,” International Trends in Welding Research Conference Proceedings, ASM International, Pine Mountain, GA, pp. 247–252.

[169] Simar A., Lecomte-Beckers J., Pardoen T., and de Meester B., 2006, “Effect of boundary conditions and heat source distribution on temperature distribution in friction stir welding,” Sci. Technol. Weld. Join., **11**(2), pp. 170–177.

[170] Wang H., Colegrove P., and Dos Santos J., 2013, “Hybrid modelling of 7449-T7 aluminium alloy friction stir welded joints,” Sci. Technol. Weld. Join., **18**(2), pp. 147–153.

[171] Wang H., 2011, “Numerical and artifitial neural network modelling of friction stir welding,” Cranfield University.

[172] Colegrove P., Williams S. W., Ikeagu C., and Thistlethwaite A., 2009, “The Impact of Different Types of Welding Processes on the Residual Stress and Distortion in 4mm Thick Butt Welds of Ship Plate,” Trends in Welding Research, Proceedings of the 8th International Conference, pp. 758–765.

[173] Preston R. V., 2000, “Modelling of residual stresses in welded aerospace alloys,” PhD Thesis. University of Cambridge.

[174] Khandkar M. Z. H., Khan J. A., and Reynolds A. P., 2003, “Prediction of temperature distribution and thermal history during friction stir welding: input torque based model,” Sci. Technol. Weld. Join., **8**(3), pp. 165–174.

[175] Lindgren L.-E., 1996, “The use of simulations and the need of experiments in material processing,” Current Advances in Mechanical Design and production VI. The Six Cairo University International MDP Conference., Cairo, pp. 149–161.

[176] Smith M. C., and Smith A. C., 2009, “NeT bead-on-plate round robin: Comparison of transient thermal predictions and measurements,” Int. J. Press. Vessel. Pip., **86**(1), pp. 96–109.

[177] Thompson M. A., Fresini M., Dos Santos J., Hedgegard J., Dithey U., Richardson I. M., and Yapp D., 2005, SYNFAB: Improving the competitiveness of the European steel fabrication industry using synchronised tandem wire welding technology, Technical Report No. 3.

[178] Leblond J. B., 1989, “Mathematical modelling of transformation plasticity in steels II: coupling with strain hardening phenomena,” Int. J. Plast., **5**, pp. 573–591.

[179] Devaux J., Pont D., and Leblond J. B., 1991, “Numerical simulation of the repair of a defect-containing zone by a manual welding procedure,” ASME Proceedings of the 10th International Conference on Ocean, Offshore and Arctic Engineering, Stavanger, Norway, pp. 31–36.

[180] Timoshenko S. P., and Gere J. M., 1963, Theory of elastic stability, McGRAW-HILL International.

[181] Pattee F., 1975, “Buckling distortion of thin aluminum plates during welding.,” MIT.

[182] Okerblom N. O., 1958, The calculations of deformations of welded metal structures, Her Majesty’s Stationery Office, London.

[183] Christensen N., Davies V. L., and Gjermundsen K., 1965, “Distribution of temperatures in arc welding,” Br. Weld. J., **12**, pp. 54–75.

[184] Zhu D.-C., Zhang L.-W., Pei J.-B., Zhang G.-L., and Wei R.-X., 2008, “Experiment research on the thermal contact conductance during the solid plastic forming,” J. Plast. Eng., **15**(2), pp. 92–96.

[185] Hearn E. J., 1997, Mechanics of materials 1, Butterworth-Heinemann.

[186] Colegrove P., Coules H. E., Fairman J., Martina F., Kashoob T., Mamash H., and Cozzolino L. D., 2013, “Microstructure and residual stress improvement in wire and arc additively manufactured parts through high-pressure rolling,” J. Mater. Process. Technol., **213**(10), pp. 1782–1791.

[187] Camilleri D., Comlekci T., and Gray T. G. F., 2005, “Computational prediction of out-of-plane welding distortion and experimental investigation,” J. Strain Anal. Eng. Des., **40**(2), pp. 161–176.

[188] Ding J., 2012, “Thermo-mechanical analysis of wire and arc additive manufacturing process,” Cranfield University.

[189] British Standards, 2004, “Hot rolled products of structural steels— Part 3: Technical delivery conditions for normalized/normalized rolled weldable fine grain structural steels,” BS EN 10025-32004.

[190] Coules H. E., Cozzolino L. D., Colegrove P., and Wen S. W., 2011, “Measurement and modelling of the transient thermal-mechanical strain field during GMA welding,” Proceedings of the IWOTE’11: International Workshop on Thermal Forming and Welding Distortion, F. Vollertsen, ed., Bias Verlang, Bremen, Germany, pp. 267–278.

[191] Shanghvi J. Y., and Michaleris P., 2002, “Thermo-elasto-plastic finite element analysis of quasi-state processes in Eulerian reference frames,” Int. J. Numer. Methods Eng., **53**(7), pp. 1533–1556.

[192] Richards D. G., Prangnell P. B., Williams S. W., and Withers P. J., 2008, “Global mechanical tensioning for the management of residual stresses in welds,” Mater. Sci. Eng. A, **489**(1-2), pp. 351–362.

[193] Coules H. E., Colegrove P., Cozzolino L. D., and Wen S. W., 2012, “Experimental measurement of biaxial thermal stress fields caused by arc welding,” J. Mater. Process. Technol., **212**(4), pp. 962–968.

[194] Masubuchi K., 1996, “Prediction and control of residual stresses and distortion in welded structures,” Trans. JWRI, **25**(2), pp. 53–67.

[195] Verhaeghe G., 1998, Predictive formulae for weld distortion - a critical review, Abington Hall, UK.

[196] Asle Zaeem M., Nami M. R., and Kadivar M. H., 2007, “Prediction of welding buckling distortion in a thin wall aluminum T joint,” Comput. Mater. Sci., **38**(4), pp. 588–594.

[197] Watanabe M., and Satoh K., 1958, “Fundamental Study on Buckling of Thin Steel Plate due to Bead-Welding,” J. Japan Weld. Soc., **27**(6), pp. 313–320.

[198] McPherson N. A., Coyle A., and Wells M., 2008, “Induction heat straightening-A distortion rework reduction tool for thin plate,” Weld. Cut., **7**(3), pp. 162–166.

[199] Wang J., and Mote C. D., 1994, “Analysis Of Roller-induced Residual Stresses In Bandsaw Plates,” J. Sound Vib., **175**(5), pp. 647–659.

[200] Wen S. W., Williams S. W., Morgan S. A., Wescott A., Poad M., and Moore G., 2009, “Rolling of friction stir welds for residual stress and distortion control,” Proc. 9th Int. Semin. on “Numerical analysis of weldability,” Graz Technical University, Graz, Austria.

[201] Cook M., and Larke E. C., 1945, “Resistance of copper and copper alloys to homogeneous deformation in compression,” J. Inst. Met., **71**, pp. 371–390.

[202] Underwood L. R., 1950, The Rolling of Metals: Theory and Experiment, Chapman & Hall, London.

[203] Coules H. E., Colegrove P., Cozzolino L. D., and Wen S. W., 2013, “High pressure rolling of low carbon steel weld seams: Part 1 - Effects on mechanical properties and microstructure,” Sci. Technol. Weld. Join., **18**(1), pp. 76–83.

[204] Coules H. E., Cozzolino L. D., Colegrove P., Ganguly S., Wen S. W., and Pirling T., 2012, “Neutron Diffraction Analysis of Complete Residual Stress Tensors in Conventional and Rolled Gas Metal Arc Welds,” Exp. Mech.

[205] Tryfyakov V. I., Mikheev P. P., Kudryavtsev Y., Paton E. O., and Reznik D. N., 1993, “Ultrasonic Impact Peening Treatment of Welds and Its Effect on Fatigue Resistance in Air and Seawater,” Proceedings of Offshore Technology Conference, The Offshore Technology Conference, Houston, USA, pp. 183–193.

[206] Teng T.-L., Fung C.-P., and Chang P.-H., 2003, “Effect of residual stresses on the fatigue of butt joints using thermal elasto-plastic and multiaxial fatigue theory,” Eng. Fail. Anal., **10**(2), pp. 131–151.

[207] Bijak-Zochowski M., and Marek P., 1997, “Residual stress in some elasto-plastic problems of rolling contact with friction,” Int. J. Mech. Sci., **39**(1), pp. 15–32.

[208] Pirling T., Bruno G., and Withers P. J., 2006, “SALSA—A new instrument for strain imaging in engineering materials and components,” Mater. Sci. Eng. A, **437**(1), pp. 139–144.

[209] Price J. W. H., Ziaraparadowska A., Joshi S., Finlayson T., Semetay C., and Nied H., 2008, “Comparison of experimental and theoretical residual stresses in welds: The issue of gauge volume,” Int. J. Mech. Sci., **50**(3), pp. 513–521.

[210] Johnson M. W., Edwards L., and Withers P. J., 1997, “ENGIN — A new instrument for engineers,” Phys. B Condens. Matter, **234-236**(6), pp. 1141–1143.

[211] Coules H. E., 2012, “Characterising the effects of high-pressure rolling on residual stress in structural steel welds,” Cranfield University.

[212] Baker R. M., Ricksecker R. E., and Baldwin W. M. J., 1948, “Development of Residual Stresses in Strip Rolling,” AIME TRANS, **175**, pp. 337–354.

[213] Baldwin W. M. J., 1949, “Residual stresses in metals,” Proceeding ASTM, **49**, pp. 538–583.

[214] Cozzolino L. D., Coules H. E., Colegrove P., and Wen S. W., 2011, “Modelling distortion reduction on pre-and post-weld rolled gas metal arc welded plates,” Proceedings of the IWOTE’11: International Workshop on Thermal Forming and Welding Distortion, F. Vollertsen, ed., Bias Verlang, Bremen, Germany, pp. 169–179.

[215] Richards D. G., Prangnell P. B., Withers P. J., Williams S. W., Nagy T., and Morgan S., 2010, “Efficacy of active cooling for controlling residual stresses in friction stir welds,” Sci. Technol. Weld. Join., **15**(2), pp. 156–165.

[216] Askeland D. R., Fulay P. P., and Wright W. J., 2006, The science and engineering of materials, Global Engineering.

[217] British Standards, 2004, “Hot rolled products of structural steels— Part 1: General technical delivery conditions,” BS EN 10025-12004.

[218] British Standards, 2004, “Hot rolled products of structural steels— Part 4: Technical delivery conditions for thermomechanical rolled weldable fine grain structural steels,” BS EN 10025-42004.

[219] British Standards, 2004, “Hot rolled products of structural steels— Part 5: Technical delivery conditions for structural steels with improved atmospheric corrosion resistance—,” BS EN 10025-52004.

[220] British Standards, 2004, “Hot rolled products of structural steels — Part 6: Technical delivery conditions for flat products of high yield strength structural steels in the quenched and tempered condition,” BS EN 10025-62004 +A12009.

[221] Orr R. L., and Chipman J., 1967, “Thermodynamic functions of iron,” Trans. Metall. Soc. AIME, **239**, pp. 630–633.

[222] Papazoglou V. J., and Masubuchi K., 1982, “Numerical analysis of thermal stresses during welding including phase transformation effects,” J. Press. Vessel Technol., **104**(August), pp. 198–203.

[223] Watt D. F., Coon L., Bibby M., Goldak J., and Henwood C., 1988, “An algorithm for modelling microstructural development in weld heat-affected zones (part a) reaction kinetics,” Acta Metall., **36**(11), pp. 3029–3035.

[224] Thompson M. A., Fresini M., Dos Santos J., Hedgegard J., Dithey U., Richardson I. M., and Yapp D., 2008, Improving the competitiveness of the European steel fabrication industry using synchronised tandem wire welding technology. EUR 23331 EN, Luxembourg.

[225] Smith M. C., and Smith A. C., 2009, “NeT bead-on-plate round robin: Comparison of residual stress predictions and measurements,” Int. J. Press. Vessel. Pip., **86**(1), pp. 79–95.

[226] ASM, 1991, ASM Handbook: volume 4: Heat Treating, ASM International.

[227] Krauss G., 1990, Steels: heat treatment and processing principles.

[228] Andrews K., 1965, “Empirical formulae for the calculation of some transformation temperatures,” J. Iron Steel Inst., (July), pp. 721–727.

[229] Oran E. S., and Boris J. P., 2001, Numerical simulation of reactive flow, Cambridge Univ Pr, Cambridge, UK.

[230] Blazek J., 2005, Computational Fluid Dynamics: Principles and Applications, Elsevier.

[231] Santisteban J. R., Daymond M. R., James J. A., and Edwards L., 2006, “ENGIN-X: a third-generation neutron strain scanner,” J. Appl. Crystallogr., **39**(6), pp. 812–825.

[232] Young W., and Budynas R., 2002, Roark’s formulas for stress and strain, McGraw-Hill.